Active Flow Control on a Nonslender Delta Wing

Williams, Nathan

Award date:
2009

Awarding institution:
University of Bath

Active Flow Control on a Nonslender Delta Wing

Nathan Michael Williams

A thesis submitted for the degree of Doctor of Philosophy

University of Bath

Department of Mechanical Engineering

March 2009

ABSTRACT

The effects of active flow control by oscillatory blowing at the leading edge of a nonslender delta wing with a Λ=50° sweep angle have been investigated. Pressure measurements and Particle Image Velocimetry measurements were conducted on a half wing to investigate the formation of leading edge vortices for oscillatory blowing, compared to the stalled flow for the no blowing case. Stall has been delayed by up to 8°, and significant increases in the upper surface suction force have been observed. Velocity measurements show that shear layer reattachment is promoted with forcing, and a vortex flow pattern develops. The time averaged location of the centre of the vortical region moves outboard with increased excitation. The near-surface flow pattern obtained from the PIV measurements shows reattachment in the forward part of the wing. There is no measurable jet-like axial flow in the vortex core, which seems to break down at or very near the apex. This highlights that unlike slender delta wings, vortex breakdown is not a limiting factor in the generation of lift for nonslender delta wings. Phase averaged measurements reveal the perturbation due to the pulsed blowing, its interaction with the shear layer and vortex, apparent displacement of the vortex core, and relaxation of the reattachment region. The flow in a phase averaged sense is highly three dimensional. Experiments indicate that unsteady blowing at Strouhal numbers in the region of St=0.5 to St=0.75, and in the region of St=1.25 to St=1.5 can be a highly effective. Reattached flow can develop from stalled flow after pulsing has been initiated with a time constant of tU_∞/c=5 for unsteady blowing at St=0.75, and tU_∞/c=7 for St=1.5. Experiments with excitation from finite span slots located in the forward half of the wing show that partial blowing can be more effective at low momentum coefficients. Force measurements of a full delta wing confirmed that the effectiveness of this method of flow control was not only confined to half delta wings.

Table of Contents

Table of Figures and Tables

Acknowledgements

I would like to acknowledge the continual support, advice and input of my supervisors Ismet Gursul and Zhijin Wang. My wife Fiona has been a great help with her steadfast love and commitment. I thank God for the opportunities, challenges and support he has given me. I would like to acknowledge the help of Martin Bitter and Simon Smith in force measurements and initial pressure measurements.

Nomenclature

$Ajet$ = Cross sectional area of jet slot, m^2

c = Wing chord, m

C_D = Drag force coefficient

C_L = Lift force coefficient

C_l = Roll moment coefficient

$C_{M\ Apex}$ = Pitch moment coefficient about the apex

C_N = Normal force coefficient

C_μ = Momentum coefficient, $2(U_{jet}^2/ U_\infty^2)(\rho_{jet}/ \rho_\infty)(A_{jet}/S)$

C_P = Pressure coefficient

C_S = Suction force coefficient, $2F_S/(\rho U_\infty^2 S)$, *where* $F_S=\int p_{suction\ surface} dA$

E = Effectiveness, $\Delta C_S/C_\mu$

f = Pulsing frequency, Hz

Re = Reynolds Number, $U_\infty c/v$

s = Semispan, m

S = Wing area, m^2

St = Strouhal number, fc/U_∞

t = Time, s

P = Period of one pulse cycle, $1/f$

U_{jet} = Jet velocity at slot exit, ms^{-1}

U_∞ = Wind tunnel free stream velocity, ms^{-1}

v = Kinematic viscosity, 1.461×10^{-5} m^2s^{-1} (air at room temperature and sea level)

x = Chordwise distance, m

y = Spanwise distance, m

z = Distance from the wing surface in a plane normal to free stream, m

α = Angle of attack, degrees

Λ = Wing sweep angle, degrees

Γ = Circulation, m^2s^{-1}

ρ_{jet} = Density of the jet, kgm^{-3}

ρ_∞ = Density of the wind tunnel free stream, kgm^{-3}

Chapter 1 Introduction

Background

Increased interest in micro air vehicles (MAV's) and the increased commercial and military use of unmanned air vehicles(UAV's) has led to non-traditional wing platforms, such as nonslender delta wings, becoming more common place [1]. In particular for micro air vehicles, where high levels of lift are required from a wing with a limited wing span, wings with aspect ratios between 1 and 2 are common. Many performance obstacles still remain in the development of practical micro air vehicles, and advances need to be made to expand the operational envelope using new flow control techniques to increase aircraft performance. The aerodynamics of nonslender delta wings, defined in this study as having sweep angles between 35° and 55°, differ from the aerodynamics of both conventional wing platforms and slender delta wings. In particular, nonslender delta wings are capable of producing high levels of lift from a compact wing platform and further research is needed to maximise the potential of nonslender platforms.

Recent studies into highly flexible nonslender delta wings indicate that incorporating some level of structural flexibility into the wing can be used as a form of passive flow control [2-4]. These studies indicate that flow induced leading edge vibrations in the post stall region are capable of energising the separated shear layer and promoting shear layer reattachment. However this method of flow control means that the wing must have the required level of flexibility, which is an added design constraint. The magnitude of the flow induced oscillations may be detrimental to any measurement equipment on the craft, and there can be abrupt changes in lift with angle or attack. There would be significant advantages if the same level of flow control could be achieved without the need for designing significant flexibility into the structure. This has been the inspiration for this study, in which active flow control by unsteady pulsing of air into the shear layer has been investigated as an alternative to the passive leading edge oscillations.

Aims and objectives

The aim of this study was to expand on the knowledge of shear layer flow control of nonslender delta wings. In particular, to investigate whether unsteady blowing could be used as a method of inducing shear layer reattachment. Further to the establishment of this method as a feasible means of flow control, the aim was to gain a better understanding as to what parameters influence the effectiveness of this method. In particular further research was needed into the effect of blowing at different momentum coefficients, and blowing at different excitation frequencies. An additional aim of this work was to better understand the interaction between the perturbation produced by the unsteady excitation and the main vortex, and to assess the way that different blowing parameters affect the interaction between the main vortex and the perturbation.

In a practical sense, the main aim of this unsteady blowing research was focused on the delay of stall by blowing at post-stall angles of attack and inducing shear layer reattachment. Secondary to this, was to investigate the effects of unsteady blowing in the pre-stall region, in particular to investigate whether pre-stall blowing was a plausible roll control technique for nonslender delta wings.

If unsteady blowing is to be considered as a practical means of flow control the transient response of the flow to the initiation of unsteady blowing needed to be investigated. The time taken for the shear layer to reattach would affect the way a MAV or UAV could be controlled. This study aimed to gain an understanding of the time required to induce reattachment using unsteady blowing.

Thesis structure

The thesis has been organised into a further eight chapters. Chapter 2 is a discussion of previously published literature surrounding the topic of nonslender delta wing flow, relating it to shear layer flow control.

The methodology used to investigate unsteady blowing over nonslender delta wings is presented in Chapter 3, which is divided into two sections. The first section outlines the experimental apparatus and measurement techniques used. The second section is an analysis of the uncertainty of measurements taken and how the data was processed.

Chapters 4 to 8 outline the results obtained and discuss what conclusions can be drawn. Chapters 4 to 7 relate to experiments conducted on a half wing platform, whereas Chapter 8 relates to experiments over a full wing platform. Chapter 4 outlines the time averaged response of the flow, using pressure measurements to indicate the relative effectiveness of different flow parameters, and PIV measurements to show the topographical features of the flow. Chapter 5 is a more in depth look at the topographical flow features, but examining PIV images in a phase averaged sense. Particular attention is given to identifying the interaction between the shear layer perturbation and the main region of vortical flow. Chapter 6 is a discussion of the transient response of the flow to the initiation of unsteady blowing, indicating how the time taken for the flow to reattach is affected by blowing parameters. Chapter 7 outlines the effect of blowing over a limited portion of the leading edge (partial blowing). This is important as blowing across the entire leading edge may not be practical for some platforms, and also gives an indication as to what areas of the leading edge are the most effective to blow from. Chapter 8 discusses the forces developed over a full span delta wing with unsteady blowing, and relates the conclusions drawn from Chapters 4 through 7 to a full delta wing.

Chapter 2 Literature review

In the past, delta wing research has focused mainly on slender delta wings, and there is a good body of literature on the topic. Research into nonslender delta wing platforms is less abundant, although increasing efforts are being made to expand the wealth of knowledge in this area. Comparisons between the fundamentals of slender and nonslender wing flow are made in this chapter, but the focus is the aerodynamics of nonslender wings.

Research into the flow control of nonslender wings is dominated by research into passively controlled flexible wings and actively controlled oscillating wings, and this forms the foundations of the current work. The topic of flow control of the free shear layer from a backwards facing step is also included in this review as it discusses the structure of the shear layer and the instabilities that may be present.

Fundamental properties of flow over delta wings

The flow structure of both slender and nonslender delta wings with sharp leading edges involves separation of the flow at the leading edge and the formation of a free shear layer. However the resultant flow over slender and nonslender wings is very different, and it is worth noting these differences before further discussing the nature of the flow over nonslender wings and potential control issues.

In the case of the slender wing, the shear layer roles up into a discrete vortex [5, 6], as shown in Figure 2-1. The high vorticity shear layer continues to feed the vortex core. At very low angles of attack, the vortex forms over the rear section of the wing only (Figure 2-2A), as the angle of attack is increased, the vortex moves towards the apex and covers the whole wing [7] (Figure 2-2B), whereby it can be said that the vortex is fully developed [8]. Primary attachment occurs at the wing's centreline. As the angle of attack is increased further, the vortex increases in strength and moves further away from the wing's surface and inboard towards the wing's centreline (Figure 2-2C). The high velocities associated with the increased vortex strength create large suction pressure on the wing's surface, increasing the lift force.

At high angles of attack, the vortex breaks down over the wings surface (Figure 2-2D). Breakdown occurs when the adverse pressure gradient causes the jet like axial flow in the vortex core to stagnate, and the vortex core expands rapidly. Downstream of the breakdown location, the flow is dominated by a low speed wake. This sudden expansion of the vortex core results in significantly increased levels of turbulence on the surface of the wing and high levels of buffeting on structures such as fins. As the angle of attack is increased further, the breakdown location moves towards the apex (Figure 2-2E). When the breakdown location reaches the apex, the wing can be said to be fully stalled [8].

By contrast, for the nonslender case, the shear layer separates from the wing's leading edge and reattaches to the wing's surface, creating a vortex bound by the reattached shear layer (shown in

Figure 2-1) [9]. It is because of this shear layer reattachment that nonslender wings have increased potential for flow control. As the angle of attack increases the point of reattachment moves inboard, and when it reaches the wings centreline, high levels of buffeting are experienced, and the wing stalls [10]. The cross-flow pattern of a Λ=50° delta wing just prior to complete stall is shown in Figure 2-3, showing a detached shear layer and weak reattachment at the centre line.

This study looks at using oscillatory blowing as a method of energising and organising vorticity in the shear layer, to induce shear layer reattachment at angles of attack where the flow would normally be stalled. Vortex breakdown is still an important feature of nonslender delta wings and, as with slender wings, the breakdown location approaches the apex of the wing as the angle of attack is increased [11]. Breakdown, however, is not as abrupt for nonslender wings and is not the dominant source of buffeting as it is in slender wings [10]. Similar to slender delta wings, prior to breakdown the axial flow in the vortex core is jet like with axial velocities significantly greater than the free stream velocity; after breakdown the axial core flow resembles a broad wake [12]. Distinct differences in slender and nonslender breakdown exist. However breakdown is not a limiting factor for the generation of lift for nonslender wings, and reattachment of the free shear layer is possible after breakdown has reached the apex of the wing [13].

At low Reynolds numbers and very low angles of attack, a notable feature of nonslender delta wing flow is that there is a dual vortex structure. This has been observed, both experimentally [10, 11, 14] and computationally [12] for a 50 degree swept wing. At low angles of attack, where the primary vortex is very close to the wings surface, the secondary vortex splits the primary vortex into two regions, creating a distinct dual vortex structure. For a set angle of attack, increasing the Reynolds number causes the outboard of the two vortices to breakdown significantly earlier than the inboard vortex, and at α=5° and Re= 2.6 x 10^4 the outboard vortex is barely visible. Although Yaniktepe and Rockwell [15] did not identify this dual vortex structure in flow visualisations of a 38.7° swept delta wing at α=7°, they did identify two distinct areas of high vorticity in the vortex wake downstream of breakdown, indicating this may be a more generic property of nonslender wings at low angle of attack and low Reynolds number (by contrast slender delta wings tend to be considered insensitive to Reynolds number). Surprisingly, Wang and Zhang [11] observed the dual vortex structure on wings with sweep from 45°-65° at Reynolds numbers of $1.2\text{x}10^4$ and $1.8\text{x}10^4$, however the range of angles of attack that the dual structure was visible over was reduced for the higher sweep angles. Although interesting, these findings only occur at a lower Reynolds number and much lower angle of attack than is the focus of this study [12]. For the Reynolds number and angle of attack range looked at in this study (Re_{min}=2 x 10^5, α=10°-35°), a more classic primary, secondary, tertiary vortex structure exists, similar to that of slender wings. In fact, Taylor and Gursul [10] noted that the effect of Reynolds number on the flow characteristics decreases significantly above Re=3 x 10^4. An example of this is shown in Figure 2-4 [10], presented by Taylor and Gursul comparing results of many authors on the spanwise location of the vortex core at a range of angles of attack and Reynolds numbers. The conclusion that there is a low sensitivity to

Reynolds number for the tests conducted in this study is also supported by the findings of Vardaki [3].

Wing sweep has a significant effect on the aerodynamics forces on a delta wing. Gursul et al. [9] made a useful summary of data originally presented by Earnshaw & Lawford [16], Taylor et al. [10] and Huang et al. on the effect of wing sweep on the maximum normal force developed over the wing. The comparison, reproduced in Figure 2-5, shows clearly that increasing the sweep angle between Λ=40° and Λ=70° results in an increase in the maximum normal force coefficient achievable. Note that for comparative purposes the normal force coefficient at zero degrees angle of attack has been subtracted from all results. The greatest rate of change in normal force coefficient with sweep angle occurs between 55 and 60 degrees, and could be a result of the change in behaviour between nonslender and slender wings.

An important consideration for this study is the difference between half and full span models. The half span model imposes a symmetry condition upon the flow. Attar et al [17] modelled a full span and half span delta wing with a sweep angle of Λ=50° computationally. Their simulation predicted that imposing the symmetry condition delayed wing stall, a conclusion which is consistent with the experimental findings of this study.

Shear layer instabilities

Separated free shear layers are a feature in many types of flow and are the only relevant instability for post stall flow control of nonslender delta wings [13]. A much studied case which can bring insight into flow over nonslender delta wings is flow over a backwards facing step. Roos and Kegelman [18] highlighted that in the shear layer it is large scale vortices that dominate the transverse momentum transfer. These vortices were clearly visible for laminar flow at low Reynolds numbers, but difficult to identify for higher Reynolds numbers with turbulent flow. The vortices that form in the shear layer are a likely result of the Kelvin–Helmholtz form of instability. Roos and Kegelman also highlighted that disturbances caused by the reattachment of the shear layer at the point of reattachment, could be fed back to the separation point through the separation bubble. Vortex pairing in the shear layer, as described by Winant and Browand [19], was also documented in both turbulent [20] and laminar flow visualisations, indicating that vortices would pair up and merge one to two times before reattachment. This was supported by spectral analysis of hotwire measurements, which showed a decrease in the frequency of the dominant spectral peak as the measurement point moved along the shear layer away from the separation point. After reattachment, flow visualisations still showed organised structures present in the mixing layer well downstream of reattachment for both laminar and turbulent cases. Flow control of the backwards facing step shear layer is discussed later in the section regarding 2D shear layer flow control.

Clear shear layer instabilities exist in the shear layer in computations of the flow over a 50° swept delta wing at α=15° [12]. Prior to vortex breakdown clear discrete vortices are formed in the shear layer surrounding the vortex core. After breakdown these are convected downstream and form

much finer structures, and appear to have no real order or time specific location. It was also shown that prior to breakdown, as well as the instabilities in the shear layer the secondary vortex would be periodically wrapped up into the main vortex as a result of interaction between the leading edge vortex and the surface boundary layer. Earlier dye flow visualisation experiments of a slender delta wing (Λ=60°) and a nonslender delta wing (Λ=45°) by Gad-el-Hak and Blackwelder [5] showed discrete vortices forming in the shear layer immediately after the flow had separated from the leading edge. These vortices formed parallel to the leading edge in the shear layer, and as they moved along the shear layer they began to pair and merge, as shown in Figure 2-6. They also noted that the frequency at which vortices developed in the shear layer was the same for the two sweep angles (45° and 60°). The graphs in Figure 2-7 and Figure 2-8 summarise the information presented (although non-dimensionalised). It is clear that there is a dependence of the shedding frequency on Reynolds number, which Gad-el-Hak and Blackwelder suggested could have been due to increasing the rate of dye injected into the flow at the leading edge as the free stream velocity was increased. Regardless of the effect of the dye injection, the effect of the Reynolds number has stabilised by $2x10^5$, the lowest Reynolds number tested in this investigation. Also, there tended to be a reduction in Strouhal number as angel of attack increased, although this trend is not as clear. An interesting observation was that the vortices would pair up as they moved along the shear layer and down stream, at least three times before reaching the trailing edge. A dye flow visualisation of this paring process is shown in Figure 2-6. Gad-el-Hak and Blackwelder went on to look at ways of actively controlling these vortices [21], discussed later in the section regarding flow control of delta wings.

Taylor and Gursul [10] found that for a 50 degrees swept wing, high levels of turbulence in the near surface plane occurred at the same location as the reattachment line, indicating the main source of turbulence on the wings surface was caused by the reattachment of the shear layer, as opposed to vortex breakdown. It was also noted that just prior to stall, there were significant spectral peaks present in the velocity fluctuations in the region of the reattached shear layer in the near surface plane. Figure 2-9 shows spectral peaks at St=0.6 and St=1.2 at α=20°. By contrast, data displayed at a lower angle of attack, α=15° displayed a much more broad band peak of lower magnitude centred around St=2. In computations [12] of the pressure coefficient in the vortex core of a 50° swept wing at α=15°, dominant spectral peaks were only found prior to breakdown, and attributed to the shedding of vortical structures in the shear layer, causing vortex wandering (St=10.7). Gordnier and Visbal were uncertain of the origin of a lower frequency peak (St=0.63) but suggested it may be due to axial motion of the vortex core. Computations simulating measurements downstream of breakdown in the region of the trailing edge showed broad band fluctuations from St=0 to St=5.

Yaniktepe and Rockwell [15] used single points in PIV measurements to calculate the vertical velocity spectrum at points in the shear layer down stream of breakdown (x/c=0.8) over a 38.7°

swept delta wing. They found that for angles of attack of α=13° and 17°, as the measurement point moves away from the leading edge, the dominant spectral peak decreases, from St ≈ 4 near the leading edge, to St ≈ 2-3 near the wings centreline. For the α=17° case, a lower frequency peak of St≈0.5 was present very close to the centreline, and is probably associated with attachment. This may have a similar origin to the spectral peak at St=0.6 identified by Taylor [10] in the reattachment region of the near surface plane for a 50° swept wing close to stall.

Due to the conical nature of the shear layer, the dominant frequency of shear layer instabilities is very much dependant on the measurement location over the wing. The longer the shear layer has to develop before reattachment, the more the vortical structures pair and merge. This means that as the measurement point moves along the shear layer, the frequency of the dominant spectral peak, indicating the frequency of instabilities, decreases. In addition to this, as the measurement point moves away from the apex along the centre of the wing, the dominant spectral peak also decreases. The decrease in frequency of the spectral peak is accompanied by a more prominent, less broad band power distribution around the dominant frequency, and an increase in magnitude of the dominant spectral peak [4]. This is summarised in Figure 2-10. Experiments indicated broadband spectral peaks centred around St=4 along the leading edge and close to the apex for a Λ=50° wing at α=20° and more narrowband peaks at around St=1 further along the shear layer and closer to the trailing edge. Furthermore, Taylor indicated that the dominant spectral peak reduced in frequency and magnitude as a 50 degree nonslender wing approached stall for a fixed measurement location in the shear layer [4].

Vortex breakdown over delta wings

There are some distinct differences between the vortex breakdown over slender and nonslender wings. Although this study does not focus on controlling vortex breakdown using unsteady excitation, as it has a small effect [13], it is worth reviewing vortex breakdown over nonslender wings as it is an important characteristic of the flow. A good comparison has been made by Gordnier and Visbal between published material on slender wing breakdown and computations on a 50° swept nonslender delta wing [12]. Slender delta wings tend to exhibit a spiral type of breakdown [22], whereby the breakdown location is marked by a spiral winding of the vortex core in the opposite direction to the vortex swirl. The spiral rotates around its axis in the direction of the vortex swirl [8]. The vortex core exhibits jet like axial flow prior to breakdown, it then breaks down in an abrupt and easily identifiable way. After breakdown the mean wake of the broken down vortex core consists of negative axial velocities, and the region reversed of flow closest to the apex is considered the breakdown location. By contrast, nonslender wing studies [12, 15] show a more gradual conical shaped breakdown. The jet like axial flow gradually changes to wake like flow after breakdown but the mean flow case does not have a region of reversed axial flow. A spiral shaped region of the vortex core was identified prior to breakdown, but this vortex wandering was attributed to shear layer instabilities. Slender delta wings tend to have discrete spectral peaks in velocity fluctuations in their wake due to the spiral nature of the vortex breakdown. By contrast,

non slender wings tend to have a much broader band of frequencies in the vortex wake due to the more gradual nature of breakdown. Ol [23] indicated that at a very low Reynolds number ($8.5x10^3$) there could be wake like axial flow in the vortex core for nonslender wings even prior to breakdown. These results compared favourably with later computations, but were also shown only to be representative of the flow at very low Reynolds numbers [12], and outside of the scope of this study.

As mentioned above, as the angle of attack is increased, the vortex breakdown location moves towards the apex. In experiments undertaken by Taylor and Gursul [10] for a 50° swept wing, jet like flow in the vortex core could be seen at α=15° extending from the apex of the wing to approximately x/c=0.3, however by α=20°, the core flow was completely wake like. The experimental results for a α=15° case compared well with the computational results of Gordnier and Visbal [12]. These computations also showed that similar to slender wings, as the angle of attack is increased, the vortex core moves away from the surface and towards the wing's centreline. Wang and Zhang [11] also showed that the vortex breakdown location moved closer to the apex as the angle of attack increased. There were slight differences to the breakdown location presented by Taylor [10], most probably due to differences in experimental setup.

The computations by Gordnier and Visbal [12] described the nature of breakdown for nonslender wings and are shown in Figure 2-11. As mentioned above, the breakdown location is preceded by a small region where the vortex core adopts a spiralling motion. The breakdown location is marked by a small scale bubble, where the vortex core appears to thicken, then contract. This is followed by a third region where the core becomes diffuse, and expands rapidly. This type of breakdown is consistent with the results of experiments by Yaniktepe and Rockwell [15].

Yaniktepe and Rockwell conducted PIV measurements downstream of vortex breakdown over a 38.7° swept delta wing. For the mean case, instead of finding discrete concentrations of vorticity at the centre of a well defined spiral pattern, they found high concentrations of vorticity confined to the free shear layer which coincided with regions of high unsteadiness in the flow. At low angles of attack (α=7°), instantaneous PIV measurements identified discrete vortices in the shear layer, but at higher angles of attack (α=13°,17°,25°) vorticity plots indicated large clusters of small regions of high vorticity. They also noted that as the angle of attack increased from α=7° to α=25°, surprisingly the maximum level of vorticity decreased, and that the region of higher vorticity became more dispersed. Instantaneous PIV measurements at α=13° showed small scale high vorticity clusters spaced approximately λ/s=0.15 apart, although these became hard to identify at higher angles of attack.

Wang and Zhang [11] investigated the effect of wing sweep on vortex breakdown for sweep angles from Λ=45° to Λ=65°, and a selection of their results is displayed in Figure 2-12. It clearly shows that for any given angle of attack, the lower the sweep angle, the closer the location of vortex

breakdown is to the apex. Although vortex breakdown location is less important than reattachment when considering the forces developing on a nonslender wing, this is consistent with the results shown by Earnshaw and Lawford [16] which showed that within this sweep angle range, the lower the sweep angle, the earlier stall occurs. It can clearly be seen from Figure 2-13, presented by Gursul et al [13], that the pre-stall flow over the nonslender wing at the subject of this study, with Λ=50° and an angle of attack range from α=10°-35°, will involve a broken down vortex and a reattached shear layer.

Miau et al. [24] conducted experiments on a 50 degree swept wing with a range of different leading edge profiles. Square, rounded, sharp double bevelled, leeward bevelled and windward bevelled leading edge profiles were compared at a Reynolds number of $7x10^3$. The windward bevelled leading edges were similar to the types of leading edges tested in this study. At α=10° the square tip, the windward bevelled tip and the tip with a 60° leeward bevel all performed similarly, with clear reattachment and strong leading edge vortices formed. In contrast, at the same angle of attack, the wings with significant leeward bevelling (greater than the 60° case) did not show the formation of a strong leading edge vortex. Instead of separation occurring at the sharp leading edge, flow separated from the start of the bevel on the suction surface of the wing, retarding the flow pattern. The wedge shaped leading edge showed similar characteristics to a leeward bevelled leading edge, and the rounded leading edge developed more traditional vortex flow downstream of x/c=0.2. For the windward bevelled leading edge at an angle of attack of 20°, the vortex appeared to breakdown at the apex, consistent with results discussed earlier regarding the fundamental properties of flow over delta wings. It has also been noted when comparing rounded and sharp windward bevelled leading edge shapes, the shape had no effect on the frequency of the formation of large coherent structures in the shear layer [5].

2D shear layer flow control

Given that the reattachment of the shear layer is essential for generating lift on nonslender delta wings, it is worth looking at previous work on 2D shear layer flow control. Roos and Kegelman [18] looked at the effect of forcing on a 2D shear layer by exciting the flow over a backwards facing step. By exciting the shear layer using an oscillating mini flap at the separation point, they discovered that the reattachment length of the separated flow could be reduced, typically by about one step height. Experiments were conducted on both laminar and turbulent boundary layers, and their method of flow control was found to be effective on both, however less so in the transition region. From a spectral analysis of the shear layer, it was determined that excitation caused a more organised shear layer, concentrating the spectral power of velocity fluctuations into the forcing frequency and at either the 1^{st} harmonic or the 1^{st} sub harmonic of the forcing frequency. The strong spectral peaks at frequencies other than the forcing frequency indicate the complexity of the flow within the shear layer. Perhaps the excitation of the first harmonic occurs when the forcing frequency is significantly below the natural formation frequency of the structures. As the measurement point moved away from the separation point, the dominant spectral peak reduced

further, indicating further vortex pairing. Downstream of the reattachment location, the effects of the large vortical structures induced by forcing could clearly be seen.

In addition to highlighting the complexity of forcing in the shear layer or a backwards facing step, Hasan and Khan [25] proposed that forcing would affect one of two distinct instability modes present in a turbulent separated shear layer. Roos and Kegelman [18] highlighted a particular case where exciting the flow caused a dominant spectral peak at the first harmonic of the excitation frequency. Hasan and Khan identified a shear layer instability mode and a step instability mode. The dominant peak in fluctuating velocity occurring in Figure 2-14 is at the step mode instability frequency, whereas the second, higher frequency peak is at the shear layer instability frequency. Excitation frequencies where the first harmonic was a multiple of the step mode instability frequency tended to excite the flow at the first harmonic, whereas at other excitation frequencies the fundamental frequency dominated the excited flow. From this, it is important to note that in flow control surrounding a backwards facing step, it is often the first harmonic that is excited in the flow, rather than the fundamental [18, 25]. The effectiveness of forcing at the separation point of a backwards facing step shown in a number of studies [18, 25-28] indicates potential for flow control over nonslender delta wing platforms.

Flow control of delta wings

Flow control is seen as having great potential to extend the boundaries of MAV and low Reynolds number flight. As discussed above, experiments showing the positive lift enhancement due to self induced leading edge oscillations point the way towards the benefits that may be gained through active flow control. Experiments where nonslender wings have been actively oscillated [29] provide additional information about the important parameters when attempting to actively control the shear layer. In 'Review of Flow control Mechanisms of Leading Edge vortices' Gursul et al [13] looks at methods for controlling flow separation, flow reattachment and the formation of delta wing leading edge vortices. Several of these methods can be linked to this study. It was concluded that for the unsteady activation methods studied for non-slender wings, oscillations of a Strouhal number in the order of 1, and usually between 1 and 2 provided significant lift enhancement and delay in stall. An interesting point to come out of this investigation was that unsteady excitation tended to be orders of magnitude more effective than steady flow control, especially in the post stall region. Due to the differences in shear layer reattachment, this review concentrates mainly on unsteady techniques for controlling nonslender wings (Λ=30°-55°), and wings in the transition between slender and nonslender wings (Λ=60°).

Flexible and oscillating nonslender delta wings

As mentioned above, lift enhancement on flexible wings and subsequent work on oscillating wings provided the motivation for this study. They will be considered separately from other forms of flow control for three reasons. The first is that oscillating nonslender delta wing experiments have primarily been studied in order to explain phenomenon seen on flexible nonslender wings, which is

a passive rather than active form of flow control. The second is that the mode of excitation is not only isolated to the leading edge. For both oscillating and flexible delta wings, displacement of the leading edge cannot be isolated from displacement of the rest of the wing, in particular the trailing edge. Thirdly, the effect of frequency is coupled to the velocity of the leading edge. For a given leading edge displacement, a higher oscillation frequency results in a higher leading edge velocity. This means it can be difficult to compare the effects of the forcing frequency with other flow control methods.

Experiments on flexible delta wings conducted by Taylor [2, 30] indicated that vibrations of the leading edge, induced passively through wing flexibility, stimulated the free shear layer, significantly increased lift and caused a delayed and sudden stall. For a 50 degree swept wing the maximum lift coefficient could be increased by over 20%. Significant increases in lift coefficient were achieved on flexible wings with sweep angles of 40-50 degrees. However a 55 degree swept wing showed only a small increase and flexibility had a detrimental effect on a 60 degree swept wing [2, 4]. Data presented by Taylor is reproduced in Table 2-1. Flow visualisations and PIV measurements at x/c=0.8 indicate that the increase in lift was due to reattachment of the shear layer to the wings surface for the flexible case, compared to a detached shear layer in the rigid wing case [3]. This conclusion was supported by oscillating wing experiments which indicate that for a Λ=50° delta wing at pre-stall angles of attack the reattachment location of the shear layer would move away from the centreline when 1° roll oscillations were introduced at St=1.0. Furthermore, for the stalled stationary wing at α=25°, oscillations induced reattachment of the shear layer, as shown in Figure 2-15. Small amplitude roll oscillations were an effective means of inducing reattachment on delta wings with sweep angles from 30°-50°, and it was concluded that this was the effective range of this method of flow control [29].

For the flexible wing case, the increase in lift was always accompanied by oscillations in the 2nd antisymmetric mode, and for the cases where there was the greatest increase in RMS tip oscillations (40° sweep) there was the greatest increase in lift. The 60° swept wing showed the smallest increase on RMS tip oscillations. The dominant spectral peak of the tip oscillations was dependant on wing sweep, ranging from St=0.58 for Λ=40° to St=0.91 for Λ=60° [2, 4]. For flexible wings a mean spanwise camber is induced by the wings flexibility, which was deemed not to be the source of the large increase in lift by further experiments comparing it to a rigid cambered wing [3].

An additional and interesting result of both flexible wing and oscillating wing experiments was the reformation of leading edge vortices. It was noted that shear layer reattachment could still be induced downstream of the vortex breakdown location, and even when vortex breakdown had reached the apex [29]. The oscillations did have the additional effect in many cases of causing vortices to reform within the reattached shear layer. The oscillating leading edge is an unsteady source of vorticity which, for a constant tip displacement, increases with Strouhal number. The

effect of this was seen in the cross-flow plane, as the measured level of vorticity increased with Strouhal number. This added vorticity was expected to advance vortex breakdown. The delay in breakdown location is likely to be due to a more favourable streamwise pressure gradient, this may be a result of the reattached shear layer. Another possibility is that the significant trailing edge oscillations result in a more favourable pressure gradient and delay breakdown. The Strouhal number of the oscillations that achieved maximum vortex breakdown delay was dependant on both the angle of attack and the sweep angle, but for all cases was between St=1-2. Increasing the magnitude of the oscillations from $\Delta\varphi=1°$ to $\Delta\varphi=5°$ increased the range of effective Strouhal numbers, and the magnitude of the breakdown delay. Strouhal numbers between ≈0.3 and 10 had some effect on delaying vortex breakdown [29]. However, assuming the oscillations were sinusoidal (this is not specified) the increase in frequency would have been coupled with an increase in forcing leading edge velocity, this may increase the effectiveness of higher frequency oscillations.

A useful insight into the structure of the shear layer of a flexible wing was shown by Taylor [4]. Hotwire measurements were taken along the reattached shear layer and spectral analysis was performed, and the results are reproduced in Figure 2-16. At measurement locations close to the leading edge, there was a strong peak at the frequency of the leading edge oscillations (St≈0.75), but this lay well below the frequency range of the natural instabilities present in the shear layer, shown as a broadband peak at St≈5. As the measurement location moved along the shear layer, the peak from the shear layer instabilities reduced in bandwidth and frequency, and by y/s=0.5, it was centred on the frequency of the leading edge oscillations and had increased in magnitude. This shows that due to the three dimensionality of the shear layer, the forcing frequency will not always coincide with the dominant instability frequency, and that in fact it is not necessary to induce reattachment. It also shows that even with significant oscillations of the leading edge, there is still a significant spectral component outside the frequency of leading edge oscillations.

Attar et al [17] performed computations on a 50 degree swept delta wing with predefined prescribed oscillations. It was found that the increase in lift coefficient induced by the oscillations was directly related to the magnitude of the oscillations. The flow appeared less sensitive to frequency, providing it was above a minimum level, and also insensitive to the mode of oscillation, whether first, second or antisymmetric. It is important to note these results are not the product of a coupled aero-structural analysis.

A flexible half model wing was tested by Taylor [2] to investigate the importance of the asymmetry of the oscillations. The half model showed no significant leading edge oscillations. Yaniktepe and Rockwell [15] found that when they introduced $\alpha=1°$ pitch oscillations about the mean chord (the oscillations were symmetrical about the centre line) to a $\Lambda=38.7°$ swept delta wing at $\alpha=17°$, they could regain the topographical flow features of $\alpha=13°$. This included more concentrated vorticity in the shear layer and a more well defined swirl pattern in the cross-flow plane at x/c=0.8. They

showed that the vorticity in the shear layer became organised into identifiable structures much closer to the leading edge when forcing was introduced. The range of frequencies tested was from St=0.5 to St=2, with St=2, the sub harmonic of the highest frequency that was found in the shear layer, proving to be the most effective. Vardaki [29] showed small amplitude pitch oscillations appeared to be even more effective than small amplitude roll oscillations at inducing vortex reformation in the post stall regime. This may indicate that it is in fact the trailing edge oscillations that have the most effect on vortex breakdown. This indicates that asymmetry of the oscillations might not be necessary for flow control over nonslender wings, but the oscillations that cause reattachment may need a full wing to develop, however the difference may also be due to structural differences due the mounting of the half wing, which was not described in detail [2].

Flow control by means of active unsteady excitation at the leading edge

Gad-el-Hak[31] considered the effect of suction and ejection from the leading edge of a Λ=60° delta wing at the first sub harmonic of the discrete vortex shedding frequency. Dye flow visualisations revealed that with flow control the shear layer became significantly more organised. The first vortex pairing process occurred closer to the leading edge of the wing, and the main vortex became more organised. Hotwire measurements revealed significant velocity peaks found in the shear layer, indicating the presence of discrete vortices. Gad-el-Hak also highlighted the highly complex nature of the shear layer.

Margalit et al. [32] looked at the effects of zero mass flux blowing along the leading edge of a 60 degree swept half wing, a transitional case between slender and nonslender wings. Pulsing was by means of a high frequency carrier pulse with a lower frequency signal superimposed on top, controlling piezoelectric actuators inside the wings cavity. A maximum increase in C_N of 29% was achieved at Cμ=0.03% and 39° angle of attack with a Strouhal number of 1.0.

Rullan, Vlachos and Telionis [33] conducted PIV measurements over a 40 degree swept cropped delta wing in a water tunnel at 13 degrees angle of attack. The model had a slot along 50% of the leading edge, starting at the apex, and water was pumped out of the slot as an unsteady jet in the same plane as the wing surface. For cases with no flow control a wing tip vortex was found in a plane along the trailing edge of the wing. When control at Cμ=0.02 was added, a typical leading edge vortex was also present in the flow. Further experiments on a Λ=42° diamond wing indicated that oscillating mini-flaps at the leading edge had a low level of effectiveness for near stall angles of attack when compared to steady spanwise blowing [34]. This result is in contrast to the majority of research on separated flow [13], however the discrepancy may be due to the fact that there was still a weak level of reattachment at the angle of attack tested (α=21°).

Nelson et al [35] investigated roll control of a UAV wing with a 47° leading edge sweep, although the trailing edge shape differed from that of a conventional delta wing, and different flow was observed compared to conventional delta wings. Leading edge vortices were still identified above

α=8°. Plasma actuators positioned on the pressure surface slightly below the leading edge of the wing were effective in increasing the lift coefficient over an angle of attack range from α=9°to α=35°.

For Margalit's zero mass flux pulsing, a frequency of St=1 was the most effective excitation frequency for a the square wave excitation signal, and St=2 for a sinusoidal excitation signal. For the square wave excitation signal, frequencies as low as St=0.42 were shown to be effective. Nelson [35] effectively used plasma actuators turned on and off at a frequency corresponding to St=1.0 for roll control purposes, but did not compare it's effectiveness with other frequencies. Greenblatt [36] presented data also indicating that St=1.0 was the most effective frequency for flow control of a Λ=60° delta wing. Actuation was by means of dielectric barrier discharge actuators with a duty cycle of 10% along the leading edge. Phase averaged PIV measurements indicated that at x/c=0.5, the vortex centre traced a circular path in a phase averaged sense, in response to the unsteady actuation.

For active control by oscillatory blowing, discrete shaped pulses, such as a square wave, tend to be more effective than sine shaped pulses [32]. Margalit et al. noted the shorter the excitation rise time, the more effective the pulse. For discrete shaped pulses, lower duty cycles (5%) are more effective at lower C_μ values (0.001%-0.01%) and pulsing at higher duty cycles was more effective at higher C_μ values (0.05%+). This was attributed to the fact that the low duty cycle is closer in form to an impulse (delta) function, comprising of all frequency components, and is able to excite all the unstable modes present, generating large coherent structures in the shear layer.

To test the importance of blowing location, Margalit divided the wing into 5 segments, each 12% of the chord. It was found that, for a square wave pulse, the station from x/c=0.76 to x/c=0.88 was the most effective blowing location, and blowing any of the locations increased the normal force. However, for a sinusoidal waveform, only pulsing from near the apex has a positive effect. Nelson et al [35] found that oscillatory blowing between x/c=0.5 – x/c=1 was more effective between α=9° and α=35°, than blowing between x/c=0 – x/c=0.5. However due to the shape of the trailing edge of the UAV wing tested, the relevance of that result to this study is questionable.

By the introduction of a phase angle between zero mass flux blowing actuators in different locations on the leading edge of the 60 degree swept half wing model, Margalit [32] found that there was a detrimental effect on the increase in normal force when compared to having all the actuators in phase. This is interesting as for flexible wing the second antisymmetric structural vibration mode proved to be highly effecting at increasing lift [3].

Control of moments acting on nonslender delta wings.

At low angles of attack, Farnsworth et al. [37] showed that synthetic jets at the leading edge of a Λ=40° MAV could be used for control purposes. By using synthetic jets in conjunction with a solid

obstruction placed at the leading edge, the pitching moment was increased over and above what would have been achieved by a 5° elevon deflection. Nelson et al [35] used oscillating plasma actuators to control a free to roll wing at α=20° between roll angles of ±40° with comparable effectiveness to a typical control surface setup.

Recent work by Williams [38, 39], the author of this review, outlines the effects of unsteady blowing from a nonslender wing with Λ=50°. Much of this material is represented in this thesis, and therefore will be discussed later.

Conclusions with application to the current work

Perhaps the most important conclusion that can be drawn from existing literature is that there are important differences between the flow over nonslender and slender delta wings. This is not limited to the fact that for nonslender wings the shear layer reattaches to the wing's surface, whereas for slender wings the shear layer rolls up into a discrete vortex. An important difference is that for nonslender wings, vortex breakdown is not the limiting factor in the generation of lift. This is relevant for flow control over nonslender wings, as the target of any flow control technique over nonslender delta wings should be to achieve reattachment, rather than delay vortex breakdown.

An important conclusion that can be drawn from the work on shear layer flow control is the complexity of the response of the shear layer, even for two dimensional cases, to active excitation. It is not uncommon for excitation to stimulate frequencies in the shear layer at the sub harmonic or 1st harmonic of the excitation frequency. Existing research also shows that the flow over nonslender wings is highly three dimensional, with the dominant frequencies in the shear layer changing and lowering as the shear layer develops. The combination of the complex response of the shear layer to excitation and the three dimensional nature of the flow over nonslender wings highlights the difficulties when trying to understand active flow control over nonslender delta wings.

When considering the method and parameters to be used for unsteady blowing over nonslender wings, the existing literature indicates that instabilities relating to the free shear layer are the only relevant instability, and should be the focus of any flow control technique. Existing research also indicates parameters that may affect flow control, in particular that unsteady blowing is most likely to be effective in the Strouhal number range of 1-2. Work on flexible wings show that for a 50° swept flexible wing, stall was delayed by 5 degrees over the rigid wing case, outlining the potential gains that may be achievable with unsteady blowing.

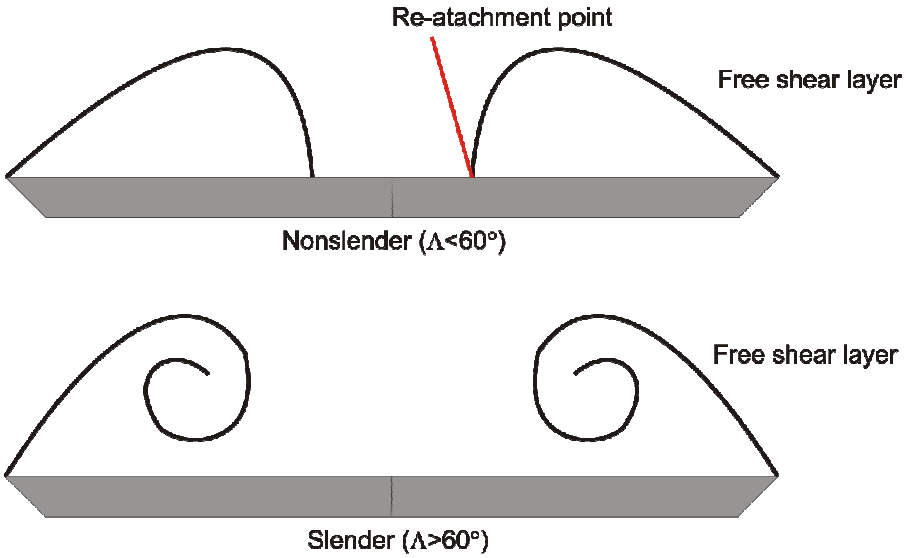

Figure 2-1 Cross-flow comparison of slender and nonslender delta wings

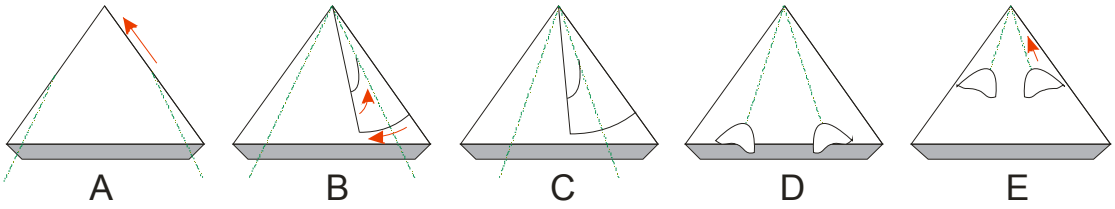

Figure 2-2 Position of the vortex core over a slender delta wing with increasing angle of attack

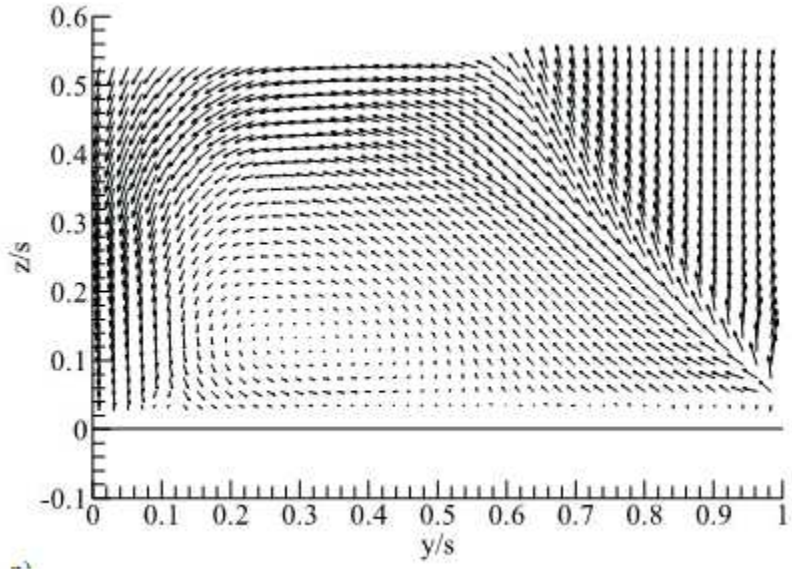

Figure 2-3 Time averaged flow in a cross-flow plane at x/c=0.5 for a delta wing with Λ=50° at α=25°.[4]

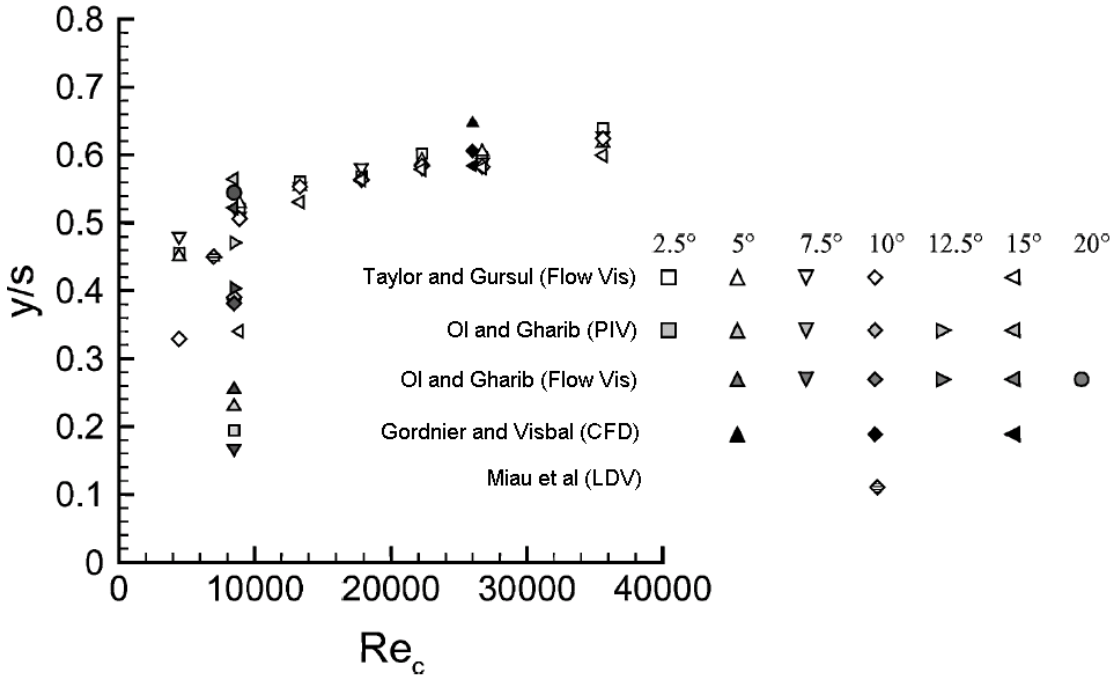

Figure 2-4 Variation of spanwise location of vortex core with Reynolds number; sweep angle of 50 deg.[10]

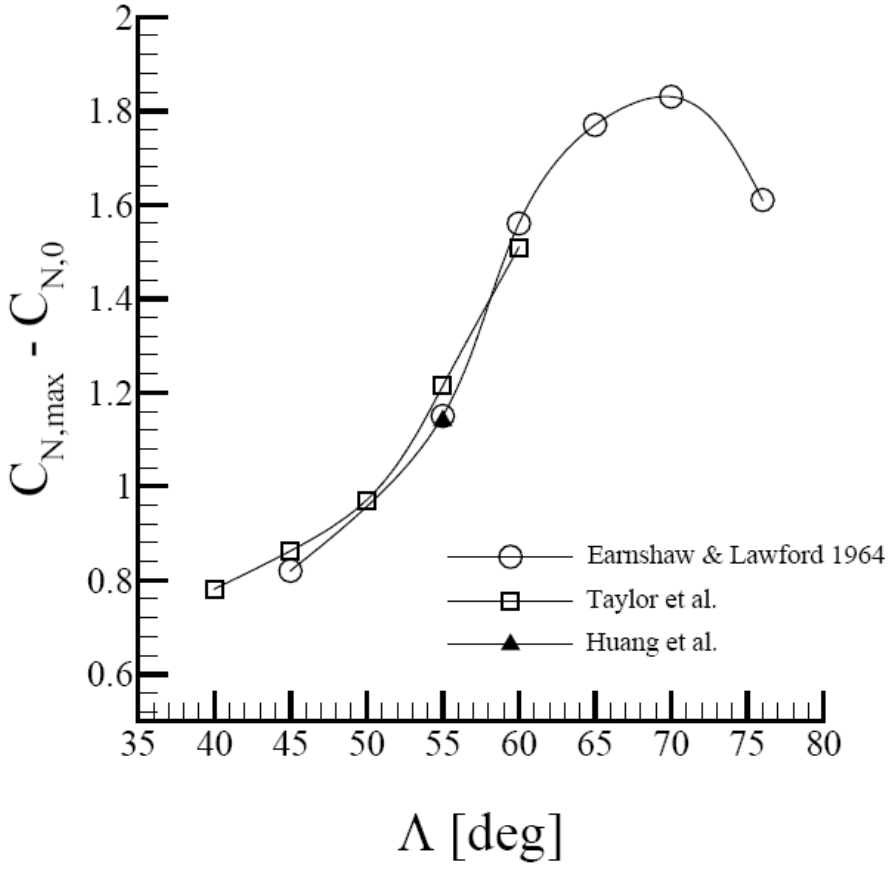

Figure 2-5 Effect of wing sweep on normal force acting on a delta wing, $C_{N,max}$-$C_{N,0}$ is the difference in maximum normal force and the normal force at α=0° [9]

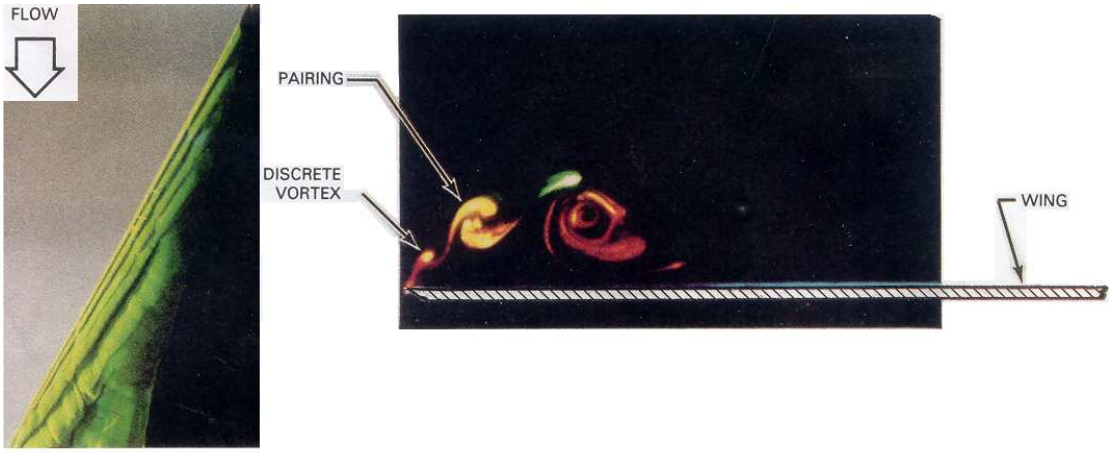

Figure 2-6 Top view (left) and a plane perpendicular to the vortex axis (right) of laser flow visualisations showing the pairing process of vortices in the shear layer of a Λ=60° delta wing, α=10°.[5]

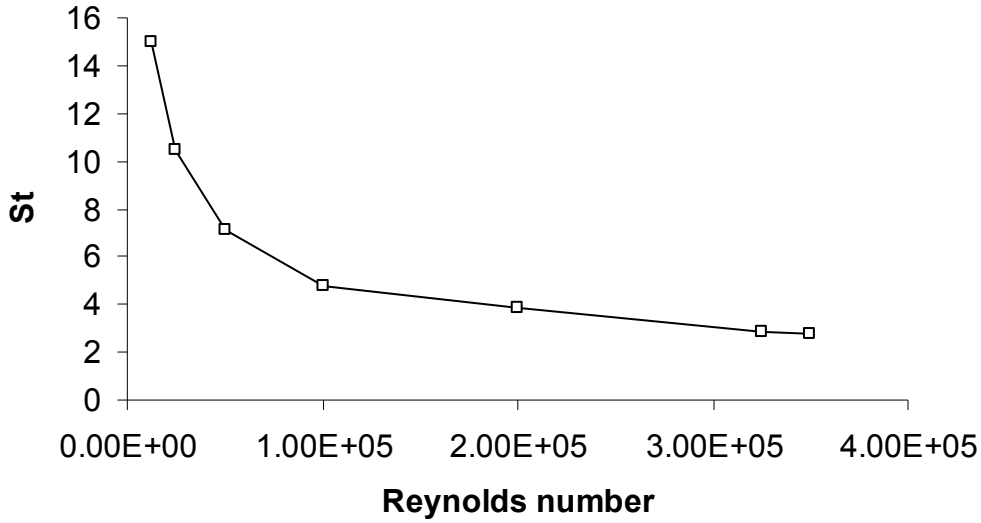

Figure 2-7 Effect of Reynolds number on the frequency of formation of discrete vortices in the shear layer of a Λ=60° delta wing, α=15°.[5]

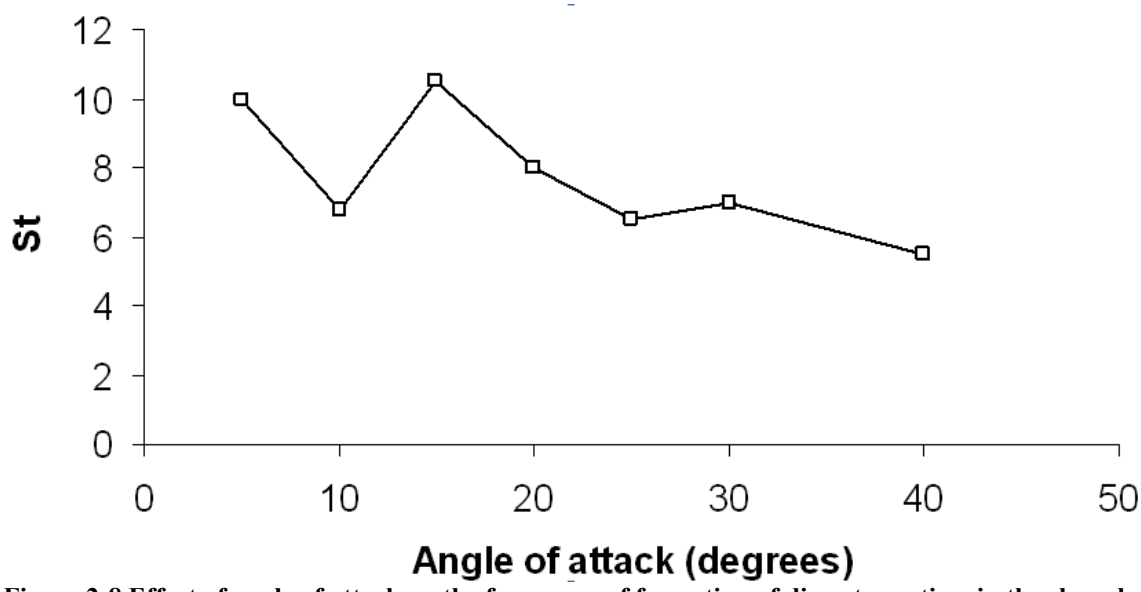

Figure 2-8 Effect of angle of attack on the frequency of formation of discrete vortices in the shear layer of a Λ=60° delta wing, Re=2.5×10^4.[5]

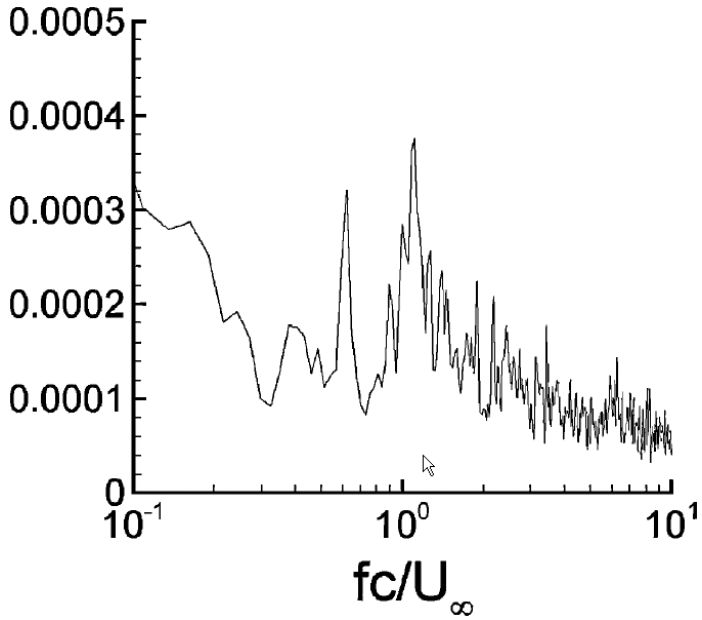

Figure 2-9 Velocity spectra in the region of the attached shear layer in the near surface plane, Λ=50°, α=20°.[10]

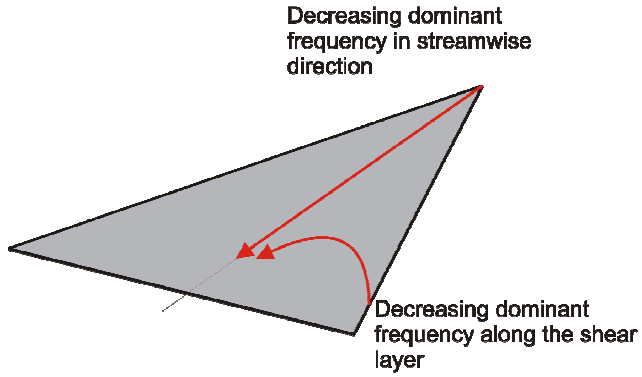

Figure 2-10 Effect of the 3 dimensionality of the shear layer on the dominant velocity spectral peak.

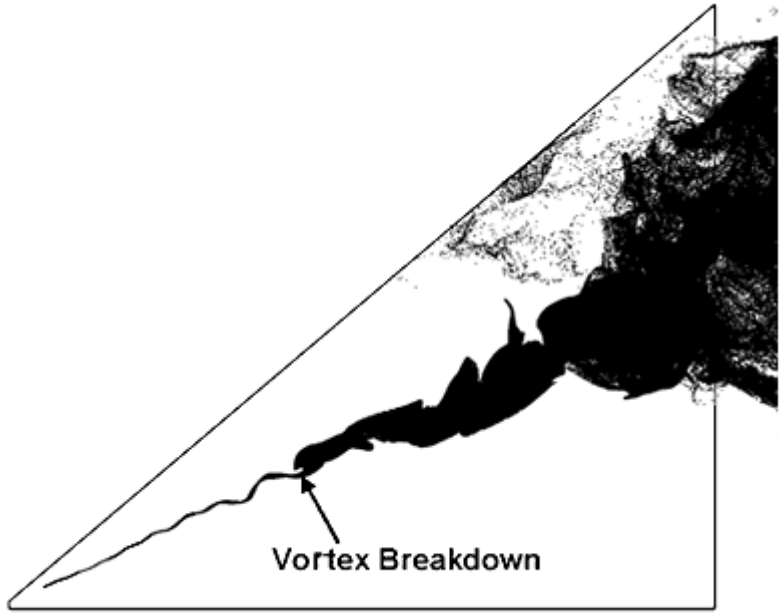

Figure 2-11 Computational streakline visualisation of vortex breakdown over a Λ=50° delta wing at α=15° [12].

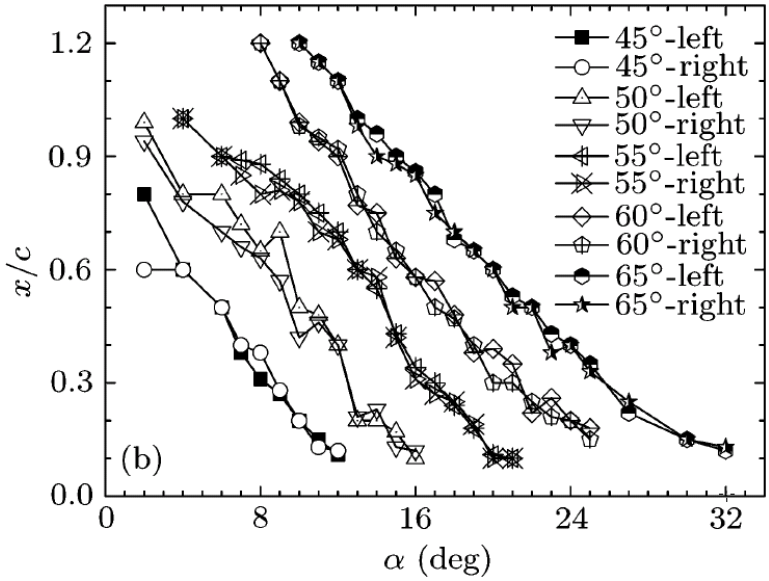

Figure 2-12 Summary of the effect of angle of attack and sweep angle on vortex breakdown location.[11]

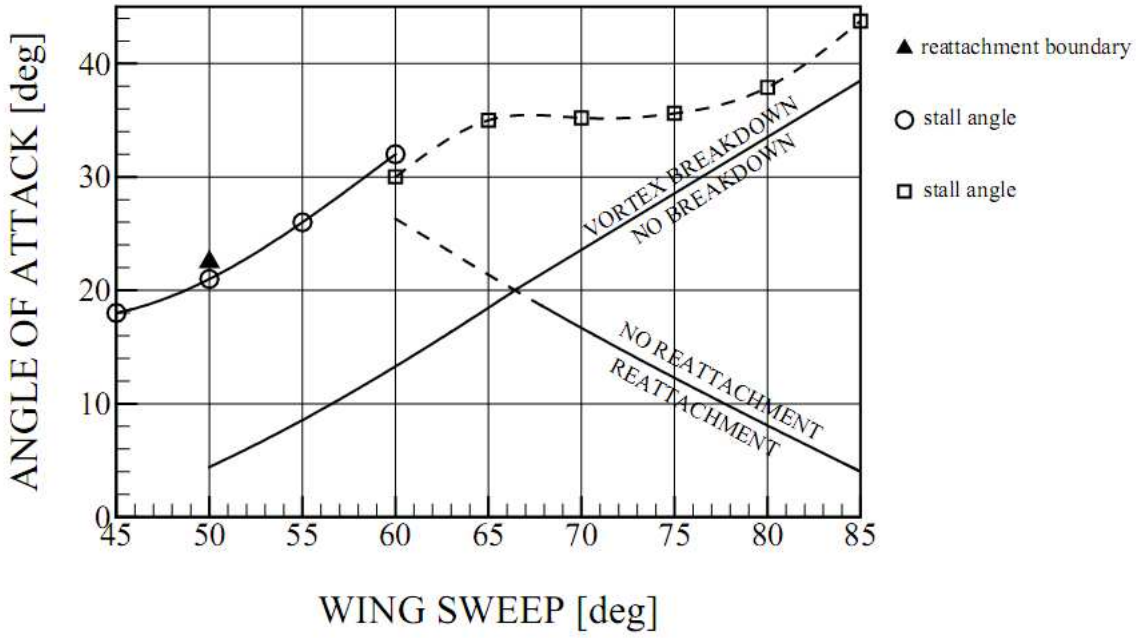

Figure 2-13 Boundaries of vortex breakdown and flow reattachment on the wing surface as a function of sweep angle.[13]

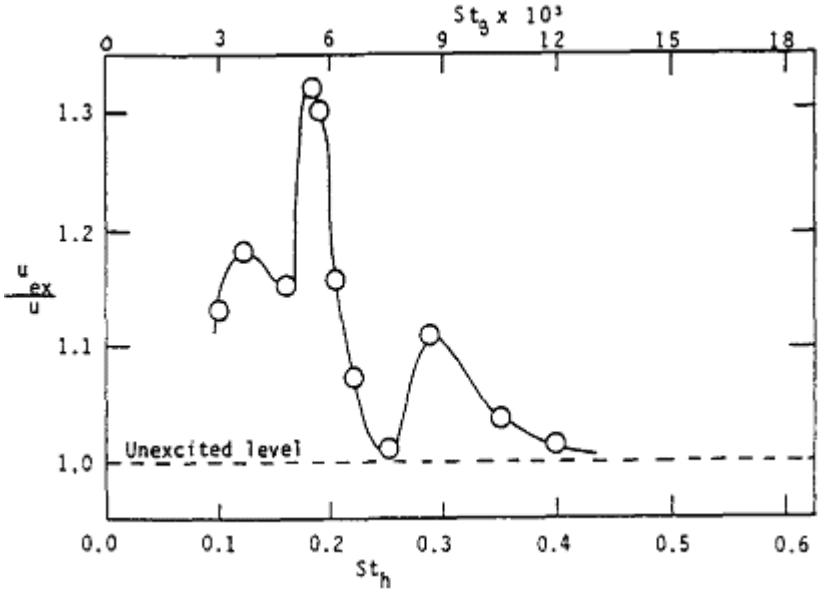

Figure 2-14 Effect of forcing frequency on the fluctuating component behind a backwards facing step undergoing forced oscillations at the separation point.[25]

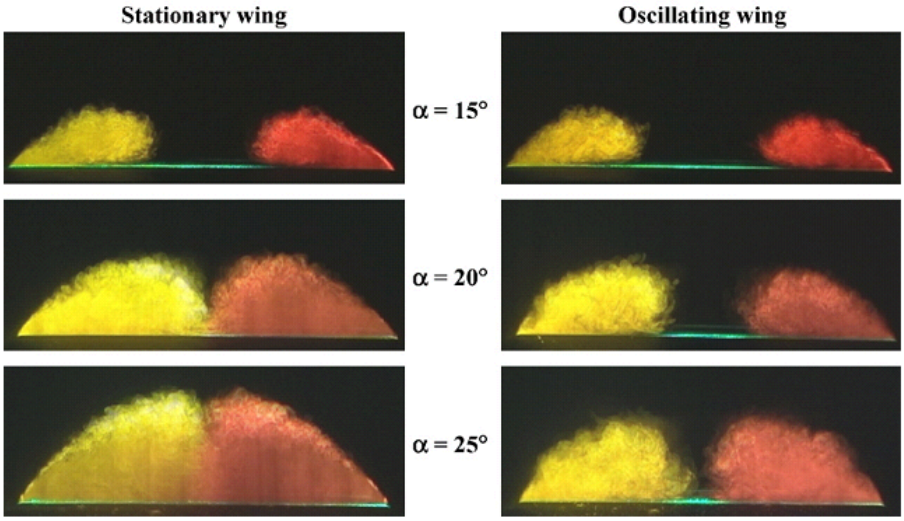

Figure 2-15 Time averaged laser fluorescence flow visualisation for stationary and rolling wings, Λ=50°, St=1.0, Δφ=1°[29]

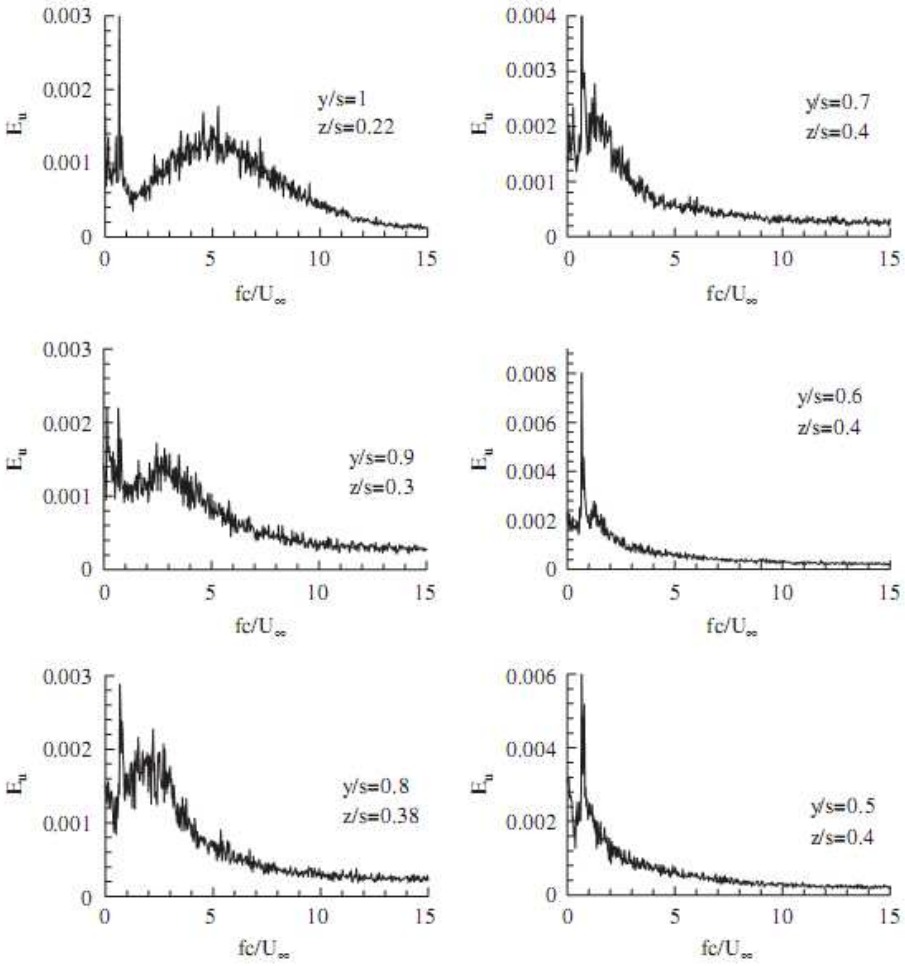

Figure 2-16 Spectrum of velocity fluctuations along the shear layer for a Λ=50° flexible wing, α=25° and x/c=0.7.[4]

Table 2-1 Comparison of the maximum lift coefficient and delay of stall for rigid and flexible wings. $\Delta C_{L\,max}$ (1) indicates the change in maximum lift coefficient and $\Delta C_{L\,max}$ (2) indicates the increase in lift at the stall angle of the flexible wing, when compared to the rigid wing at the same angle.

	$C_{L\,max}$		$\Delta C_{L\,max}$		
Λ	Rigid	Flexible	1	2	$\Delta\alpha_{stall}$
40	0.77	1.09	42%	53%	7 deg
45	0.83	1.14	38%	49%	6 deg
50	0.92	1.13	23%	45%	5 deg
55	1.07	1.08	1%	23%	3 deg
60	1.24	1.18	−5%	−5%	0 deg

Chapter 3 Method

Experimental setup

Open section wind tunnel setup

Experiments investigating the pressure distribution and flow over a nonslender delta wing with a Λ=50° sweep angle were conducted in the University of Bath open jet wind tunnel. The tunnel has a 1 m long test section, and a 0.782 m jet exit diameter. The tunnel has a maximum speed of 30 m/s and a freestream turbulence level of 0.1% when run at the velocity range of the current experiments [40]. The tests were conducted at a freestream velocity of 15 m/s equating to a Reynolds number of 2×10^5 based on the wing chord length of 0.2 m. The velocity was indirectly measured by recording the dynamic pressure with a pitot-static tube upstream of the model connected to a Digitron 2020P manometer, with an accuracy of 2% of the typical values measured. The instantaneous freestream velocity calculated from the manometer pressure readings would fluctuate with time but never more than 0.3% of the target tunnel freestream velocity. A half wing model was constructed and used for pressure and PIV measurements in the open jet wind tunnel. For these tests the half body wing was mounted on a splitter plate. The half wing model and splitter plate are shown in Figure 3-1.

Pressure measurements

Pressure measurements were conducted on the suction surface of the half wing model in the open section tunnel. Pressure taps were positioned at three streamwise stations, corresponding to x/c=0.28 (station A), x/c=0.48 (station B) and x/c=0.68 (station C). A schematic of the wing including all pressure tap locations is shown in Figure 3-2. Each of the 38 0.5mm pressure tapings was connected to a manifold at each station, and then connected to a scannivalve. The scannivalve switched between taps, connecting each tap in turn to a Druck STX 2100 Smart/Hart differential pressure transducer, with a range of 0-10 mbar and a sensitivity of +/- 0.13%. Samples were taken at 1000 Hz, each tap was measured for 4 seconds, and 1.5 seconds was allowed for switching between each station of the scannivalve. Tests of the response of the measured pressure to scannivalve switches indicated 1.5 seconds was sufficient for the pressure to stabilise. The pressure tap assembly is shown in Figure 3-3.

Experiments were performed predominantly in the post-stall region. Oscillatory blowing with a pulsed jet from a slot near the leading-edge was used as the method of unsteady excitation. Various tip and slot geometries, shown in Figure 3-4, were tested in preliminary experiments. The slot width in these experiments was 1.2 mm (0.6% of the chord length). These initial tests showed that, of the four tip geometries compared, tip 3 consistently gave the greatest increases in suction pressure over the wing and was therefore used as the tip configuration for all subsequent tests, unless otherwise stated.

The air was blown into the wing via a manifold. The manifold was linked to a chamber below the chamber housing the pressure taps. The two chambers were completely sealed off from one another, to prevent the blowing from affecting the pressure readings. The air then exited the internal wing cavity from the leading edge slot. In order to evaluate the effect of blowing from particular areas of the leading edge, thin adhesive tape was used to block parts of the leading edge. The setup for these experiments, referred to as partial blowing experiments, is shown in Figure 3-5. A summary of the partial blowing configurations that were tested is also shown in Figure 3-5. Two types of partial blowing tests were conducted. The effect of changing the length of a slot extending from the apex was tested, as was the effect of moving the location of a slot of 25% of the leading edge length to different positions on the leading edge.

Unsteady blowing valve setup

For oscillatory blowing, two valves were used to vary the flow rate, creating high frequency oscillations in the leading edge jet velocity. Initially a Dynamco Dash-1 solenoid valve controlled by a Feedback PFG605 Power Function Generator was used to provide pulses of air. However, due to the low maximum aperture of the valve, the desired momentum coefficient range could not be achieved. The Dynamco Dash-1 was replaced by an Enfield Tech LS-V15C continually variable flow control valve, controlled by a LSC-10 controller. The setup was used to vary the pulsed air flow rate with time. The LS-V15C was capable of opening and closing at up to 200 Hz at a high level of repeatability. All results presented are of cases where the valve and controller setup was the Enfield Tech LS-V15C valve coupled with the LSC-10 controller, unless otherwise stated. A basic schematic of the pneumatic setup is shown in Figure 3-6. The valve command signal was generated by a personal computer running a LabView code that output a square wave pulse to the controller using a Data Translations data acquisition card. The data acquisition card was capable of simultaneously outputting the signal to the valve and logging test parameters, such as the pressure tap readings. As previous investigations [29] show that the most effective frequencies correspond to $fc/U_\infty=1$ to 2, the majority of the experiments were conducted at a Strouhal number of $St=fc/U_\infty=1.5$. The valve command signal duty cycle was 20%. Initial experiments indicated that short sharp pulses were the most effective. For the valve configuration selected, a minimum duty cycle of 20% was required to achieve the desired momentum coefficient range. The momentum coefficient was controlled by increasing the maximum valve aperture for a given frequency. The momentum coefficient range tested was from 0 to 1%. The momentum coefficient for each case was found by traversing a Dantec hotwire probe across the slot at a distance of 1 mm from the leading edge. The gold plated Dantec 55P01 straight probe was connected to a DISA 56C16 general purpose bridge. The signal was further amplified and then digitised using a A/D card. Samples were recorded at 3000Hz for a minimum of 3 seconds. The traverse was conducted in either 0.1 mm or 0.2 mm steps, and the length of the traverse depended on the profile of the jet. The overall momentum coefficient was found by integrating across the width of the slot, and then over the length of the slot. Typical examples of pulses produced by this method are shown in

Figure 3-7; for these examples the maximum velocity at each point in the traverse has been aligned in order to get a clear picture of the pulse shape. The greatest uncertainty comes from non-uniform blowing velocity along the slot. An example of the non-uniformity from 0-100% the length of the slot blowing at 112.5 Hz (St=1.5 for the half wing case) is shown in Figure 3-8. The non-uniformity becomes significant as C_μ increases beyond 0.4%. A manifold and some internal deflectors were used to encourage a uniform distribution, but some non-uniformity had to be accepted as excessive barriers impinging the jet flow tend to increase the mean flow component of the pulse (decreasing the fluctuating component). The level of non-uniformity of the momentum coefficient did not change with Strouhal number, and for any given momentum coefficient was consistent across all tests. The effect of the non-uniformity of the jet on the momentum coefficient is discussed later in this chapter. For cases where a part of the leading edge was blocked (in order to encourage blowing from specific areas of the leading edge), the level of non-uniformity was greatly reduced, shown in Figure 3-8.

Mean and phase averaged Particle Image Velocimetry setup

Particle Image Velocimetry (PIV) measurements were taken to gain a better understanding of the flow dynamics over the wing. For the mean flow and phase averaged results presented, A TSI 2-D Digital PIV system was used. The PIV system produces pairs of pulses up to 120 mJ focused into a laser sheet, at a rate of 3.75 Hz. The PIV camera is a digital CCD camera with a resolution of 2048 x 2048 pixels. The seeding for the PIV was provided from a TSI 9306A jet atomiser, generating particles with a diameter of approximately 1μm. Typically, 150 – 200 pairs of images were taken for each case using an interrogation area of 32 x 32 pixels. The PIV setup was controlled by the TSI Insight 6.0 software. The uncertainty of the velocity measurements is estimated to be 3% of the freestream velocity. Also, phase-averaged measurements were taken by triggering the PIV system at desired phases of the unsteady excitation. The LabView programme that generated the valve command signal also generated the trigger input for the PIV system. Measurements of velocity in a cross-flow plane were taken as shown in Figure 3-9. The laser sheet was set perpendicular to the freestream at selected streamwise locations. Measurements were taken at locations corresponding to the location of the pressure tap rows, at x/c=0.28, 0.48, 0.68. The PIV camera was put into an optical glass box and placed inside the wind tunnel downstream of the delta wing, thus measuring the cross-flow velocity field. The effective grid size was around 1.3 mm for these measurements. Vortex core locations were identified from these cross-flow PIV results. The laser sheet was then aligned with the vortex core so that the velocity field in a plane that passes through the vortex core and the apex was measured, with the aim of obtaining the axial velocity in the core. Near-surface measurements were also taken by firing a laser sheet parallel to the wing surface at a distance of 1.5 mm as shown schematically in Figure 3-10. For some measurements in the near surface and vortex core planes, it was necessary to align the laser with a mirror. This setup, with laser safety curtains removed, is shown in Figure 3-11. For measurements both in the vortex core plane and the near surface plane the PIV camera was removed from the glass box and positioned outside of the

tunnel. As mentioned above for pressure measurements, PIV experiments were conducted with parts of the leading edge slot blocked. Very thin masking tape was used to block the slot. A range of blocking configurations were tested and the effect will be discussed in Chapter 7.

Transient Particle Image Velocimetry setup

Transient PIV experiments were also conducted using a high frame rate PIV system. The PIV system coupled a New Wave Pegasus Nd:YLF (Neodymium Yttrium Aluminium Garnet) double pulse high speed laser with a TSI PowerView HS-3000 high speed CMOS camera. Three thousand pairs of images were recorded at 1500Hz (1500 pairs of images per second) for each test. The resolution of each image was 1024 x 1024 pixels and the processing interrogation area was 20 x 20 pixels. The PIV vector grid spacing was 1.3% of the local semispan for the cross-flow cases, and 0.86% of the chord for the near surface measurements. The TSI Insight 3G software package was used to control the PIV setup. A light arm was used to position in the laser sheet at the same chordwise positions, corresponding to the pressure tap locations (Figure 3-9) and in the near surface plane (Figure 3-10), as described above regarding the mean flow and phase averaged PIV tests.

Force measurements

A full wing model was used in order to measure the effect of oscillatory blowing on the forces that develop on a nonslender delta wing. As for the half body wing, a sweep angle of $\Lambda=50°$ was used. A chord length of 0.3m was chosen to best match the forces expected to the accurate range of the force balance. Tests were conducted in the high speed section (2.13m x 1.52m x 2.7m) of the University of Bath closed loop wind tunnel. The test speed ranged from $15ms^{-1}$ to $20ms^{-1}$, giving a Reynolds number range of 3.2×10^5 to 4.3×10^5. The wing in the tunnel is shown in Figure 3-12. The leading edge slots were rapid prototyped out of nylon, allowing a slot width of 0.75mm, or t/c=0.25%. Internal deflectors were installed to encourage an even flow distribution. The leading edge investigated corresponded to the same shape as tip 3, but with a smaller t/c ratio (Figure 3-13).

A six component JAGUAR force balance was used to measure the forces on the wing. The force balance and wing setup is shown in Figure 3-14. Due to damage to the force balance whilst in storage, for later tests, in particular those using the Enfield valve setup, only the normal force component of the balance was operable. Earlier tests using the Dynamco valve setup utilised all six components of the balance. Taylor [4] indicated a level of 2% uncertainty for the lift coefficients for a very similar experimental setup utilising the same balance and tunnel. The dynamic pressure of the freestream was monitored using the same method as used in the open section tunnel.

The air supply for the oscillatory blowing for the force measurements was blown through highly flexible pipes. In order to blow out of the leading edge, the air supply pipes had to cross the force balance. Their effect was evaluated by testing the model with and without the air supply pipes at $U_\infty=20ms^{-1}$ and comparing the difference in the forces acting on the wing. Tests were also

conducted at U_∞=0ms^{-1} and at high jet velocities to see if pulsing directly induced significant forces on the wing or the force balance. In both cases the effect of the pipes crossing the balance was negligible, and these results discussed in more detail in Chapter 8.

Data Analysis and measurement uncertainty

Pressure measurements

Much effort has been made to minimise the level of uncertainty of the experimental results, however a level of uncertainty will always remain, and attempts have been made to evaluate and address the main sources of uncertainty. The methods for estimating uncertainty used are those outlined by Moffat [41, 42]. The recommended method for combining uncertainty for the majority of engineering applications is the Constant Odds combination, utilising Equation 1 (below). For the quantities calculated, the equations were of the form of Equation 2, and as specified by Moffat [41], the following simplification outlined in Equation 3 was used.

$$\delta R = \left\{ \left(\frac{\partial R}{\partial x_1} \delta x_1 \right)^2 + \left(\frac{\partial R}{\partial x_2} \delta x_2 \right)^2 + ... \left(\frac{\partial R}{\partial x_N} \delta x_N \right)^2 \right\}^{\frac{1}{2}} \tag{1}$$

$$R = x_1^a x_2^b x_3^c ..... \tag{2}$$

$$\frac{\delta R}{R} = \left\{ \left(a \frac{\delta x_1}{x_1} \right)^2 + \left(b \frac{\delta x_1}{x_1} \right)^2 + ... \right\}^{\frac{1}{2}} \tag{3}$$

For all uncertainty estimations, errors due to the digitisation of a measured signal by data acquisition hardware were not considered significant. Due to appropriate amplification of the measured signal, and by using data acquisition cards with a minimum 12-bit resolution, any error was insignificant when compared to that of the measurement apparatus. The uncertainty analysis of the pressure measurements is outlined in Table 3-1, with all uncertainties quoted to two significant figures. As mentioned above, when recording the free stream dynamic pressure, the two main sources of uncertainty were the accuracy of the manometer, and the small fluctuation of the dynamic pressure with time. These have been accounted for, along with the uncertainty of the pressure transducer to give an overall uncertainty of 2.1% for the pressure coefficient.

Table 3-1 Summary of pressure measurement uncertainty

Quantity	Uncertainty	Measurement Technique	Factors Considered	Order
Freestream Dynamic Pressure	2.1%	Measured directly - digitron 2020P manometer connected to a pitot-static tube	Accuracy of manometer (2%) Fluctuation of reading with time (1%)	Second
Pressure tap reading	0.13%	Measured directly - Druck STX 2100 pressure transducer	Transducer accuracy (0.13%)	Zeroth
Pressure coefficient $C_p = \frac{p - p_\infty}{q}$	2.1%	Uncertainty calculated from freestream dynamic pressure and pressure tap reading		

Calculation of the momentum coefficient

The uncertainty of the momentum coefficient is difficult to evaluate. The main area of uncertainty comes from the non-uniform distribution of velocity over the length of slot. For this reason, the level of uncertainty for the momentum coefficient has been divided into two quantities. A calculated uncertainty for comparison of the results presented here with each other, and an estimated uncertainty for comparison with the results of other researchers. For the calculated uncertainty, the limited number of measurement points over the slot length is not considered. For any given momentum coefficient, regardless of Strouhal number, the distribution of the jet velocity across the length of the slot is highly similar. The uncertainty of the free stream dynamic pressure has been addressed, and along with the other quantities considered, is included in the uncertainty analysis surmised in Table 3-2. In addition to the variation in dynamic pressure, the uncertainty of the wing geometry was considered. The wing chord, semispan and leading edge were measured, and the uncertainty comes from the finite resolution of the ruler used. For the calculation of the momentum coefficient, the jet velocity was integrated over the length of the hotwire traverse, and therefore, instead of using the slot width in the uncertainty calculation, the length of the traverse over the width of the slot was used. The main uncertainty here was the spatial resolution of the automatic traverse. A considerable component of the uncertainty comes from the jet velocity. This has been estimated by looking at the calibration data for the hotwire. The calibration of the hotwire measurements are of the form described by the bridge manufacturer in Equation 4, where ‘n’ is given by the bridge manufacturer, and ‘A’ and ‘B’ are selected as best fit parameters, dependant on the calibration.

$$U_\infty = \left(\frac{Voltage^2 - A}{B} \right)^{\frac{1}{n}} \qquad (4)$$

By analysing the deviation of the velocity from the best fit calibration curve over a range of cases, a conservative estimate for the accuracy of the measured jet velocity of 4% was made. This value is

particularly significant, as in accordance with Equation 3, the uncertainty value is multiplied by 2. When considering the above factors, the momentum coefficient uncertainty is calculated to be 8.3%.

Table 3-2 Summary of momentum coefficient uncertainty

Quantity	Uncertainty	Measurement Technique	Factors Considered	Order
Freestream Dynamic Pressure	2.1%	Measured directly - digitron 2020P manometer connected to a pitot-static tube	Accuracy of manometer (2%) Fluctuation of reading with time (1%)	Second
Jet slot width	0.33%	Length of the traverse of the hotwire over the jet	Minimum step size of the traverse mechanism	Zeroth
Jet slot length	0.19%	Measured directly with ruler		Zeroth
Wing Chord	0.25%	Measured directly with ruler		Zeroth
Wing semispan	0.30%	Measured directly with ruler		Zeroth
Jet Velocity	4.0%	Dantec hotwire probe	Deviation of measurement from calibration curve	Zeroth
Momentum coefficient $C_\mu = \frac{\dot{m} V_{jet}}{qS}$	8.3%	Uncertainty calculated from freestream dynamic pressure, slot area (accounting for thickness and length), wing area (accounting for chord and semispan) and jet velocity		

Although the level of variation of the momentum coefficient over the slot length is unknown, other jet parameters, such as jet volume flow rate, can be compared with partial blowing experiments for the same blowing conditions (valve frequency, amplitude etc.) For cases where a part of the leading edge was blocked (in order to encourage blowing from specific areas of the leading edge) the level of non-uniformity was greatly reduced, as shown in Figure 3-8. Partial blowing experiments have a more uniform and predictable momentum coefficient variation. Comparisons of partial and full blowing cases with the same valve input signal indicate that that the other blowing variables, such as volume flow rate, are similar and that an estimate of 5%-10% uncertainty for the momentum coefficient is not unreasonable. For the purposes of comparing results with other work, a more conservative uncertainty estimation is made of 10%.

PIV Measurements

The mean and phase averaged PIV data was processed using the TSI Insight 6.0 software. The processing algorithm used was the TSI FFT Correlator algorithm, which for the measurements taken was the best compromise between code efficiency and minimising processing errors. Any holes or missing values in the vector field corresponding to a bad vector (where an acceptable cross correlation could not be obtained) which were identified by the Insight software were interpolated using MATLAB. The number of bad vectors indicated across the vector field was typically less than 0.3%. The number of vector fields processed for each case was between 150-200, and all

vector fields for each case were then averaged to create a single mean vector field. This is well above the minimum images that experiments by Bearman et al. [43] indicate are required to give a good estimate of the mean flow. Marles [44] indicated that a main area of PIV error for the particular PIV system used for these measurements is due to out of plane motion of the seeding particles. For the cross flow case, as the PIV particles travel in the out of plane, or axial direction, and move through the measurement plane with a thickness of 1mm-2mm, the PIV system measures an apparent radial velocity which is zero in the middle of the PIV image, but increases towards the edge of the field of view. Marles conducted experiments which indicated that the setup used had a maximum velocity error of 5% of the free stream. Given that these errors occur at the extremities of the field of view, and the area of interest of the measurements is much closer to the centre of the field of view, an error of 3% is a more appropriate figure. The three main parameters discussed are velocity (Equation 5), vorticity (Equation 6) and turbulence intensity (Equations 7). Vorticity is a differential quantity, and tends to have a greater level of noise when compared to velocity, and the uncertainty has been estimated to be 6%. The turbulence intensity, in this case due to the low frame rate of the PIV system used, can not be considered the true turbulence, but rather an indication of the relative magnitude of velocity fluctuations in the flow. The uncertainty of the turbulence is estimated at 3%.

$$U = \sqrt{u^2 + v^2} \tag{5}$$

$$\omega = \frac{\partial w}{\partial y} - \frac{\partial v}{\partial z} \tag{6}$$

$$U_{Std} = \sqrt{\frac{\sum_{n=1}^{n} (U - \overline{U})^2}{n}} \tag{7}$$

Another important source of uncertainly for PIV measurements is that user error can be significant. In particular, the level of seeding is very important and for each experiment the level of seeding was monitored closely to ensure that there was adequate seeding before the experiment began. The process was also monitored real time to ensure that the PIV images were not under seeded or saturated with excess seeding. Another source of error for PIV measurements is due to misalignment of the PIV setup. If the laser sheet is not perpendicular to the camera axis, the particles illuminated by the laser sheet do not appear in focus as they are outside of the field of view of the camera. In general this is easy to identify at the setup stage, as the illuminated particles appear to move out of focus in a particular part of the field of view. For all measurements alignment was ensured using a variety of techniques including laser level alignment, and in all cases the image quality and level of cross correlation were examined before and after running the experiment.

For the transient PIV measurements, due to a lower level of laser power, the level of seeding was increased. Conditioning was used to increase the image quality. Then a single image was created which was made up of the mean minimum intensity of each individual pixel over the 3000 images acquired for each test. That level of intensity was then subtracted from each corresponding pixel for all 3000 of the transient frames. This process is incorporated into the TSI Insight 3G software. The resulting images were then processed with the TSI Insight 3G software using the direct correlator engine.

As a considerable source of error in PIV measurements is a result of the user, it is worth noting that the University of Bath have a team with significant experience using TSI PIV systems. The approach taken for PIV data acquisition is a systematic approach whereby a series of reliable configurations for PIV parameters, such as delay and laser intensity, are worked through systematically for each case to identify what set of setup and processing parameters best suit the particular experiment. The system parameters are then fine tuned for each specific case. Initially the PIV system is setup as a team of researchers and initial results are verified in real time by more than one user. This sharing of knowledge and experience helps to reduce user error to a minimum.

Force Measurements

As with the pressure measurements, the dynamic pressure is a source of uncertainty, and treated in the same way for calculations of the uncertainty of the normal force coefficient. An additional uncertainty is the reference area of the wing, which has been included in the analysis summarised in Table 3-3. The force measurements were conducted using the University of Bath sting force balance. The force balance used is no longer supported by the balance manufacturer and it has not been possible to acquire data as to the accuracy of the balance. Based on the previous research conducted with the balance, the accuracy has been estimated at 2%. Uncertainty is therefore calculated at 2.9%. This however, does not account for other considerations such as the air supply pipes crossing the force balance strain gauges. An analysis of the effect of the pipes is included in Chapter 8. Experiments indicate that the pipes have negligible effect on the forces measured; however it remains a source of uncertainty. Considering this, a more realistic estimation of the experimental uncertainty may be 5%.

Table 3-3 Summary of force measurement uncertainty

Quantity	Uncertainty	Measurement Technique	Factors Considered	Order
Freestream Dynamic Pressure	2.1%	Measured directly - digitron 2020P manometer connected to a pitot-static tube	Accuracy of manometer (2%) Fluctuation of reading with time (1%)	Second
Wing area	0.20%	Uncertainty calculated from the wing chord and semispan, which were measured directly with a ruler		
Force balance reading	2%	JAGUAR Force balance	Uncertainty assumed, consistent with previous work in the department	Zeroth
Normal Force coefficient $C_N = \frac{F_N}{1/2 \rho U_\infty^2 S}$	2.9%	Uncertainty calculated from freestream dynamic pressure, the force balance reading and the wing area.		

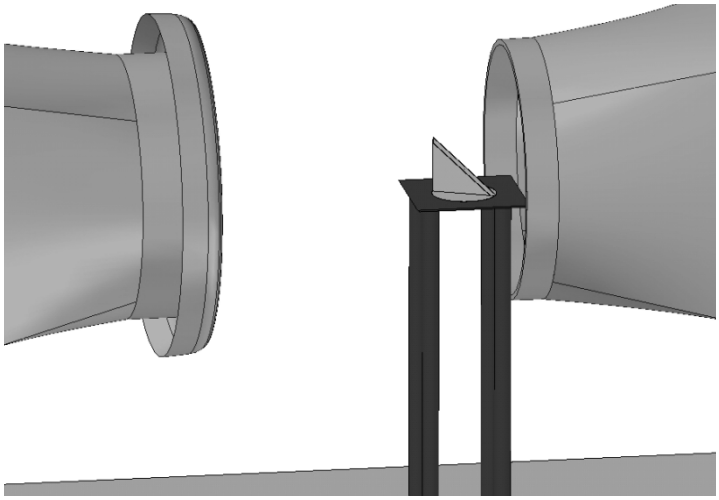

Figure 3-1 Half wing and splitter plate setup in the open section tunnel, this setup was used for pressure measurements.

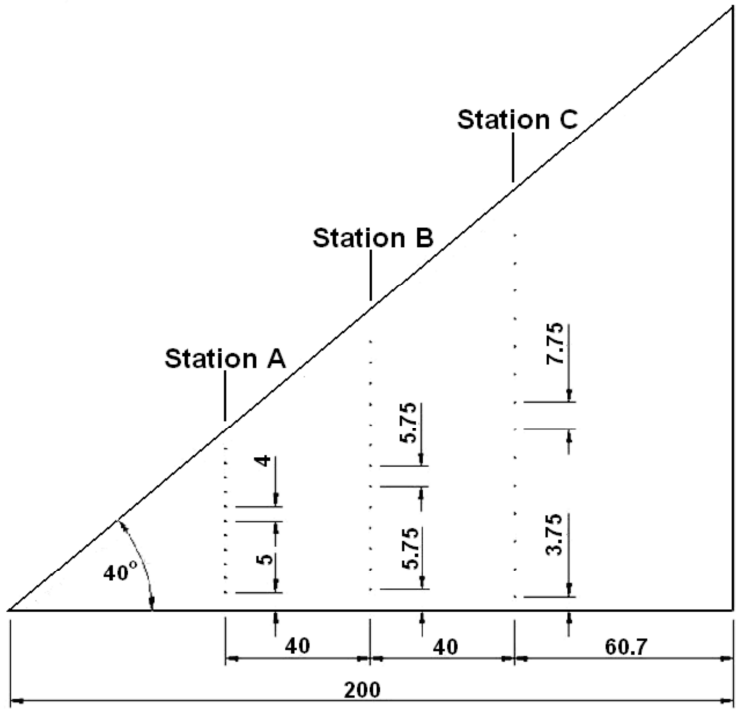

Figure 3-2 Plan view of half wing including pressure tap locations organised into three chordwise stations.

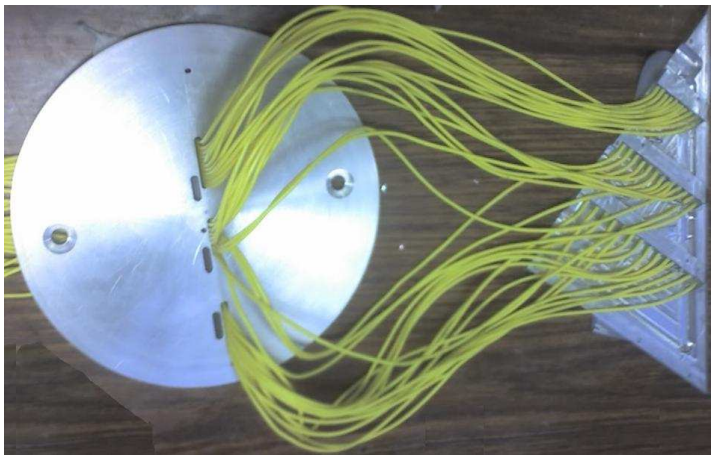

Figure 3-3 Internal view of pressure tap connections

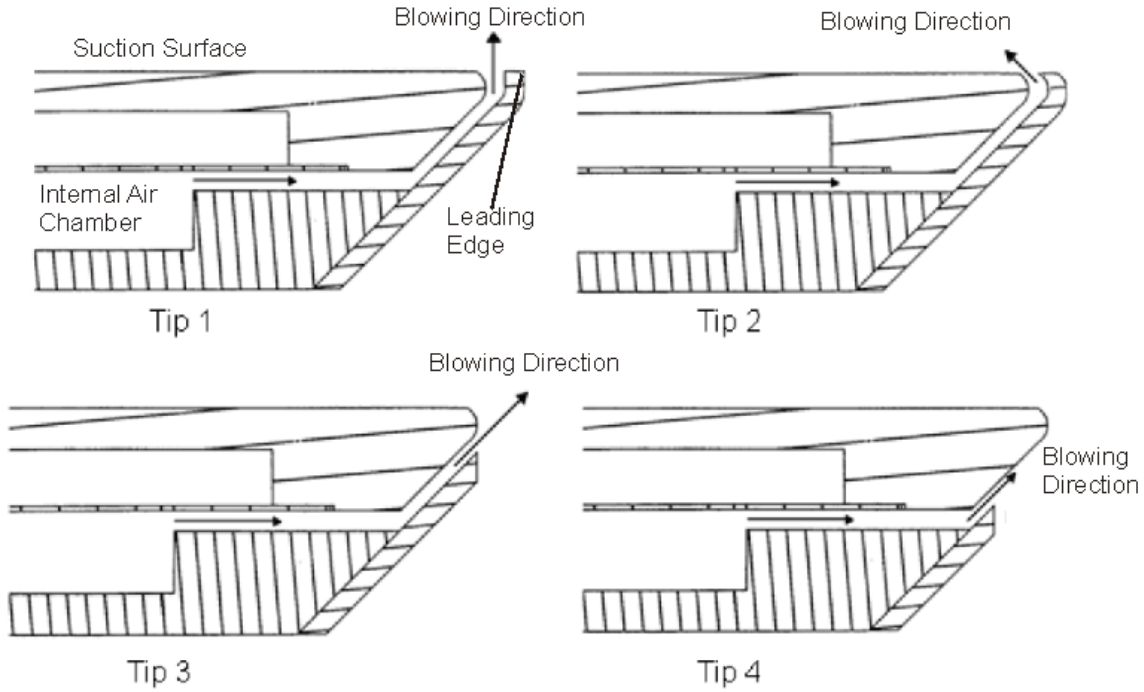

Figure 3-4 Section view of leading edge tip geometries tested.

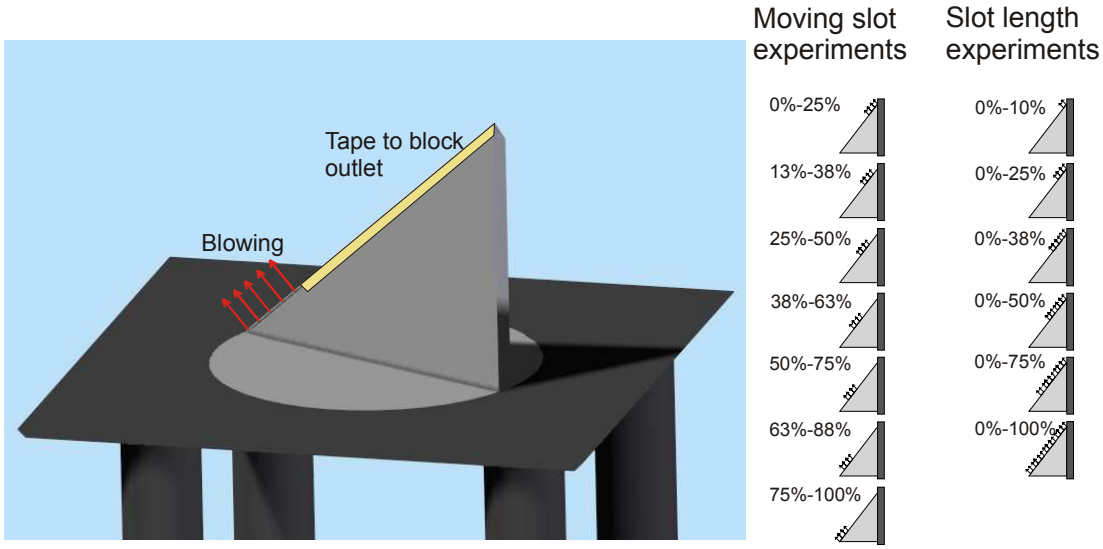

Figure 3-5 Partial blowing setup for the half delta wing. Slot locations of the experiments conducted are indicated.

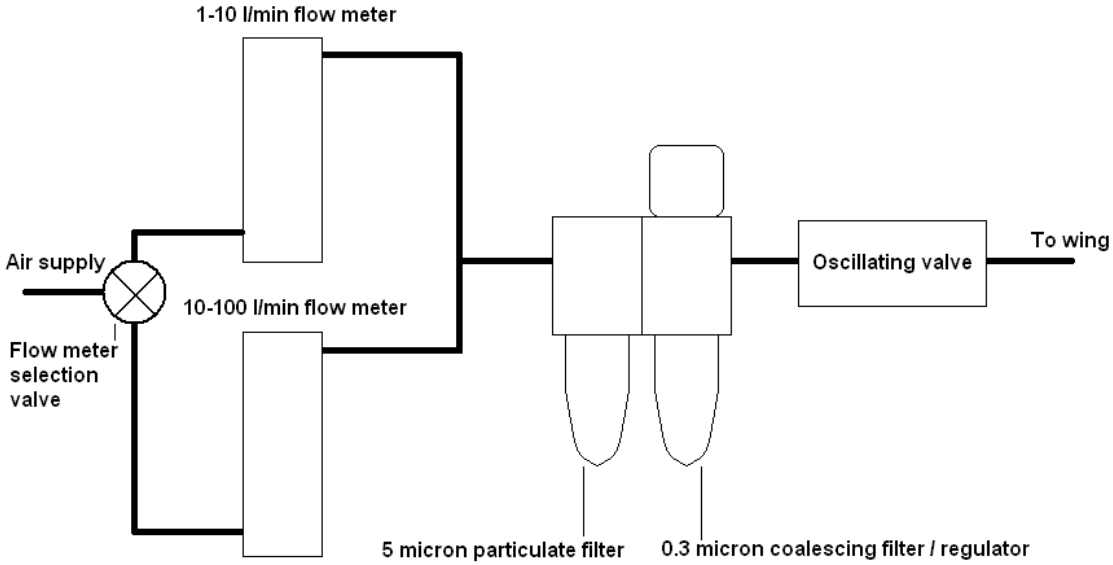

Figure 3-6 Schematic of the pneumatic valve setup.

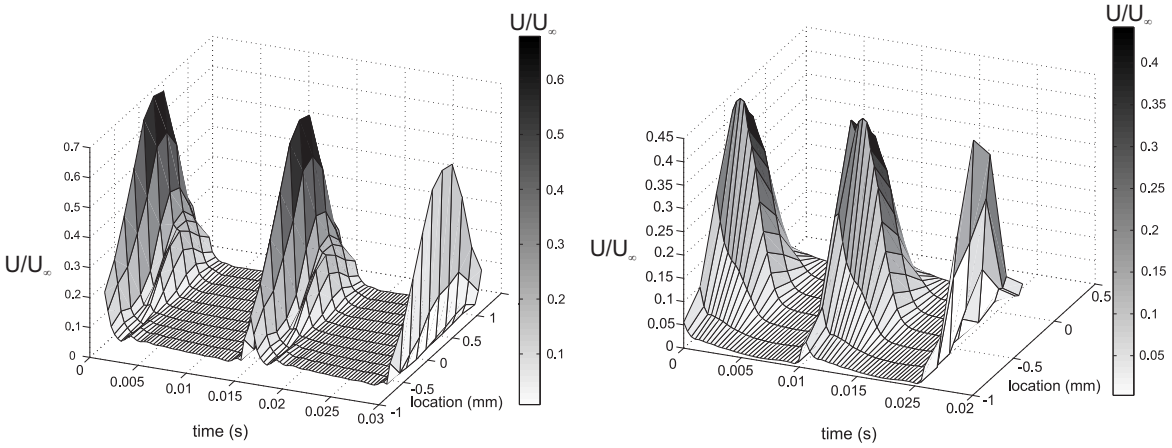

Figure 3-7 Typical pulse shapes derived from hotwire measurements for the half wing (left hand side), and the full wing (right hand side).

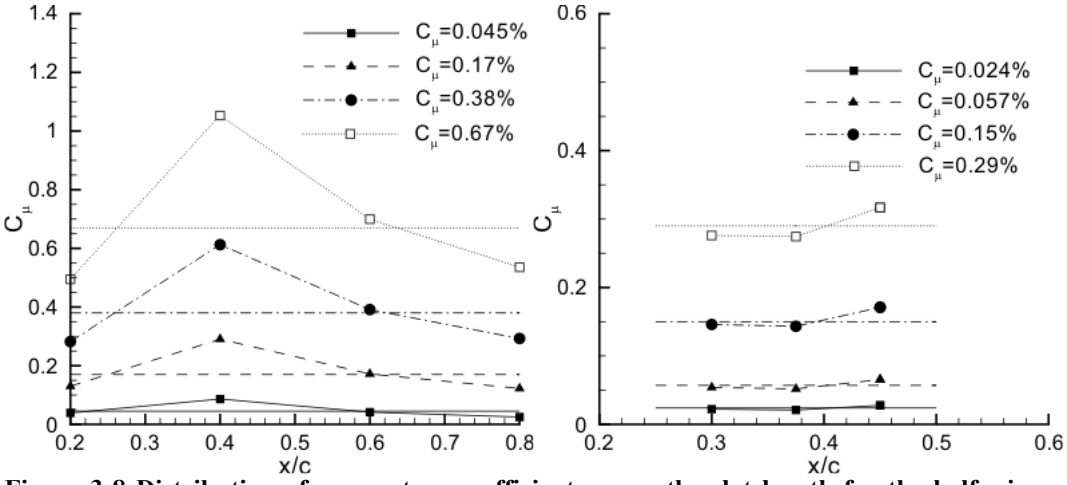

Figure 3-8 Distribution of momentum coefficient across the slot length for the half wing with a slot length of 0-100% (left hand side) and a slot length of 0-50% (right hand side) of the leading edge.

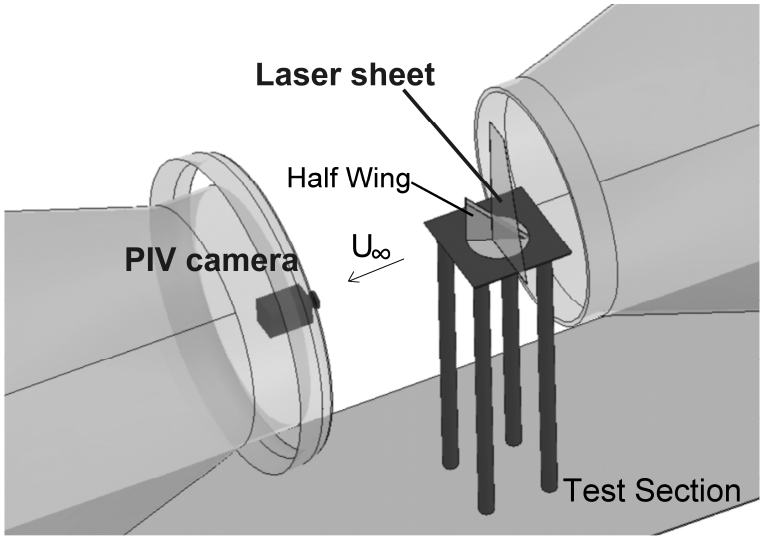

Figure 3-9 Cross-flow PIV setup.

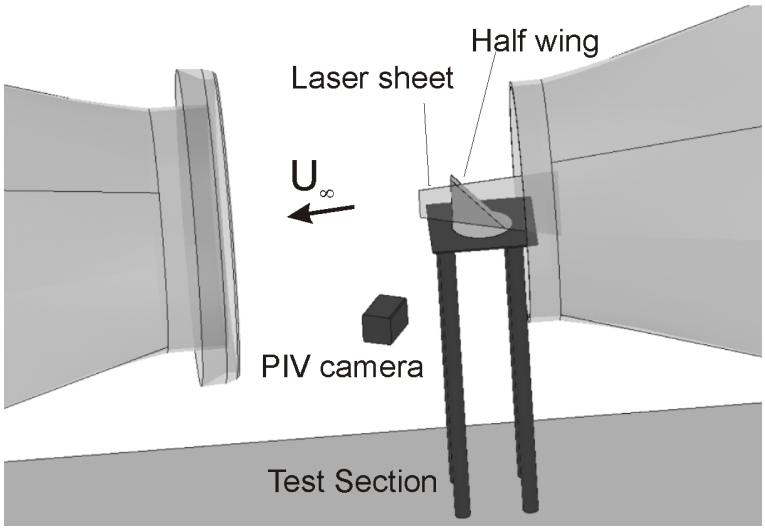

Figure 3-10 Near surface flow PIV setup.

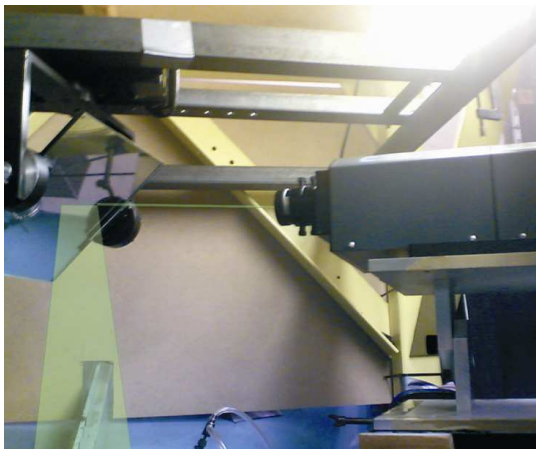

Figure 3-11 Laser and mirror setup (laser sheet location is approximate).

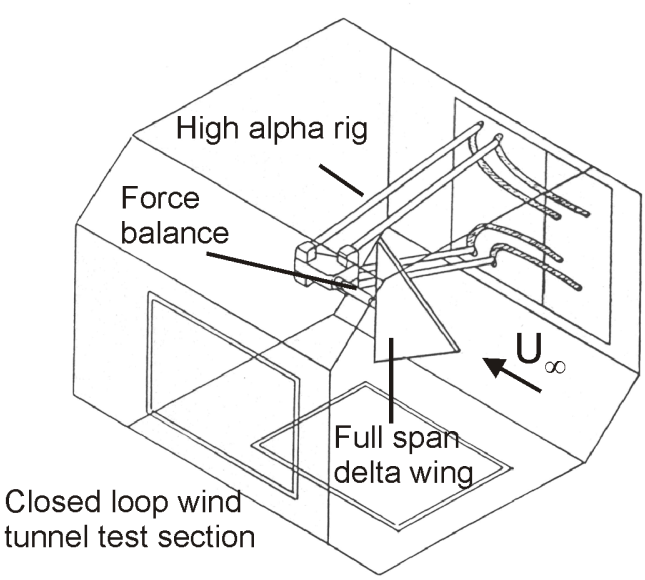

Figure 3-12 Full wing force measurement setup.

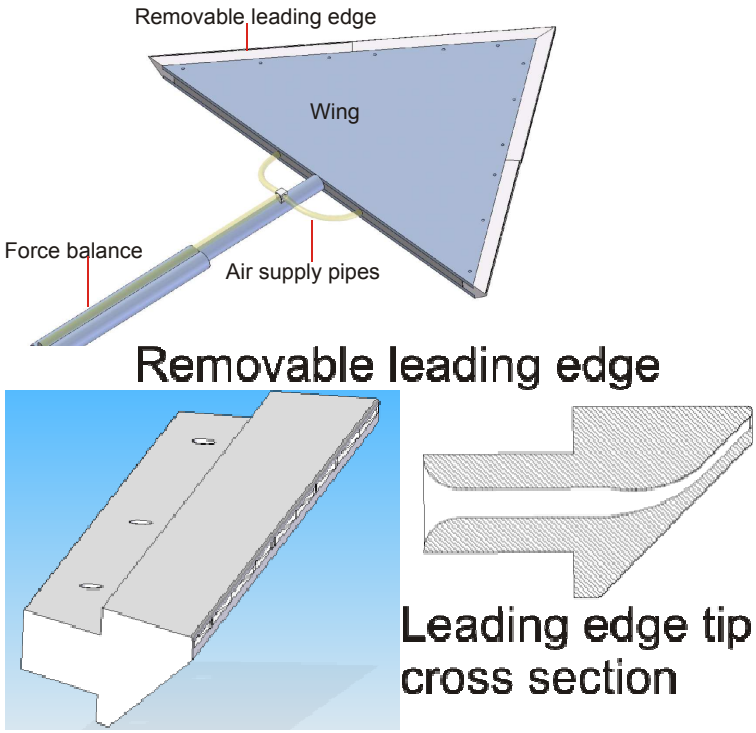

Figure 3-13 Full wing leading edge blowing tips, manufactured using rapid prototyping.

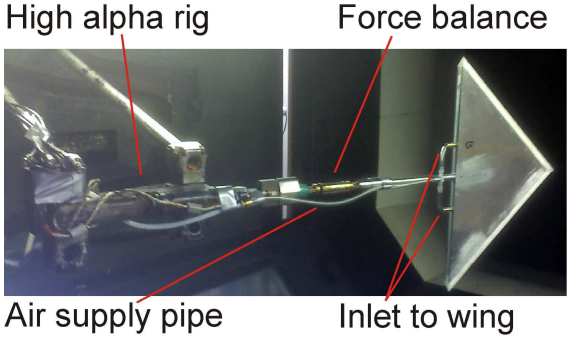

Figure 3-14 Force balance and full wing blowing setup.

Chapter 4 Time averaged measurements

The literature discussed in Chapter 2 points to the potential benefits of unsteady blowing, in particular the delay of stall and increase in the maximum lift that can be developed over nonslender delta wings. The focus of this chapter is first to quantify the benefits of unsteady blowing, and then to understand the effect of unsteady blowing on the flowfield in a time averaged sense. Initial pressure measurements were conducted as a means of quantifying and comparing different blowing parameters. This was followed by PIV measurements which explain the nature of the flow. The effect of pulsed blowing on the time-averaged pressure distribution was investigated in detail, with examples in the pre-stall, near-stall, and post-stall regimes shown here. Based on the previous investigations in a similar Reynolds number range, it is expected that stall is around $\alpha \approx 20°$ for full-span models [4]. Attar et al. [17] showed by computational simulations for a nonslender delta wing (with sweep angle of 50°) that the onset of stall is delayed for a half-span model compared to a full-span model. The results indicated that imposing the symmetry of the flow at the wing symmetry plane delays the upstream propagation of vortex breakdown and stall. The pressure data suggest that the stall angle is α=23°-24° for the half-span model used.

As discussed earlier, a range of wing tip profiles were selected for initial testing, shown in Figure 3-4. The comparison shown in Figure 4-1 is typical of the results obtained, where tip 3 consistently developed a vortical type pressure distribution at a lower momentum coefficient than the other tip profiles tested. A more complete comparison is shown in Figure 4-2. Tip 4 was the only tip profile where the point of blowing was prior to separation, and the pressure distribution showed little or no response to flow control. It is believed that pulsing prior to separation is not an effective way of exciting instabilities that only occur once separation has taken place. Unsteady blowing from tips 1-3 showed some effect on the pressure distribution, recovering the pre-stall flow structure to some extent. Of the three tips, tip 3 is the only tip that has a blowing direction perpendicular to the shear layer, and the pulsing location is particularly close to the separation point. It is believed that it is a combination of these reasons that make tip 3 particularly effective. It is possible that there may be some Coanda effect causing pulsing to be in line with the shear layer, but it is significantly more effective than tips 1 and 2, indicating that this is probably not the case. Tip 3 was selected for further experiments and, other than the results presented on steady blowing, all data presented corresponds to tip 3.

Figure 4-3 shows the pressure distribution at x/c=0.28 (station A) at α=15°, 20°, 25°, and 30°, for St=1.5 and various momentum coefficients. For α=15°, a well-defined suction peak is observed for the no blowing case (C_μ=0). The effect of pulsed blowing is very small for this incidence. For α=20°, the suction peak is nearly the same as that of α=15°, and the effect of the vortex is distributed over a larger area for the no blowing case. Based on previous studies for full-span wings, the location of vortex breakdown is expected to be close to the apex [10]. However, for the half-span model, vortex breakdown appears to be delayed. The effect of forcing is a little more

pronounced for α=20°, with the suction peak exceeding $-C_p$=3. For α=25° and 30°, it is observed for C_μ=0, that the wing is stalled, and has a very flat pressure distribution. In both cases, the introduction of unsteady blowing produces a suction peak and pressure distribution that is characteristic of a leading-edge vortex. As the momentum coefficient increases, initially a broad vortex pressure distribution occurs, indicating a reattachment line close to the wing centreline, as seen for C_μ=0.01% at α=25° and C_μ=0.4% at α=30° in Figure 4-3. For α=25°, as the momentum coefficient increases further, the pressure distribution reaches a limit, where both the maximum suction peak and the shape of the pressure distribution are no longer affected by an increase in C_μ. The flow response at this point becomes saturated, indicating that the reattachment process is complete. This occurs at C_μ=0.05% for 25 degrees angle of attack. It is evident that increasing C_μ causes reattachment, and that after initial reattachment occurs, increasing C_μ causes the reattachment line to move outboard, forming a tighter vortex like pressure distribution. For α=25°, even very small momentum coefficients are able to produce a pressure distribution characteristic of a vortex, whereas this happens at much larger momentum coefficients for α=30°. An interesting comparison is that of the pressure distribution for the saturated case at α=25° and the C_μ=0.8% case at α=20°. Even though the α=25° case is saturated, it still does not exhibit the very sharp peak in pressure at x/c=0.6 shown for the α=20° case. This difference may be a result of a reattached shear layer and conventional vortex in the case of α=20°, compared to a reattached shear layer and broken down vortex for α=30°.

PIV measurements of the cross flow field corresponding to the pressure measurements at x/c=0.28 for α=25° are shown in Figure 4-4. There is a slight difference in the unsteady blowing Strouhal number of the PIV measurements shown (St=1.3 compared to St=1.5), however in a time averaged sense, in this Strouhal number and momentum coefficient range, the flow fields are believed to be similar. For the C_μ=0 case in Figure 4-4, the separated shear layer is seen to separate from the leading edge, with weak reattachment seen near the wing's centreline. This weak level of reattachment corresponds to the low levels of suction seen in the pressure measurements at this station. In contrast, blowing at C_μ=0.07% shows higher velocities in the reattachment region and a strong vortical flow pattern as the shear layer reattaches to the wing's surface. The corresponding stream line patterns and the nature of the shear layer are discussed in greater detail later in this chapter.

Moving downstream, Figure 4-5 shows the pressure distribution at x/c=0.48 (station B) and Figure 4-7 shows the pressure distribution x/c=0.68 (station C). As the pressure tap location moves downstream, for all angles of attack, the pressure distribution broadens, and the magnitude of the suction peak is reduced. The effect of increasing the momentum coefficient on the reattachment location can be seen in the α=25° case for all three stations. As the momentum coefficient increases, the spanwise point at which the magnitude of the suction pressure starts increasing moves further outboard.

Figure 4-5 shows a pressure point at x/c=0.48 and y/s=85% which, although being responsive to the changes in pressure, appears consistently lower in value than surrounding pressure points. This is not seen at either of the other chordwise stations, nor is it consistent with previously published pressure distributions. As a result this point is not considered in future discussion, but included in the plots for completeness. The error is possibly due to a small blockage in the pressure tap line, not allowing pressure to stabilise before a measurement is taken.

Figure 4-6 shows the crossflow velocity field at a higher angle of attack, α=30° at x/c=0.48 with unsteady blowing at St=1.5. This corresponds to the pressure measurements shown in Figure 4-5 for α=30° and C_μ=0.4%, where a broad vortex type pressure distribution is present at this station on the wings surface. With the introduction of unsteady blowing, even at this high angle of attack Figure 4-6 shows that the shear layer reattaches to the wing's surface and a coherent vortical structure is formed.

An interesting point to note is that for all cases presented, if reattachment appears to occur at x/c=0.28 (station A), there is also a similar effect at x/c=0.48 and x/c=0.68 (stations B & C). This indicates that for all cases where reattachment of the shear layer occurs, it occurs between x/c=0.28 and x/c=0.68 and probably along the entirety of the leading edge.

As shown in the discussion of the previous figures, the introduction of pulsing has a strong influence on the pressure across the suction surface in the post stall region. For the purpose of demonstrating the effect of flow control, the pressure distribution at these streamwise stations of the wing (x/c=0.28, 0.48, 0.68) has been integrated across the span to obtain a sectional suction force coefficient, and then over the surface of the wing to give a suction force coefficient for the wing. This is only an indication of the normal force coefficient, but is sufficient for comparative purposes. Results from a similar method, albeit with more pressure points have been compared favourably with the total measured force on a delta wing [45]. The estimated suction force coefficient C_S is shown in Figure 4-8 as a function of angle of attack for St=1.5. In Figure 4-8, it is clear that even pulsing with momentum coefficients as low as 0.01% can have significant effect on the suction force produced. The maximum suction force coefficient increased from C_S=1.05 at α=24° for C_μ=0, to C_S=1.23 at α=30° for C_μ=0.4%. This equates to a 17% increase in maximum suction force coefficient. Stall can also be delayed by up to 8 degrees in the case of pulsing at C_μ=0.8%. For C_μ values of 0.01% and above, it appears that the suction force coefficient is saturated for angles of attack below α=28°. As the angle of attack is increased, larger values of momentum coefficient are required to prevent the onset of stall. Using active flow control with pulsed blowing, high lift can be maintained at angles of attack greater than α=30°. An interesting point on Figure 4-8 is the stall angle of the wing with no flow control. At this angle, all the flow control cases of different momentum coefficients collapse to a singular point, and have the same C_S value. Using the above method, the suction force has been calculated for each station. This is simply a reflection of the change in suction pressure at each station. When comparing the three

stations, it can be seen that for x/c=0.28 (station A), shown in Figure 4-9, at low angles of attack unsteady blowing has very little effect (as previously discussed) and that for angles of attack under α=28°, saturation occurs at even the lowest momentum coefficients. For this station there is no detrimental effect to blowing at momentum coefficients higher than what is required to saturate the suction force coefficient. By contrast stations x/c=0.48 (station B, Figure 4-10) and x/c=0.68 (station C, Figure 4-11) do show that unsteady blowing can be effective for pre-stall cases. As shown in Figure 4-5 and Figure 4-7, for α=15°, the magnitude of the suction peak can be increased with unsteady blowing. This is a promising result, as it shows there may be some potential for pre-stall flow control. This is probably due to the pre-stall vortical flow at x/c=0.48 and x/c=0.68 being less intense than at x/c=0.28 and not completely saturated. Figure 4-10 and Figure 4-11 also highlight that the result that excessive blowing can have a slight detrimental effect for any given angle of attack, is a attributed to the pressure distributions at stations B and C, and not at station A. This is most pronounced at x/c=0.68, station C, where lower momentum coefficients generate higher suction at low post-stall angles of attack, and higher momentum coefficients generate higher suction at high post-stall angles of attack.

The difference between the pre-stall and post-stall behaviours can clearly be seen in the plot of percentage increase in C_S (i.e. $\Delta C_S/C_S$), against angle of attack, shown in Figure 4-12. For the pre-stall incidences, the greater the momentum coefficient, the greater the percent increase in C_S, although the increase is small (less than 9%). In the post-stall region, much larger increases are possible. The effect of excitation becomes saturated at some minimum value of C_μ for each angle of attack. For example, at α=28°, the effect of flow control becomes saturated between C_μ=0.02% and C_μ=0.05%. As the angle of attack increases, the minimum C_μ required to saturate the effect of flow control increases, as does the maximum percentage increase in C_S achievable. In the maximum case, a C_μ of 0.8% is required to increase C_S by 64%, which happens at an angle of attack of α=32°.

Effectiveness is an important parameter when considering the efficiency of a flow control method. For this case, the effectiveness is defined as the ratio of change in suction force coefficient to momentum coefficient, i.e. $\Delta C_S/C_\mu$. Pulsed blowing is more effective at lower momentum coefficients and at incidences slightly larger than the stall angle, as shown in Figure 4-13. At very large incidences (past 30°) for which maximum increases in suction force are observed, the effectiveness is low, due to the high momentum coefficients needed to maintain attached flow. Effectiveness levels of up to 2,000 attained for C_μ=0.01% are comparable to previous findings for a Λ=60° wing [32]. Figure 4-13 also indicates that lower momentum coefficients are more effective. This is because the effect of the flow control technique becomes saturated at a set momentum coefficient. Control of re-attachment using unsteady blowing in the post-stall region is orders of magnitude more effective than steady blowing [13].

The unsteady forcing Strouhal number has been shown in previous literature to be an important parameter in unsteady flow control. Tests were conducted over the range of the most effective frequencies indicated by Vardaki [3]. The percentage increase in suction force coefficient for a range of Strouhal numbers is shown in Figure 4-14. It shows that the effectiveness of the flow control method is highly dependant on Strouhal number. These results can be organised into narrow momentum coefficient bands to give an indication of the relative effectiveness of each Strouhal number, as shown in Figure 4-15. There appear to be two regions of higher effectiveness, centred at around St=0.6 and St=1.25. This appears similar to the results for an excited free shear layer presented by Hasan and Khan [25] in Chapter 1, Figure 2-14. The spectral peaks also coincide with the frequency of velocity fluctuations recorded in the region of the reattached shear layer in the near surface plane by Taylor and Gursul [10] for a Λ=50° wing just prior to stall. Force measurements using a different setup also confirm this finding, and will be discussed in Chapter 8. These results are in contrast with results of the effect of wing oscillations on vortex breakdown location presented by Vardaki [29], that indicated a singular peak in maximum vortex breakdown delay, centred at around St=1.5. There are two possible reasons for this difference. The first is that for small amplitude roll oscillations, an increase in frequency is coupled with an increase in forcing velocity. Oscillations at a Strouhal number of 1.2 will have twice the maximum leading edge velocity of oscillations at a Strouhal number of 0.6. This makes comparing Strouhal numbers difficult. The second is that the location of vortex breakdown is not a direct indicator of the forces developed on the wing, and not a direct indicator as to whether the shear layer has reattached. It is important to note that, despite a drop in effectiveness at St=1.0, a significant increase in suction force coefficient can still be achieved at this Strouhal number, albeit at higher momentum coefficients. The physical mechanism for this phenomenon will be discussed in Chapter 5. A more in depth study was conducted for unsteady blowing at a Strouhal number of St=0.5, as it appeared to be more effective than unsteady blowing at St=1.5. The variation in suction force coefficient with angle of attack is shown in Figure 4-16. At both St=1.5 and St=0.5, a significant increase in suction force coefficient is observed, however there are significant differences in the relationship between suction force coefficient and angle of attack. At angles of attack shortly after stall, St=1.5 appears to be more effective, however as the angle of attack is increased, St=0.5 becomes more effective, and shows a more gradual stall. The increase in maximum suction force coefficient for both Strouhal numbers is similar (17%-18%). Although the excitation spectrum for the St=0.5 case does contain significant spectral content at St=1.5, this does not account for the increased effectiveness at higher angles of attack of the lower excitation frequency. A possibility is that different frequencies may be more effective at different angles of attack, i.e., the optimum frequency range might depend on the angle of attack. This appears to be the case when comparing the suction force coefficient plots for St=0.5 (Figure 4-16) and St=1.5 (Figure 4-8). The effectiveness of the Strouhal number of St=0.5 case is shown in Figure 4-17. As expected, for any given momentum coefficient, the peak effectiveness level occurs at a higher angle of attack than for the St=1.5 case. In addition to this, the shape of the peak tends to be less sharp, indicating a better

level of effectiveness over the angle of attack range, and perhaps unsteady blowing at St=0.5 is more practical than unsteady blowing at St=1.5.

As the wing tested was a half body wing platform, it is difficult to assess the full effectiveness of leading edge unsteady blowing from one side of the wing for the purpose of roll control. In the following analysis it was assumed that pulsing from only one side of the symmetry plane, would not have an affect on the flow on the other side of the symmetry plane. This assumption is unlikely to be correct, however for the purposes of estimating the potential of this method of flow control it is adequate. Figure 4-18 shows the roll moment developed over the wing with unsteady blowing at St=1.5, and Figure 4-19 shows the comparative St=0.5 case. St=1.5 shows potential for roll control across the angle of attack range tested, particularly there is potential shown for the pre-stall case. For the pre-stall case, the higher the momentum coefficient, the greater the level of roll control achievable. The maximum change in roll moment at $\alpha=15°$ was $\Delta C_L=0.01$, which compares favourably to an analysis conducted by Nelson et al. [35] estimating the level of roll control that could be achieved by an aileron at maximum deflection on the $\Lambda=47°$ UAV model tested to be $\Delta C_L=0.004$. As mentioned earlier, direct comparisons can be misleading given the approximation made, but the fact that the results are of similar magnitude is promising. The St=0.5 case however shows significantly less roll control potential for the pre-stall angle of attack range, but is effective post stall. Another consideration is that additional control may be achieved using the detrimental effect of steady blowing on the other half of the wing.

Brief experiments were conducted on the effectiveness of steady blowing for the half wing configuration with the four tip shapes shown in Figure 3-4, the results are shown in Figure 4-20. Figure 4-20 shows the change in suction force coefficient using the pressure distribution of station A (x/c=0.28). Plots of the suction force coefficient using station C (x/c=0.68), not shown here, show a similar trend. Almost all results indicated that steady blowing had a detrimental effect on the suction force coefficient. All tip shapes showed a negative peak in percentage change in suction force coefficient at around $C\mu=0.05\%$, followed by a general upward trend. As the momentum coefficient was increased above $C_\mu=0.4\%$, tips 1 and 2 began to show positive, although small increases in suction force coefficient. It is interesting to note that the tip profile that had the most detrimental effect for steady blowing was that of tip 3, which had the most positive effect for unsteady blowing.

In addition to being able to quantify the potential gains achievable by unsteady blowing, the topographical nature of the flow field and its progression from a stalled state to a reattached state needed to be investigated. Additional PIV measurements to those shown earlier in this chapter are presented to investigate the nature of the flow at different blowing parameters in more detail. In addition to measurements in the cross flow planes corresponding to the pressure measurement locations, measurements were taken in the near surface plane and in a plane through the vortex core. The intension of taking measurements in a plane through the vortex core was to indicate

whether jet like or wake like flow develops in the vortex core, and to indicate the location at which the vortex undergoes breakdown.

The time-averaged cross-flow velocity shown in Figure 4-21, an expansion of Figure 4-4 including all chordwise stations, indicates that the wing is near the stall at α=25°, as the shear layer reaches the wing centreline. When pulsing is introduced, in this case at C_μ=0.07% and St=1.3, the flow reattaches to the wing and a vortex flow pattern develops. This occurs for all three stations, with the highest cross-flow velocities occurring at station A (x/c=0.28) and approaching the free stream velocity in magnitude. The velocity field appears to be roughly conical as the flow structure is similar in all three stations. High velocities occur along the shear layer as well as the reattachment region. This is confirmed by the streamlines (Figure 4-22) getting closer together in these regions. The calculated streamlines from the averaged PIV measurements show distinct differences between the forced and reference (unforced) cases. At C_μ=0, a weak recirculation region is present. The location of the centre of this pattern is at y/s=0.26-0.33, depending on the streamwise station. An interesting point to note is that the streamlines in this case emanate outwards from the centre of the recirculation region. This indicates that the radial velocity in the vortex centre region is directed outwards. The streamlines for the C_μ=0.07% case show a significantly stronger vortex flow pattern. The streamlines converge to the centre of the vortex core in station B (x/c=0.48). The nature of the axial flow in the core will be discussed later in this chapter. With forcing, the centre of the vortex flow pattern moves outboard to y/s=0.45 – 0.53, significantly further outboard of the C_μ=0 case. This is because the flow has completely reattached, and the attachment line has also moved outboard. When comparing the streamlines near the leading-edge of the wing, the main difference is that for the C_μ=0 case, the streamlines leave the leading-edge at an angle of approximately 45°, towards the centreline of the wing. By contrast in the C_μ=0.07% case, the streamlines leave the wing tip almost vertically. The effect of flow control on the vortical flow is also evident from the examination of the velocity fluctuations. Normalised turbulence intensity is shown for station C (x/c=0.68) in Figure 4-23. The C_μ=0.07% case clearly shows a high level of turbulence distributed uniformly throughout the vortex, which is an indication of vortex breakdown upstream of this station. In contrast, the C_μ=0 case shows the presence of the shear layer, coming from the leading edge of the wing.

Figure 4-24 and Figure 4-25 show the cross-flow velocity and streamlines at x/c=0.28 for a larger angle of attack, α=30°. In this case, the wing is in deep stall for the reference case (no blowing), as evidenced by the velocity and the streamline pattern, which suggest that the stagnation point moves onto the wing centreline at z/s ≈ 0.8. The streamlines appear to spiral out in the recirculation region. With forcing, the reattachment is observed with much larger cross-flow velocities inboard (y/s ≈ 0.2) and also near the wing surface. In this case, the streamlines spiral in towards the centre of the vortical flow. The other features of the streamline pattern are similar to those of the lower incidence of α=25°. Figure 4-24 and Figure 4-25 also outline the effects of gradually increasing the momentum coefficient. The pressure measurements in Chapter 4 did indicate that there was a

significant change in suction pressure across the wing, but it was difficult to ascertain the effect that small changes to the momentum coefficient had on the flow field. Figure 4-24 shows the increase in cross-flow velocity magnitude as the momentum coefficient is increased. Without forcing, the velocity magnitude in the region close to the wing's centreline is close to zero. As the momentum coefficient is increased, the shear layer reattaches to the wing's surface (shown in Figure 4-26), and the velocity in the reattachment region increases until it is near that of the freestream. The region close to the wings surface also undergoes a significant increase in velocity magnitude as the shear layer wraps around and reattaches. Clear changes in the streamline flow pattern can be seen in Figure 4-25. In particular, the spanwise location of the centre of the swirl pattern moves outboard with increasing momentum coefficient. The centre of the swirl pattern at C_μ=0% is at y/s=0.275 and at C_μ=0.57% it is y/s=0.425. An important thing to note is that the centre of the swirl pattern moves gradually over the momentum coefficient range. This is similar to a nonslender delta wing moving away from stall (reducing in angle of attack). Another interesting feature is the reduction in the extent of the flow not being recirculated over the wing as the momentum coefficient is increased. At C_μ=0%, the detached shear layer can clearly be identified, and a significant portion of the flow does not swirl around the vortex structure, and does not interact with the wing's surface. As the momentum coefficient increases to C_μ=0.17%, most of the flow becomes entrained into the vortex flow structure, indicating a stronger vortex and a reattached shear layer. This is reinforced by measurements of the cross-flow vorticity, shown in Figure 4-26. For the case with no forcing, the shear layer contains low levels of vorticity distributed along the detached shear layer that was clearly visible in Figure 4-25. There is a slight increase in vorticity levels at the symmetry plane. As forcing is introduced, the concentration of vorticity in the shear layer increases significantly. As the unsteady forcing is a source of vorticity, this is to be expected, but the significant increase also implies a more concentrated and organised shear layer, and the possibility that vorticity from upstream is feeding the shear layer after reattachment. When the momentum coefficient is increased to C_μ=0.17%, the shear layer reattaches completely to the wings surface, and vorticity levels in the region of reattachment, and along the wings surface increase significantly. Even after the shear layer has reattached, increasing the momentum coefficient further increases the maximum vorticity, and the extent of the high vorticity region on the wing's surface.

The corresponding turbulence intensity in the cross-flow plane being discussed is shown in Figure 4-27. The separated shear layer can be clearly identified for the unforced case in Figure 4-27, which is similar to the α=25° angle of attack case shown in Figure 4-23. As the momentum coefficient is increased, the shear layer can be seen to wrap round and attach to the wings surface. As the momentum coefficient is increased above C_μ=0.17%, the turbulence is no longer confined to the shear layer and close to the surface, and becomes distributed throughout the region enclosed by the shear layer, comparable to Figure 4-23. The fact that the turbulence intensity becomes more distributed throughout the vortex flow pattern with increasing momentum coefficient indicates that

in addition to the reattachment of the flow, a conventional vortex with jet like axial flow may have formed at the apex of the wing, and broken down upstream of the measurement point, forming turbulent wake.

The near-surface velocity measurements shown in Figure 4-28 reveal a large reversed flow region on the wing surface for the no control case. With excitation, the flow reattaches near the wing centreline, as evidenced by the streamlines becoming very close to each other and also diverging further downstream. The approximate reattachment line is indicated by the red dotted line in Figure 4-28. A small movement in the reattachment location is seen as the momentum coefficient is increased, but as the shear layer has almost completely reattached at C_μ=0.11%, it is difficult to identify a more gradual progression. This surface flow pattern at α=30° is similar to that of a lower incidence before stall [10]. The streamline patterns presented are supported by velocity magnitude plots in Figure 4-29, which include lower momentum coefficients at C_μ=0.03% and C_μ=0.06%. For the no blowing case, low velocity regions dominate the flow, and reattachment does not occur. As the momentum coefficient is increased, the magnitude of the velocity near the centreline increases, and the region of low velocity magnitude reduces in extent and moves outboard. At C_μ=0.06% partial reattachment occurs, shown by a thin, high velocity region near the wing's centreline. As the momentum coefficient increases further, the extent of the high velocity region increases, in particularly in the spanwise direction. Above C_μ=0.11%, only small changes can be seen in the near surface velocity magnitude.

One important aspect of the reattachment and the vortical flow established over the wing is the nature of the axial flow in the vortex core. This was investigated by PIV measurements of a plane through the vortex core. The location of the centre of the vortical flow or recirculation region was identified from the cross-flow measurements, and the PIV laser sheet was placed at an angle ϕ with respect to the free stream velocity to pass through the core. This angle was the same (ϕ=21°) for all cases from C_μ=0 through to C_μ=0.59%. The time-averaged velocity fields in these planes are shown in Figure 4-30. It is seen that the separated region with low axial velocity or almost stagnant fluid is evident for the reference (no blowing) case. This massively separated region covers most of the wing, including the region near the centreline (the dashed line shows the projection of the leading-edge in the measurement plane). With active flow control, the region of low velocity is smaller, but still substantial. This indicates that there is virtually no axial flow in the vortex core in the region studied. Upstream of x/c≈0.1 accurate measurements cannot be obtained due to reflection of the laser sheet very close to the apex. This result confirms that vortex breakdown is at the apex or very close to the apex. All measurements, including those for the largest momentum coefficients indicate that the leading-edge vortex always underwent breakdown before x/c=0.1. Although delayed breakdown could be observed for the oscillating wings [3-5], the equivalent momentum coefficients are thought to be much larger than those used in the experiment presented here. The fact that the jet like core of the leading edge vortex does not extend past x/c=0.1 for unsteady blowing from the leading edge, may be an indication of the importance of the

oscillations of the trailing edge in the flexible wing case, and their role creating a more favourable pressure gradient. Research into steady and unsteady trailing edge blowing from a Λ=50° wing indicated that flow control at the trailing edge could have a significant effect on the nature of axial flow in the vortex wake [14, 46, 47].

Investigations were also made into the effect of the Strouhal number on the cross-flow and near surface flow fields using PIV. The cross-flow time averaged velocity magnitude for Station A at x/c=0.28 is shown in Figure 4-31. It appears that as frequency increases from St=0.25 to St=0.75, the velocity magnitude of the reattached flow increases. At St=0.9 the velocity magnitude and flow pattern revert back to flow similar to the C_μ=0% case, and the shear layer is detached. The shear layer reattaches for St=1.25 and St=1.5, with high velocities present, and then at St=2.0 again, the flow pattern reverts back to flow similar to the C_μ=0% case. This progression is similar to the effect of Strouhal number on the suction force coefficient obtained from the pressure measurements. One difference is that the St=0.5 case appears to have lower cross-flow velocities than the St=0.75, St=1.25 and St=1.5 cases, even though pressure measurements had shown that unsteady blowing at St=0.5 was particularly effective. One possible reason for this could be that C_S as a parameter is not particularly sensitive to small changes in the pressure distribution, and as discussed earlier, PIV measurements tend to show the effect of increasing the momentum coefficient much better than the suction force coefficient. In general, once the flow is attached, as it is in the St=0.5 case, there tends not to be significant further increase in C_S, even if the shape of the pressure distribution and the PIV results indicate a stronger vortex. In addition to this, the PIV results presented are only for x/c=0.28 (station A) and do not show any information about the flow at stations at x/c=0.48 and x/c=0.68, whereas the calculation of C_S does.

Figure 4-32 shows the streamline patterns for the cases corresponding to Figure 4-31. This is further evidence supporting the conclusions drawn from Figure 4-31, and in particular highlights the stalled flow at St=0.9 and St=2.0, and its similarity to the C_μ=0% case. Blowing at St=0.25 and Cμ=0.15% appears to have a very similar mean flow streamline pattern to blowing at St=0.5 and C_μ=0.16%. This is interesting as it shows that despite differences in Strouhal number, the time averaged nature of the flow pattern is similar, and the way that the shear layer reattaches is similar. It is likely that the form of the reattached flow and its progression from fully detached to fully reattached is the same in the mean flow sense, regardless of the Strouhal number, although the progression from stalled to reattached flow occurs at different momentum coefficients, as shown by the cases for other Strouhal numbers presented.

The vorticity in the cross-flow plane is shown in Figure 4-33. Of particular interest is the high level of vorticity in the St=1.25 case. Previous experiments at one Strouhal number (St=1.5) indicated increased vorticity as the momentum coefficient increased. Figure 4-33 shows that for very similar momentum coefficients, the level of vorticity concentration is also dependant on Strouhal number and that the increased vorticity in the shear layer is not simply a direct result of the additional

vorticity from the unsteady blowing, but also perhaps a greater level of organisation of vorticity present in the shear layer. These plots indicate that pulsing in the region just above St=1.0 can be as effective as pulsing in the region of St=0.5 and both cases are preferable to unsteady blowing at St=0.9.

The corresponding near surface velocity magnitude and streamline flow patterns are shown in Figure 4-34 and Figure 4-35 which support the results and discussion of the previous paragraph. Again, topographically the flow is similar to the St=1.5 case at different stages of reattachment. It is important to note that for this case, the momentum coefficient range is slightly larger. The results are in agreement with the cross-flow cases, indicating that the St=0.9 case is the least effective of the cases tested. The region of high axial velocity near the centreline, an indication of shear layer reattachment, grows as the Strouhal number increases from St=0.25 to St=0.75. Unsteady blowing at St=0.9 shows a small increase in velocity magnitude and reduction in reversed flow region, however the shear layer has not reattached to the wing's surface. The slight increase in velocity magnitude is probably due to increased interaction of the shear layer with the splitter plate. As the Strouhal number increases to St=1.25 and St=1.5, the flow reattaches completely. Of particular note is that the St=1.25 case, which has a significantly lower momentum coefficient than the other cases, still shows a high level of flow reattachment. The physical mechanism that causes the change flow properties with momentum coefficient will be discussed in Chapter 5.

Pressure measurements over the suction surface indicate that unsteady blowing at post-stall angles of attack increases the suction force acting on the wing's surface, creating a vortex type pressure distribution. PIV measurements reveal that this increase in suction force is due to the reattachment of the shear layer. At angles of attack higher than stall, weak or no reattachment of the shear layer occurs, as blowing is introduced, the shear layer reattaches to the wing's surface. As the level of unsteady blowing increases, the reattachment point moves outboard, until further blowing has no effect. The effect of blowing can be considered saturated when a vortex type pressure distribution has developed and no further gains in suction force coefficient can be achieved.

Further measurements were conducted to understand the nature of the flow in both the near surface plane and through the vortex core. Near surface PIV measurements show large regions of reversed flow over the wing's surface. As blowing was introduced, reattachment occurred near the wing's centreline, and this region became dominated by chordwise flow of a similar magnitude to the freestream. Measurements through the vortex core showed that even for unsteady blowing at high momentum coefficients that show reattachment in the cross flow planes, vortex breakdown occurs near or at the apex, highlighting that vortex breakdown is not the limiting factor for lift generation on nonslender delta wings.

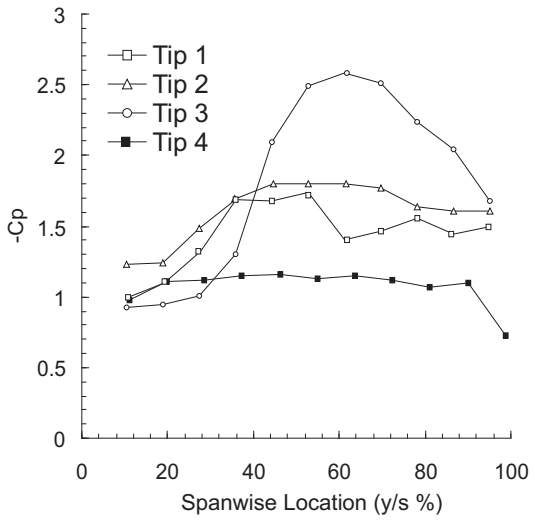

Figure 4-1 Comparison of unsteady blowing from different leading edge tip profiles, α=25°, C_μ=0.4%, x/c=0.28.

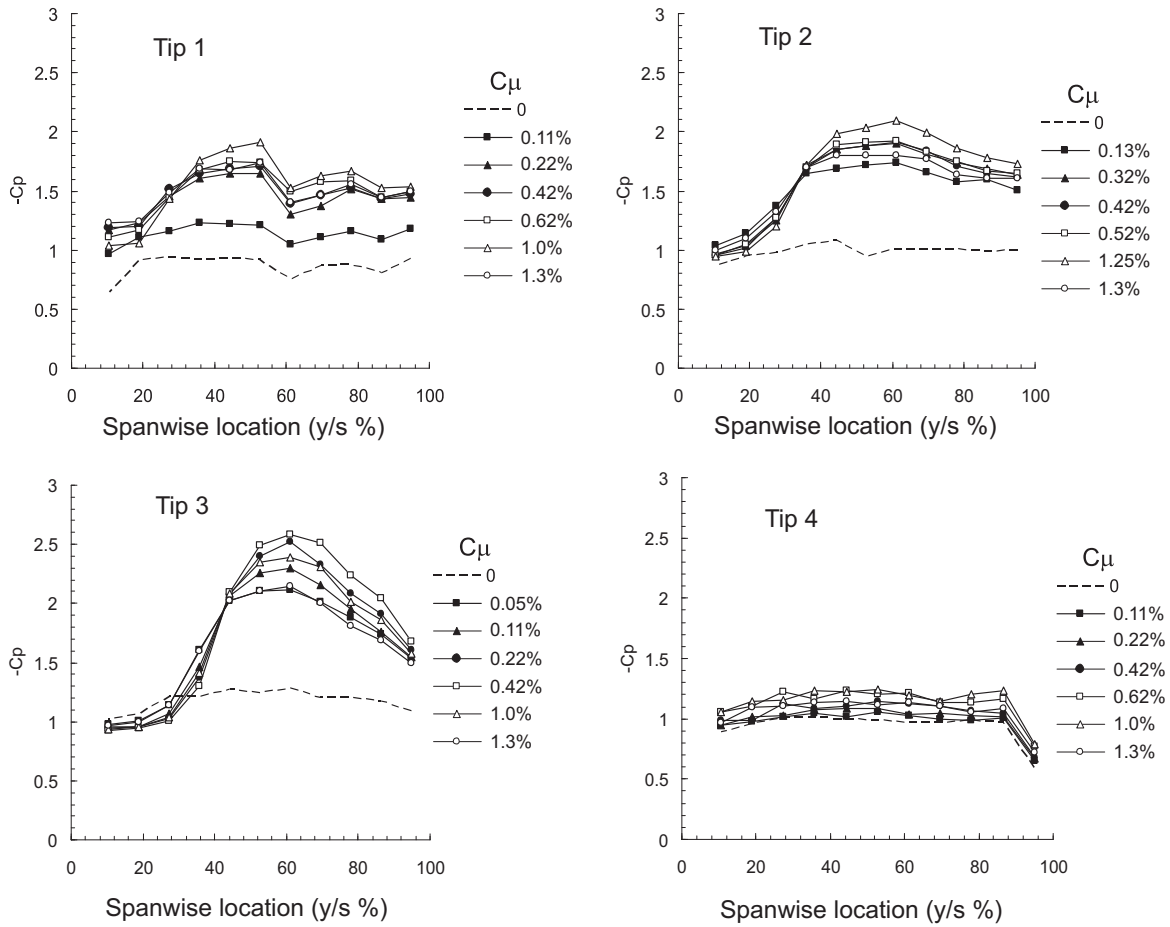

Figure 4-2 Comparison of unsteady blowing at a range of momentum coefficients from different leading edge tip profiles, α=25°, x/c=0.28.

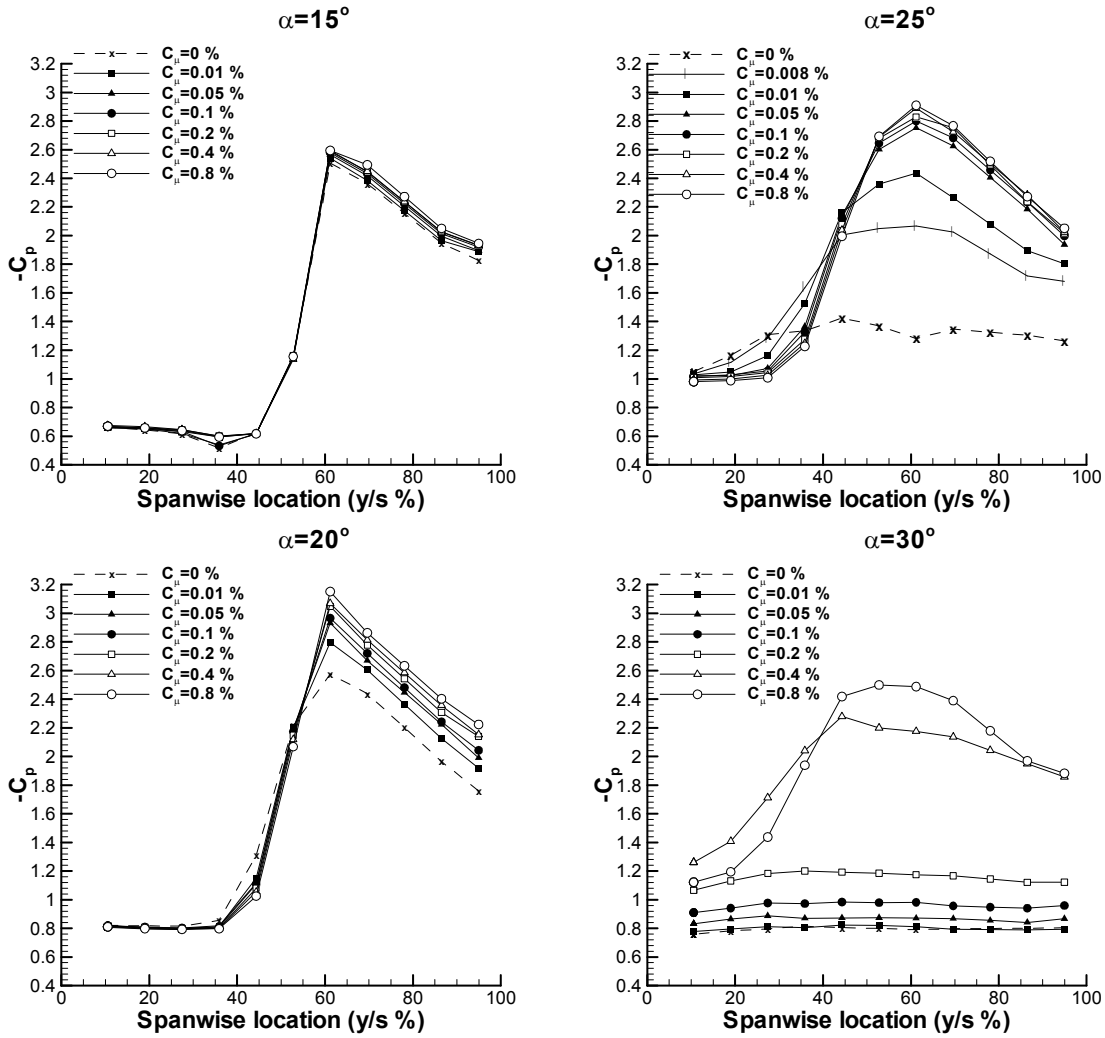

Figure 4-3 Spanwise variation of pressure at different angles of attack, x/c=0.28, St=1.5.

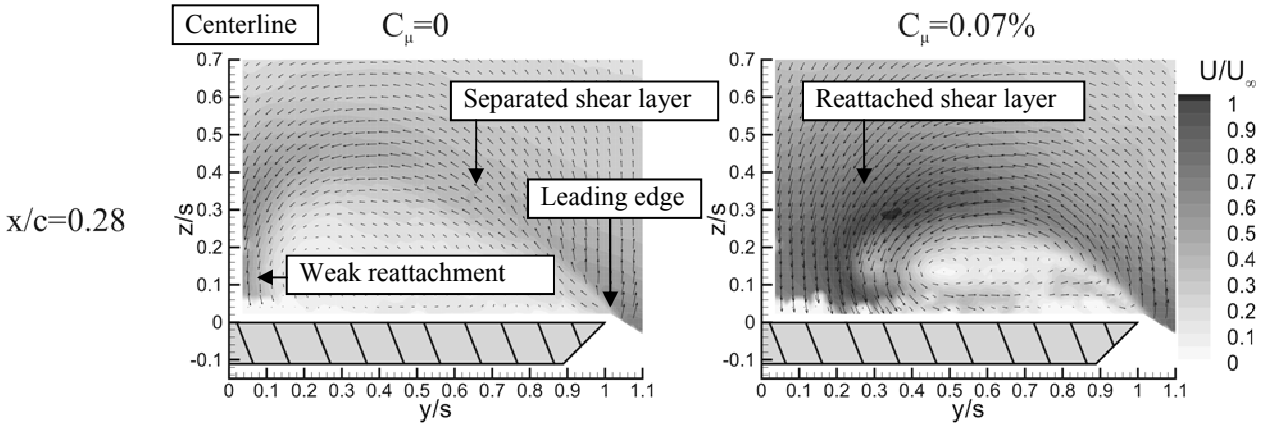

Figure 4-4 Magnitude of time averaged cross flow velocity at x/c=0.28, for St=1.3 and α=25°.

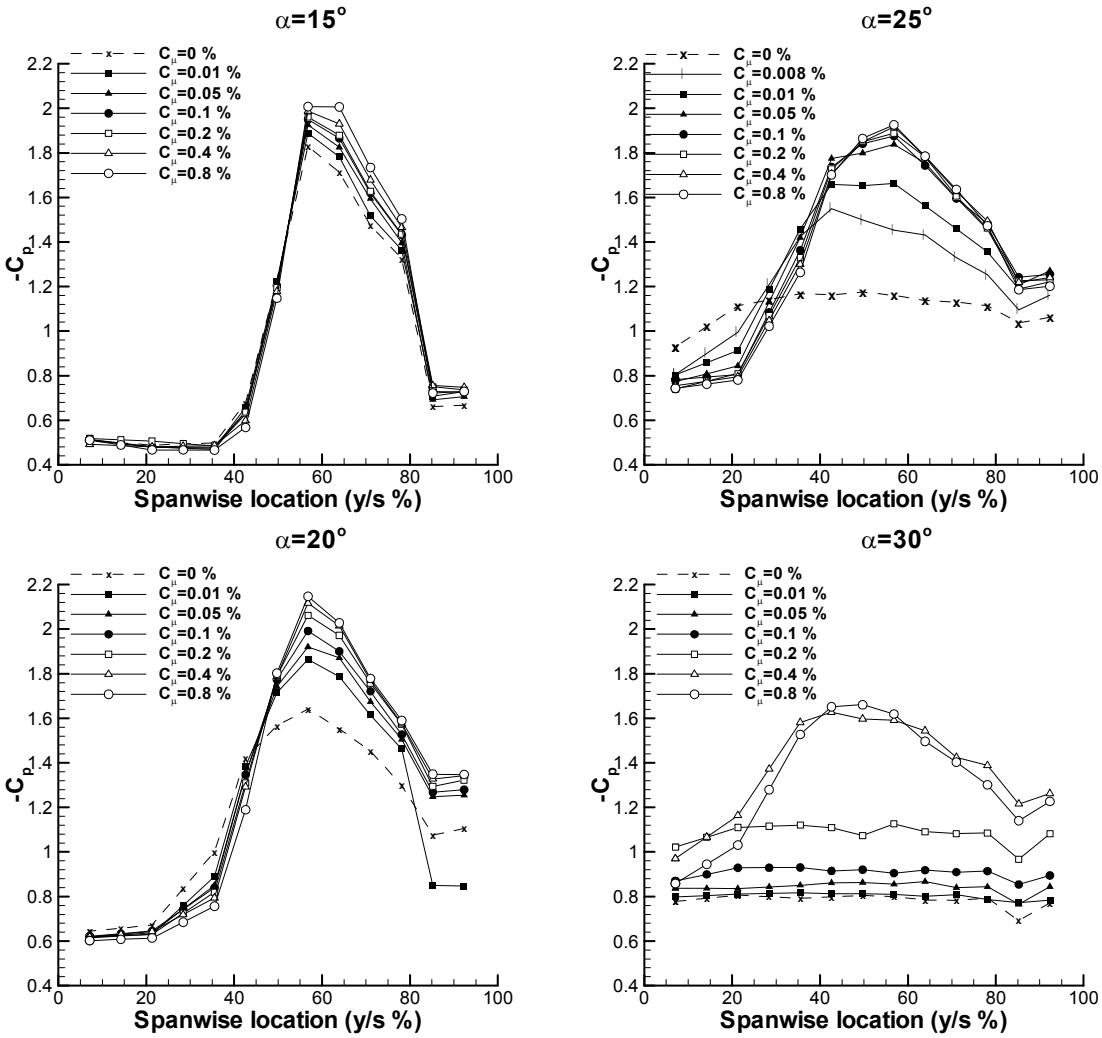

Figure 4-5 Spanwise variation of pressure at different angles of attack, x/c=0.48, St=1.5.

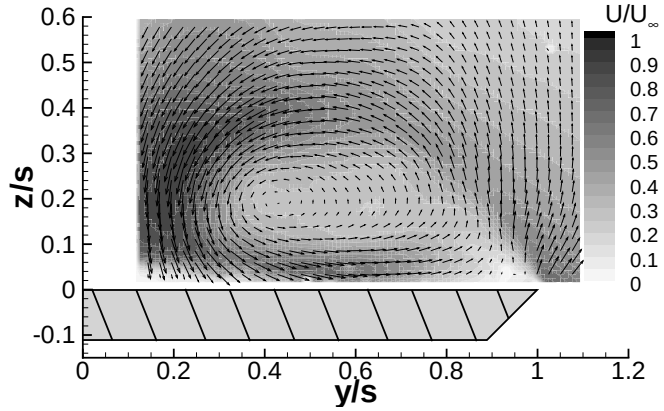

Figure 4-6 Magnitude of time averaged cross flow velocity at x/c=0.48, for C_μ=0.4%, St=1.5 and α=30°.

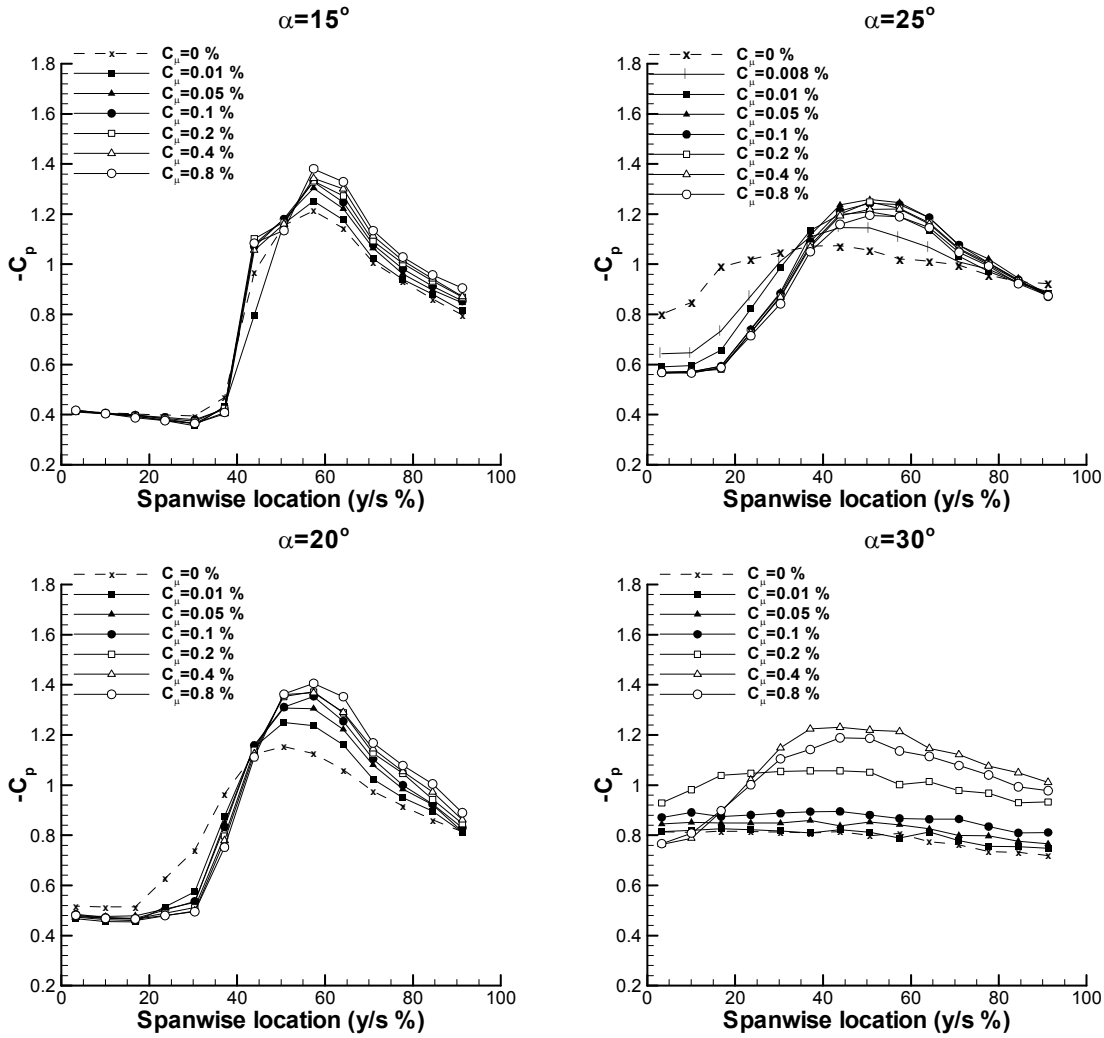

Figure 4-7 Spanwise variation of pressure at different angles of attack, x/c=0.68, St=1.5.

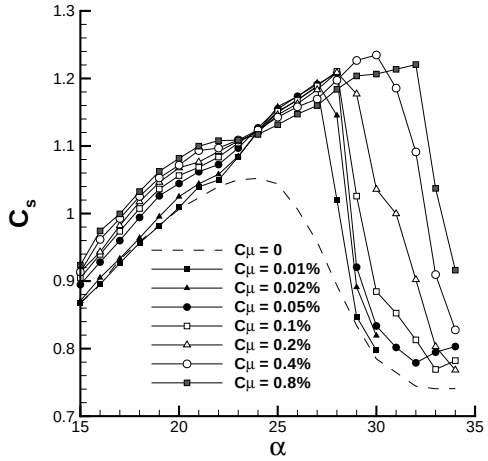

Figure 4-8 Variation of suction force coefficient as a function of angle of attack, St=1.5.

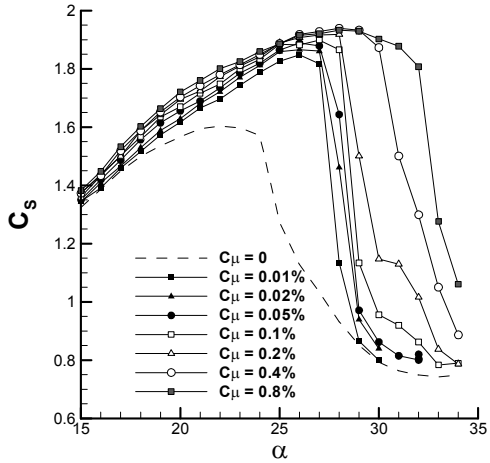

Figure 4-9 Variation of suction force coefficient for x/c=0.28 as a function of angle of attack, St=1.5.

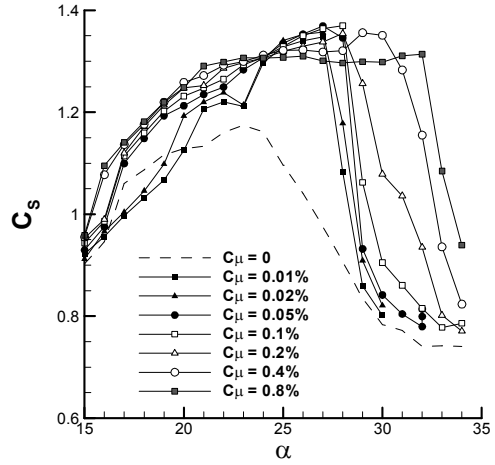

Figure 4-10 Variation of suction force coefficient for x/c=0.48 as a function of angle of attack, St=1.5.

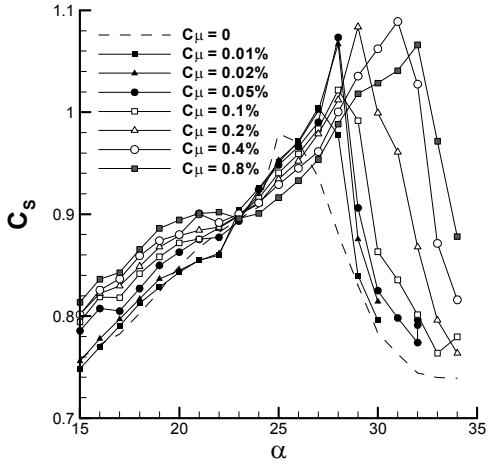

Figure 4-11 Variation of suction force coefficient for x/c=0.68 as a function of angle of attack, St=1.5.

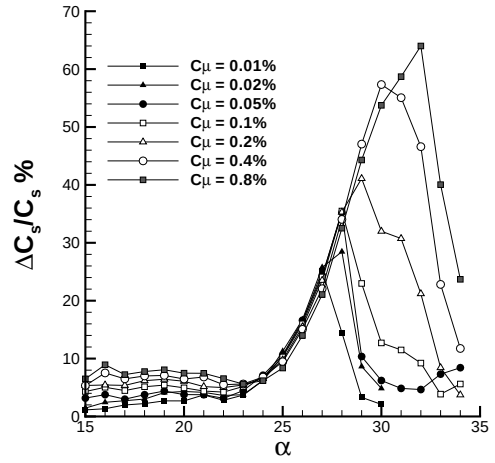

Figure 4-12 Variation of percent increase in suction force coefficient as a function of incidence, St=1.5.

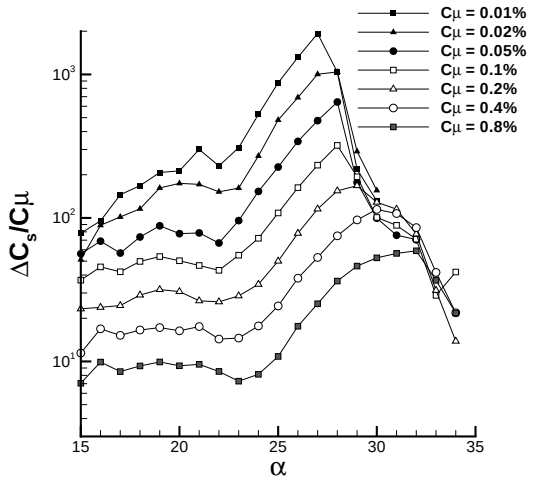

Figure 4-13 Variation of effectiveness as a function of angle of attack, St=1.5.

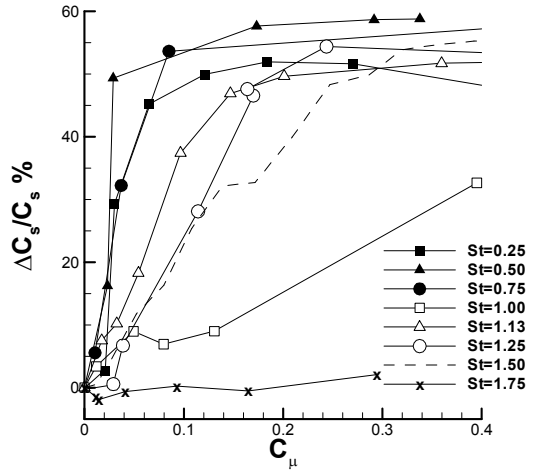

Figure 4-14 Comparison of suction force coefficient for different Strouhal numbers over the tested momentum coefficient range, α=30°

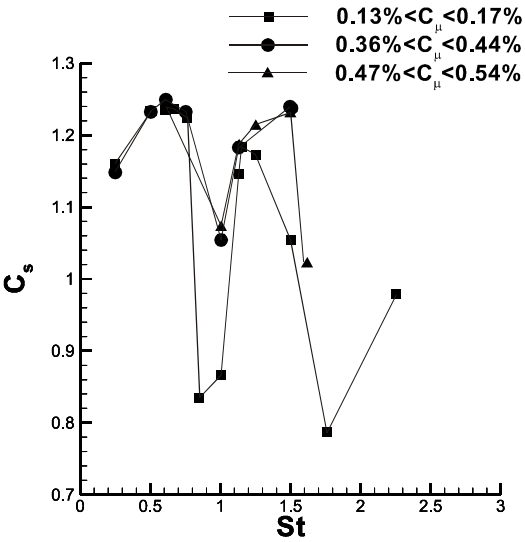

Figure 4-15 Comparison of suction force coefficient over the tested Strouhal number range, α=30°

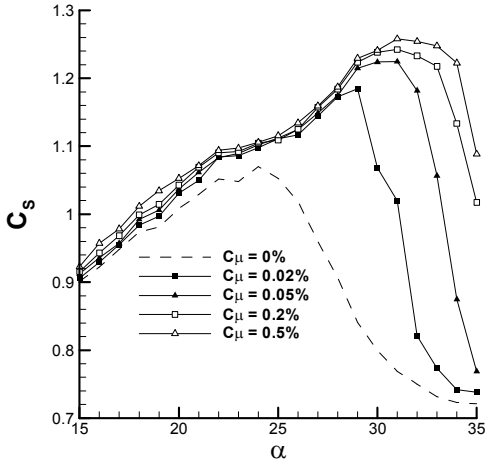

Figure 4-16 Variation of suction force coefficient as a function of angle of attack, St=0.5.

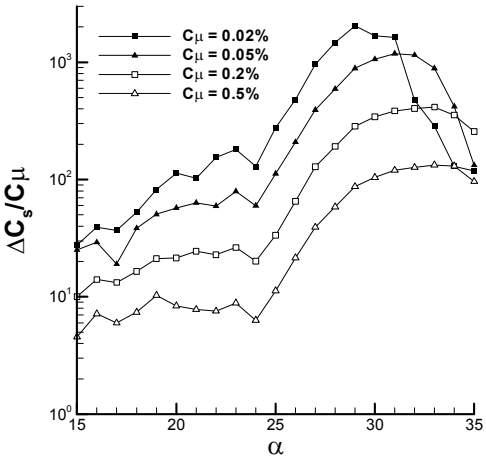

Figure 4-17 Variation of effectiveness as a function of angle of attack, St=0.5.

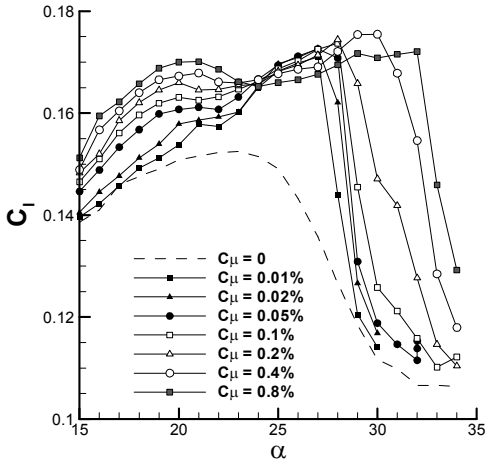

Figure 4-18 Variation of roll moment coefficient as a function of angle of attack, St=1.5

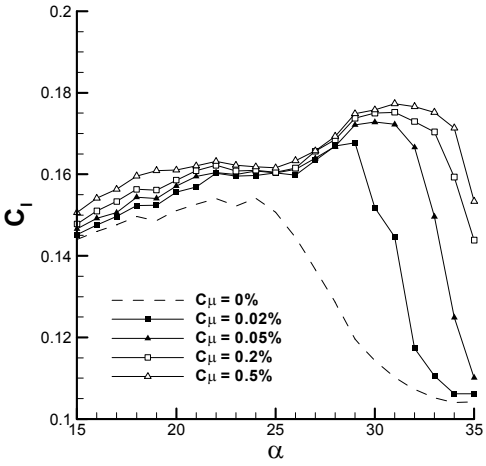

Figure 4-19 Variation of roll moment coefficient as a function of angle of attack, St=0.5

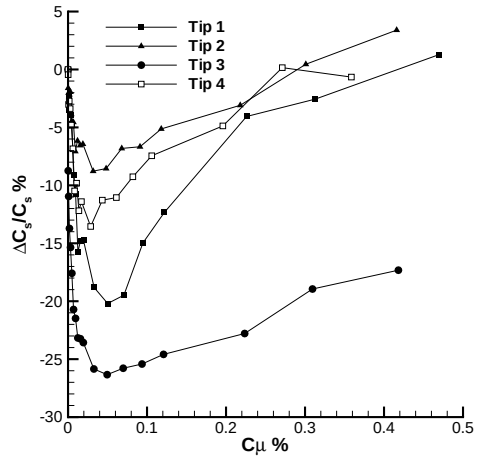

Figure 4-20 Comparison of the percentage change in suction force coefficient for x/c=0.28 with steady blowing from different leading edge tip profiles

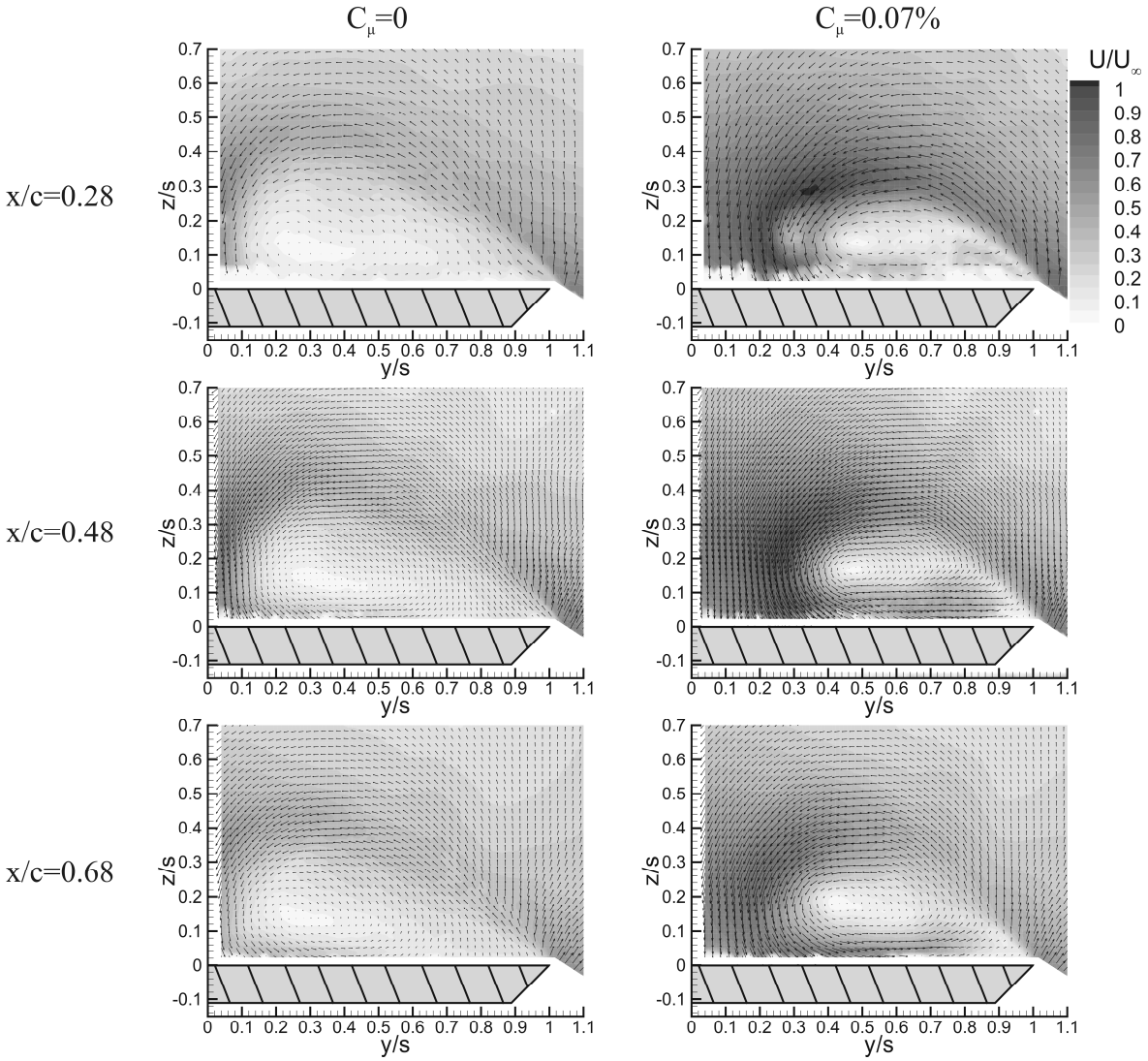

Figure 4-21 Magnitude of time-averaged cross-flow velocity, α=25°, St=1.3.

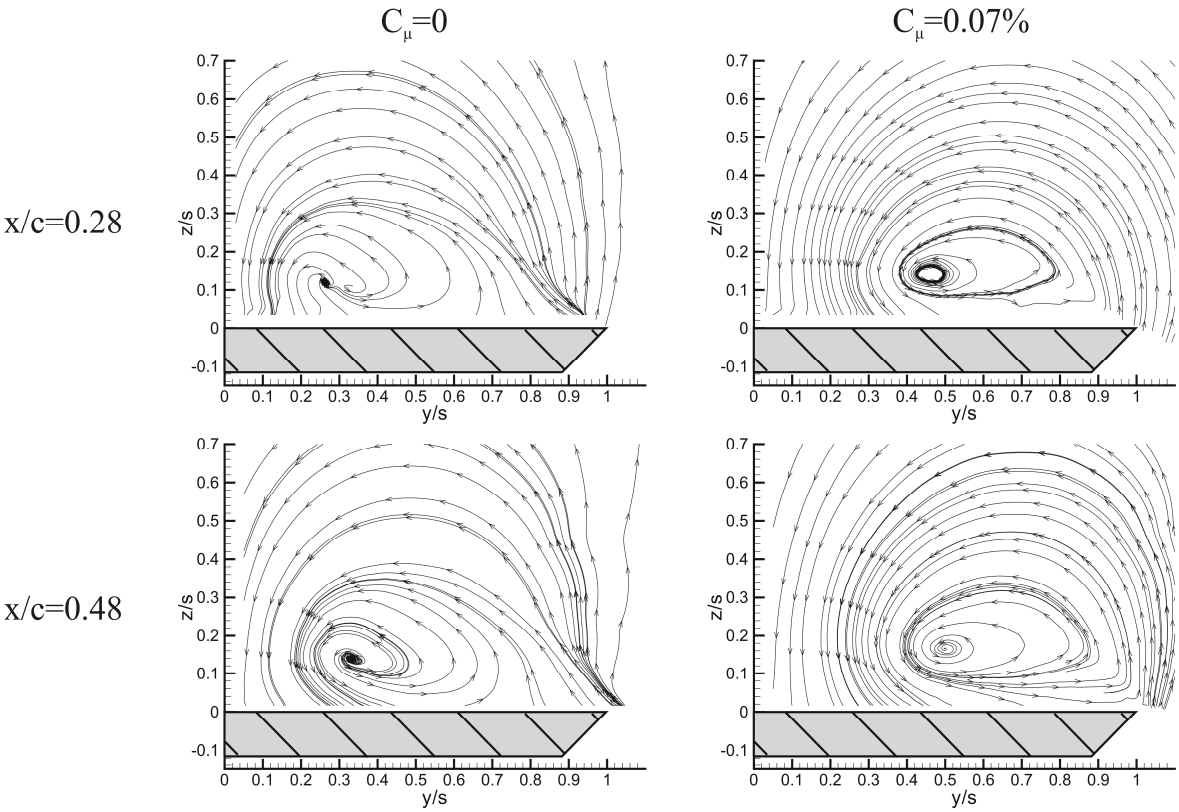

Figure 4-22 Time-averaged streamline patterns in a cross-flow plane, α=25°, St=1.3.

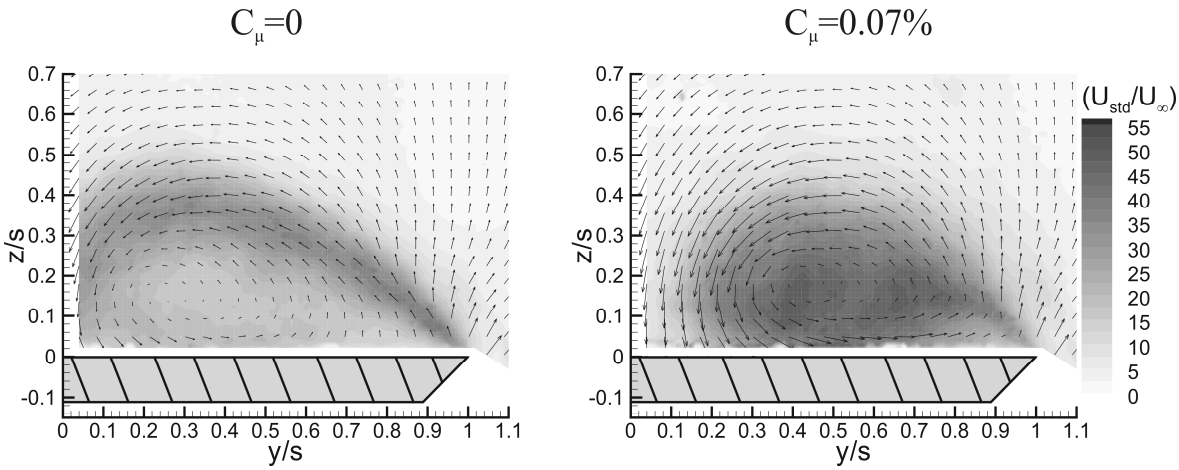

Figure 4-23 Variation of turbulence intensity in a cross-flow plane, x/c=0.68, α=25°, St=1.3.

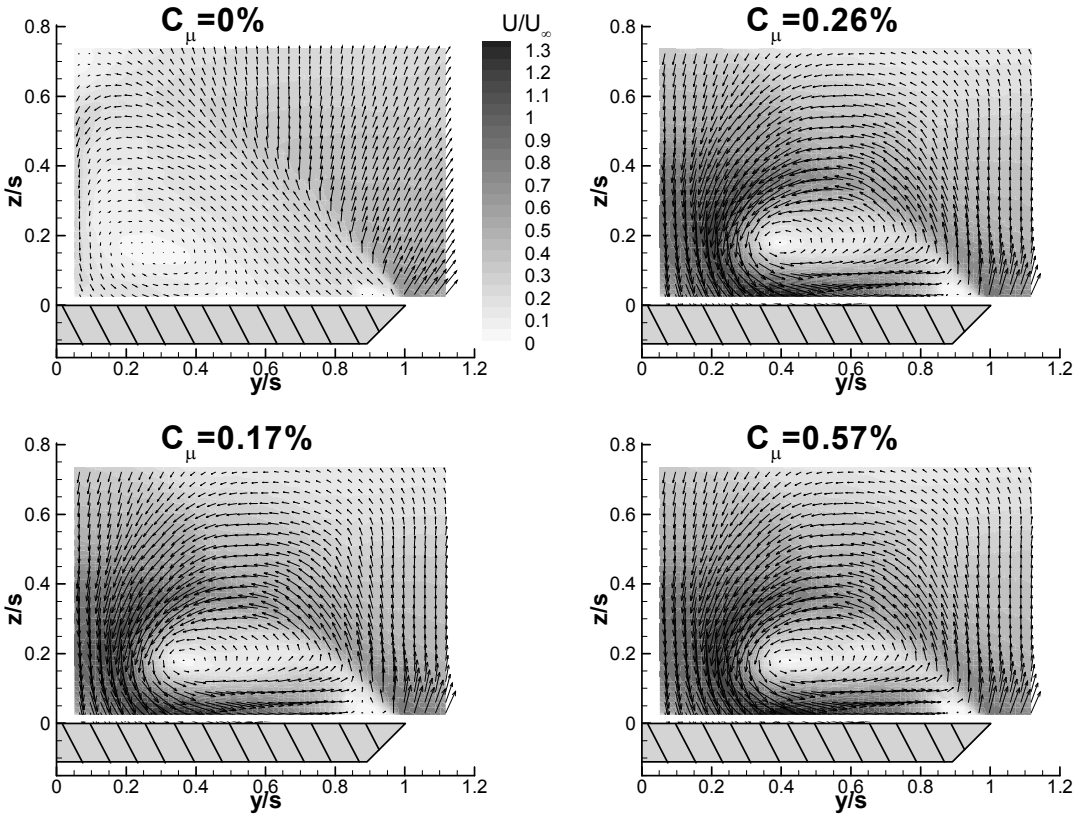

Figure 4-24 Magnitude of time-averaged cross-flow velocity, x/c=0.28, α=30°, St=1.5

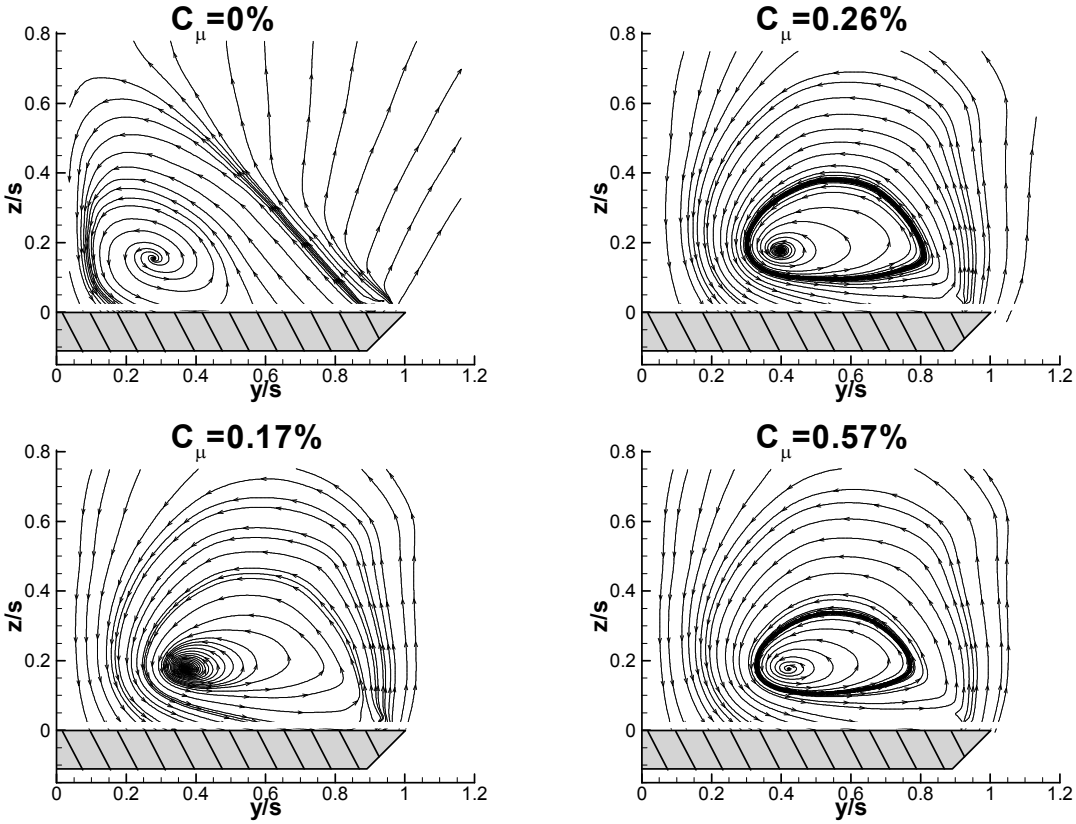

Figure 4-25 Streamline flow patterns of time-averaged cross-flow velocity, x/c=0.28, α=30°, St=1.5

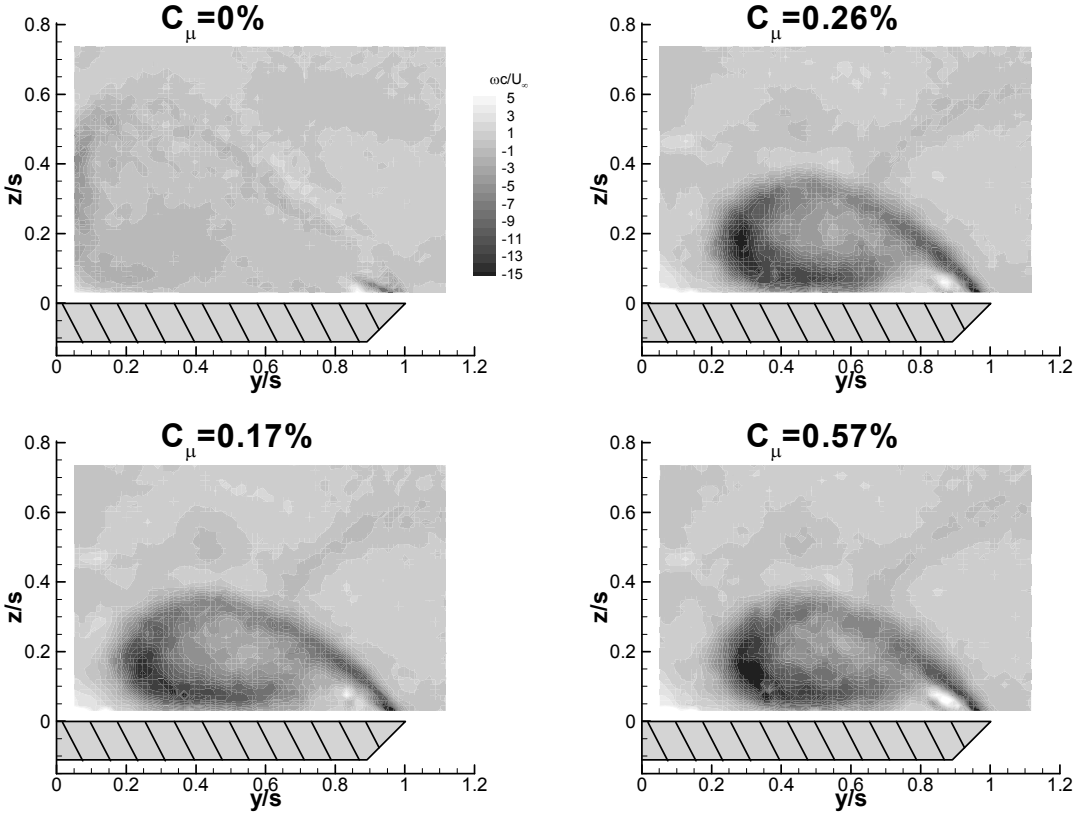

Figure 4-26 Time-averaged cross-flow vorticity, x/c=0.28, α=30°, St=1.5

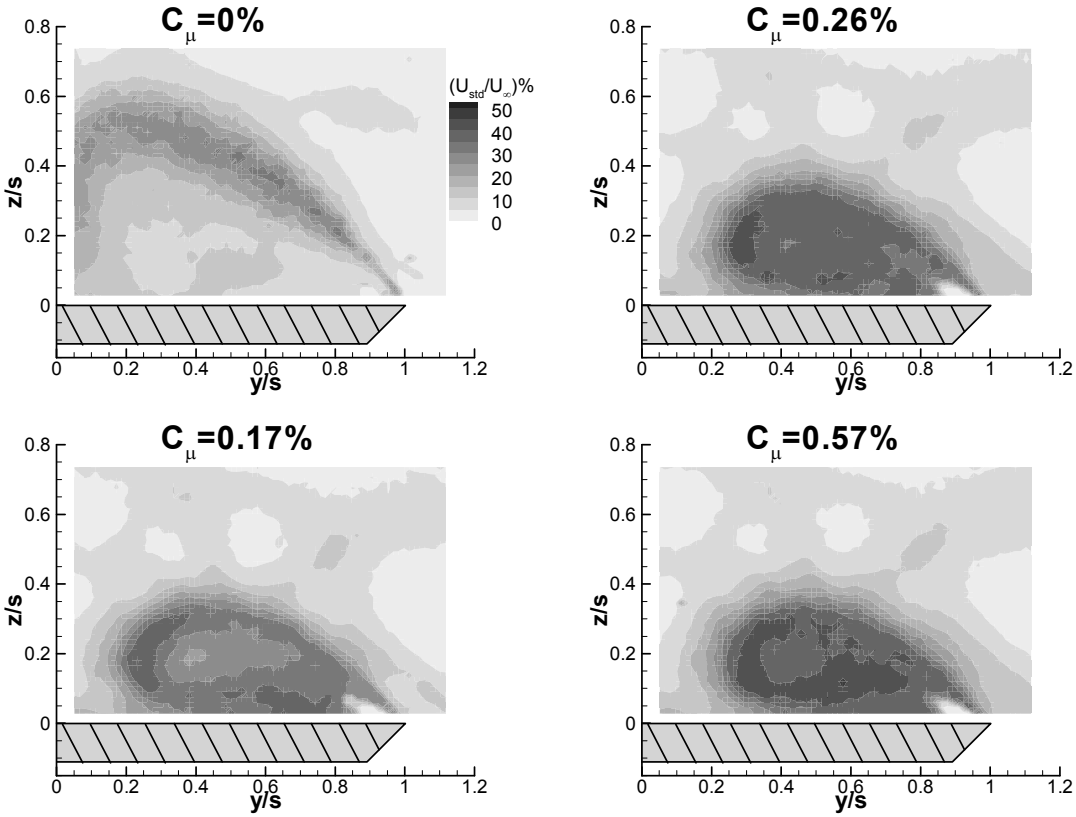

Figure 4-27 Variation of turbulence intensity in a cross-flow plane, x/c=0.28, α=30°, St=1.5.

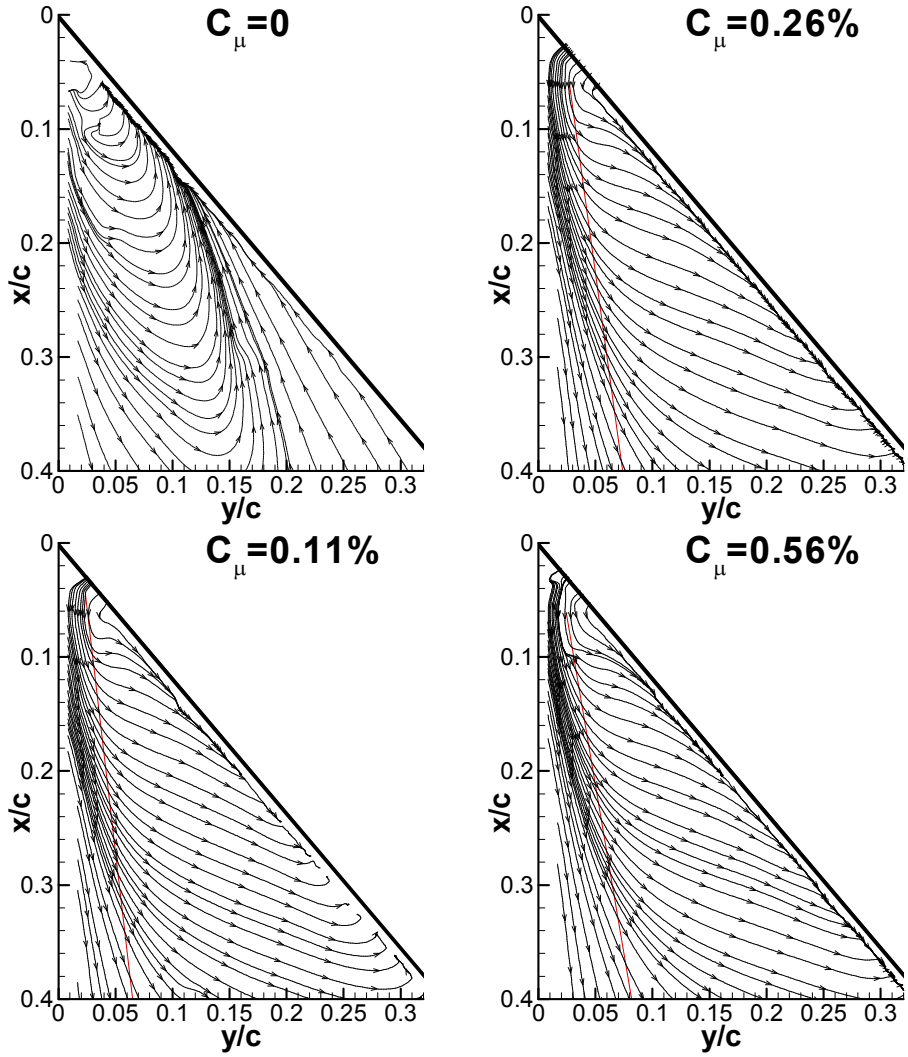

Figure 4-28 Time-averaged near-surface streamlines, α=30°, St=1.5.

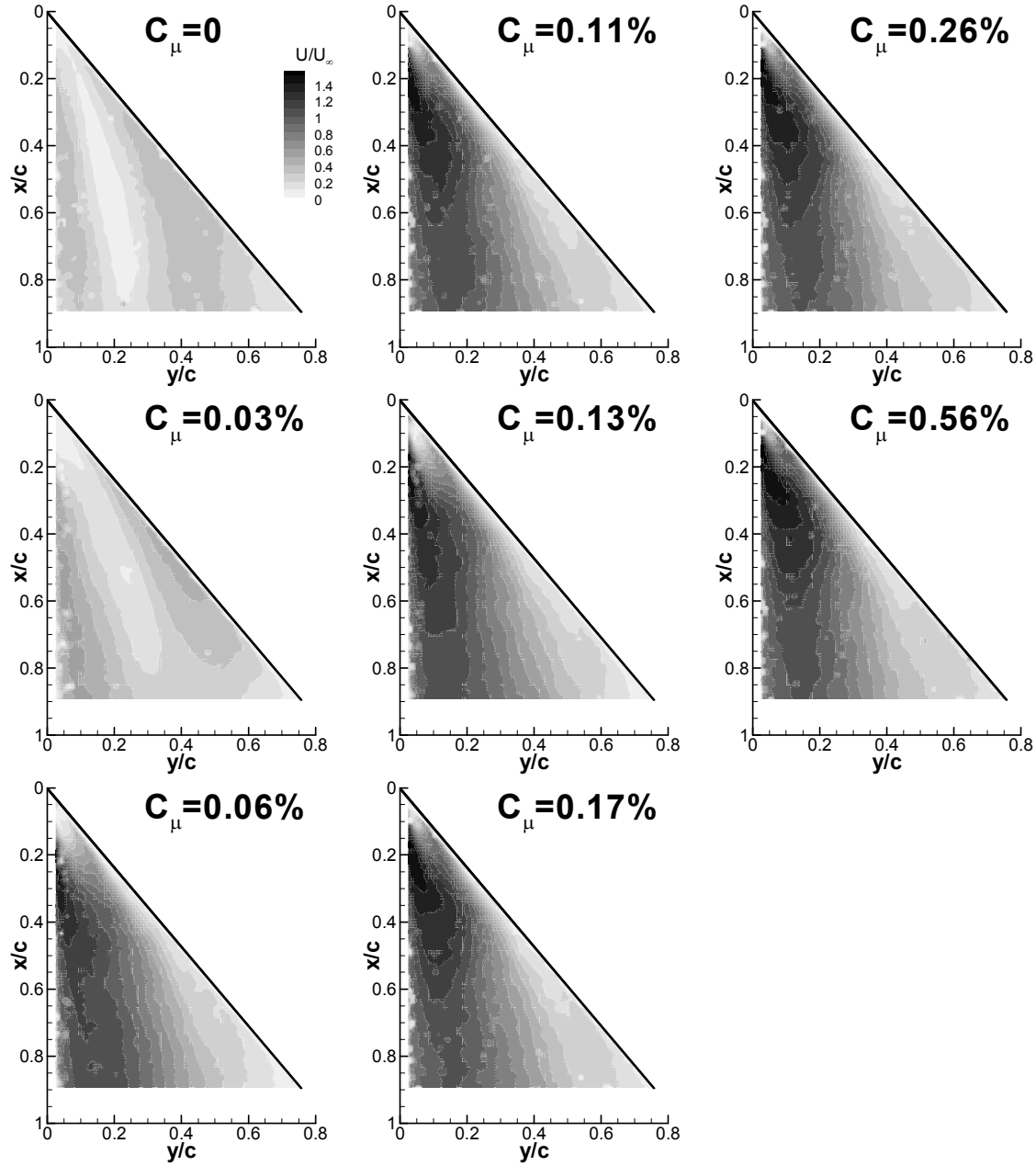

Figure 4-29 Magnitude of time-averaged velocity in the near-surface plane, α=30°, St=1.5.

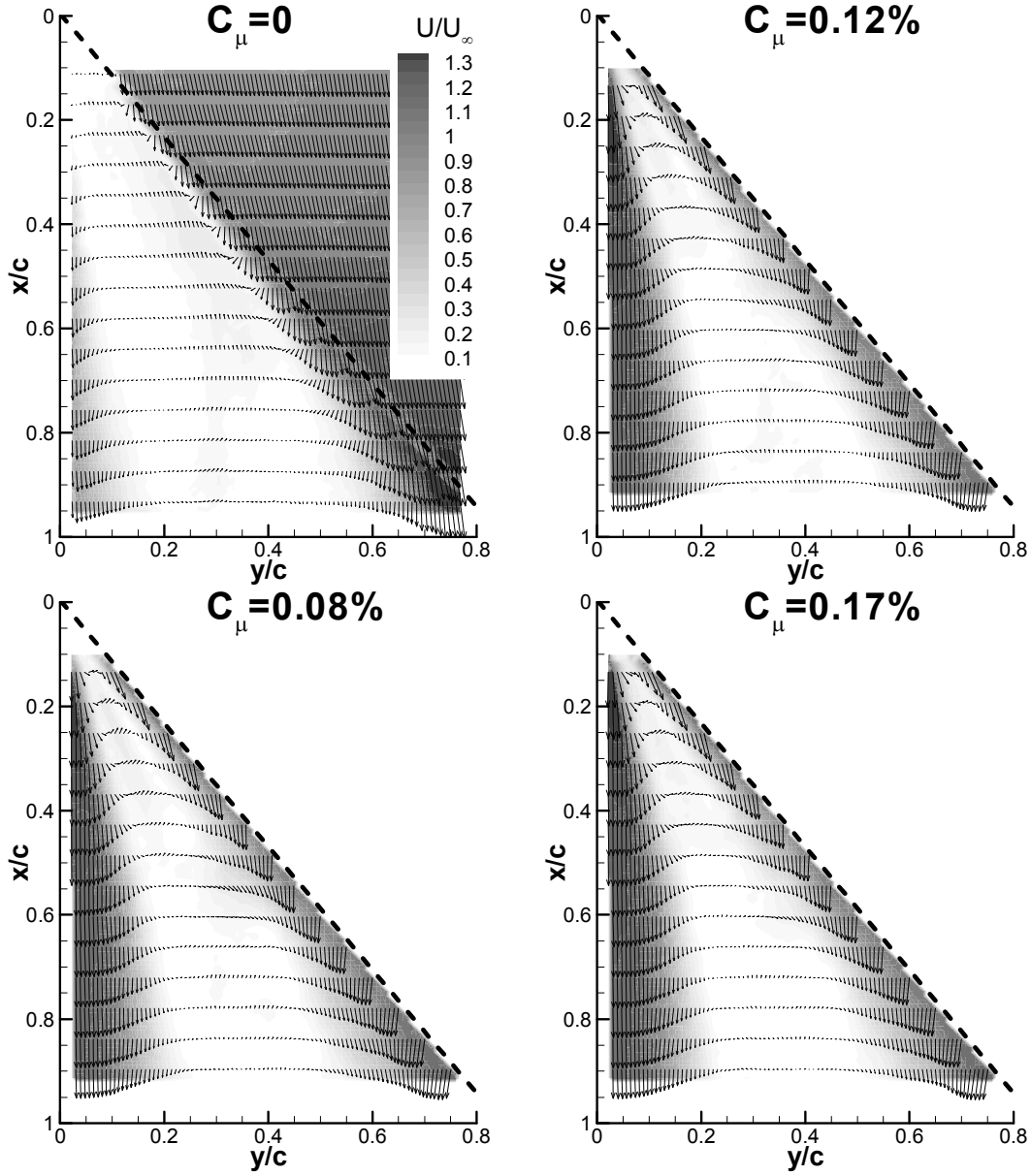

Figure 4-30 Time-averaged velocity field in a plane through the vortex core, α=30°, St=1.5.

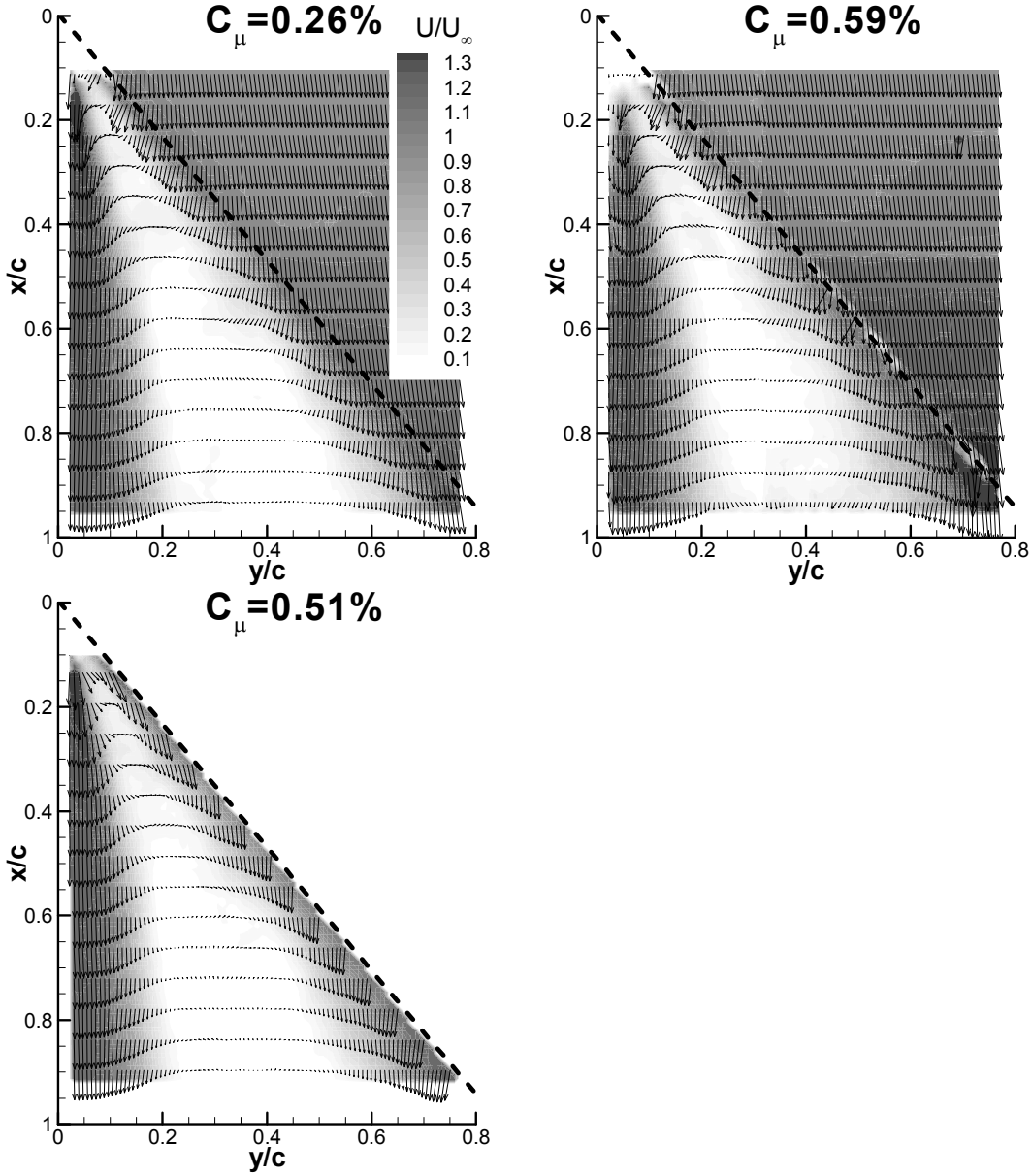

Figure 4-30 Continued

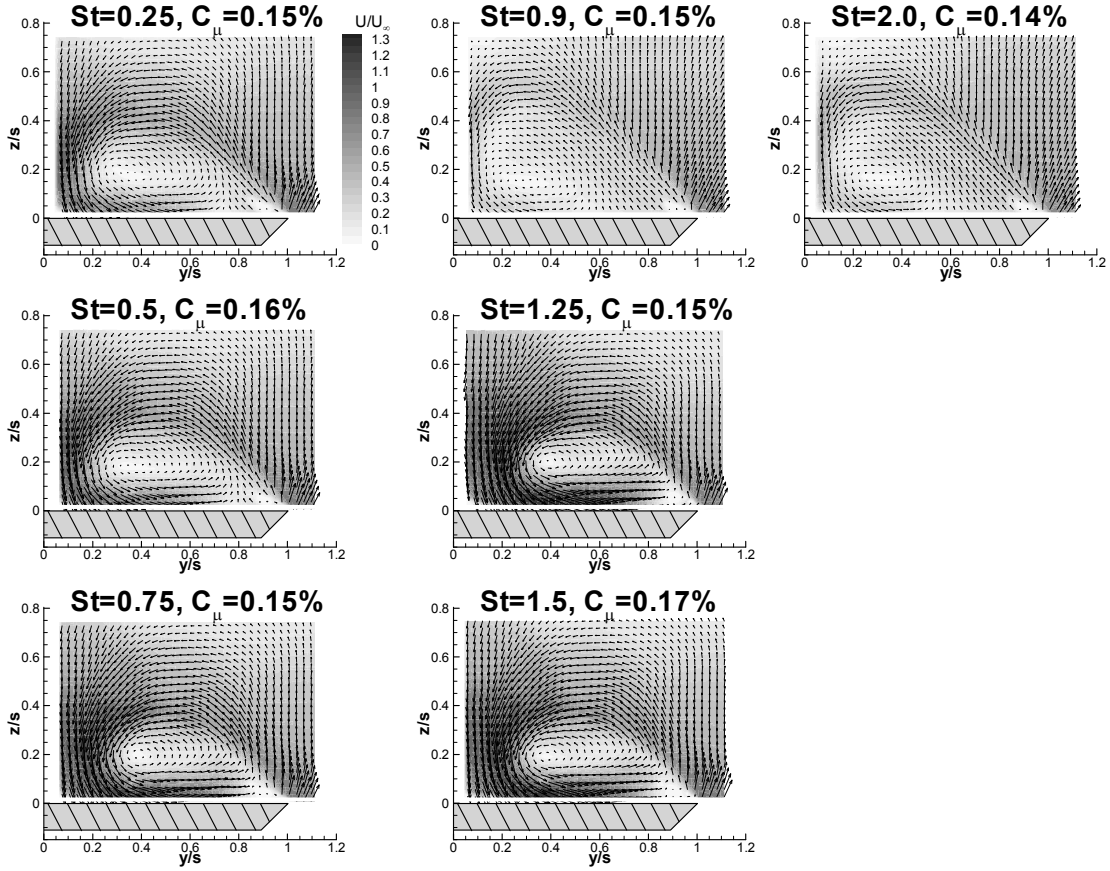

Figure 4-31 Comparison of the magnitude of time-averaged cross-flow velocity over a range of Strouhal numbers for $0.14\%<C_\mu<0.17\%$, x/c=0.28, α=30°.

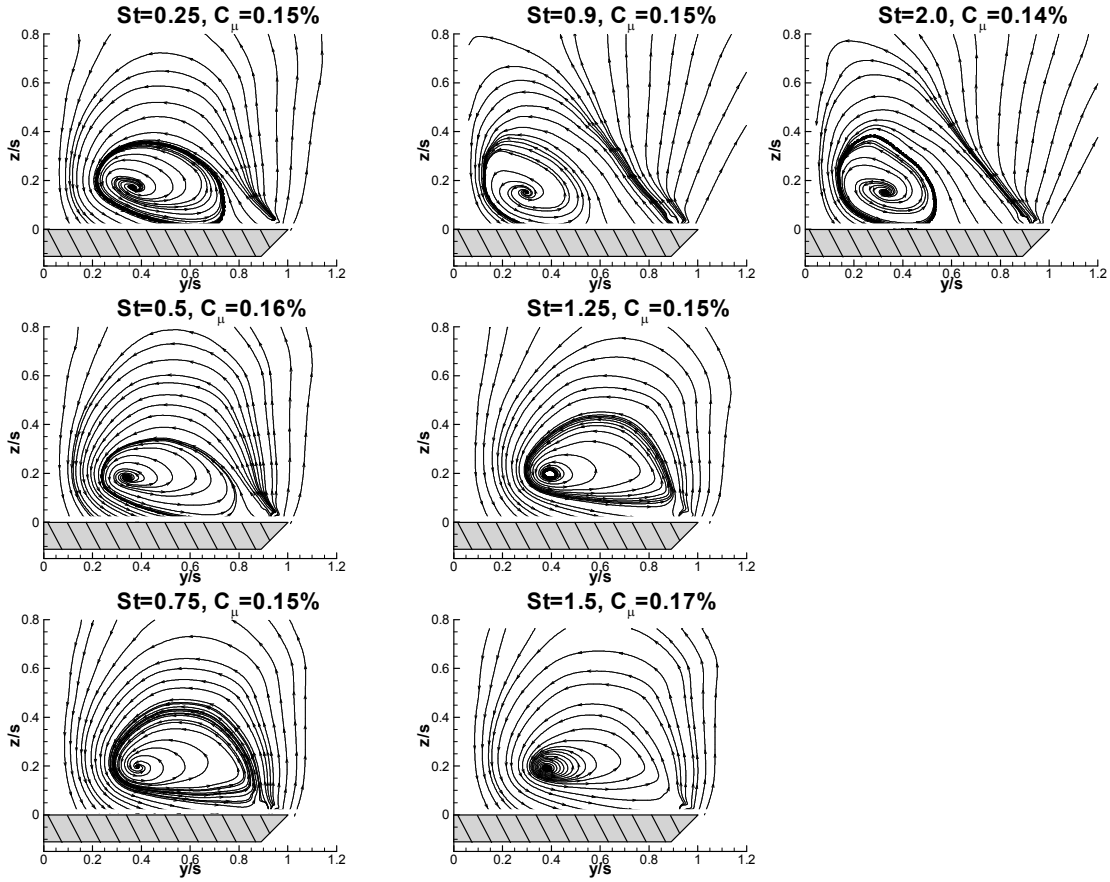

Figure 4-32 Comparison of the time-averaged cross-flow streamline patterns over a range of Strouhal numbers for $0.14\%<C_\mu<0.17\%$, x/c=0.28, α=30°.

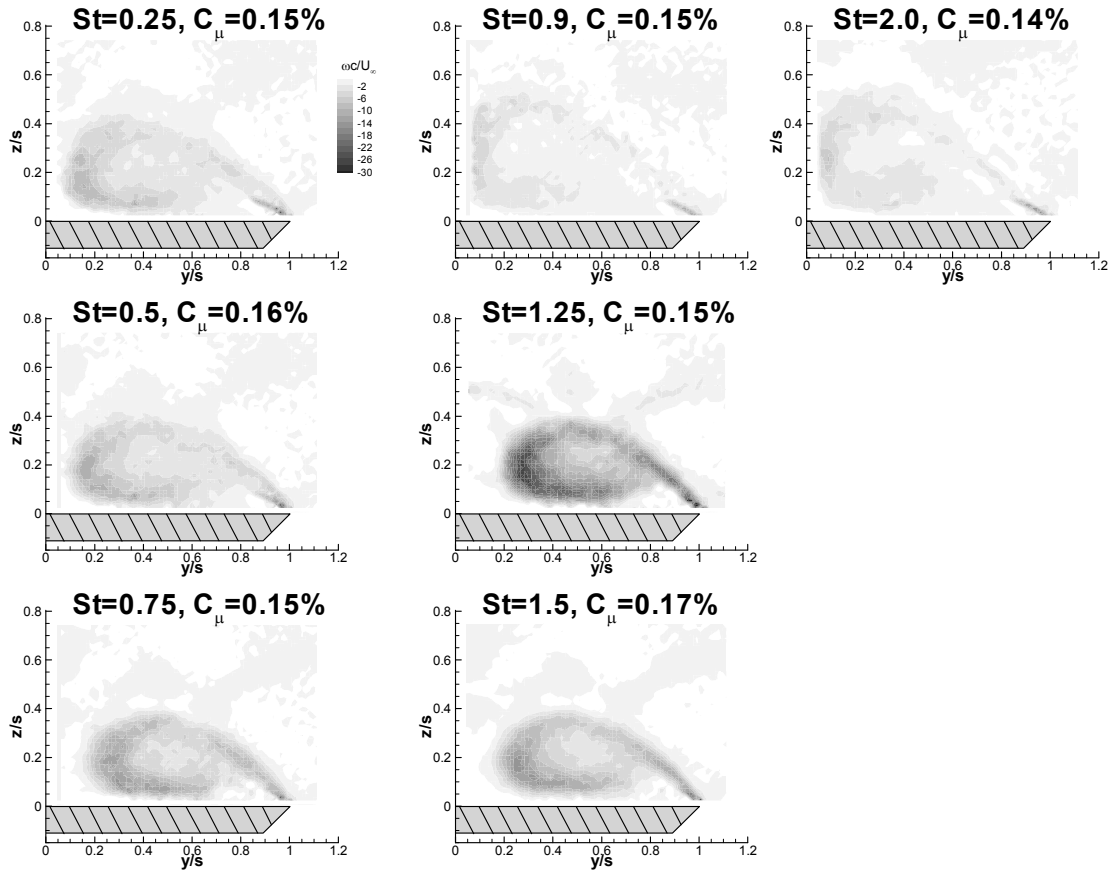

Figure 4-33 Comparison of the time-averaged cross-flow vorticity over a range of Strouhal numbers for 0.14%<C_μ<0.17%, x/c=0.28, α=30°.

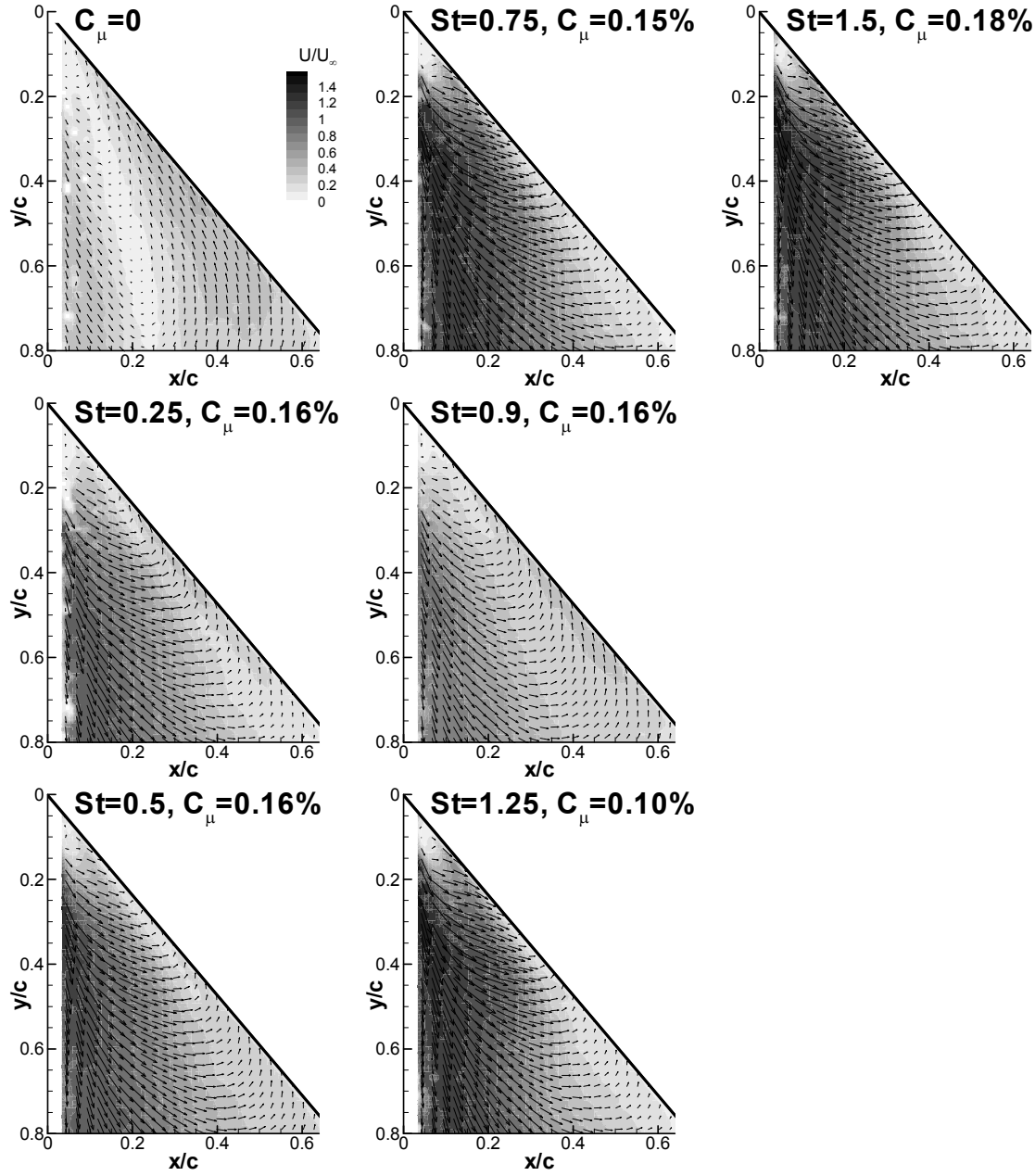

Figure 4-34 Comparison of the magnitude of time-averaged velocity in the near surface plane over a range of Strouhal numbers for $0.14\%<C_\mu<0.17\%$, $\alpha=30°$.

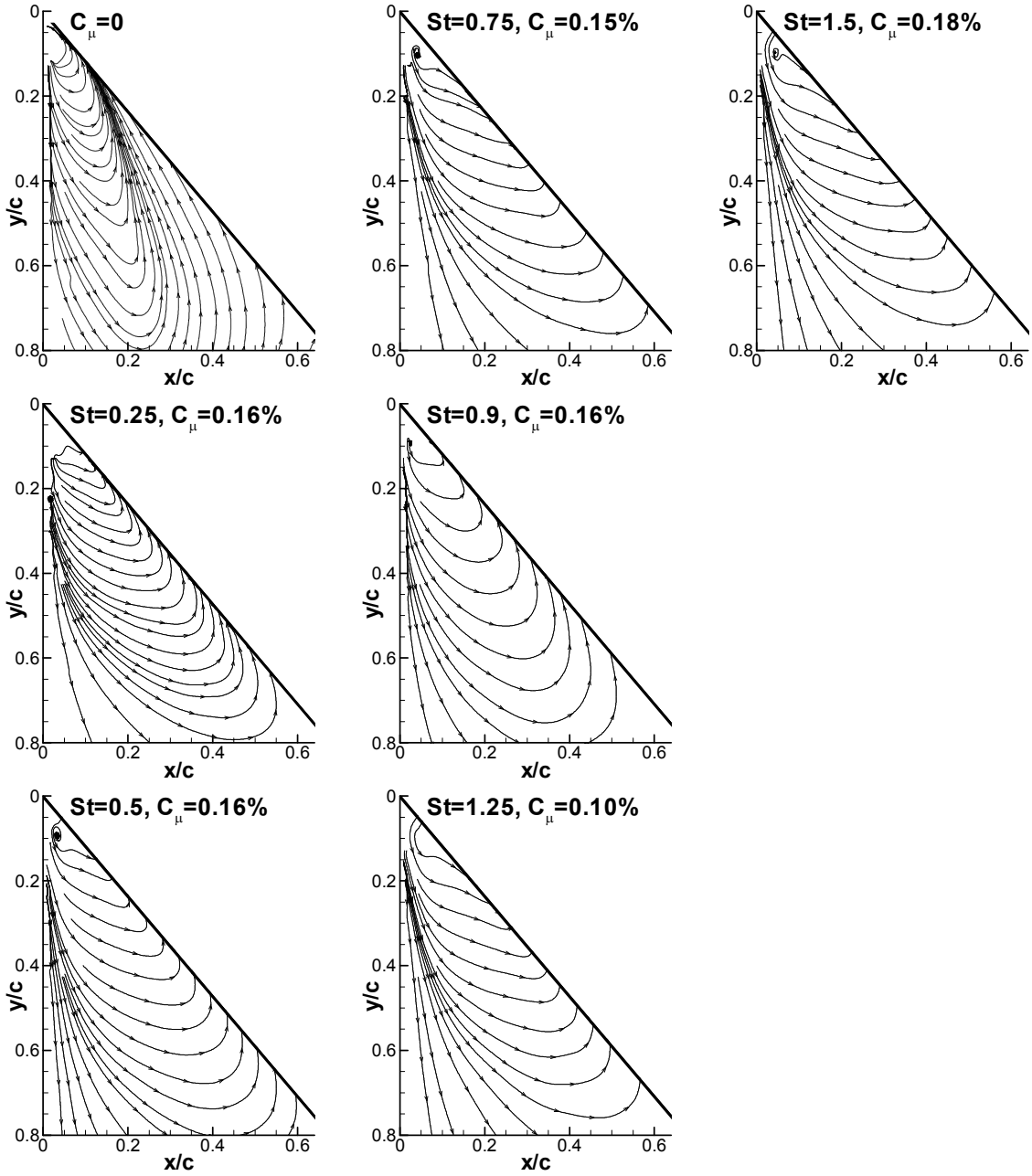

Figure 4-35 Comparison of the time-averaged streamline patterns in the near surface plane over a range of Strouhal numbers for $0.14\%<C_\mu<0.17\%$, $\alpha=30°$.

Chapter 5 Phase averaged PIV measurements

The focus of Chapter 4 was to quantify the benefits of unsteady blowing, and the effect on the flow in a time averaged sense. Chapter 5 looks at the way the perturbation interacts with the shear layer and the main vortical region to further develop an understanding of why reattachment takes place. Chapter 5 shows the way that the perturbation progresses along the shear layer, and feeds into the main vortical region, and will also highlight the highly three dimensional nature of the flow field. Further to this, the effect of the Strouhal number of the unsteady blowing on the nature of perturbation and its interaction with the shear layer is discussed. In order to gain an understanding of the interaction between the unsteady blowing perturbation and the shear layer, the PIV setup was phase locked to different points in the pulsing cycle. This process has been described in more detail in the method section. Initially the St=1.5 case will be discussed in detail, and then the effects of pulsing at other Strouhal numbers will be considered.

Phase-averaged PIV measurements in a cross-flow plane at x/c=0.48 are shown in Figure 5-1 for α=30°, C_μ=0.4%, and St=1.5. For clarity, only every third vector is plotted and the corresponding streamline patterns are plotted in Figure 5-2. The velocity field at different phases of the pulsing cycle is shown. The blowing starts at t/T=0 and ends around t/T=0.20 (a duty cycle of 20%). The introduction of the perturbation has a cyclic effect on the location of the vortical region bound by the reattached shear layer. At t/T=0, high velocity perturbation is can be seen at the leading edge, which induces a discrete vortex. The region of high velocity associated with the vortex travels along the shear layer and begins to merge with the high velocity flow of the reattachment region near the wing's centreline ($y/s \approx 0.3$) at t/T=0.3. As the discrete vortex merges with the main region of vortical flow, the apparent centre of the large vortical region moves inboard and away from the surface ($0.20 \leq t/T \leq 0.40$). After t/T=0.3 the perturbation can no longer be seen independently from the main vortical flow structure. The centre of the vortical region then moves outboard and closer to the wing's surface ($0.50 \leq t/T \leq 0.80$) and high velocities develop in the reattachment region. At t/T=0.80, the whole flow field relaxes back to a flow field resembling the mean flow case.

The vorticity for the case corresponding to Figure 5-1 is shown in Figure 5-3. For all stages of the pulsing cycle, and in the mean case, there appears to be a region of high vorticity at the leading edge of the wing. This is as expected, and indicates the presence of the shear layer and that the leading edge is a continuous source of vorticity. In addition to this, for the mean flow case, vorticity is distributed throughout the shear layer, the reattachment region, and along the surface of the wing. The perturbation can be identified as a region of high vorticity being shed from the leading edge at t/T=0. There are other regions of high vorticity in the flow, and the location of the region associated with the perturbation can be seen by comparing the vorticity field with the velocity magnitude in Figure 5-1. The discrete region of vorticity induced from the unsteady blowing travels along the shear layer and merges with the main region of vorticity at t/T=0.4.

Between t/T=0.4 and t/T=0.6, the flow field is dominated by a large area of concentrated vorticity at y/s≈0.3 as a result of the discrete shear layer vortex merging with the main region of high vorticity. The large region of concentrated vorticity is fed by the vorticity from the discrete vortex shed from the leading edge. By t/T=0.8, the vorticity more closely resembles the mean flow case.

The effect of unsteady blowing at three different momentum coefficients on the cross-flow velocity magnitude is presented for different points in the cycle in Figure 5-4. For a momentum coefficient of C_μ=0.12%, the perturbation can be seen travelling along the shear layer, and interacting with a weak recirculating region close to the wing's centreline. There is a low level of reattachment to the wing's surface (reattachment is evident from streamline patterns and turbulence plots not shown here). It is possible that without the imposition of the symmetry condition, the flow would be detached, as there appears to be a reaction with the splitter plate (at y/s=0), however the flow close to the centreline can not be examined due to significant reflection noise. The main and shear layer vortices appear to merge, but the shear layer vortex has significantly higher vorticity than that of the recirculating region, and after they have interaction, the concentration of vorticity is significantly reduced. It can be seen from Figure 5-4 that the highest velocities present in the flow field are associated with the perturbation, and although there appears to be an increase in velocity near the reattachment point, this is small compared to the Cμ=0.4% case. At the higher momentum coefficient, C_μ=0.56, the flow is almost identical to the C_μ=0.4% case, indicating that once the effect of the flow control has become saturated, the mechanism for reattachment does not change. In this case, there looks to be negligible effect when the momentum coefficient is increased from C_μ=0.4% to C_μ=0.56%.

The flow over nonslender delta wings is truly three dimensional, and to gain a greater understanding of the total flow field, phase locked PIV measurements were taken at the two other stations, x/c=0.28 and x/c=0.68, and have been compared with x/c=0.48 in Figure 5-5**.** Each station is compared for phase locked intervals of t/T=0.1. For all stations, the pulse is initiated at t/T=0% and can be seen travelling along the shear layer. For the x/c=0.28 case, the mean velocity across the field is higher, and the perturbation is more difficult to identify. Downstream, the cross-flow velocities are much lower, as a result the progression of the perturbation is less difficult to identify. A clear vortex can be seen at x/c=0.68 and t/T=0.2. The progress of the perturbation along the shear layer is progressively slower for each station as the measurement plane moves from x/c=0.28 to x/c=0.68. This is partly because the semispan length of each station increases linearly with its location downstream. Also the cross-flow velocities are significantly lower further away from the apex. This highlights the truly three dimensional nature of the flow, and although the vortex induced by the perturbation emanates from the leading edge simultaneously at all stations, it is quickly wrapped around into the main vortical flow region close to the apex of the wing, whilst still remaining in the shear layer towards the trailing edge of the wing. The result is that in three dimensions the vortex is wound around the main vortical flow region. The percentage of the cycle that it takes for the perturbation to reattach to the surface is best looked at by examining the flow in

the near surface plane, presented later in this chapter. The main region of vortical flow is also highly three dimensional, as shown by the streamline patterns in Figure 5-6. Earlier in Chapter 5, it was stated that the x/c=0.48 case relaxed to what was more similar to the mean flow case at around t/T=0.8. By contrast, the x/c=0.28 case relaxes more quickly, by t/T≈0.3-0.4 and the x/c=0.68 case never truly resembles a mean flow case and is highly dynamic at all stages of its cycle. Unsurprisingly, it seems that the time taken for the effect of the perturbation to stabilise increases downstream.

For all cases, the main vortical flow pattern undergoes oscillations as it interacts with the shear layer perturbation, as described earlier for the x/c=0.48 case. Comparatively, the x/c=0.28 case is more stable, other than a broadening of the streamline pattern around t/T=0.4, the centre of the region remains at y/s≈0.4. The x/c=0.68 plane shows comparative movement of the main vortical flow region to that of the x/c=0.48 plane, however it appears to lag behind by the x/c=0.48 case, which can be seen by the similarities between x/c=0.48, t/T=0.2 and x/c=0.68 and t/T=0.5, as the perturbation moves above the main vortical region. Similarities can also be seen between x/c=0.48, t/T=0.3 and x/c=0.68 at t/T=0.7-0.8 as the perturbation starts to merge with the main vortical flow in the reattachment region.

The vorticity corresponding to Figure 5-5 and Figure 5-6 is shown in Figure 5-7. At x/c=0.28, at all positions in the cycle, the high vorticity shear layer is evident, emanating from the leading edge and reattaching to the wing's surface. The reattachment region is dominated by a region of high vorticity, which increases in magnitude at t/T=0.2 as the perturbation enters the region. The two stations downstream show significantly lower concentrations of vorticity both in the shear layer and the reattachment region. For all stations, the discrete vortex can be seen in the form of a small concentrated region of vorticity emanating from the leading edge, moving down the shear layer and merging with the area of high vorticity above the reattachment location at y/s≈0.4. As mentioned earlier, the rate of progression of the vortex along the shear layer is dependant on its chordwise station.

In addition to the discrete vortex, which is a direct result of unsteady blowing, there are other structures present in the shear layer. For x/c=0.28 at t/T=0, a region of vorticity is present at y/s=0.75. This appears to be independent of the region of high vorticity at the leading edge, attributed to unsteady blowing. It appears that at t/T=0.1, its location coincides with that of the discrete vortex, and remnants can still be seen at t/T=0.2. There appears to be no evidence of the high vorticity region at t/T=0.9 (which as the measurements are periodic, is the instance immediately before t/T=0). The origin of the region is uncertain. It is possible that it could be a result of a discrete vortex formed upstream of the measurement location. At x/c=0.48 and t/T=0.2, there also appear to be multiple discrete concentrations of vorticity in the shear layer. It is possible that the singular high velocity perturbation results in more than one vortex formed, but this is not evident visually from the velocity vectors from which the vorticity data is obtained.

In addition to phase locked measurements of the St=1.5 case, other Strouhal numbers have been examined, and representative cases will be discussed. For St=0.5 and St=1.0, measurements were taken in all three chordwise planes. The velocity magnitude and corresponding vectors for St=0.5 at a momentum coefficient of C_μ=0.4% is shown in Figure 5-8. The reattachment location appears slightly further inboard compared to that of the St=1.5 case, which is consistent with the mean flow measurements shown in Chapter 4. Similar to the St=1.5 case at t/T=0, a discrete vortex develops in the shear layer at the leading edge, and progresses along the shear layer at different rates depending on its chordwise location. The discrete vortex then merges with the main vortical flow region as it approaches the reattachment region. An important point of difference between the St=1.5 and St=0.5 case is that in addition to the discrete vortex as a result of unsteady blowing, for the St=0.5 case there is a second vortex that can clearly be seen to develop in the shear layer at the leading edge, and interact with the main vortical flow in a similar way to the induced vortex. Hot wire measurements of the unsteady blowing jet in addition to PIV measurements of the flow with close to zero freestream velocity indicate a singular high velocity pulse emanating from the leading edge. For the purposes of this discussion, the vortex associated with the unsteady blowing pulse will be referred to as the induced perturbation, and the additional vortex the secondary perturbation. The secondary perturbation is seen as a region of high turbulence at the leading edge for t/T=0.65-0.7 in Figure 5-9. The streamlines bend sharply around the turbulent region, indicating a concentration of vorticity. There appears to be a slight thickening of the highly turbulent region of the shear layer near the leading edge just prior to the secondary perturbation. Given the three dimensional nature of the flow, it is interesting to note that the secondary perturbation occurs almost simultaneously for all three chordwise stations. It is difficult to say whether the cause of the formation of the secondary perturbation is a result of a phenomenon that acts across the leading edge or whether instigation at one singular point causes formation of secondary perturbation across the entire leading edge.

An interesting point of difference between the induced perturbation and the secondary perturbation is the way that the flow responds to the perturbation. The induced perturbation travels along the turbulent shear layer in a manner similar to the St=1.5 case, where the shear layer arcs from the leading edge to the reattachment location. By contrast the secondary perturbation causes the region of high turbulence to flatten as seen at t/T=0.75 for x/c=0.48 and t/T=0.85 for t/T=0.85. The secondary perturbation is not only a perturbation in the shear layer, but results in significant deformation of the shear layer.

As expected, the plot of the velocity magnitude for the St=1.0 case, shown in Figure 5-10, shows a weak recirculation region. The initial perturbation can be seen at t/T=0, and can be followed along the shear layer until it is above the main recirculation region. It is difficult to ascertain whether the induced vortex merges with the main region of vortical flow. A secondary perturbation can also be seen for the St=1.0 case, however it does not appear to emanate from the leading edge. The origin of the secondary perturbation can be seen at t/T=0.45-0.55 for x/c=0.48 and t/T=0.75 for x/c=0.68.

It is difficult to identify a secondary perturbation at x/c=0.28, however this may be due to lower spatial resolution at this station. The secondary perturbation then continues along the shear layer in a similar way to the induced perturbation. In Figure 5-11 two distinct vortical regions, one passing over the other can be indentified at x/c=0.48 for t/T=0.45 (as a result of the induced perturbation) and t/T=0.75 (as a result of the secondary perturbation). It is possible that strong reattachment does not occur from St=1.0 because the induced vortex does not interact strongly with the main recirculating region.

The streamline patterns presented were used to record the centre of the vortical swirl pattern, and its position at different points in the unsteady blowing cycle. The results are plotted in Figure 5-12. For the cases where reattachment of the shear layer does occur (St=0.5 and St=1.5), the variation of the position of the centre of the vortical region is much greater than the St=1.0 case, where only weak reattachment occurs. The St=1.0 case shows very little movement, at x/c=0.28 and x/c=0.68. When comparing the two cases where reattachment does occur, the effect of the secondary perturbation on the St=0.5 case is evident. For x/c=0.48 and x/c=0.68, the centre of the swirl pattern moves from the leading edge to the trailing edge and back again once per cycle for the St=1.5 case and twice per cycle for the St=0.5 case. The phase lag in the motion of the main vortical region is also evident when comparing stations of the same Strouhal number. For St=1.5, the centre of the swirl pattern is closest to the centreline at t/T=0.5, whereas for x/c=0.68 this occurs at t/T=0.

Measurements were also taken for x/c=0.48 for Strouhal numbers St=0.25, 0.75 and 1.25, and the respective velocity magnitude plots are presented in Figure 5-13, Figure 5-14 and Figure 5-15. The Strouhal number plots appear to fit into two categories; cases where only one perturbation is evident, and cases where two perturbations are evident. The cases in each category are summarised in Table 5-1. Of the cases tested, only Strouhal numbers of 0.75 and 1.5 showed no form of secondary perturbation. Table 5-1 also shows the point in the pulse cycle where the perturbation can be first identified. It is difficult to ascertain the origin of the secondary perturbation, but this will be discussed later in this section. It is worth noting that dominant velocity fluctuations in the shear layer at frequencies other than the excitation frequency, in particular the first harmonic of the excitation frequency, have been observed in literature regarding the flow over a backwards facing step [18, 25].

Near surface phase-locked PIV measurements corresponding to the presented cross-flow measurements, were taken to gain further understanding of the flow reattachment, and the progress of the leading edge perturbation at stations other than those shown for the cross-flow case. Presented in Figure 5-16 are the near surface measurements for the St=1.5 case. For all stages in the pulsing cycle, there is a region of high velocity near the centreline of the wing. Consistent with the mean flow case, this represents reattached flow with high axial velocity. In addition to the region of high axial flow, there is a moving region of high axial and high spanwise flow that moves

from the region of reattached flow towards the trailing edge down the wing as the pulse cycle progresses. Near the apex, the moving high velocity region is somewhat masked by the region of high axial flow. Downstream of x/c≈0.35 it can be easily identified, for example at x/c≈0.5 for t/T=0.7. The region of high spanwise velocity is associated with the perturbations present in the shear layer. As established earlier, the shear layer reattaches to the wing's surface. Periodically the perturbations initiated at the leading edge travel along the shear layer and increase the velocity near the reattachment point, and as a result can be seen increasing the velocity in the near surface plane. The origin of the high velocity region can be confirmed by comparing its location to the cross-flow plane data. For the cross-flow case, shown in Figure 5-1, at x/c=0.48, the perturbation can be seen to travel along the shear layer between 0<t/T<0.48, interact with the main region of vortical flow and attach to the surface at t/T≈0.6. The corresponding near surface flow measurements show a high velocity region crossing the point of x/c=0.48 at t/T≈0.6-0.7. The relationship between the cross-flow plane and the near surface measurements is more pronounced when they are presented in three dimensions in a single figure, as in Figure 5-17. For this case, the high velocity region moved down the wing at a velocity close to $U/U_\infty \approx 0.5$. However, it is difficult to see what the progression rate is near the apex, and over the entire wing, from t/T=0 until the perturbation crosses the trailing edge, the mean velocity of the region of high velocity movement is $U/U_\infty \approx 0.75$. For the St=1.5 case, there are positions in the pulse cycle, such as at t/T=0.5, where two moving regions can be seen. This is because for unsteady blowing at St=1.5, it takes two complete cycles (t/T=0-2) for the high velocity region to cover the length of the wing. Given that the initiation of the perturbation is fixed at t/T=0, and that the perturbation moves at an almost constant rate, the time it is expected to cross the trailing edge coincides almost exactly with the initiation of the induced pulse, two cycles later. As discussed, Figure 5-17 shows the relationship between the cross-flow planes and the near surface flow. It also is a very good way to get an appreciation for the flow field across the wing, and the relationship between the stations. The progress along the shear layer of the perturbation at the different stations shows the way that the induced vortex winds itself around the main vortical flow region. Figure 5-17 reinforces the cross-flow PIV results presented and again highlights the highly three dimensional nature of the flow. It also indicates that it is highly likely that at chordwise locations close to the trailing edge, two induced perturbations would be clearly identifiable in the shear layer. In light of this plot, it is more easily understood that the rate at which the high velocity region moves down the wing's surface is an indication of the level of winding around the central vortical region, or bending within the shear layer the perturbation undergoes. If the high velocity region in the near surface plane were to move quickly, it would indicate a low level of winding, and a perturbation vortex that remained reasonably straight. If the high velocity region in the near surface plane were to move very slowly, it would indicate a high level of winding, and the apparent lag in the movement of the perturbation vortex between chordwise stations would be greater. A sketch of the perturbation in the shear layer is shown in Figure 5-18. At position B, the perturbation can be seen to be wound round the shear layer, even though it began simultaneously across the leading edge (A).

As for the cross-flow cases, near surface PIV measurements for St=0.5 and St=1.0 were conducted. Figure 5-19 shows the near surface velocity magnitude for St=0.5. Similarly to the St=1.5 case, distinct regions of high velocity can be seen to move in a chordwise direction down the wing, corresponding to the perturbations observed in the shear layer for the cross-flow case. One important difference is that two distinct regions are seen to form and move down the wing per cycle. This is in contrast to the singular high velocity region formed per cycle for the St=1.5 case. This is consistent however, with the observations of the cross-flow case, where both an induced perturbation and a secondary perturbation could be seen in the shear layer per cycle. The discrete region of high velocity seen at $x/c\approx0.5$ for $t/T=0$ is actually attributed to the secondary perturbation, as the induced perturbation would be close to the leading edge of the wing at $t/T=0$. The high velocity region associated with the induced perturbation can be seen at $t/T=0.4$, and forms very close to the secondary region of high velocity. The induced perturbation region moves in a chordwise direction slightly faster then the secondary perturbation region. It is possible that the preceding secondary vortex has the effect of increasing the level of winding or bending of the induced vortex about the shear layer, causing it to appear to move faster.

The St=1.0 case, shown in Figure 5-20, shows a significantly lower level of reattachment. Note that the velocity magnitude scale is lower than in the previous figures. A region of higher velocity that moves down the wings surface is still present; however it can only be seen from $x/c\approx0.5$. The region of higher velocity progresses down the wing at the same rate as the St=1.5 case, and the secondary region of the St=0.5 case. This high velocity region indicates that the perturbation does interact with the wings surface. It is interesting to note that the shape of the high velocity region is much more elliptical than that of the other Strouhal numbers, and it does not extend past $y/c\approx0.15$. By contrast for the other Strouhal numbers (St=0.5 and St=1.5), its extent is usually approximately half the local semispan. There is also an additional region of high velocity magnitude near the leading edge of the wing. This is a region of high velocity reversed flow.

One possible explanation for the origin of the secondary perturbation in the St=0.5 case, is that it occurs due to the region of high velocity associated with the induced perturbation, passing over the trailing edge of the wing. If this is the case, it would explain why oscillations with Strouhal numbers which are multiples of St=0.75 only show one perturbation, whereas all other cases show an additional induced perturbation. For the cases of St=0.75 and St=1.5, as the mean velocity of the perturbation downstream in the near surface plane is $U/U_\infty=0.75$, (for the St=0.75 case $UT/c=1$, and it would take one period for the region to cover the length of the wing) any secondary perturbation would occur at approximately the same time as the induced perturbation, and would not be evident. The secondary perturbation is only visible in the cross-flow planes for St=1.0, as it is either too weak to be evident in the near surface plane, or does not actually reattach to the surface. However, its point of initiation in the pulse cycle can still be predicted by looking at the point at which the induced perturbation is likely to pass over the trailing edge of the wing. At its expected rate of movement, the perturbation should cross the trailing edge at $t/T=0.4$ for the St=1.0 case, which is

very close to the instance when the secondary perturbation can be identified in the cross-flow planes (t/T=0.45). Another possibility is that the secondary perturbation is a result of some cyclic disturbance from the primary perturbation being fed into the main vortical structure. However this occurs at different instances for each chordwise location, whereas the secondary perturbation appears to emanate from the leading edge more or less simultaneously.

Another possible explanation for the origin of the secondary perturbation is that instabilities form naturally in the shear layer. The high level of periodicity of the secondary perturbation could simply be a result of the natural instability forming at a point in the cycle when the induced instability does not occur, and therefore being constrained to form in-between the induced perturbations. Another possibility is that the natural frequency of the natural instabilities may be St=0.75. Inducing instabilities at multiples of St=0.75 would excite the natural instability mode. However, when inducing perturbations at frequencies above or below St=0.75, instabilities may also still occur at the natural frequency, St=0.75, and may be the origin of the secondary instability. It is worth noting that the phase averaged PIV measurements are an indication of the average flow at that period of the pulsing cycle, and it might simply be the case that the PIV results show the most likely position in the pulse cycle for the formation of the natural instability. In terms of flow control, it is perhaps only necessary to excite the shear layer near to the natural frequency or near its first harmonic. This would account for the low effectiveness of unsteady blowing at St=1.0, as it is directly in between the natural frequency and its first harmonic and is not effective at exciting either mode. It is possible that the natural frequency of the shear layer fluctuations is related to the frequency at which the high velocity regions cover the length of the wings surface. The time taken for the high velocity regions to cover the length of the wing is an indication of the time taken for perturbations that reattach near the trailing edge, to cover the length of the shear layer. Although the natural frequency of the shear layer instabilities is expected to be highly three dimensional, it may be that exciting the instabilities at a certain point on the wing, such as those that correspond to reattachment near the trailing edge, is sufficient to induce reattachment over the wings surface.

Whether or not the secondary perturbation is a result of the induced perturbation or a natural instability in the shear layer, there is a definite periodicity in addition to that of the induced perturbation. Figure 5-21 shows phase averaged turbulence intensity plots of the x/c=0.48 plane at different positions in the pulse cycle. For each Strouhal number, the position in the pulse cycle has been chosen to correspond to a set interval of time after an arbitrary point, where the position in the pulse cycle is t/T=0. The first interval, $\Delta tU_\infty/c=0.2$ is intended to show the point immediately after the induced perturbation has left the leading edge. A perturbation can be seen in all cases, except for that of St=1.5, where it has already begun to merge with the main vortical region. The second two time intervals, $\Delta tU_\infty/c=1.4$ and $\Delta tU_\infty/c=1.6$, have been chosen to represent the interval in time when the induced pulse is close to the leading edge for the next cycle of the St=0.75 case. For all Strouhal numbers a perturbation can be seen in the shear layer at either $\Delta tU_\infty/c=1.4$ or $\Delta tU_\infty/c=1.6$.

This indicates an additional level of periodicity, at approximately St=0.75, on top of that of the induced perturbation. This corresponds well with the observations in the near surface plane.

Phase locked measurements presented here indicate that unsteady blowing at the leading edge induces a perturbation that moves along the shear layer and interacts with the main vortical structure. The centre of the vortex swirl pattern moves inboard as the perturbation merges with the main vortical region, and then outboard again once the perturbation has fully merged into the main vortical structure. The flow structure is highly three dimensional, and the perturbation progresses along the shear layer at different rates at different chordwise stations. For cases where reattachment occurs, when the perturbation reaches the wing's surface, it induces a high spanwise velocity in the near surface plane. This region of high spanwise velocity moves in a chordwise direction from the apex of the wing to the trailing edge, and indicates the reattachment of the perturbation induced at different locations of the leading edge. These results give insight as to what is physically happening as the high velocity perturbation interacts with the shear layer.

Table 5-1 Effect of Strouhal number on perturbations occurring in the shear layer for x/c=0.48.

St	Instabilities in cycle	t/T of first instability	t/T of second instability
0.25	2	0	0.4
0.5	2	0	0.65
0.75	1	0	-
1.0	2	0	0.45
1.25	2	0	0.5
1.5	1	0	-

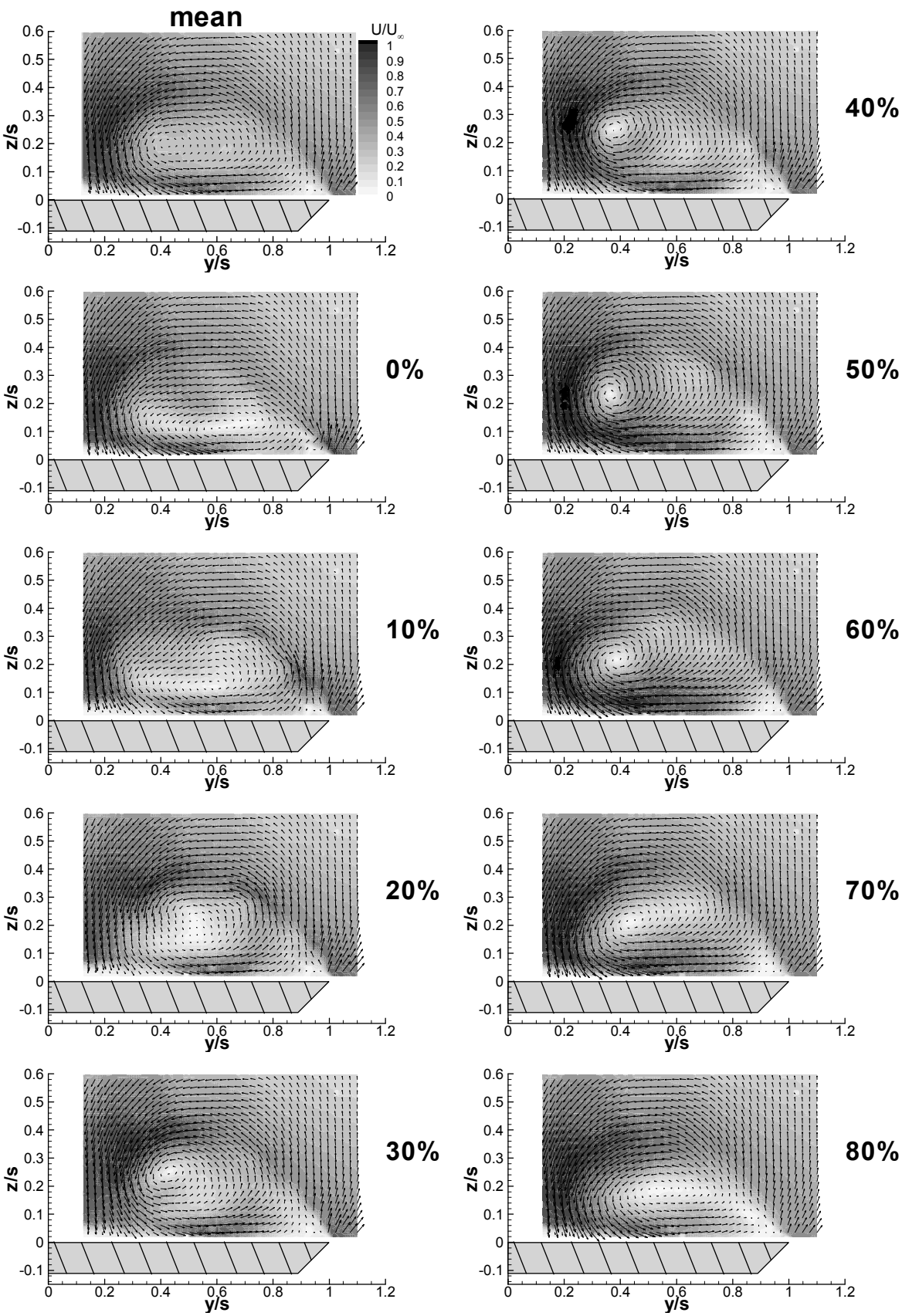

Figure 5-1 Magnitude of phase-averaged cross-flow velocity, x/c=0.48, α=30°, C_μ=0.4%, St=1.5.

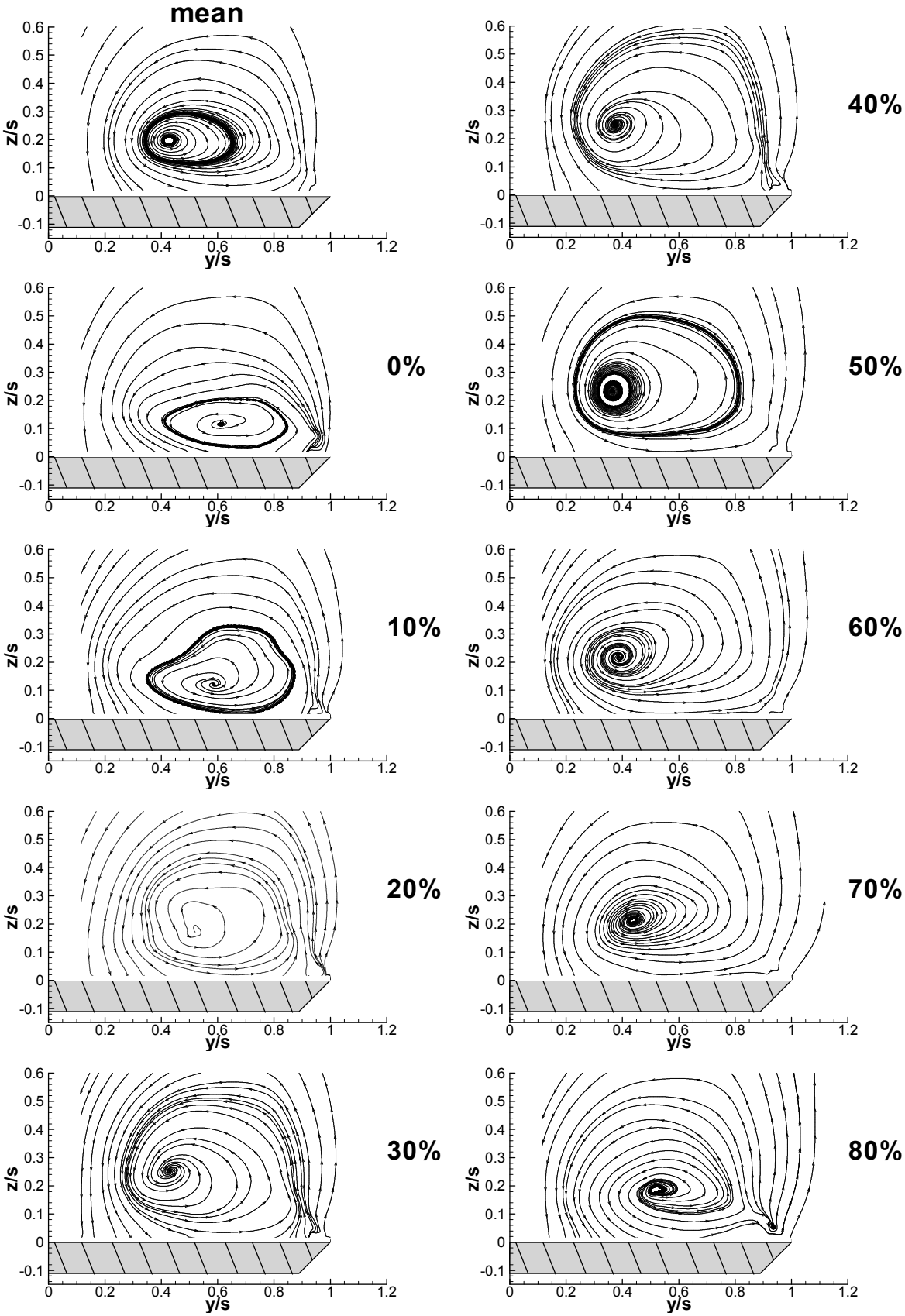

Figure 5-2 Phase averaged cross-flow streamline patterns, x/c=0.48, α=30°, C_μ=0.4%, St=1.5.

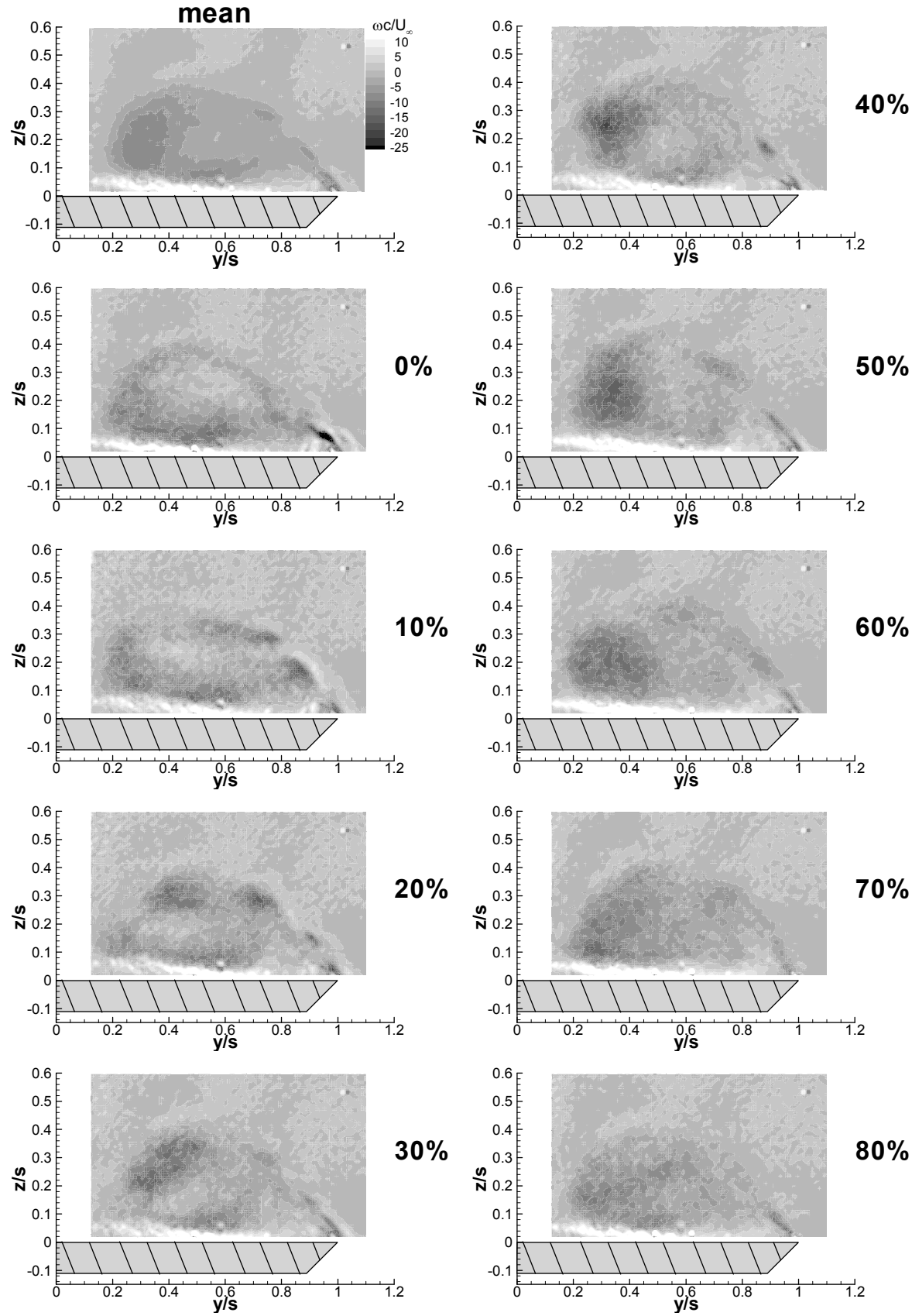

Figure 5-3 Phase averaged cross-flow vorticity, x/c=0.48, α=30°, C_μ=0.4%, St=1.5.

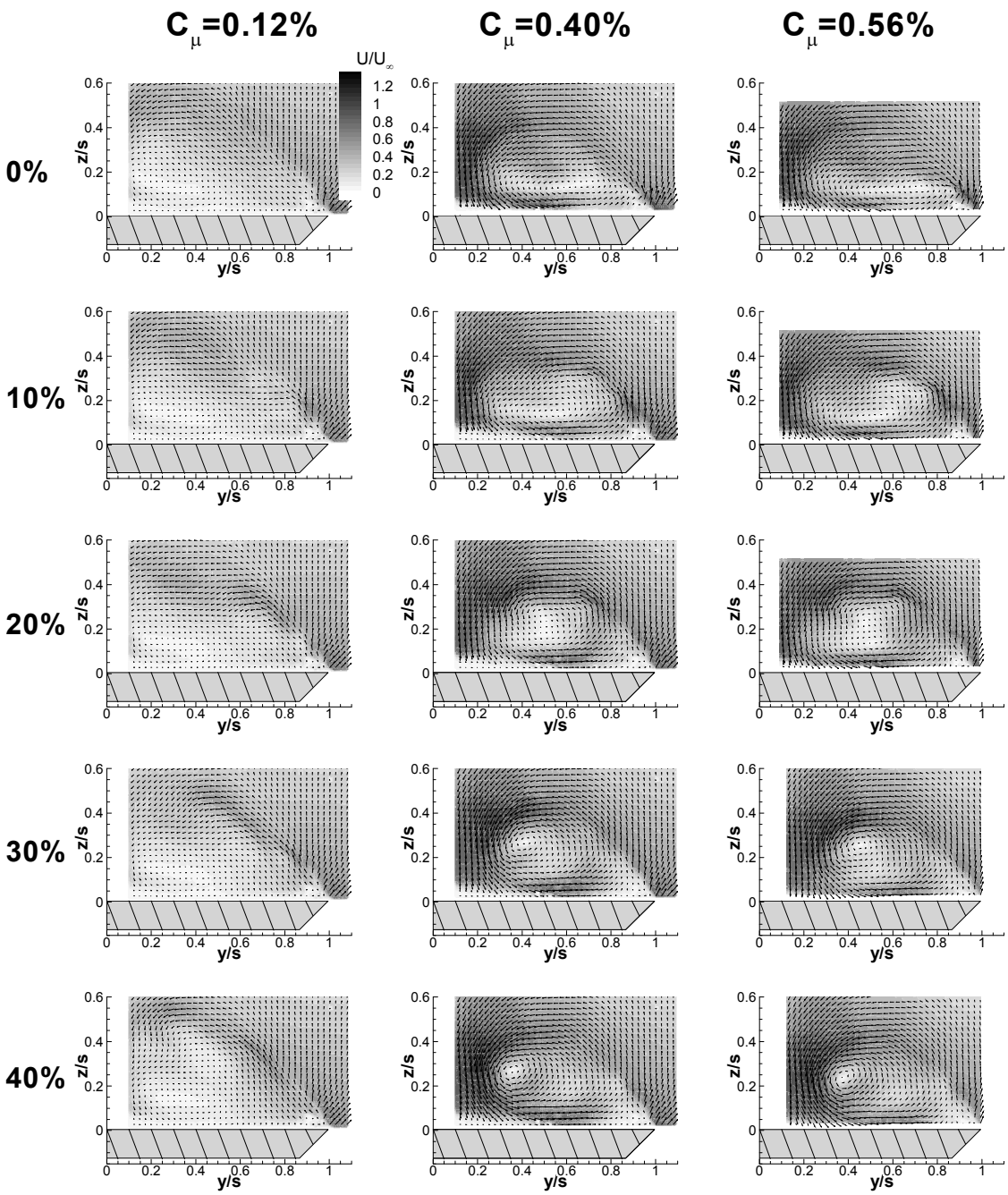

Figure 5-4 The effect of momentum coefficient on the magnitude of phase-averaged cross-flow velocity, x/c=0.48, α=30°, C_μ=0.12%-0.56%, St=1.5.

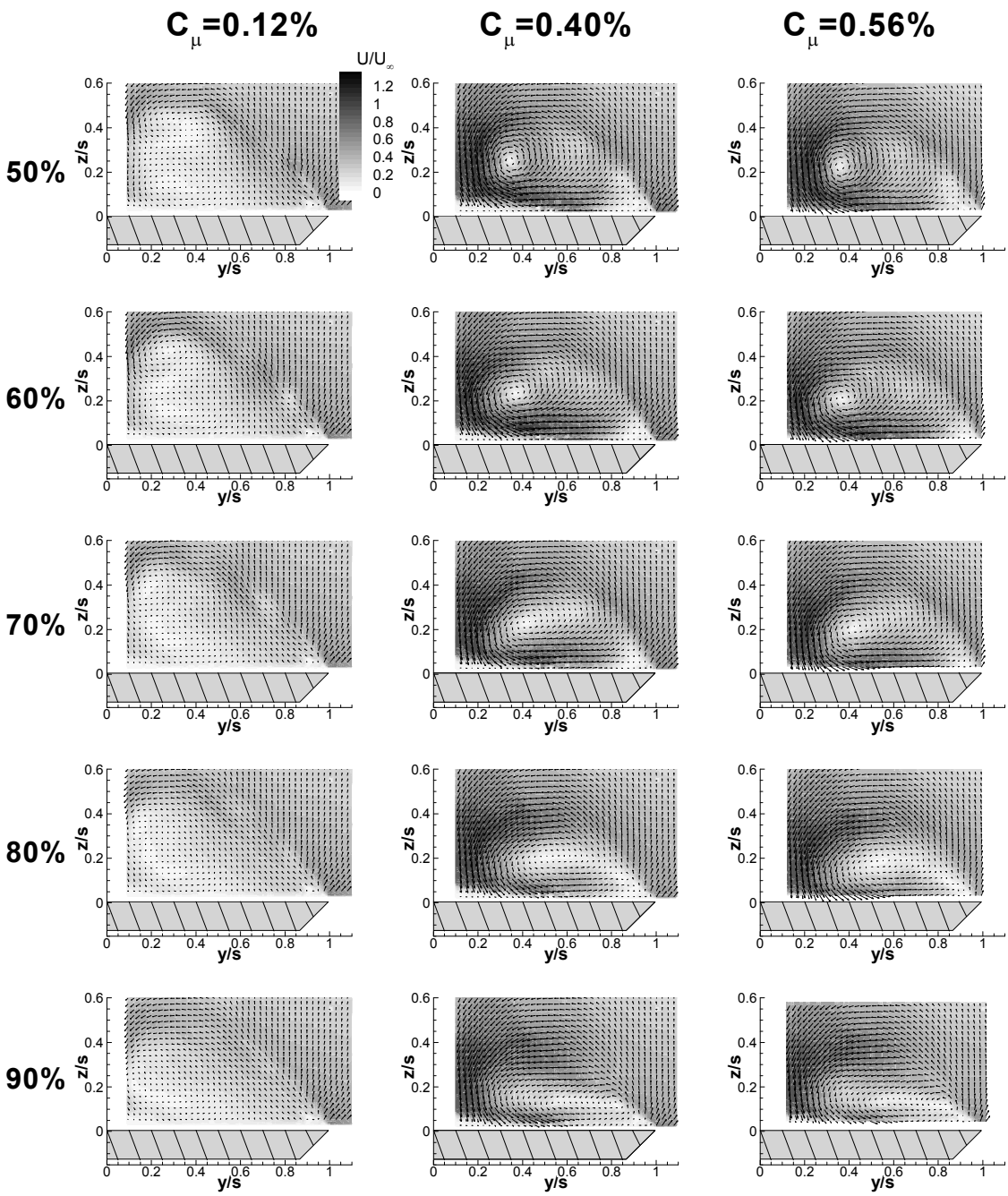

Figure 5-4 Continued

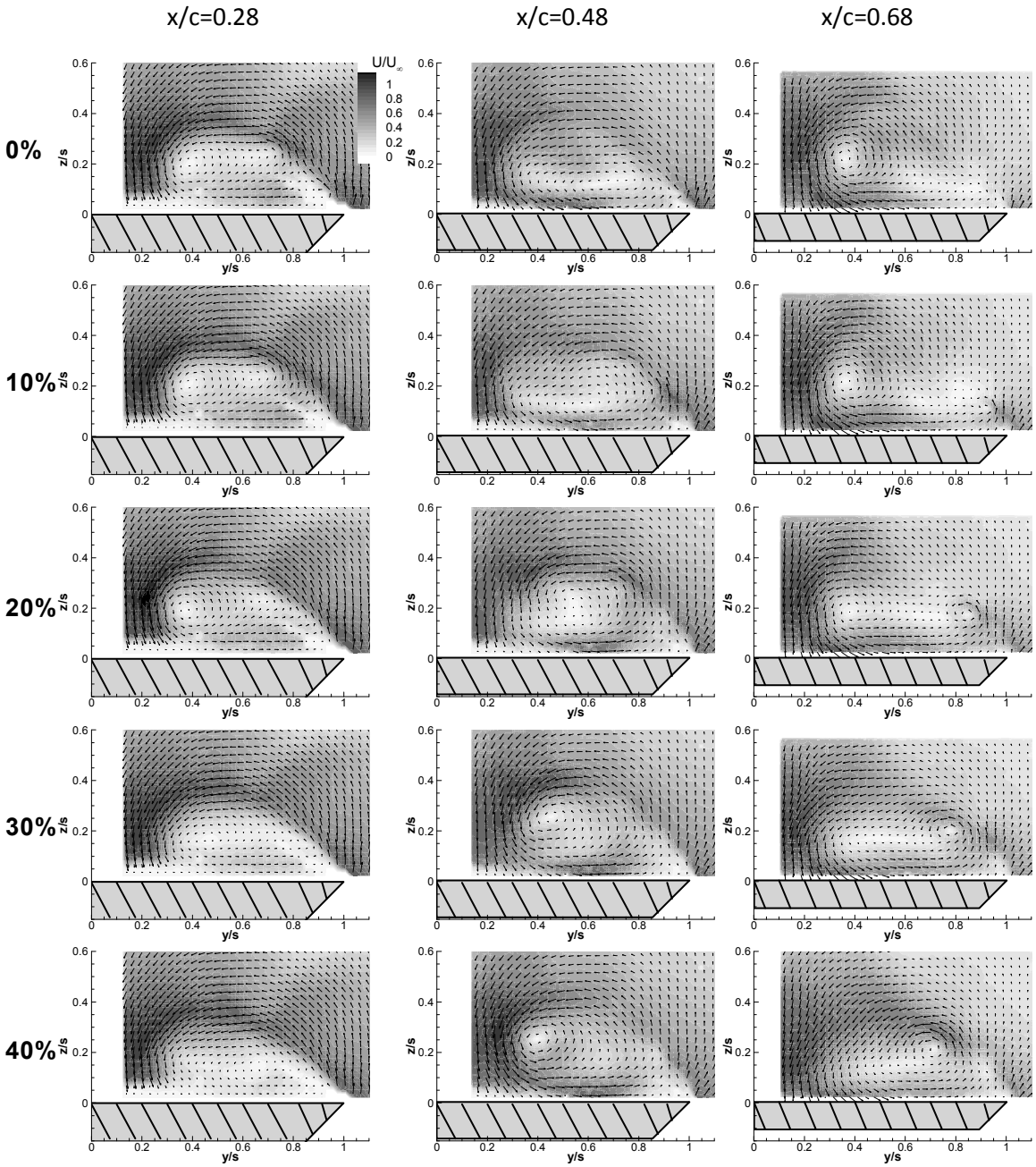

Figure 5-5 Comparison of the magnitude of phase-averaged cross-flow velocity at stations A, B and C, α=30°, Cμ=0.4%, St=1.5.

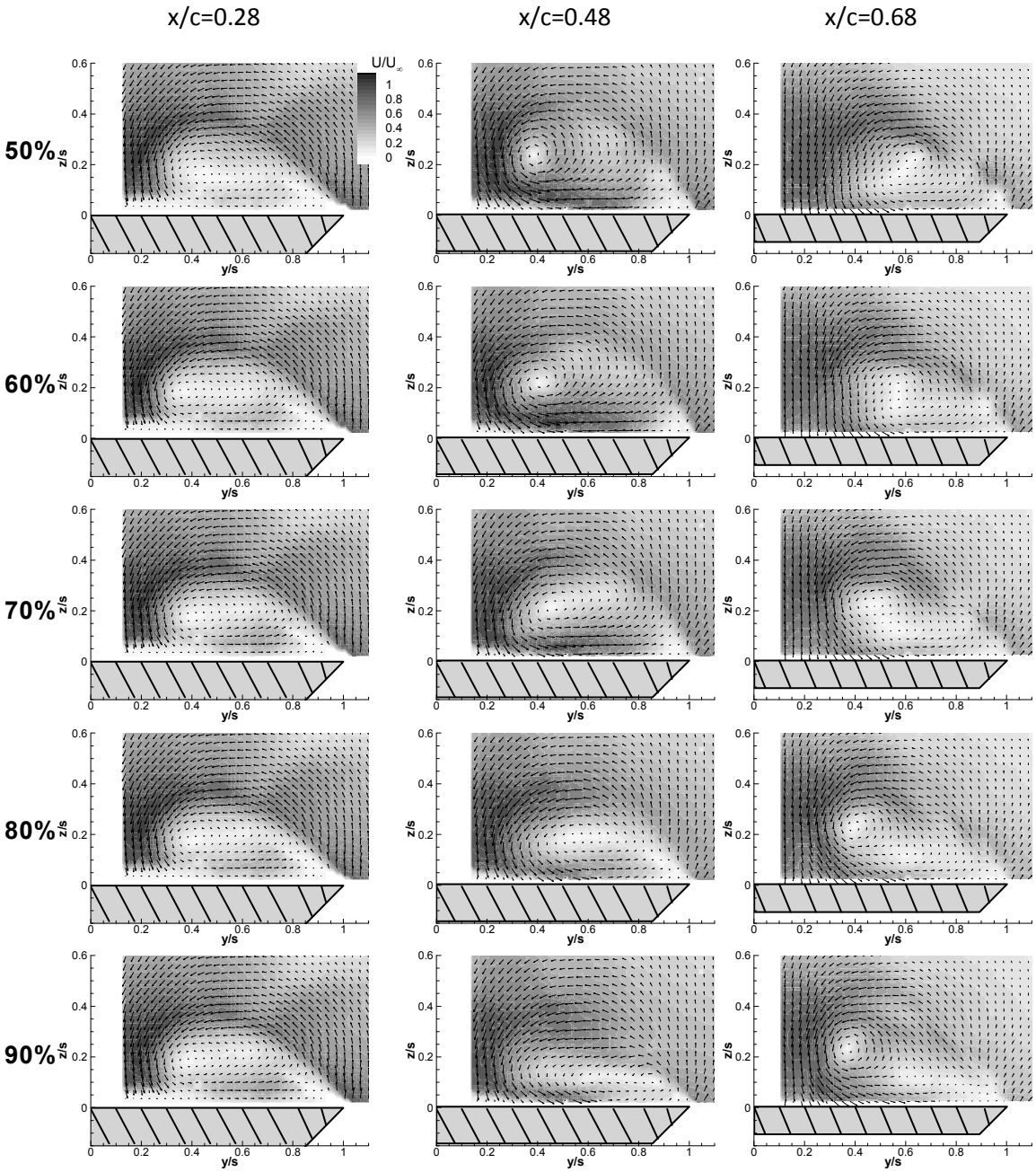

Figure 5-5 Continued

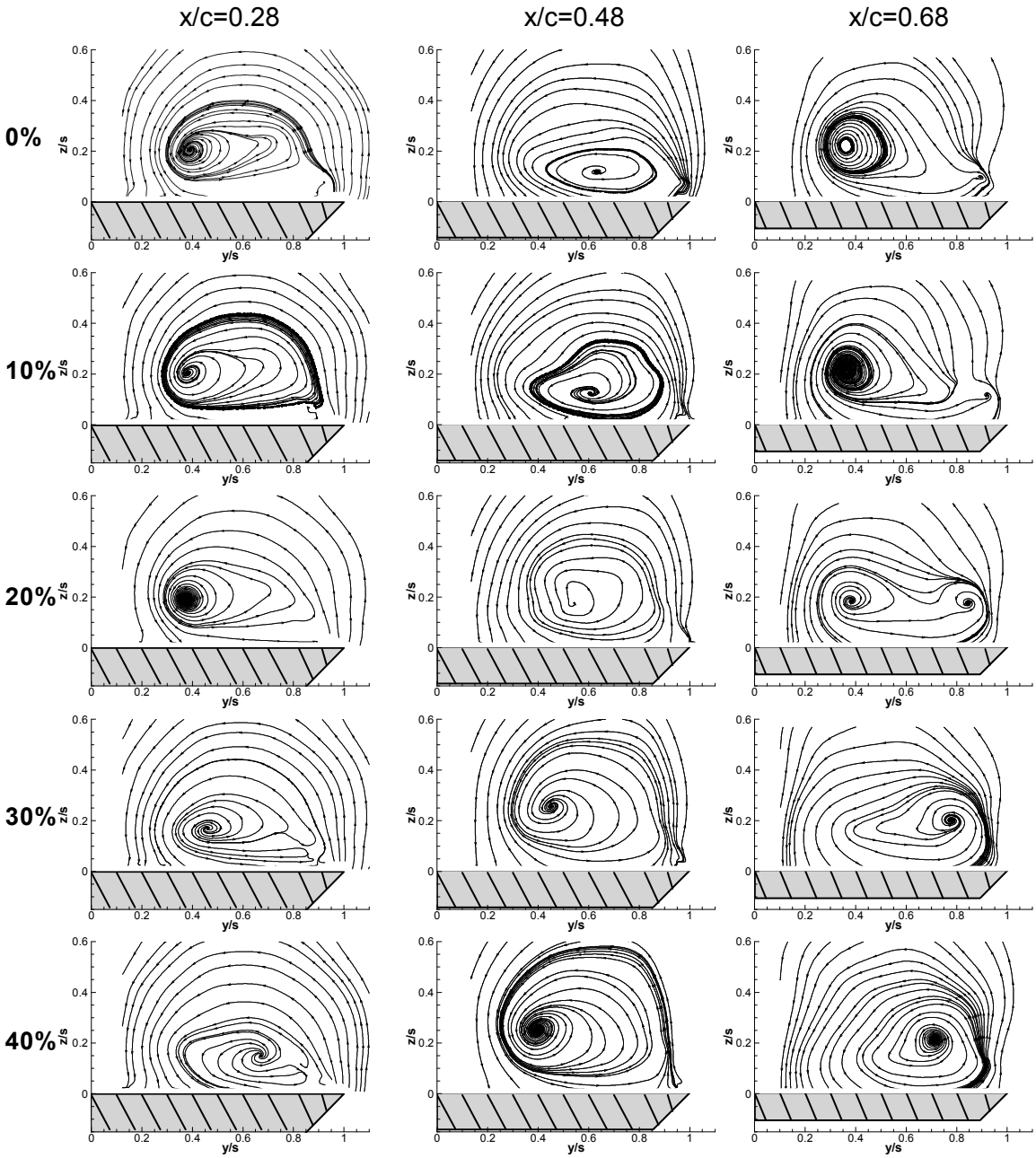

Figure 5-6 Comparison of phase-averaged streamline pattern at stations A, B and C, α=30°, C_μ=0.4%, St=1.5.

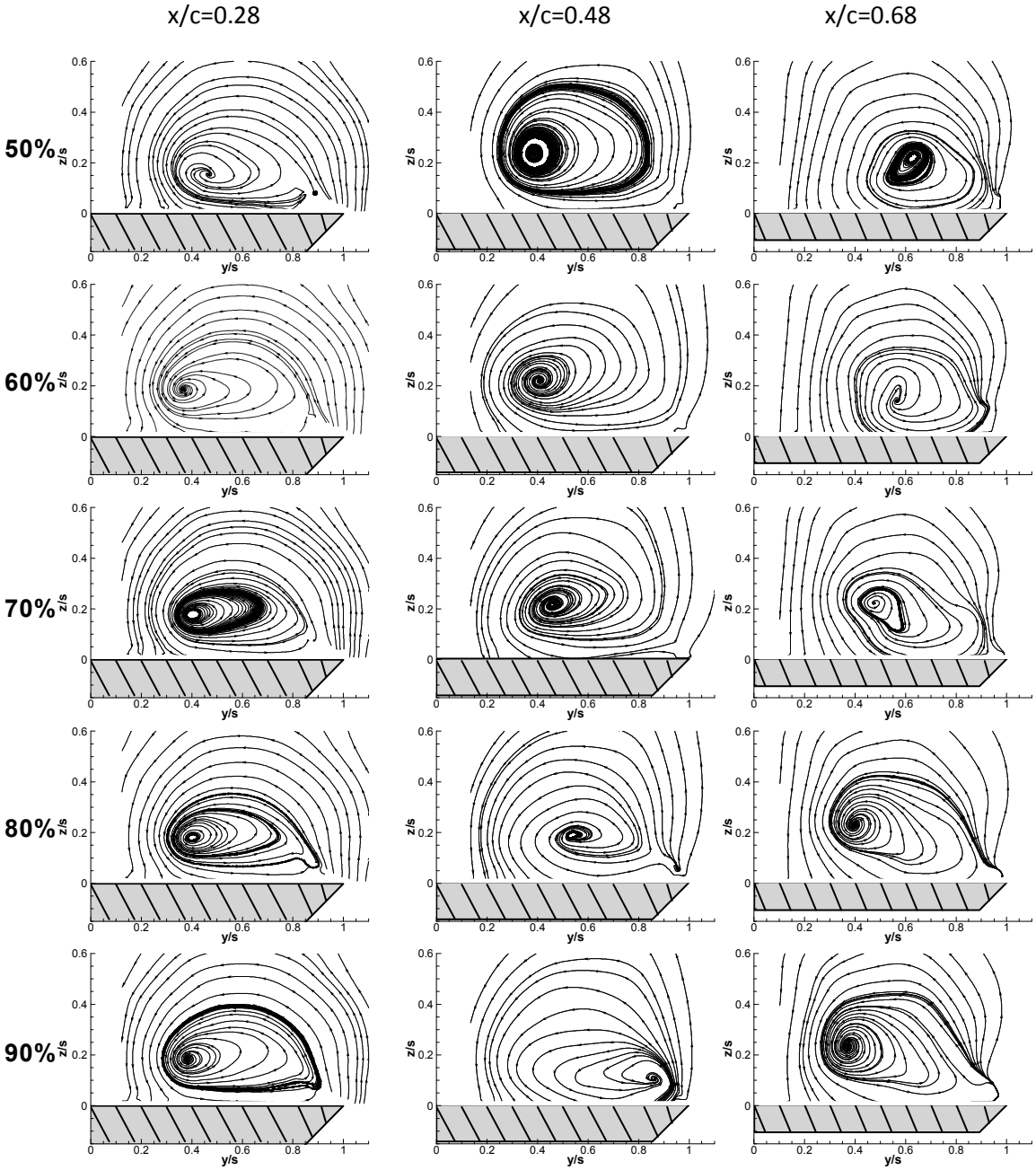

Figure 5-6 Continued

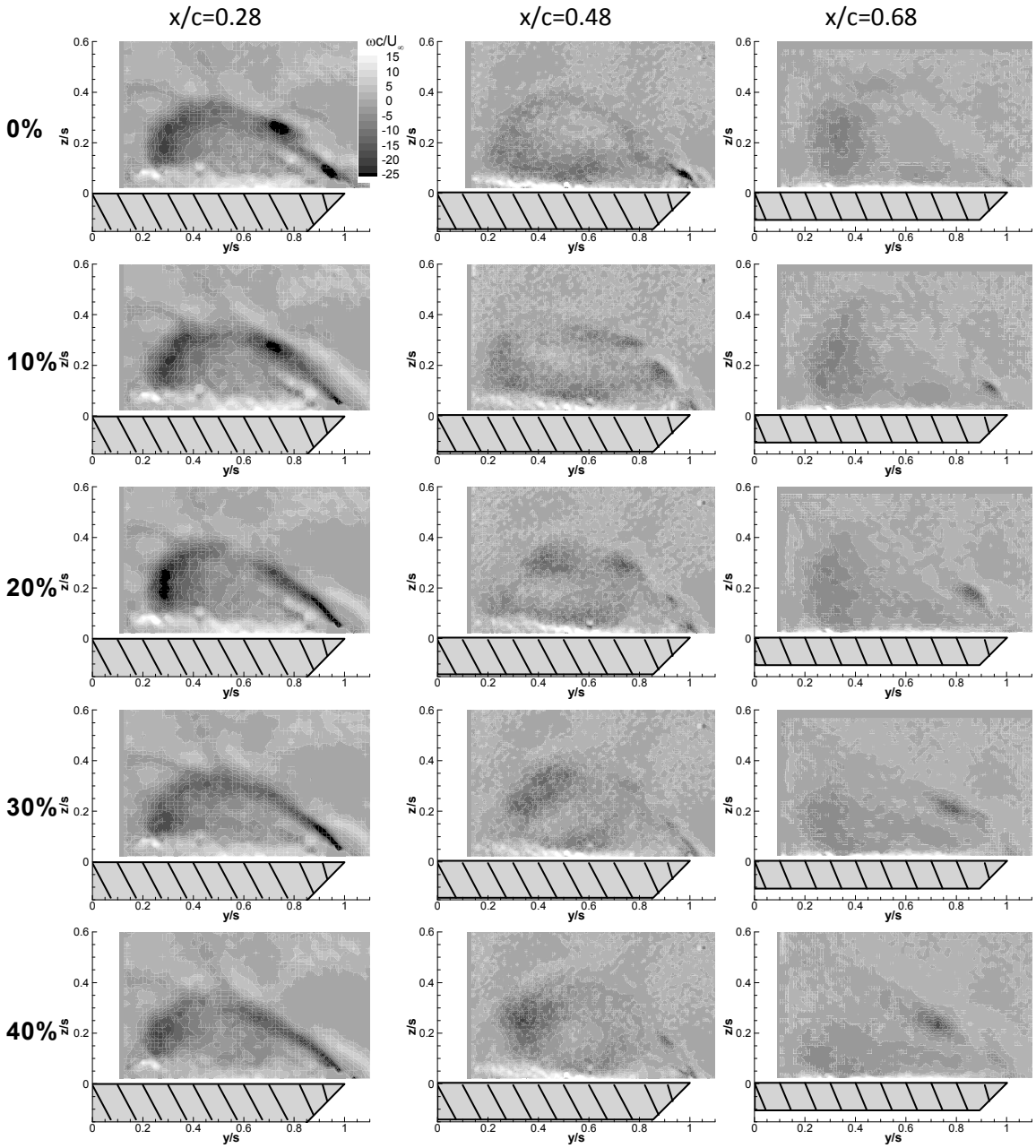

Figure 5-7 Comparison of the phase-averaged cross-flow vorticity at stations A, B and C, α=30°, Cμ=0.4%, St=1.5.

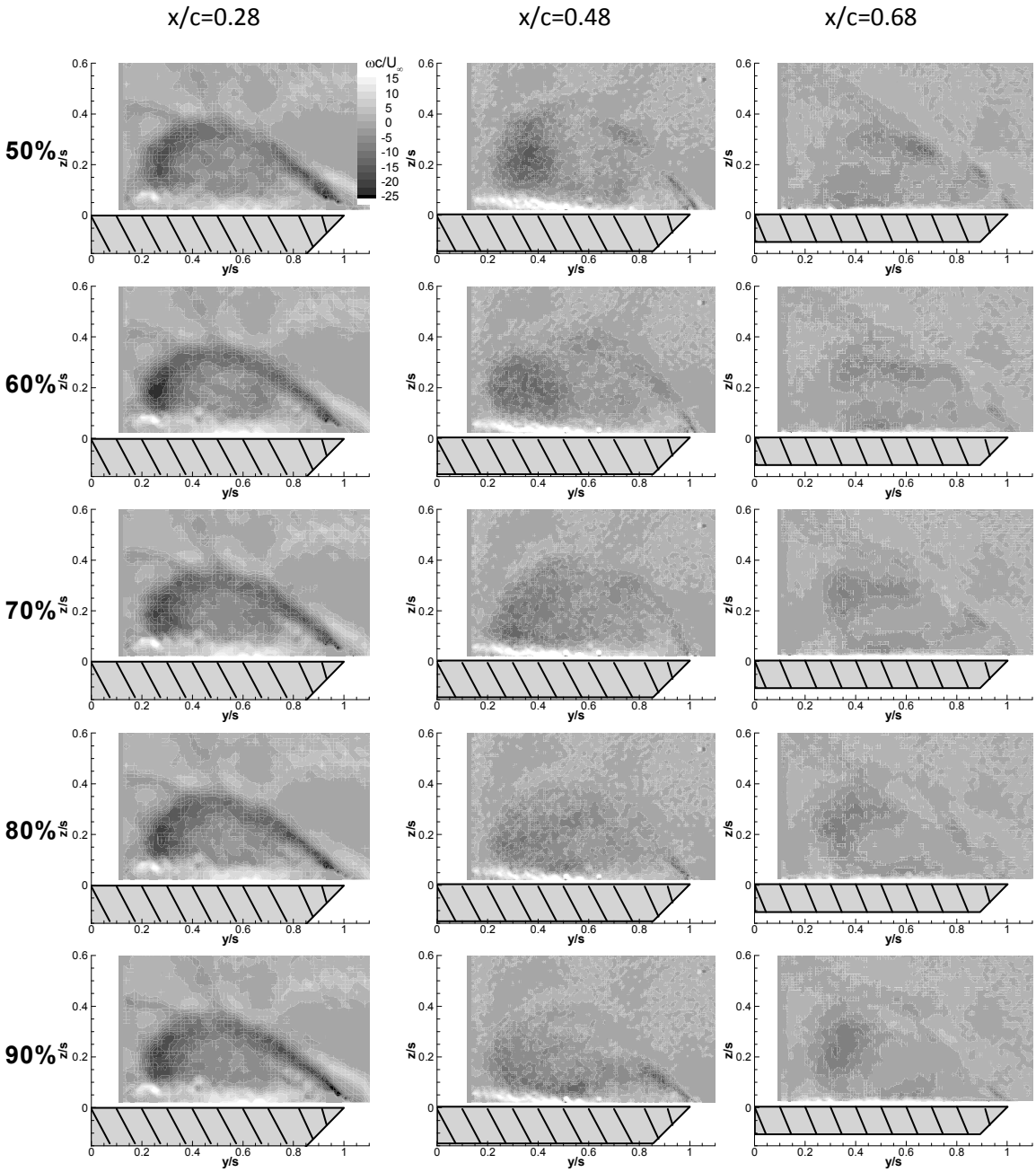

Figure 5-7 Continued

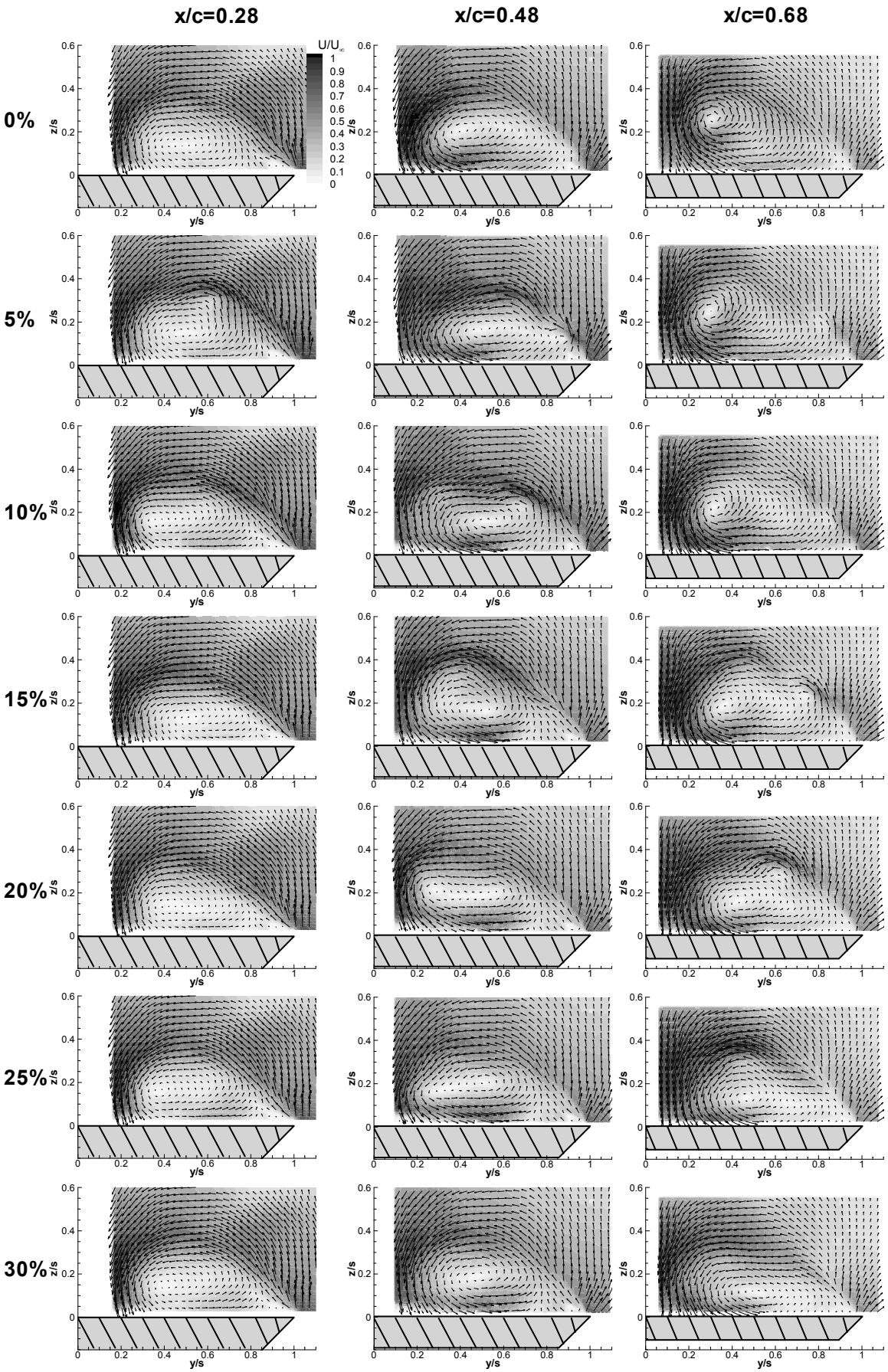

Figure 5-8 Comparison of the magnitude of phase-averaged cross-flow velocity at stations A, B and C, α=30°, C_μ=0.4%, St=0.5

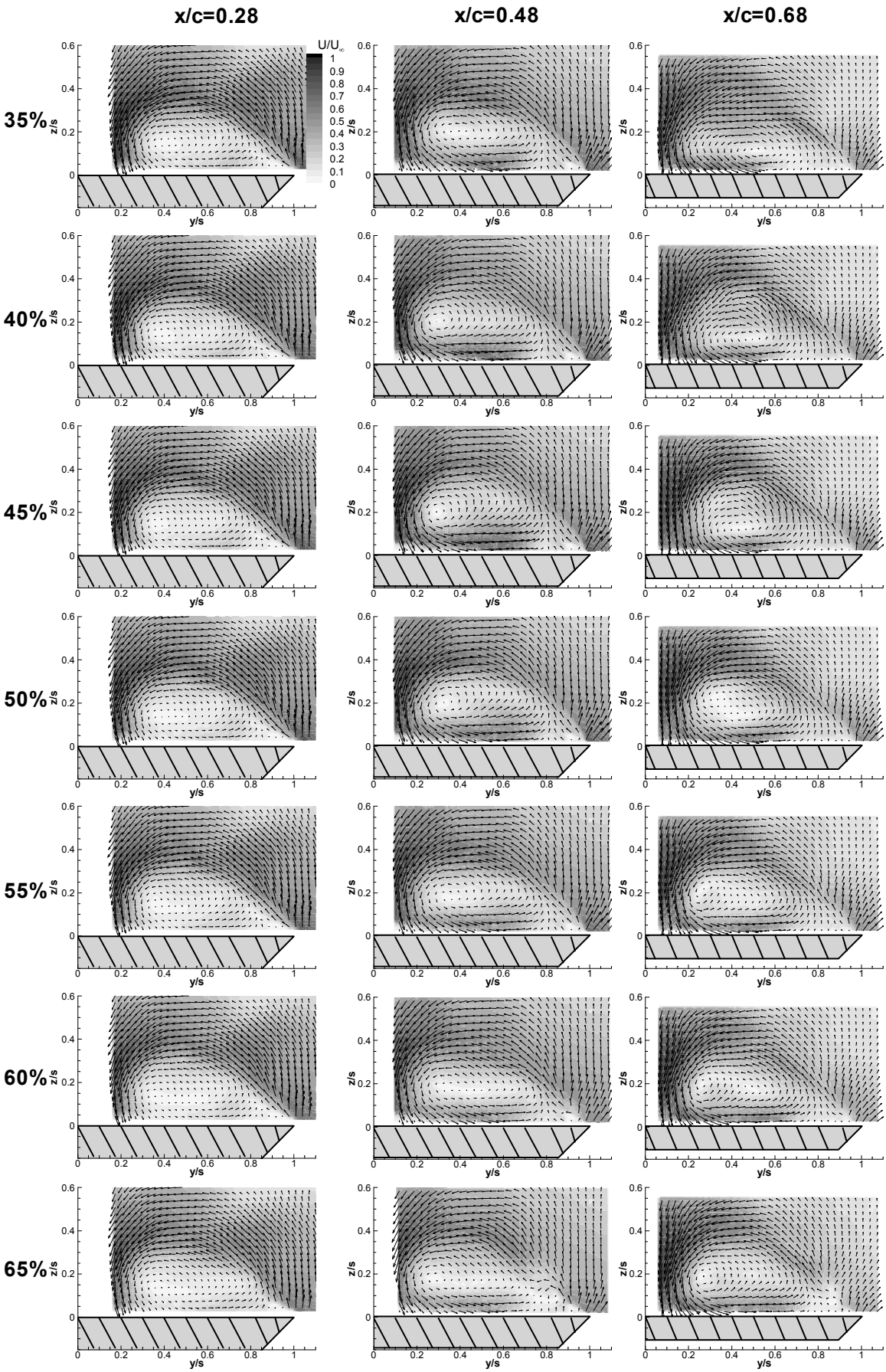

Figure 5-8 Continued

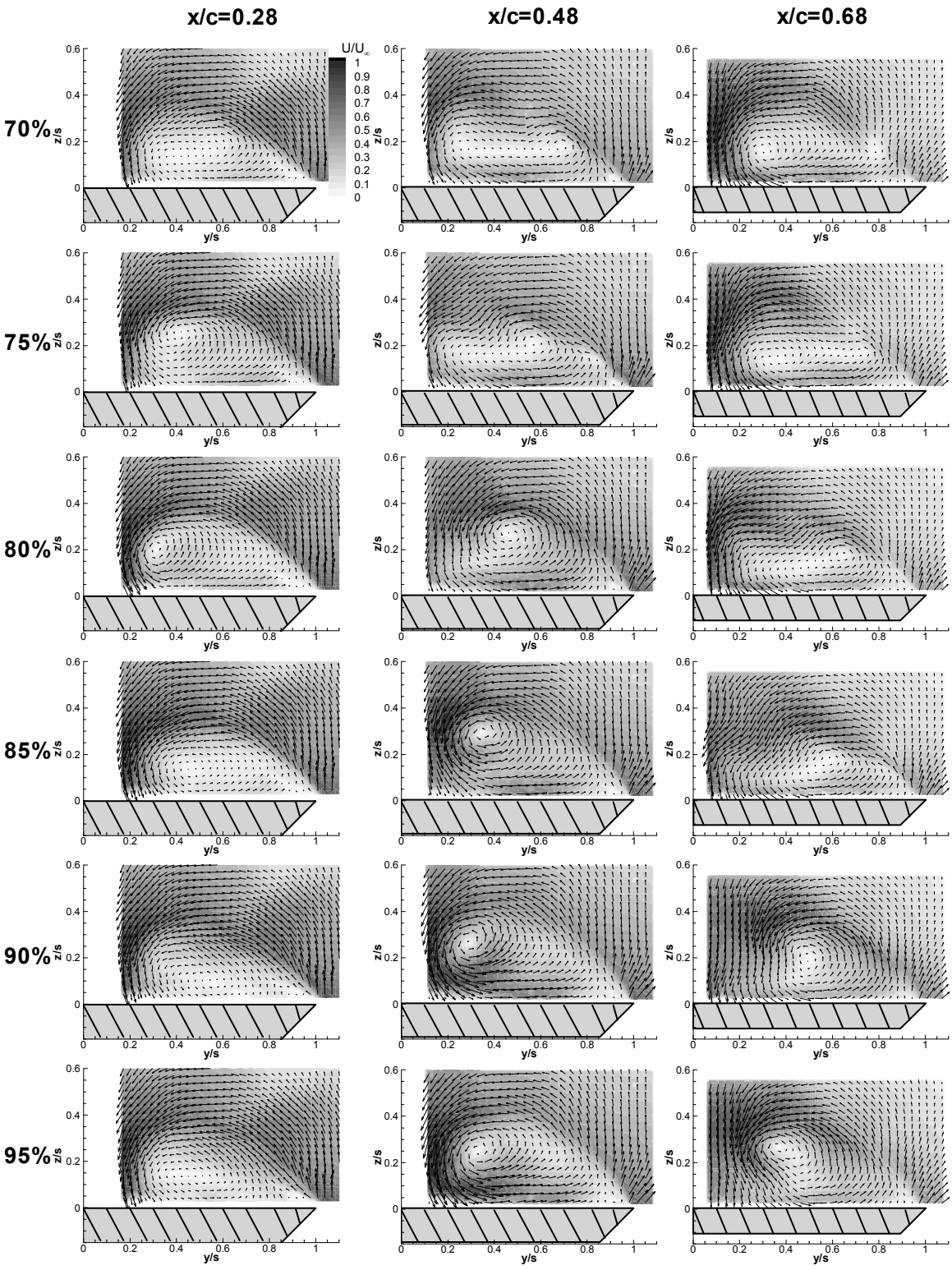

Figure 5-8 Continued

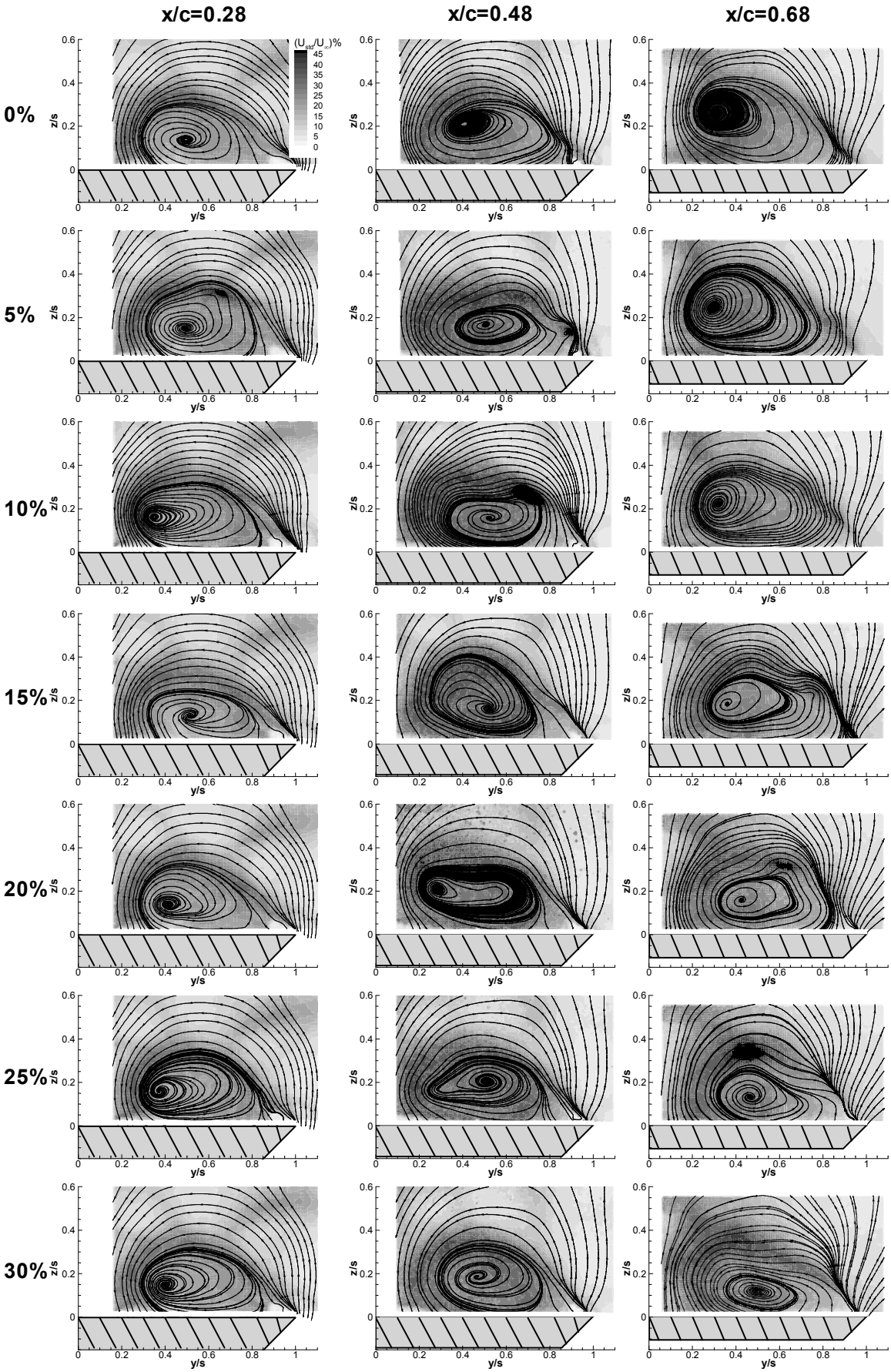

Figure 5-9 Comparison of the cross-flow streamline patterns at stations A, B and C, α=30°, C_μ=0.4%, St=0.5. Turbulence intensity contours are included in the plot.

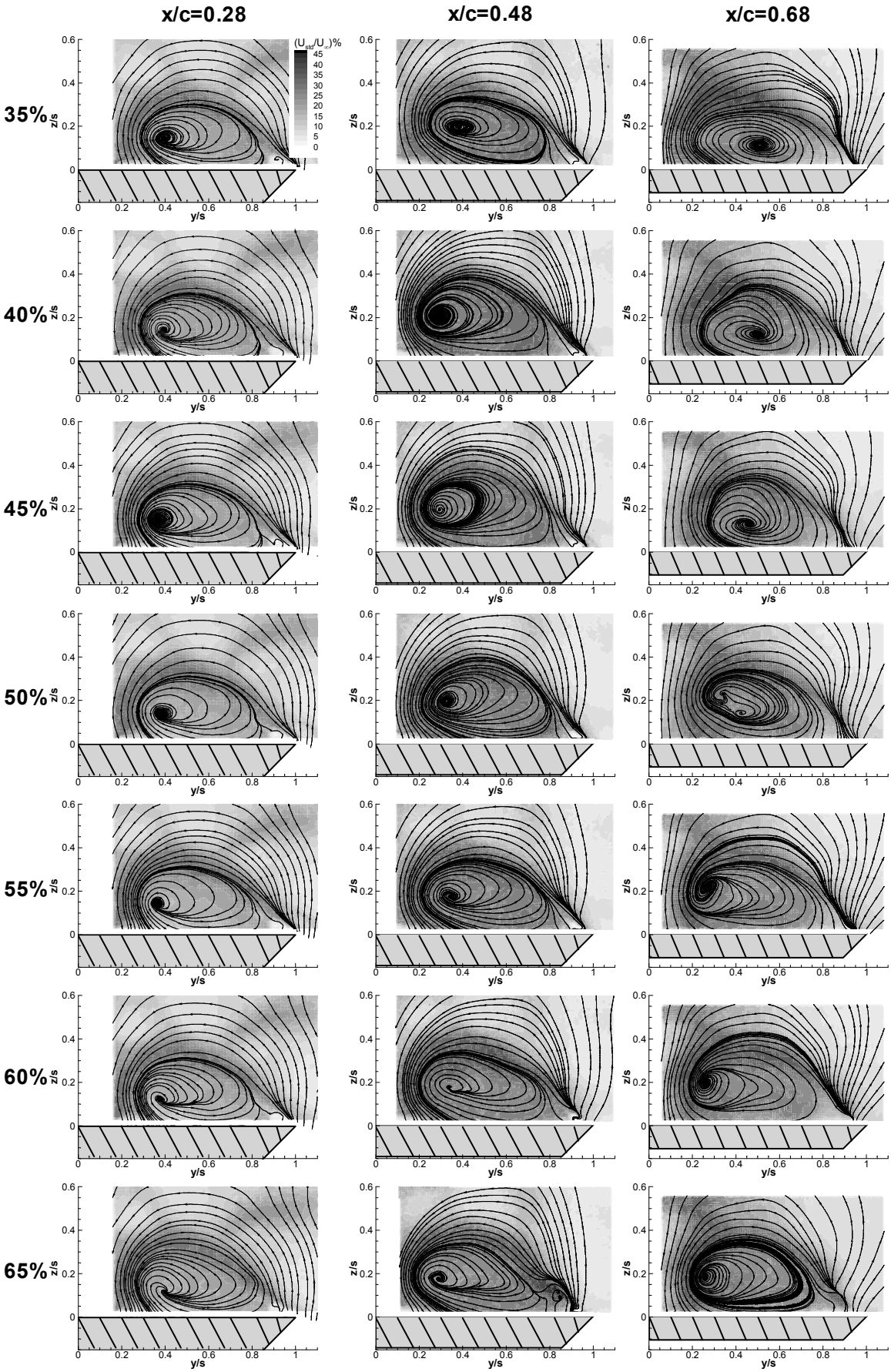

Figure 5-9 Continued

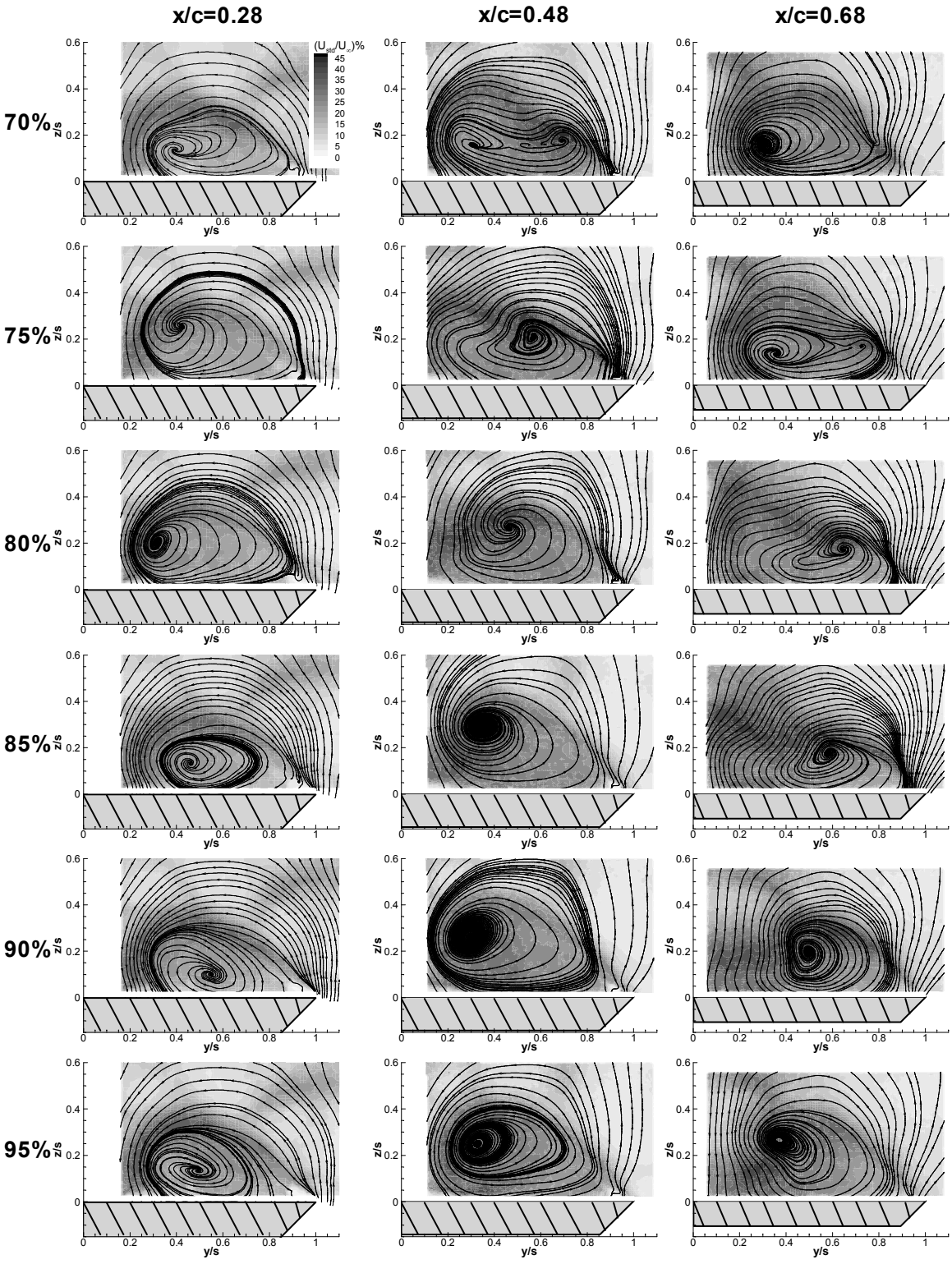

Figure 5-9 Continued

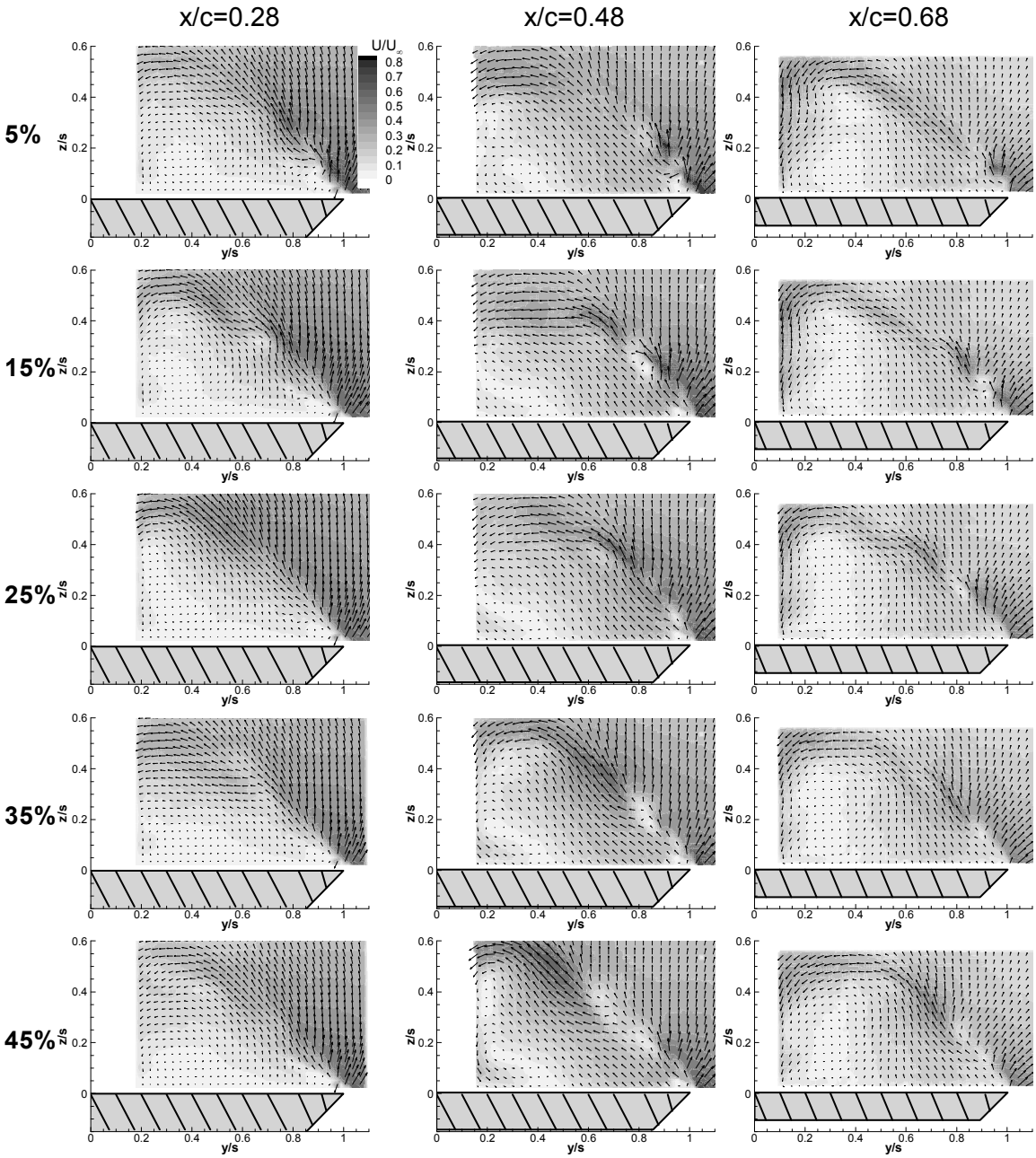

Figure 5-10 Comparison of the magnitude of phase-averaged cross-flow velocity at stations A, B and C, α=30°, Cμ=0.4%, St=1.0

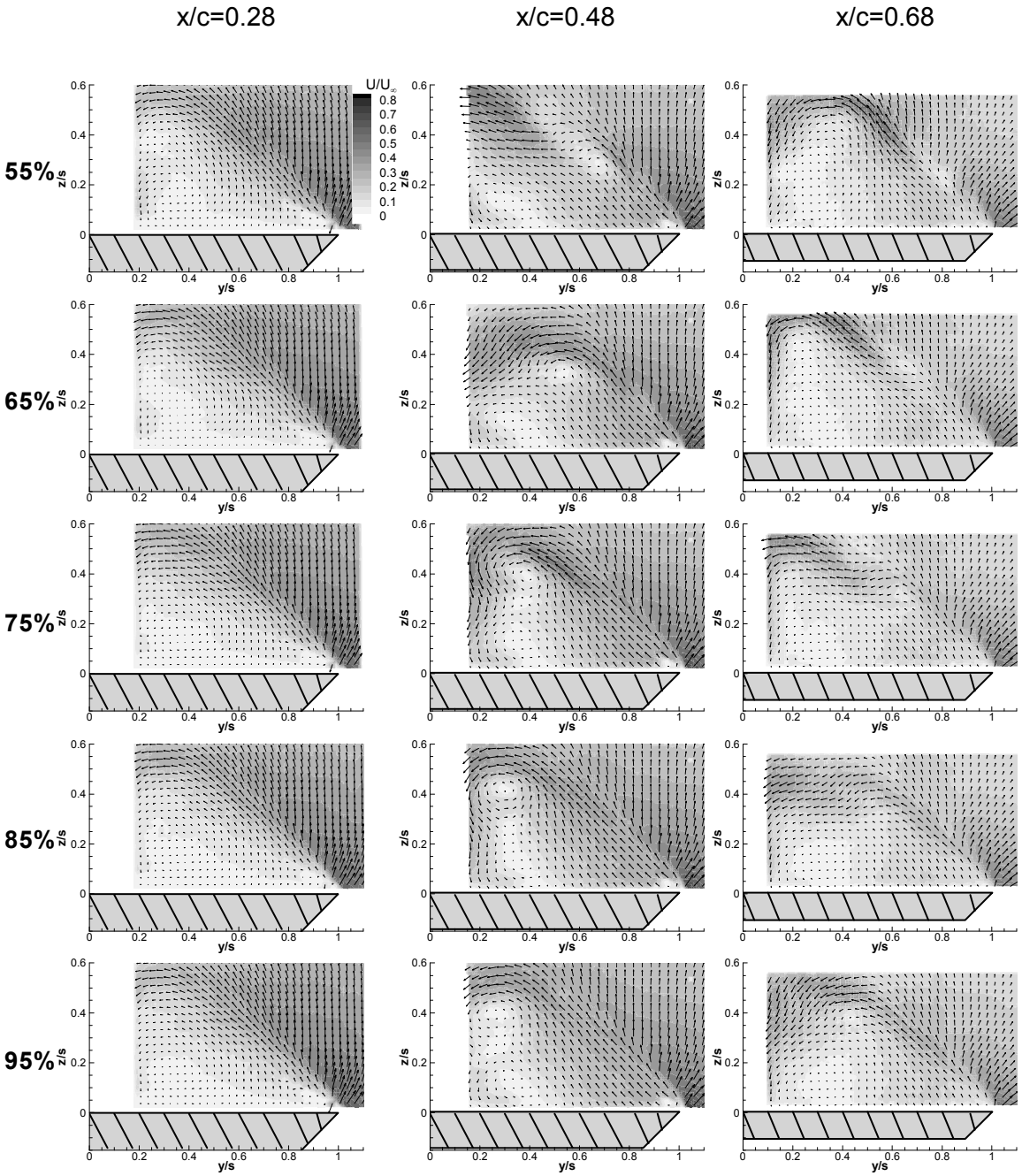

Figure 5-10 Continued

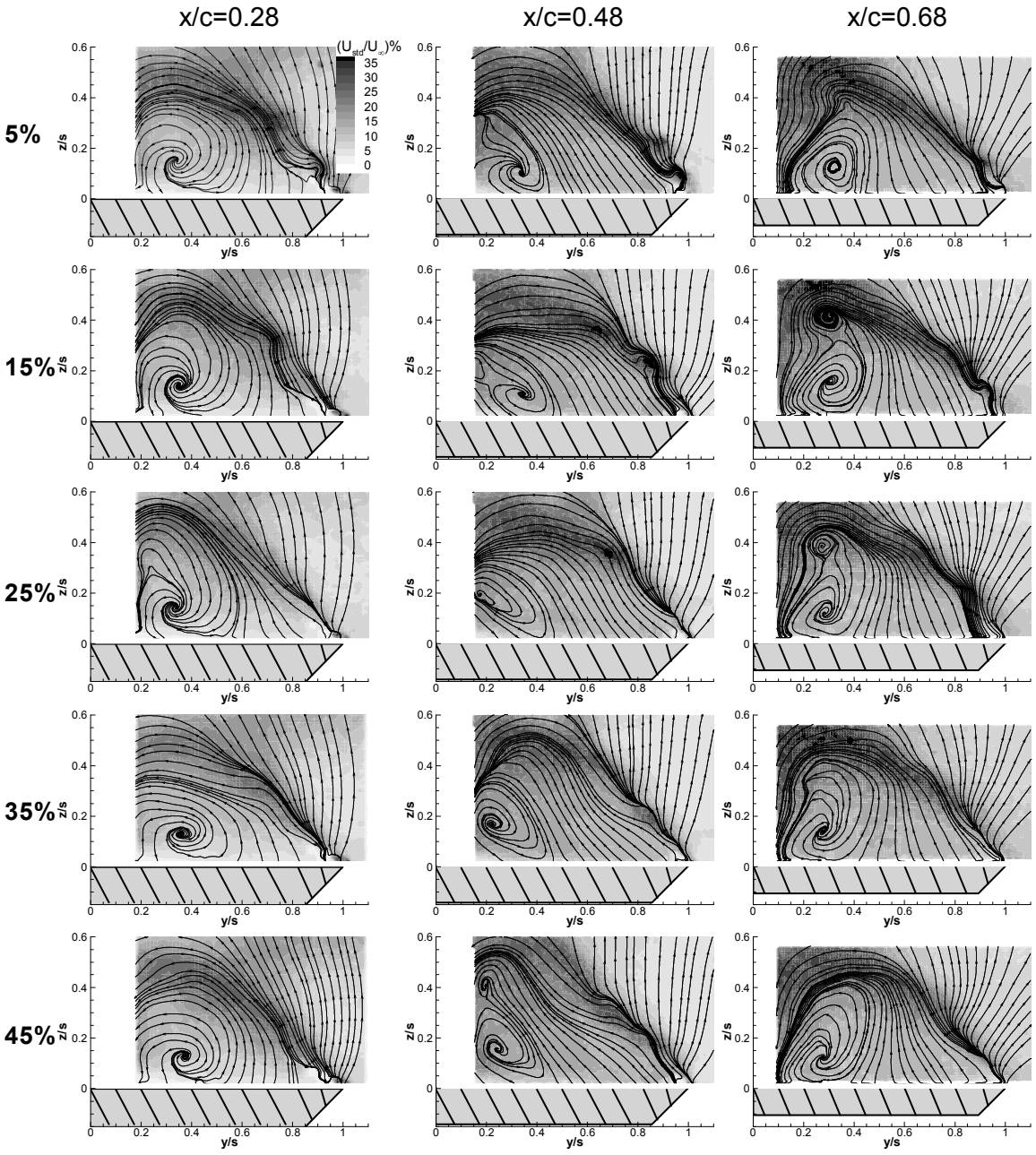

Figure 5-11 Comparison of the cross-flow streamline patterns at stations A, B and C, α=30°, Cμ=0.4%, St=1.0. Turbulence intensity contours are included in the plot.

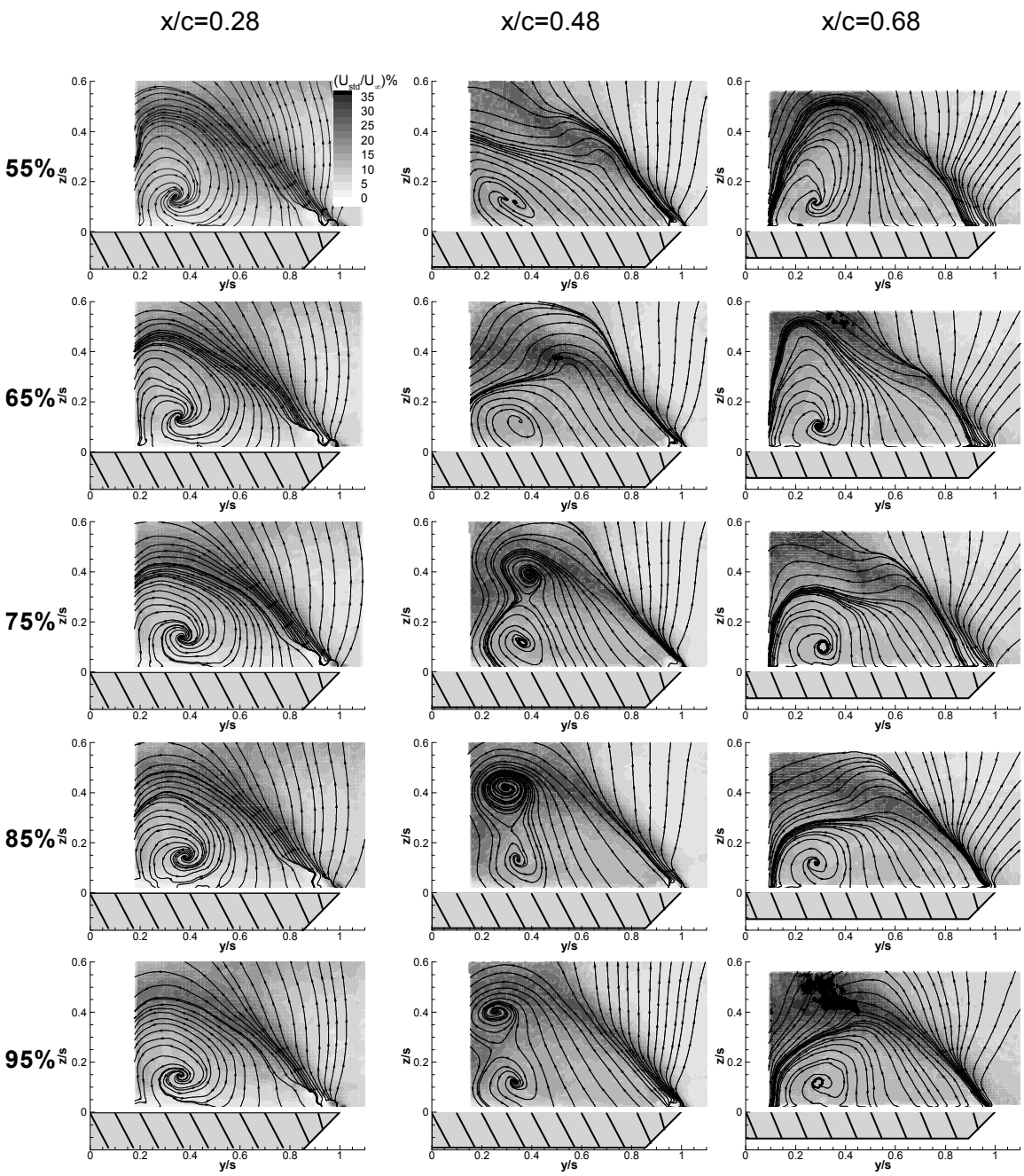

Figure 5-11 Continued

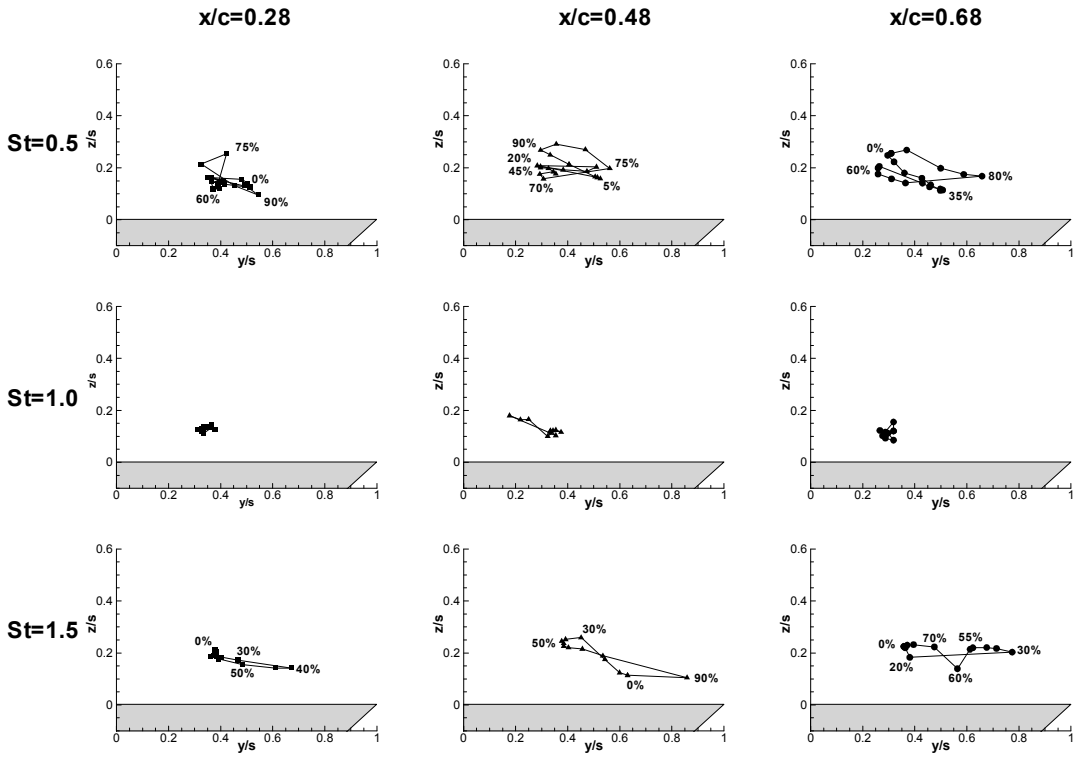

Figure 5-12 Centre of vortex swirl pattern for the phase-averaged cross-flow streamlines, x/c=0.48, α=30°, C_μ=0.4%.

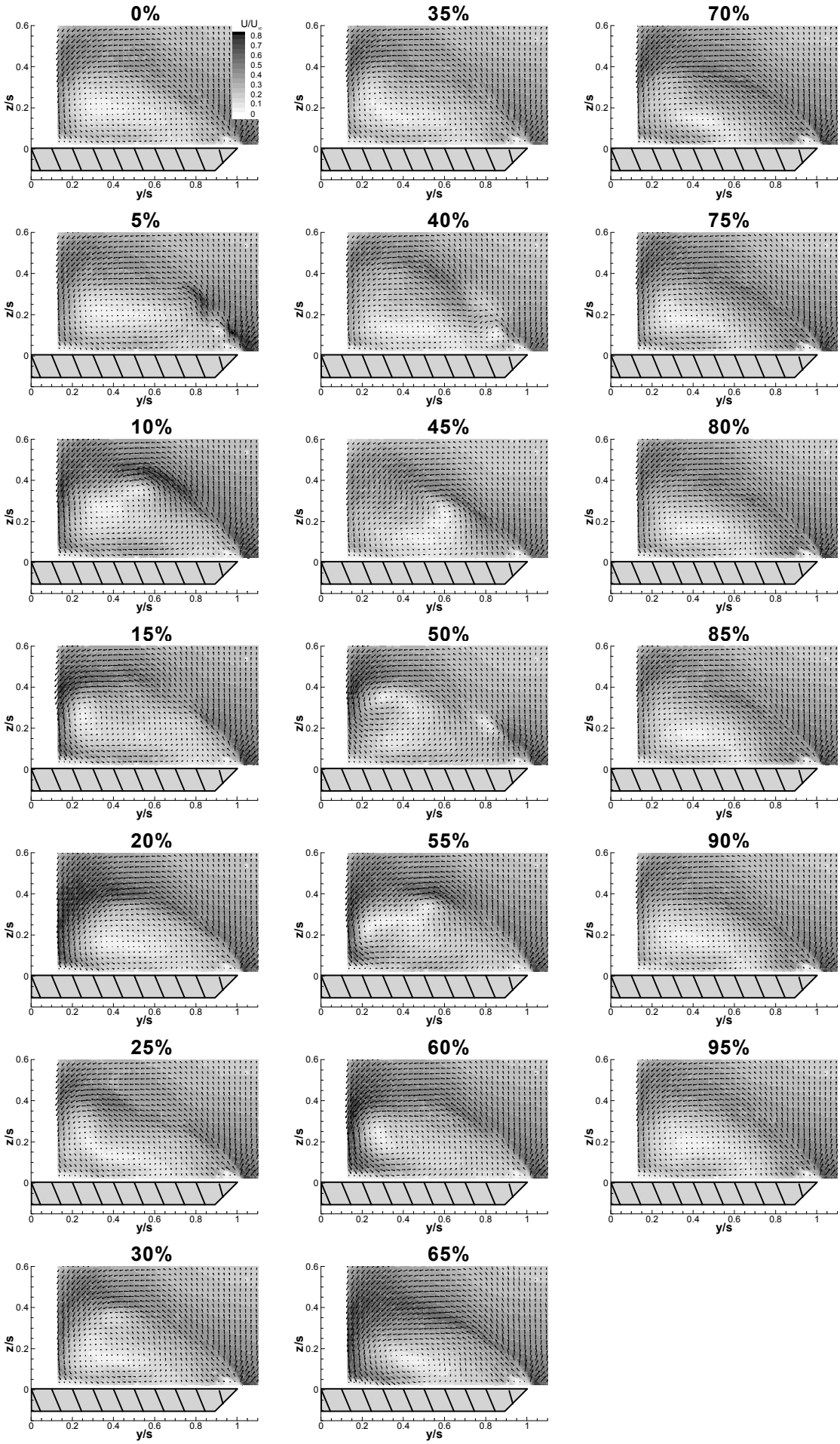

Figure 5-13 Magnitude of phase-averaged cross-flow velocity, x/c=0.48, α=30°, C_μ=0.4%, St=0.25.

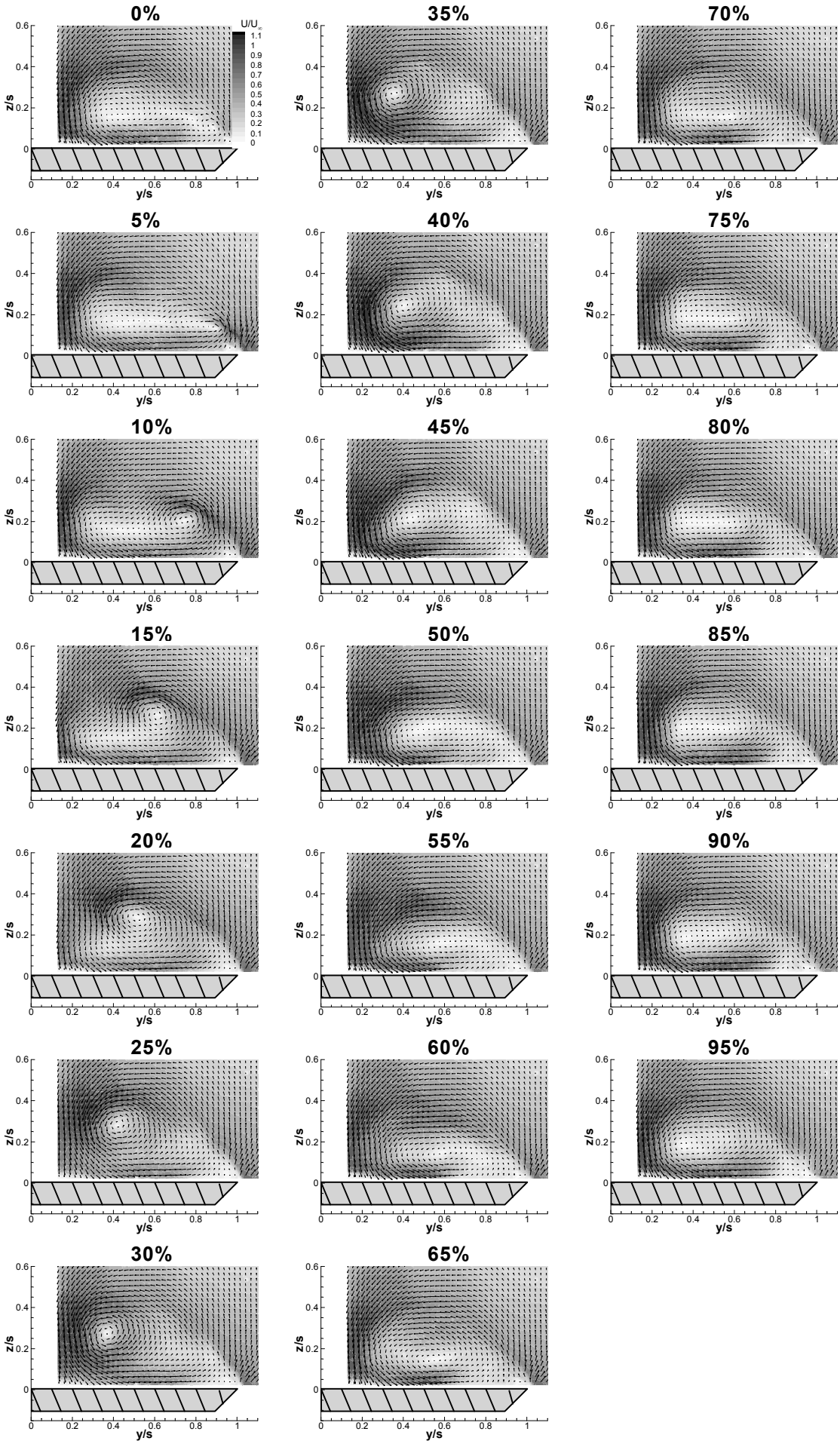

Figure 5-14 Magnitude of phase-averaged cross-flow velocity, x/c=0.48, α=30°, C_μ=0.4%, St=0.75.

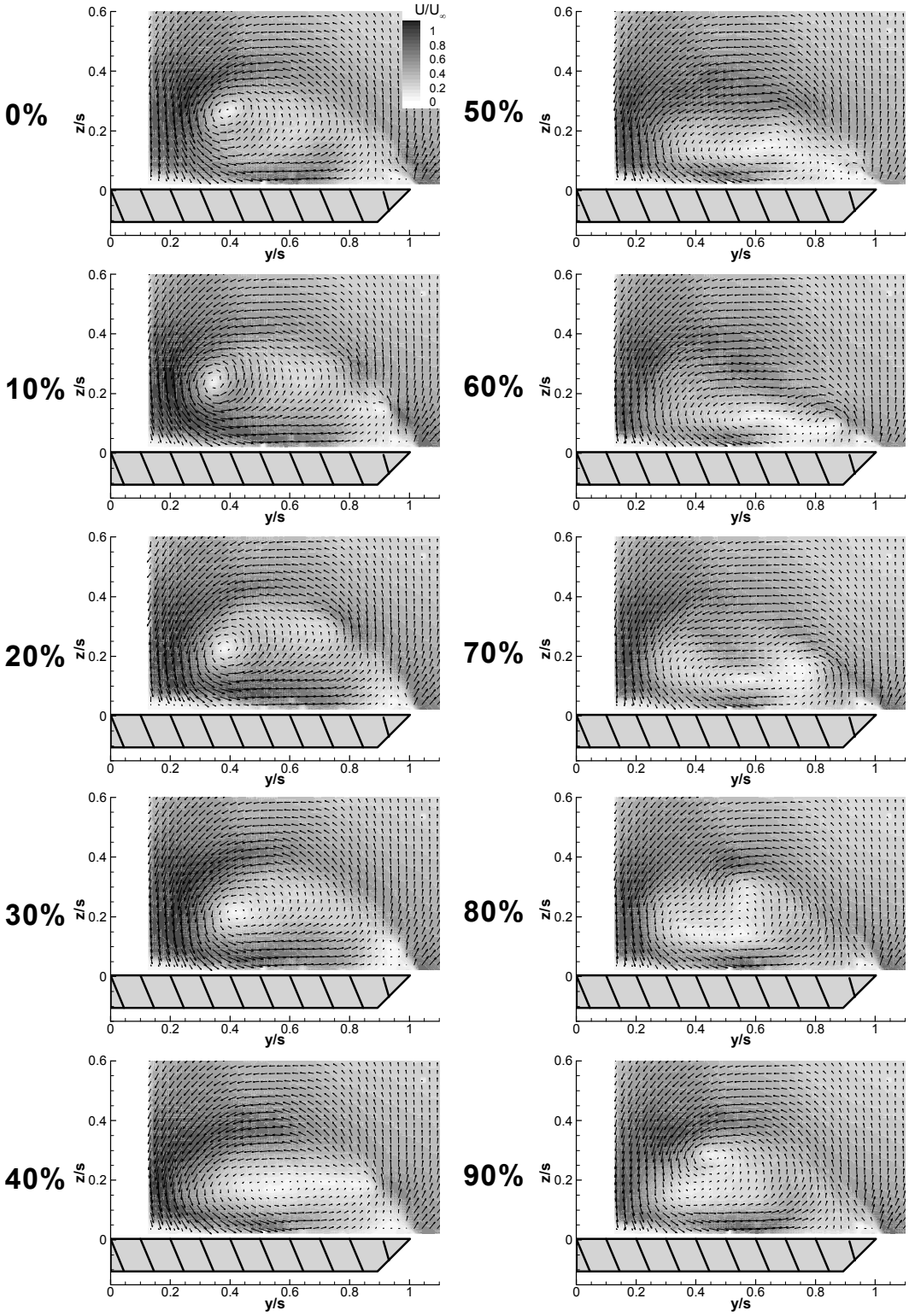

Figure 5-15 Magnitude of phase-averaged cross-flow velocity, x/c=0.48, α=30°, C_μ=0.4%, St=1.25.

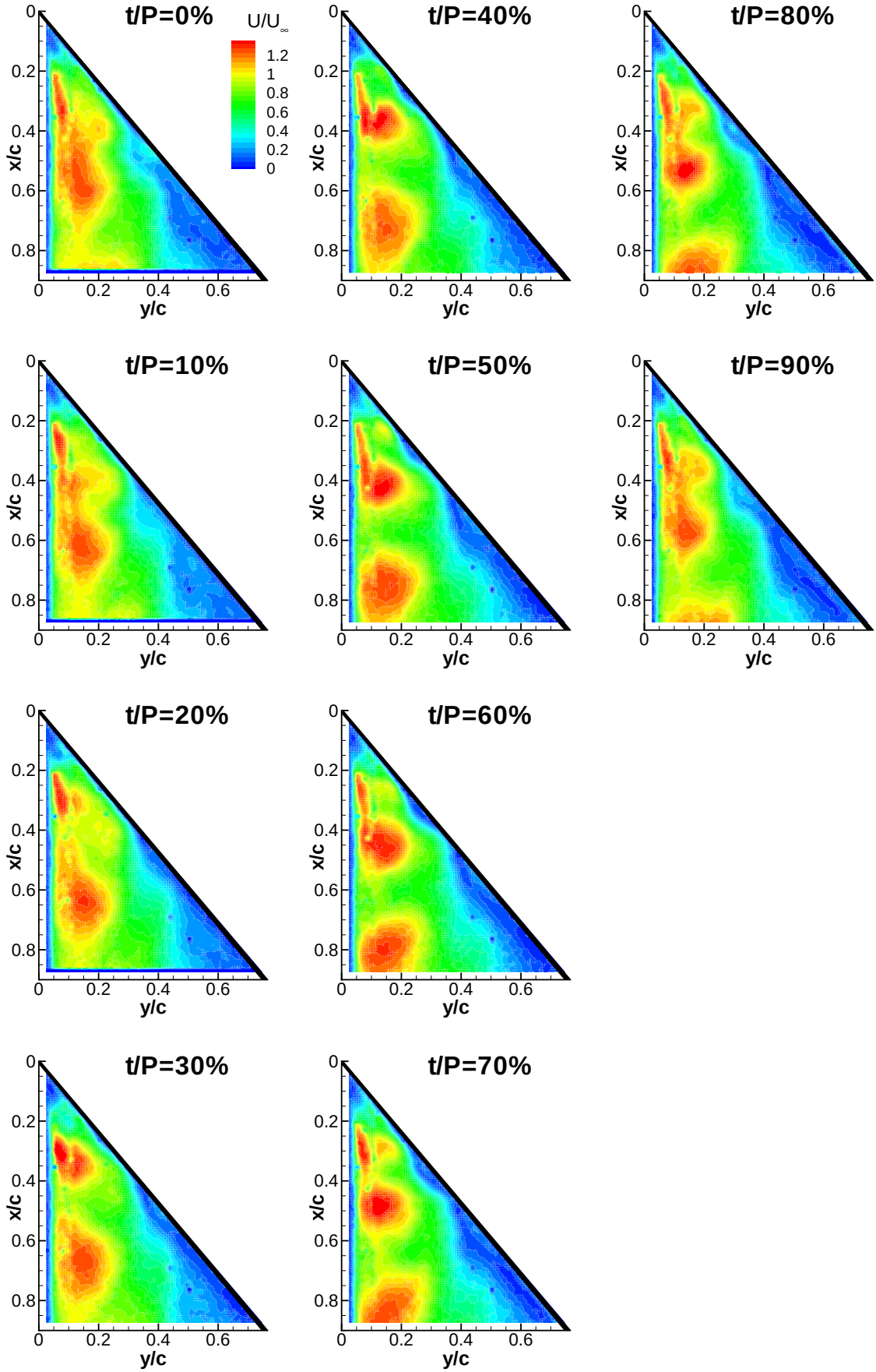

Figure 5-16 Magnitude of phase-averaged near surface velocity, α=30°, C_μ=0.4%, St=1.5.

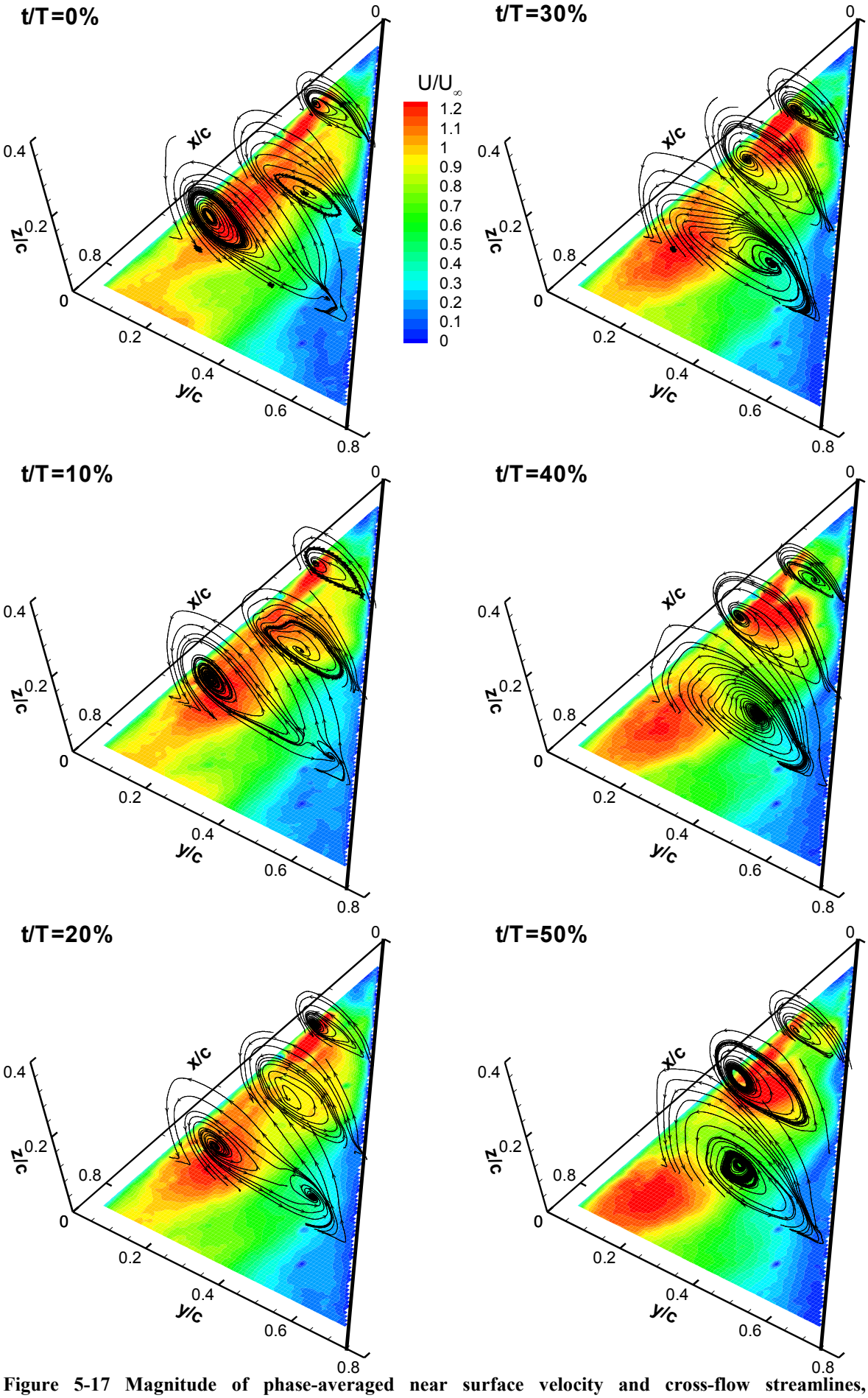

Figure 5-17 Magnitude of phase-averaged near surface velocity and cross-flow streamlines, x/c=0.28,0.48,0.68, α=30°, C_μ=0.4%, St=1.5.

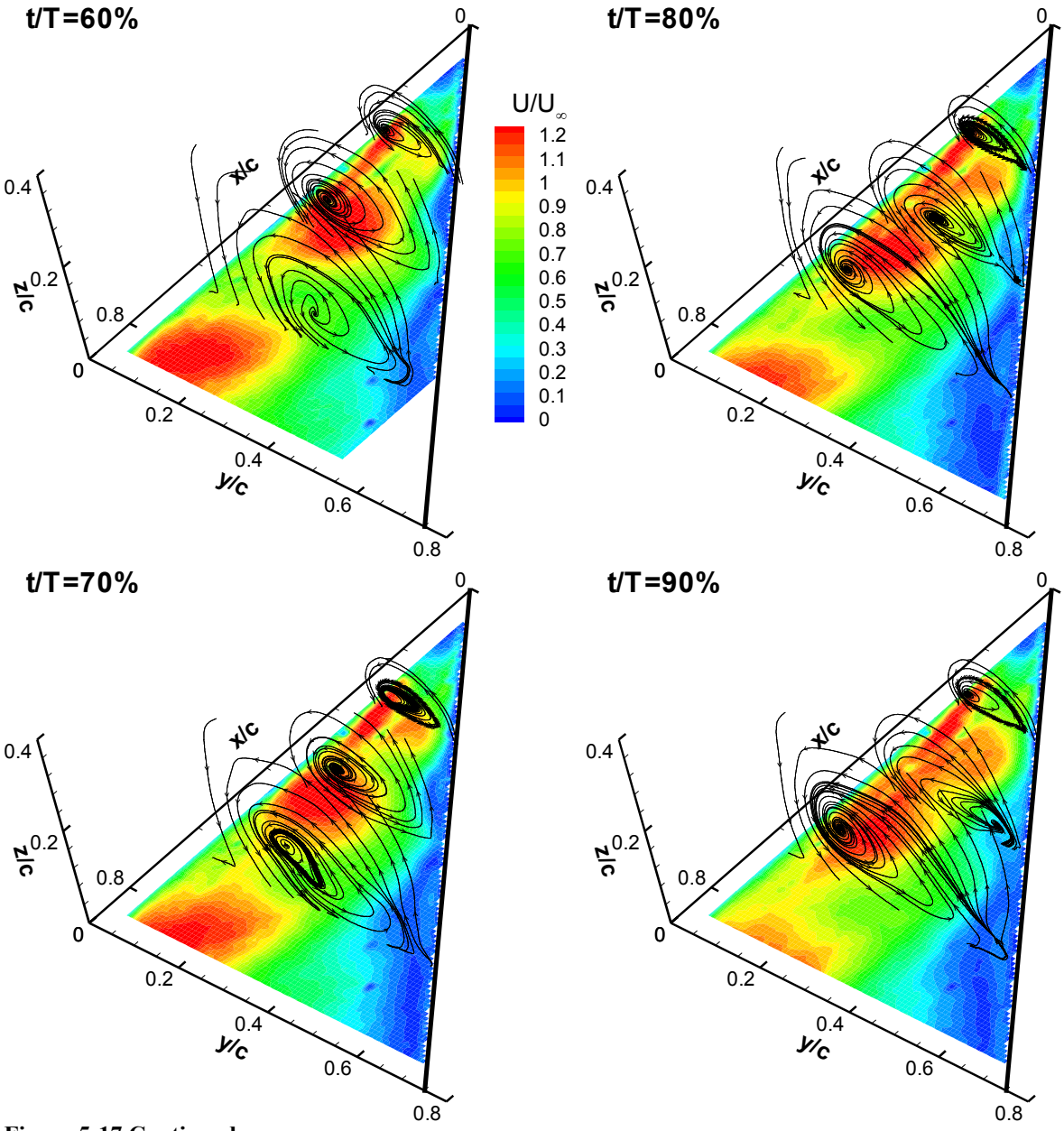

Figure 5-17 Continued

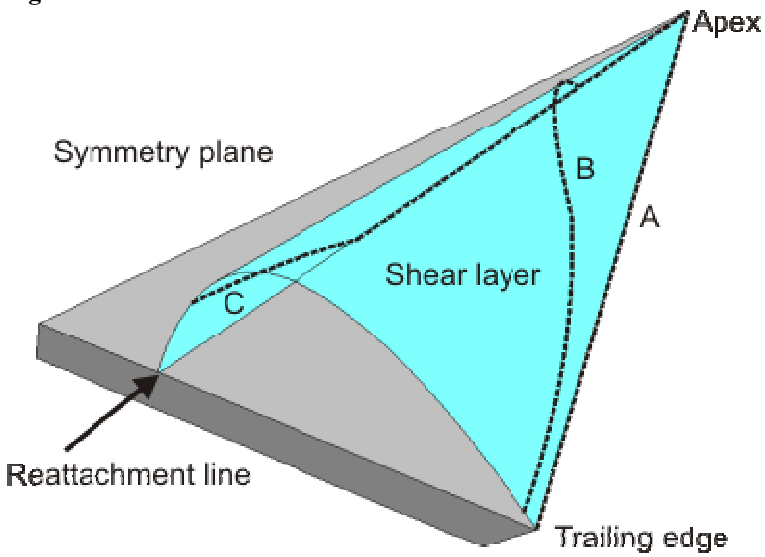

Figure 5-18 Sketch of the reattaching shear layer and the wrapping of the perturbation. The dashed lines indicate the perturbation axis. A) Perturbation forms at the leading edge. B) Perturbation is wrapped around the main vortical structure. C) Perturbation reattached to the wings surface and feeds the main vortical region.

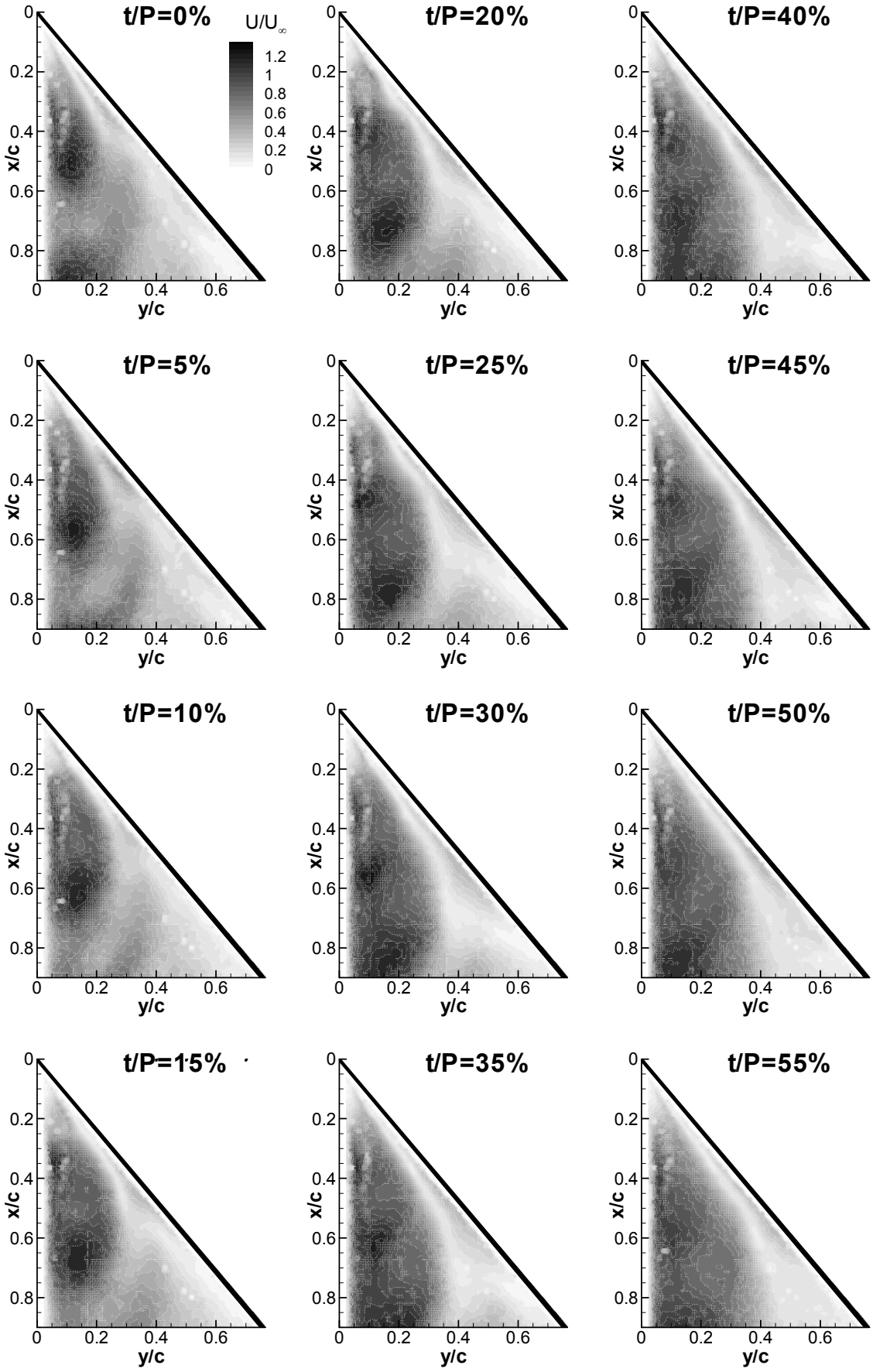

Figure 5-19 Magnitude of phase-averaged near surface velocity, α=30°, C_μ=0.4%, St=0.5.

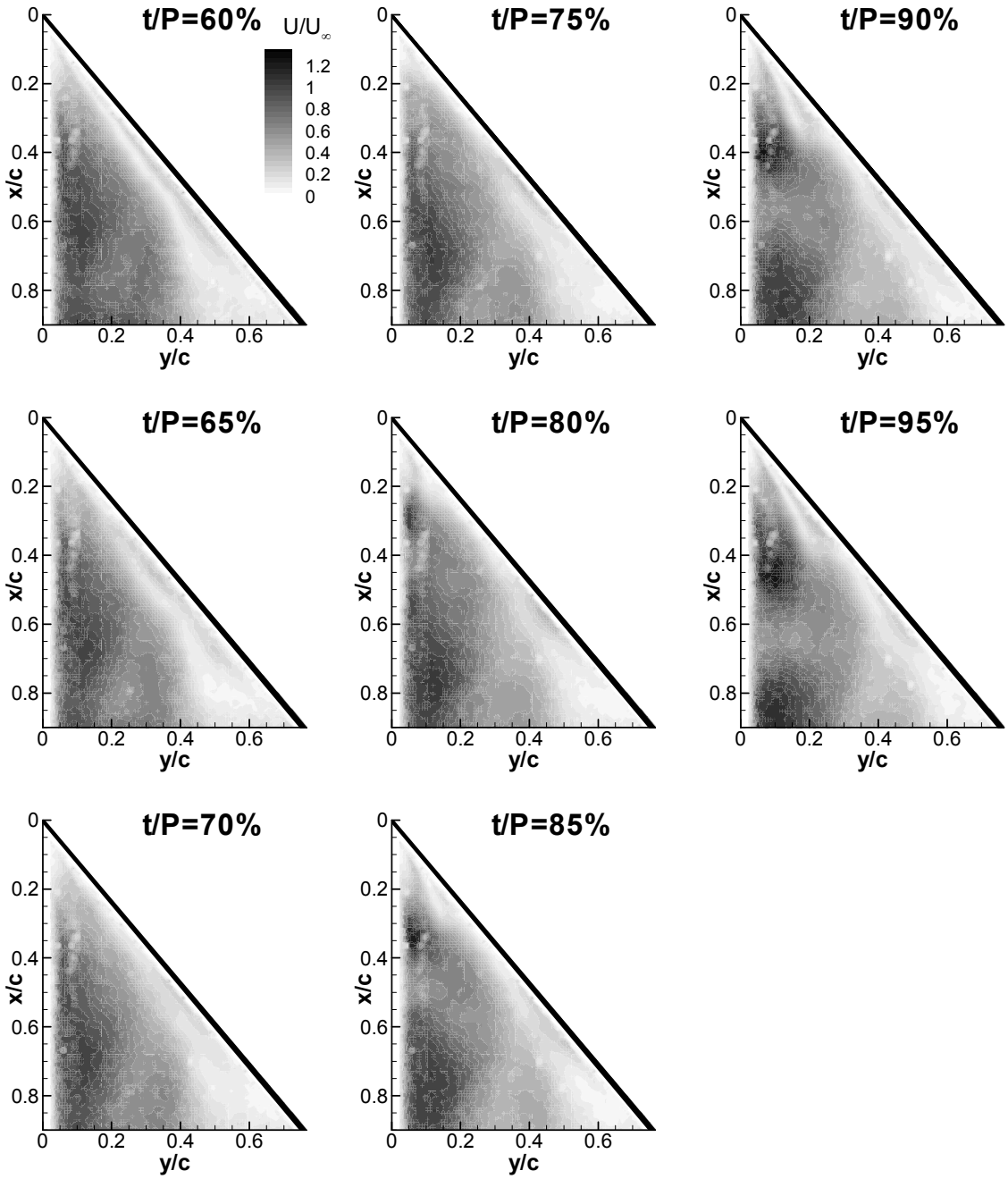

Figure 5-19 Continued

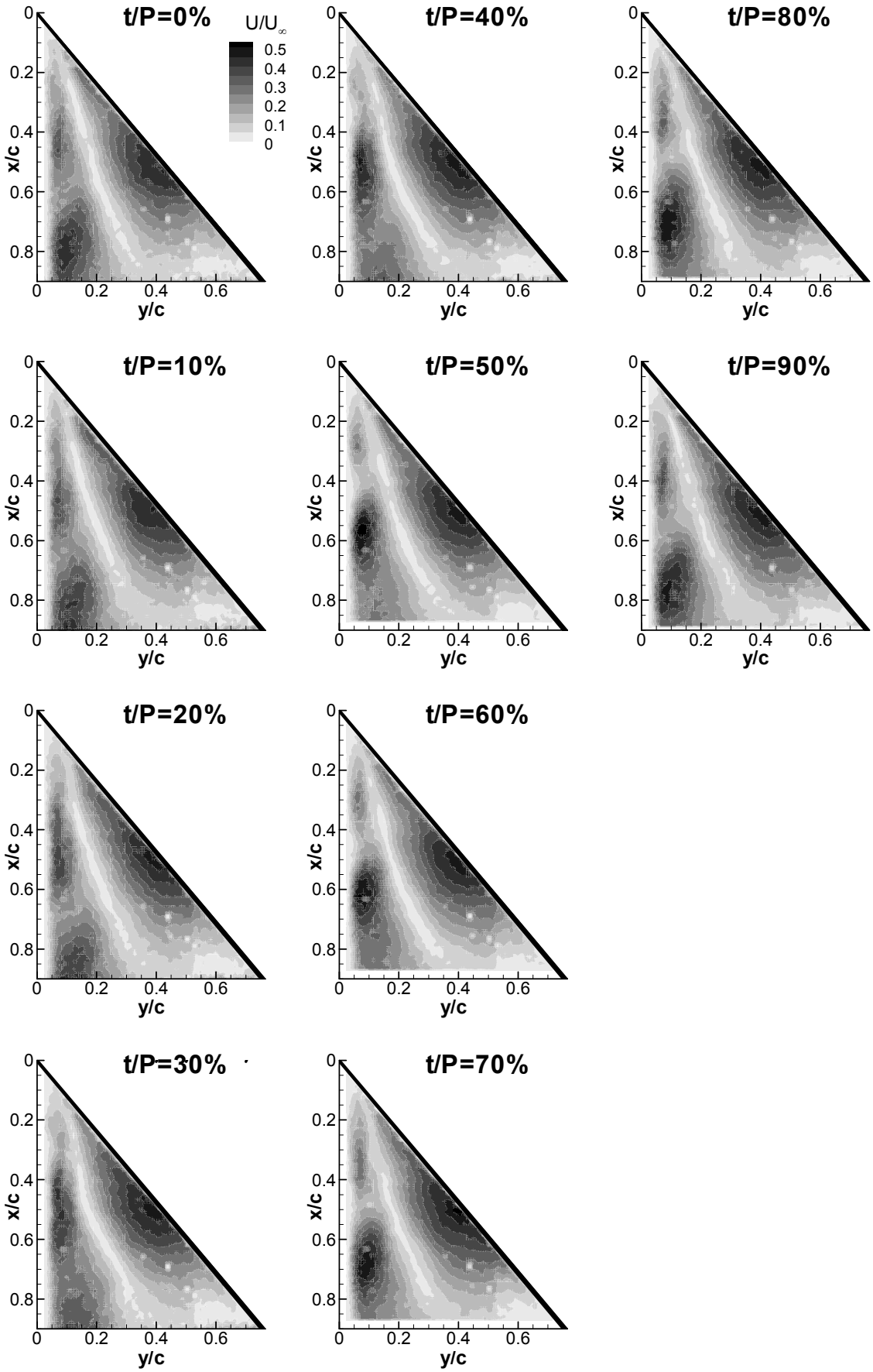

Figure 5-20 Magnitude of phase-averaged near surface velocity, α=30°, C_μ=0.4%, St=1.0.

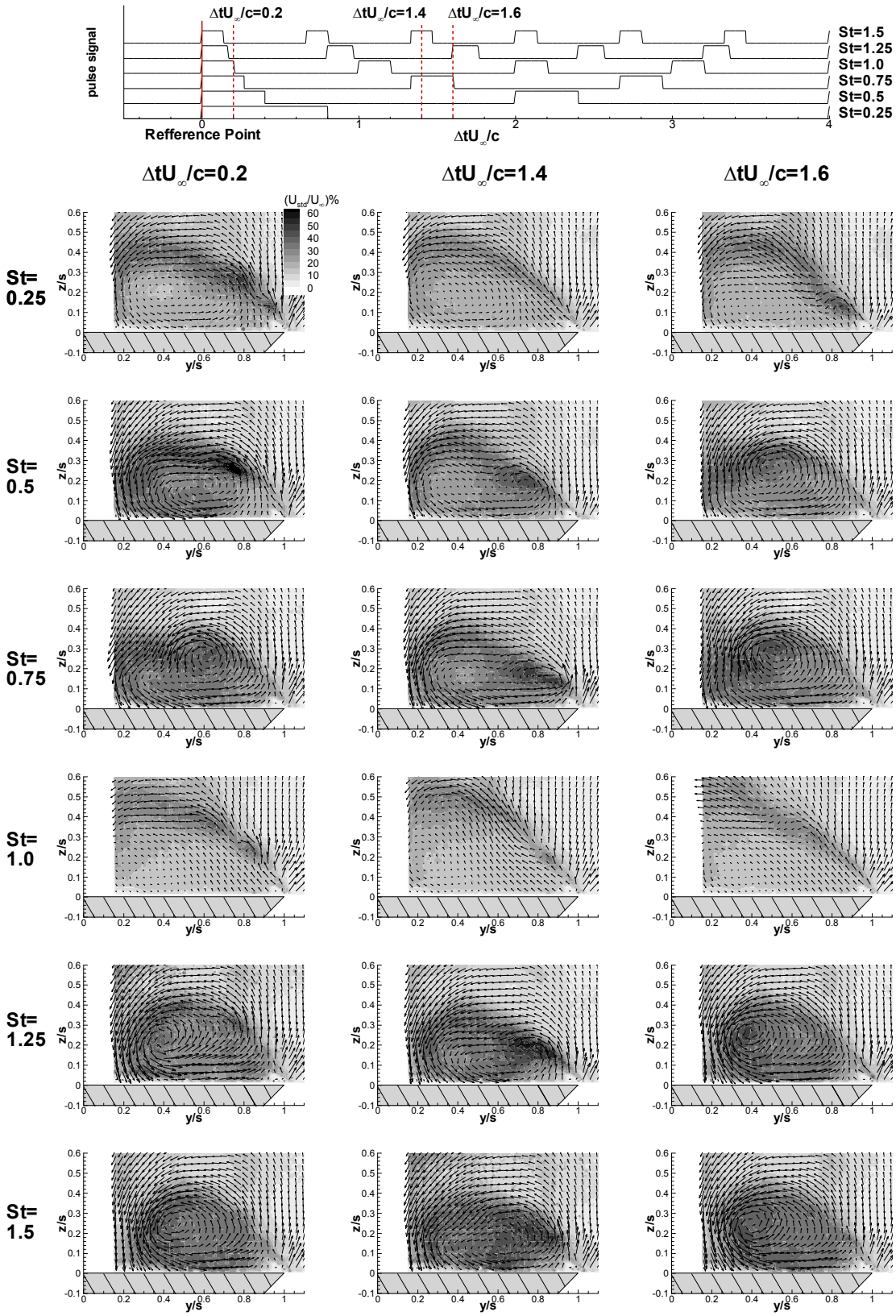

Figure 5-21 Comparison of the phase-averaged cross-flow turbulence intensity and velocity vectors for unsteady blowing at a range of Strouhal numbers at different points in the pulsing cycle, x/c=0.48, α=30°, C_μ=0.4%.

Chapter 6 Transient PIV measurements

For the practical implication of unsteady blowing on a nonslender delta wing platform, an important consideration is the transient response of the flow to the initiation of blowing. This element of the research was aimed at finding the time taken for stalled flow to become reattached flow after the initiation of unsteady blowing.

High frame rate PIV experiments were conducted to record the transient response of the cross-flow and near surface flow fields to unsteady blowing. The PIV frame rate of all the data presented is 1500Hz (1500 pairs of images per second), significantly higher than the highest pulsing frequency presented of 112.5Hz. The high frame rate allowed the investigation of the transient response of the flow to the initiation of unsteady blowing. To validate the high frame rate data, the mean of the high frame rate cross-flow PIV measurements is shown in Figure 6-1. The mean of the high frame rate near surface PIV measurements is shown in Figure 6-2. The data compares well with the mean flow cases, and there is good agreement between the two sets of results taken on the two different PIV systems.

Circulation of the region indicated in Figure 6-3 was calculated using the line integral method. Figure 6-3 shows the response of the level of circulation in a cross flow plane at x/c=0.48 to the initiation of unsteady blowing at t/T=0. For the no blowing case, $\Gamma U_\infty/c$ is centred around -0.3. The value undergoes fluctuations with time, but they are small compared to the cases where flow control is applied. Unsteady blowing at Strouhal numbers where the research presented in previous chapters indicated a high level of reattachment had a significant effect on the level of circulation. For St=0.5 and St=1.5, the response to the introduction of unsteady blowing was an increase in the magnitude of the circulation level, from $\Gamma U_\infty/c$ =-0.3 to approximately $\Gamma U_\infty/c$ =-1.2. This is an indication that reattachment has occurred. The magnitude of circulation increased between $0<tU_\infty/c<7.5$ for the St=0.5 case and between $0<tU_\infty/c<10$ for the St=1.5 case, after which the mean level remained approximately constant, with circulation fluctuating about $\Gamma U_\infty/c \approx -1.2$. This highlights that the response of the flow field to unsteady blowing occurs over a short time period. In practical terms, the free stream flow only has to cover a distance of 7.5 times the wing's chord before full reattachment has occurred. As expected, the circulation levels for unsteady blowing at St=1.0 show a weak response. Although the level of circulation undergoes significant oscillations, there is not a significant change in the magnitude of the mean circulation levels. The fluctuation of circulation levels shown in Figure 6-3 indicate that some vorticity is entering and leaving the selected region. The level of fluctuations in circulation would probably be lower if the measured region were closer to the wing's surface and centreline. Significant reflection noise prevents accurate measurements in these areas, and the measured region represents the closest point to the wing's surface and splitter plate where data of acceptable quality could be obtained. Figure 6-4 shows the power spectrum of the circulation data presented in Figure 6-3. The data indicating the initial response to unsteady blowing has been removed. For all cases, the fluctuations show a high level of periodicity. In particular the St=1.5 case shows a strong spectral peak at fc/U_∞=1.5 (the forcing frequency), and a

very low level of higher order harmonics. The St=1.0 case shows a fundamental peak at fc/U_∞=1, and higher harmonics of a similar magnitude at fc/U_∞=2, 3 and 4. The dominant spectral peak in the St=0.5 case is at fc/U_∞=1.5. A slightly smaller peak can be seen at fc/U_∞=0.5 (the forcing frequency). Spectral peaks can also be seen at fc/U_∞=2.0 and fc/U_∞=0.2. There are no other significant higher order harmonics present. The fact that the fundamental frequency is not the dominant frequency is interesting, and probably due to the secondary perturbation present in the shear layer. It would be expected that if two equally spaced perturbations (one at t/T=0 and one at t/T=0.5) were present in a cycle, there would be significant spectral power at fc/U_∞=1.0. However the time spacing between each perturbation in the cycle is significant in calculating the spectral power. The phase locked measurements of the St=0.5 case showed two perturbations in the shear layer. The induced perturbation occurred at t/T=0. The secondary perturbation occurred at t/T=0.65, as shown in Figure 5-8. It is this uneven spacing, at approximately two thirds of the period which, causes the spectral peak at fc/U_∞=1.5. This indicates that the secondary perturbation is also present in the high frame rate data for the St=0.5 case.

A useful analysis technique is to look at the transient response of the components of velocity for specific points in the flow, such as the reattachment location, and near the wing's surface. The left hand side of Figure 6-5 shows the vertical velocity component for a point in the region of reattachment. By comparing mean flow PIV results of the no blowing case and a case where the shear layer has reattached in Figure 6-1, the vertical component of velocity in the region of reattachment looks to be a good indication that reattachment has occurred. Oscillations in the velocity are also expected as perturbations from the leading edge reach the reattachment region. With no flow control it is reasonable to say this point is below the separated shear layer, and the mean flow is very low, as reflected by the low mean velocity for the no blowing case. There do seem to be some lower velocity peaks, which may indicate the natural formation of structures in the shear layer, as documented by Gad-el-Hak [21] , however they do not lead to reattachment. St=1.0 is an interesting case for this point in the reattachment region, as consistent with the phase locked measurements, there is a large fluctuation of velocity in this region. Because only weak reattachment occurs, the mean negative vertical velocity component is only in the order of half the freestream velocity. However, particularly high velocity fluctuations can be seen for the St=1.0 case, which are attributed to high velocity perturbations that move through the measurement point. Again, the St=0.5 case and the St=1.5 case show strong signs of a reattached shear layer after the introduction of unsteady blowing, with the mean negative vertical velocity component approaching a level close to the freestream velocity. The velocity appears to undergo periodic oscillations due to the shear layer perturbations.

The right hand side of Figure 6-5 shows the horizontal component of flow near the wing's surface. As expected, the no blowing case has a very low velocity in this region, and there are almost no fluctuations. With the wing in deep stall, there is very little cross-flow movement of fluid near the wing's surface. High spanwise velocities would indicate the presence of a region of vortical flow

above the measurement point, a good indication that the shear layer has reattached. For the St=0.5 and St=1.5 cases, there is a clear increase in the horizontal component of velocity. When comparing the time constants between the two measurement points (in the reattachment region, and near the surface), the mean vertical velocity in the reattachment region appears to stabilise by $tU_\infty/c=5$. By contrast, the mean horizontal velocity near the wing's surface stabilises around $7<tU_\infty/c<10$. This indicates that the time constant for the velocity, in the flow field, to reach its mean flow state varies at different locations. If the shear layer reattaches gradually over multiple periods, as is indicated by the velocity fluctuations, it is not surprising that the velocity in the reattachment region reaches its maximum before the vortical flow is fully developed.

The power spectrum for the vertical velocity of a point in the reattachment region is shown on the left hand side of Figure 6-6. Similar to the power spectrum for the circulation level, clear spectral peaks are seen at the forcing frequency and higher harmonics. The St=0.5 case shows a more dominant spectral peak at $fc/U_\infty=1.5$, reasons for which have been discussed regarding the circulation spectrum. For the St=1.0 case, the strong spectral peak at $fc/U_\infty=2.0$, similar in magnitude to that of $fc/U_\infty=1.0$ may be a result of the secondary perturbation shown in the phase locked measurements in Figure 5-10.

The power spectrum of the horizontal flow below the main vortex structure is shown on the right hand side of Figure 6-6. The main contrast to the spectrum of the oscillations present in the reattachment region is that the St=1.0 case shows no significant spectral peaks. Because the recirculation region is very weak for St=1.0, the level of velocity fluctuations in this area is lower, and not concentrated at any specific frequency. This is consistent with the measurements outlining the cyclic nature of the centre of the vortex swirl pattern, presented in Figure 5-12, which showed that the centre of the vortical flow region does not move significantly in a periodic sense. Also, the centre of the vortical region is further inboard for St=1.0 when compared to the cases with fully reattached flow, and the effects of the perturbation are not seen in the horizontal velocity power spectrum at this measurement point.

The velocity power spectrum for the vertical component of velocity at a point very close to the leading edge is shown in Figure 6-7. For all cases of unsteady blowing, there is a dominant spectral peak at the fundamental forcing frequency, and lower magnitude higher harmonics. For the St=0.5 case, this is in contrast to the spectral data presented in Figure 6-4 and Figure 6-6. For the St=0.5 case the spectral peak at $fc/U_\infty=1.5$ is lower in magnitude than the spectral peaks at $fc/U_\infty=0.5$ and $fc/U_\infty=1.0$, which is a more typical magnitude relative to the fundamental (St=0.5) spectral peak when compared to the power spectrum for a signal with a similar shape to a square wave. This indicates that the flow close to the excitation point is not significantly affected by the secondary perturbation.

The time constants for reattachment derived from the near surface flow measurements were similar to those derived from the cross-flow measurements. Figure 6-8 shows the chordwise and spanwise

velocity components at a position in the high velocity reattachment region in the near surface plane. When unsteady blowing is introduced, the cases with Strouhal numbers of St=0.5, St=0.75 and St=1.5 show a significant increase in the magnitude of both the spanwise and chordwise flow. The St=0.75 case has not been presented previously in this chapter for high frame rate tests, but is included here to show that the response of the flow to unsteady blowing at St=0.75 is similar to that of the St=1.5 and St=0.5 case. As expected, the St=1.0 case showed very little response to the introduction of unsteady blowing.

The transient response of the velocity components of an additional point, outboard and downstream of the point discussed in Figure 6-8 are shown in Figure 6-9. When examining the response of the chordwise velocity component to unsteady blowing for the cases which indicate reattachment, it seems there is a slight delay in response of $tU_\infty/c\approx3$, where the mean velocity remains $u/U_\infty\approx0.2$. Figure 6-8 does not show such a delay, other than possibly a small delay for the St=1.5 case. This indicates that when reattachment does occur, it occurs at the centreline of the wing, and then the region of high velocity flow grows in the outboard direction. Another interesting point to note from this figure is the initial negative component of the spanwise velocity between $tU_\infty/c=0$ and $tU_\infty/c=3$ for the cases where reattachment occurs. The origin of this reversed flow can be seen by looking at the development of velocity vector fields over time. When flow control is initiated, a high chordwise velocity develops near the wing's centreline. This interacts with the rest of the flow field. Small recirculating regions form at the boundary between the fast and slow moving fluid, and at certain points, the spanwise flow in the surrounding region is temporarily directed towards the wing's centreline. As the flow develops to a more steady state case, the high velocity region covers more of the wing, and the spanwise velocity is directed outboard. This is the origin of the aforementioned spanwise flow towards the wing's centreline.

So far, the transient response to the initiation of flow control has been presented. The transient response of the flow when flow control was turned off was also briefly studied. The chordwise velocity component for a Strouhal number of St=1.5, at x/c=0.25 and y/c=0.05 is shown in Figure 6-10. For this case, the flow control was tuned on, time was given for the flow field to stabilise, and then the unsteady blowing was stopped. The dashed lines on the figure indicate the points at which flow control was turned on and turned of. As expected, when unsteady blowing is turned off, the flow reverts back to its stalled, no blowing state. An interesting point to note is that the time constant for the flow to develop is significantly less than the time constant for the flow to revert back to the no blowing case. For this measurement point, the mean time for the chordwise velocity to reach its mean steady state is $tU_\infty/c=4.4$. When flow control is removed it takes $tU_\infty/c=11.7$ for the velocity to revert back to the no blowing case. These values are expected to vary with the location of the measurement point, but are indicative of the time difference between the flow control on and off cases. This indicates that the time taken for the wing to revert back to stalled flow from reattached flow (under unsteady blowing) is greater than the time taken for reattached flow to develop.

A time constant was developed for each case by taking the mean of the time constants for a range of points on the wings surface. Each point was analysed by taking a 9 point sample moving average to help identify the location where flow can said to be fully attached. This process and a sample of the results processed with the sample moving average method are shown in Figure 6-11. A 9 point moving average was sufficient to smooth the fluctuations in the velocity data, allowing a clear identification of the time constant, but the use of 9 points (4 backward and 4 forward) did not alter the time constant significantly. The derived time constants are shown in Table 6-1. The St=1.0 case has been left out, as flow did not reattach fully, and a time constant could not be ascertained. For the three cases presented (St=0.5, St=0.75, St=1.5), all the time constants are of a similar magnitude, with the St=0.75 case appearing to have the lowest response time to the initiation of flow control. The St=1.5 case has the slowest response to flow control of the three cases shown, but the delay between the cases is relatively small.

Specific instances in the development of the flow field have been selected and are displayed in Figure 6-12. Instance A, at $tU_\infty/c=4$ represents a case as the flow reattached. Instance B, at $tU_\infty/c=8$ represents a case just after reattachment has occurred, and instance C, at $tU_\infty/c=12$ represents a case significantly after reattachment has occurred. Instantaneous vector fields for different instances in the reattachment process are compared in Figure 6-13. As expected, at $tU_\infty/c=0$ the flow is stalled. At $tU_\infty/c=4$, for the cases where reattachment occurs, the shear layer can be seen to be reattaching near the wing's centreline. For all cases, small vortical structures can be seen in the shear layer which has wrapped around and attached to the wing's surface. It is difficult to state whether the vortices are natural instabilities present in the shear layer or induced vortical structures. The high velocities associated with the shear layer are not present close to the surface outboard of y/s=0.2, and there is no region of high spanwise velocity near the wings surface. The St=1.0 case has developed a weak level of reattachment, but does not develop any further past this point. By $tU_\infty/c=8$, the flow has reattached, as indicated by the time constants in Table 6-1. There now is a significant region of high spanwise velocity near to the wing's surface. However, when it is compared to $tU_\infty/c=12$, it appears that the region of high spanwise velocity near the wing's surface is slightly larger and extends to the leading edge. The region of low velocity associated with the centre of the vortical flow region is also slightly smaller. This indicates that a small amount of further development past the values indicated by the time constants is possible, but it may not significantly affect the near surface plane from which they were derived, and probably has little effect on the forces over the wing as the flow has definitely reattached at $tU_\infty/c=8$. Another possibility is that the time constants which were quoted previously were the average of points over the whole wing, and may not be indicative of the flow at x/c=0.48, as reattachment may occur at lower time constants towards the apex. However examining the surface flow data presented in Figure 6-14 indicates no significant difference in the flow field between $tU_\infty/c=8$ and $tU_\infty/c=12$ for St=0.5 and St=1.5. The difference could also simply be due to the high level of variability of the

flow with time. As these are instantaneous vector fields, they only show the flow at one point in time, and do not necessarily reflect the flow field immediately before or after that point in time.

Instantaneous near surface PIV vector fields corresponding to the same time instances discussed above are shown in Figure 6-14. Similar to the cross-flow case, at $tU_\infty/c=0$ the flow is stalled, dominated by low velocities and large regions of reversed flow. As time advances, axial flow begins to develop near the wing centreline. At $tU_\infty/c=4$ all cases show reversed flow along the leading edge, with partial reattachment near the centreline. By $tU_\infty/c=8$, the flow has reattached and a high velocity region dominates the wing for the St=0.5 and St=1.5 cases. As with the cross-flow instantaneous vector fields, the St=1.0 case does not develop beyond $tU_\infty/c=4$. For the St=0.5 and the St=1.5 case there is very little change in the extent of the high velocity region beyond $tU_\infty/c=8$. An interesting feature of the near surface flow is the presence of swirl patterns between the reattached flow and reversed flow at $tU_\infty/c=4$ and the reattached flow and leading edge at $tU_\infty/c=8$ and $tU_\infty/c=12$. At $tU_\infty/c=4$ for the St=0.5 case, there is a region of low velocity magnitude between the reattached and reversed flow. In this region, at x/c=0.46, y/c=0.26, a swirl pattern is seen. These patterns are seen to form in this region towards the apex as reattachment begins, and travel down towards the trailing edge. Swirl patterns are also seen near the leading edge for fully reattached flow, at x/c=0.4, y/c=0.3 for St=1.5 at $tU_\infty/c=8$, and at x/c=0.24, y/c=0.24 for St=0.5 at $tU_\infty/c=12$. The mean flow measurements shown in Figure 6-2 indicate a low velocity region along the leading edge, and this interacts with the reattached flow to form swirl patterns that travel along the leading edge towards the trailing edge.

Instantaneous cross-flow fields for a time span covering part of the reattachment process for unsteady blowing at St=0.5 are shown in Figure 6-15. It is worth noting that the flow is not two dimensional, and it can be difficult to follow specific structures in the fixed measurement plane. At $tU_\infty/c=2.14$ a small vortex can be seen near the leading edge, and associated with it is a region of higher velocity directed towards the wing's surface. Between $tU_\infty/c=2.14$ and $tU_\infty/c=2.35$ the region of high velocity grows and moves along the shear layer. At $tU_\infty/c=2.35$ the region begins to react with flow near the wing's centreline. The high velocity region then moves towards the wings surface and its direction changes towards the leading edge, forming the beginnings of the main vortical flow region described for the mean flow case. A small vortex of the same sign as the shear layer vortex can also be seen to form at the wings centreline at $tU_\infty/c=2.4$ and move down towards the wings surface between $tU_\infty/c=2.4$ and $tU_\infty/c=2.6$, as the high velocity region interacts with flow near the centreline. As this vortex gets closer to the wings surface, it appears to interact with the high velocity region of the flow directing it towards the leading edge of the wing. It appears that the free shear layer first interacts with the splitter plate at the wing's centreline. Vortices form as they interact, and encourage the flow downwards to the wing's surface. There are points in the flow where multiple discrete vortices appear to be present in the shear layer, indicating natural as well as induced vortices are present before reattachment.

The introduction of unsteady blowing appears to induce reattachment over multiple pulsing cycles. As pulsing begins the level of cross flow circulation increases gradually. The velocity magnitude of key points in the flow that indicate reattachment also increase gradually. In addition to this, in the cross flow plane, points near the wing's centreline show an earlier increase in velocity magnitude when compared to points near the wing's surface, further evidence that the flow reattaches over multiple pulsing cycles. The time constant for reattached flow can be as low as $tU_\infty/c=5$ for the St=0.75 case. Spectral analysis shows that at measurement points near the leading edge, the forcing frequency dominates velocity fluctuations. At points further along the shear layer, evidence of a secondary perturbation in the flow can be seen by an additional spectral peak in the St=0.5 case, supporting the evidence of a secondary perturbation discussed in chapter 5.

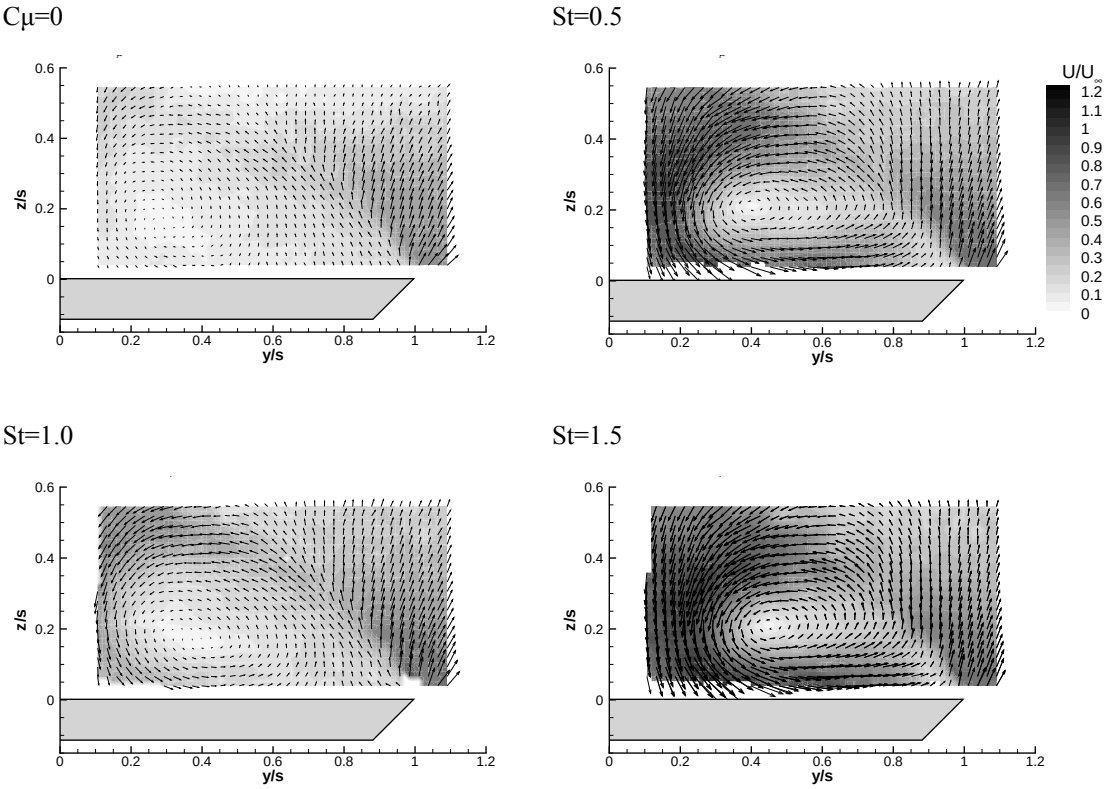

Figure 6-1 Mean flow of cross flow high frame rate measurements Cμ=0.44%, x/c=0.48.

Cμ=0

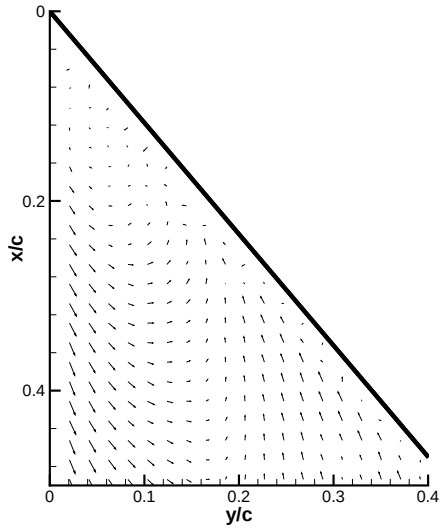

St=0.5

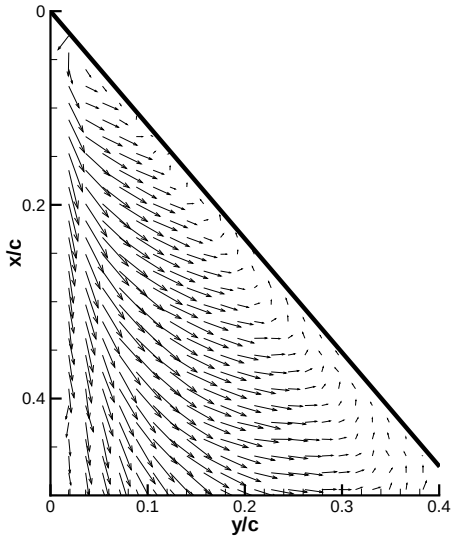

St=1.0

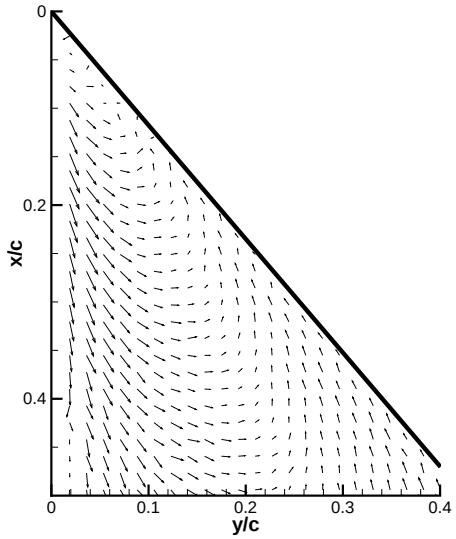

St=1.5

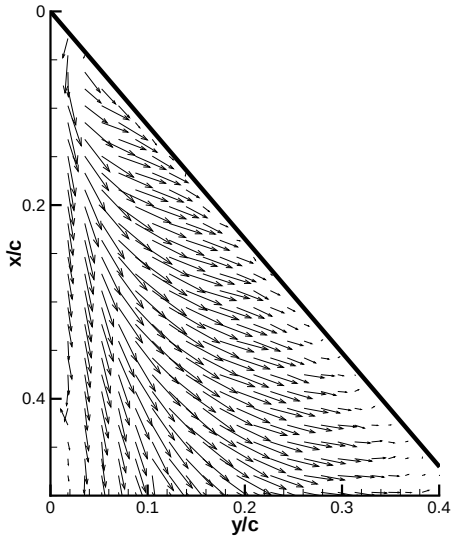

Figure 6-2 Mean flow of near surface high frame rate measurements Cμ=0.44%

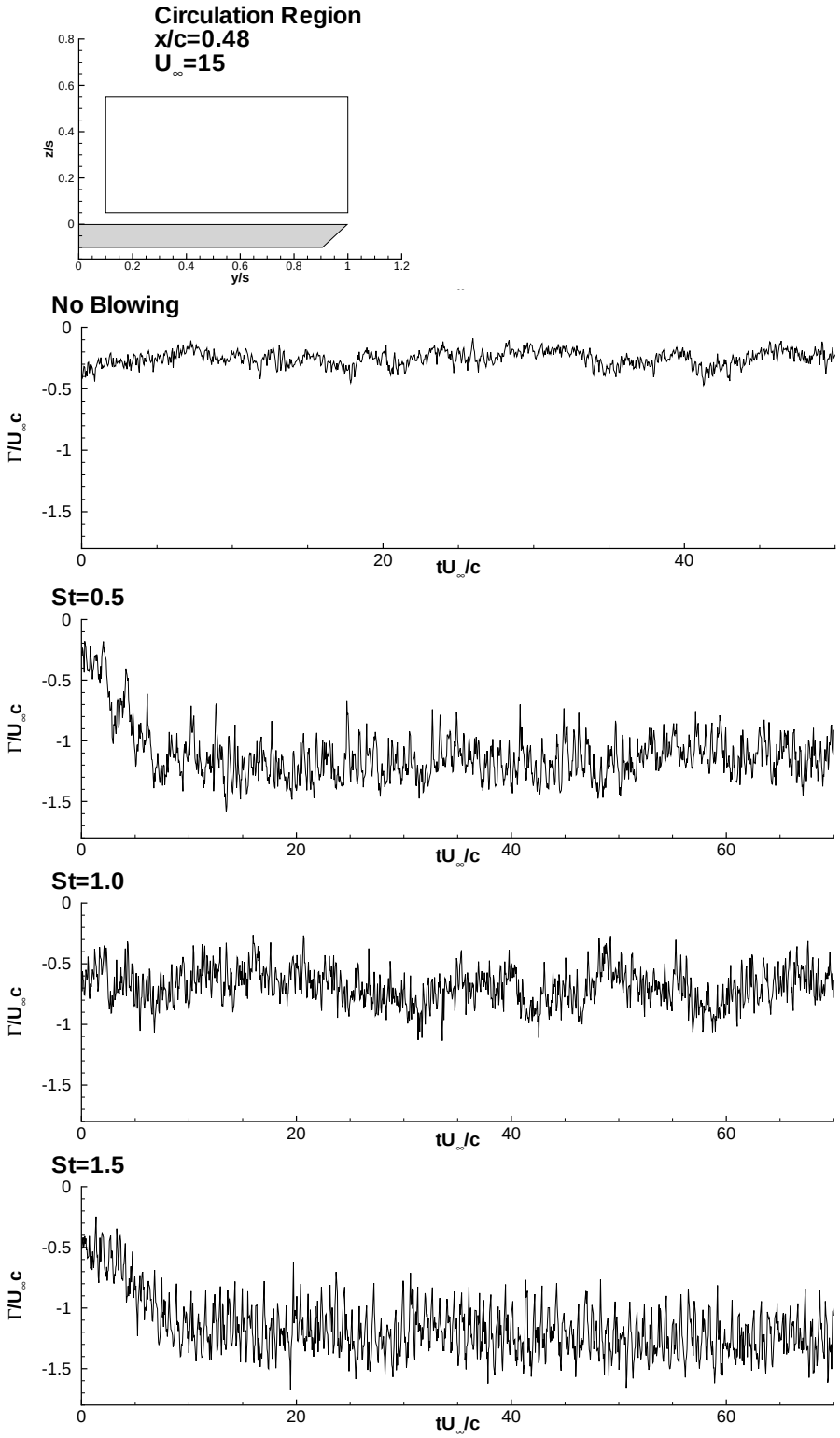

Figure 6-3 Cross-flow circulation at x/c=0.48, Cμ=0.44%

St=0.5 St=1.0 St=1.5

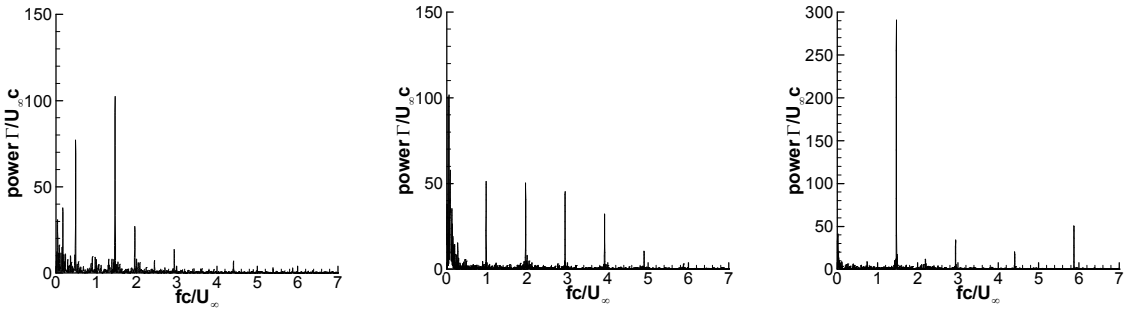

Figure 6-4 Power spectrum for cross-flow circulation at x/c=0.48, C_μ=0.44%

w/U∞ velocity component, near wing centreline

v/U∞ velocity component, near wing surface

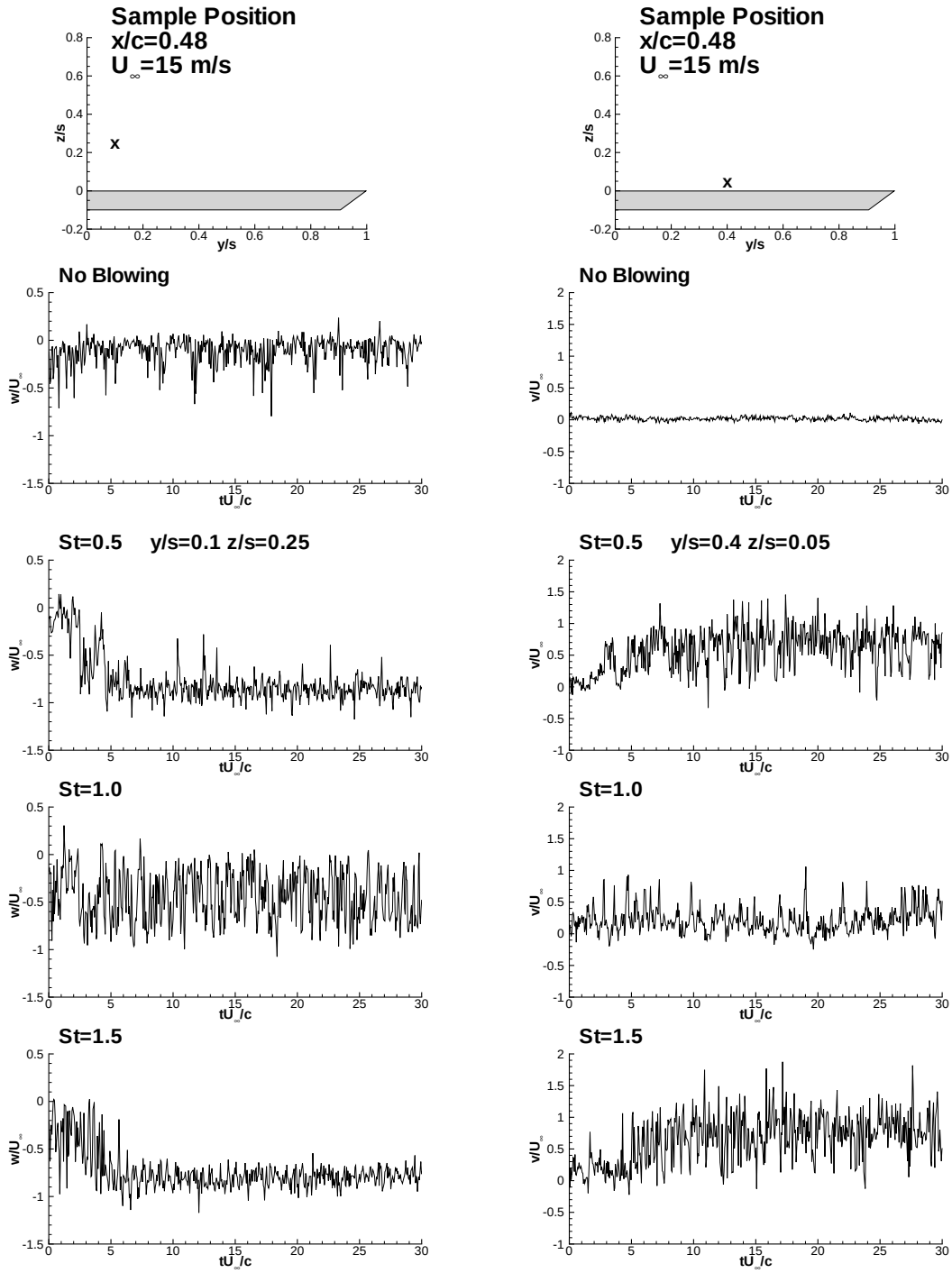

Figure 6-5 Cross-flow velocity components at x/c=0.48, Cμ=0.44%. Vertical component at y/s=0.1, z/s=0.25, and span wise component at y/s=0.4, z/s=0.05.

w/U∞ power spectrum, near wing centreline

v/U∞ power spectrum, near wing surface

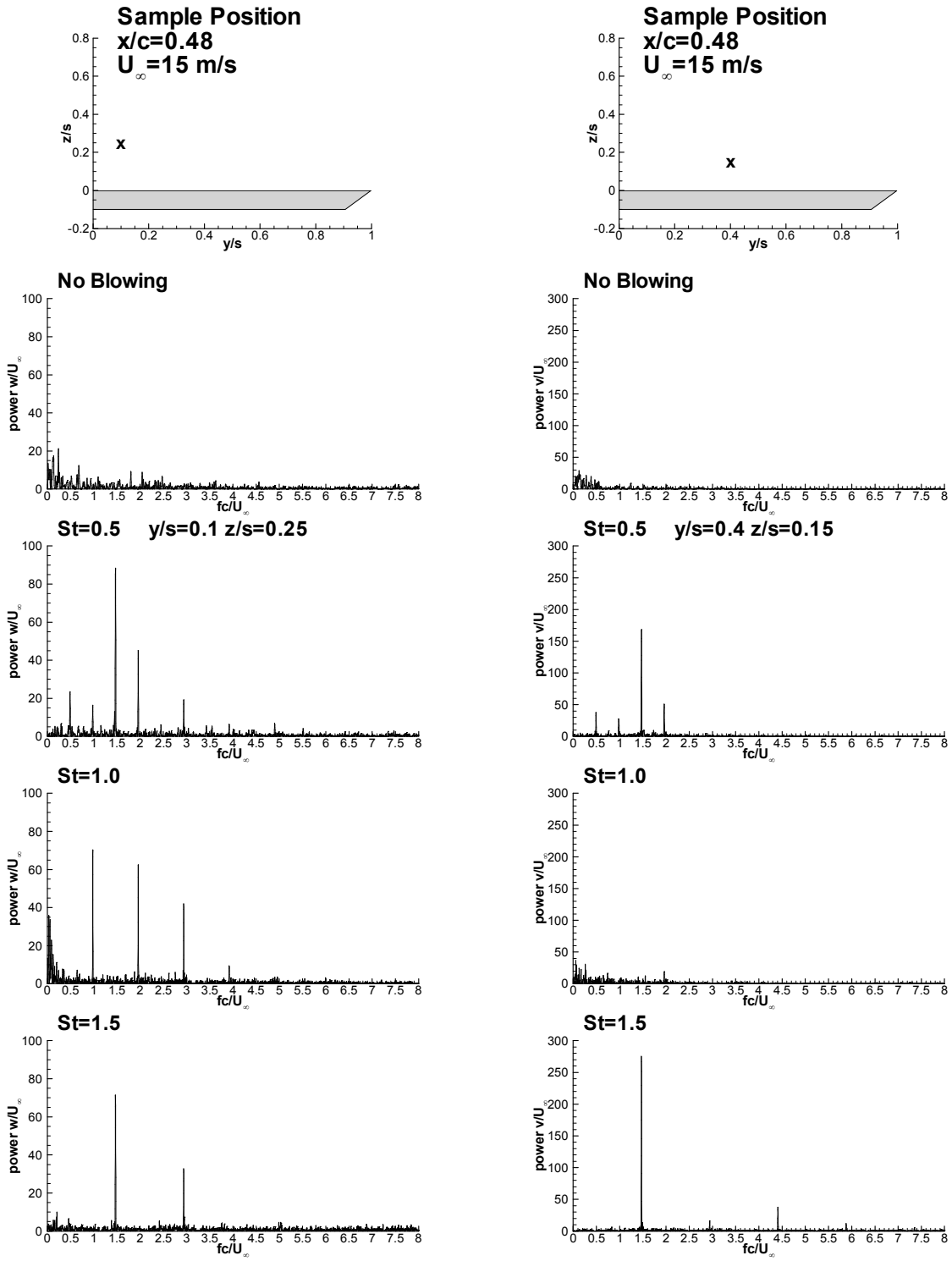

Figure 6-6 Power spectrum for cross-flow velocity components at x/c=0.48, C_μ=0.44%. Vertical component at y/s=0.1, z/s=0.25, and span wise component at y/s=0.4, z/s=0.15.

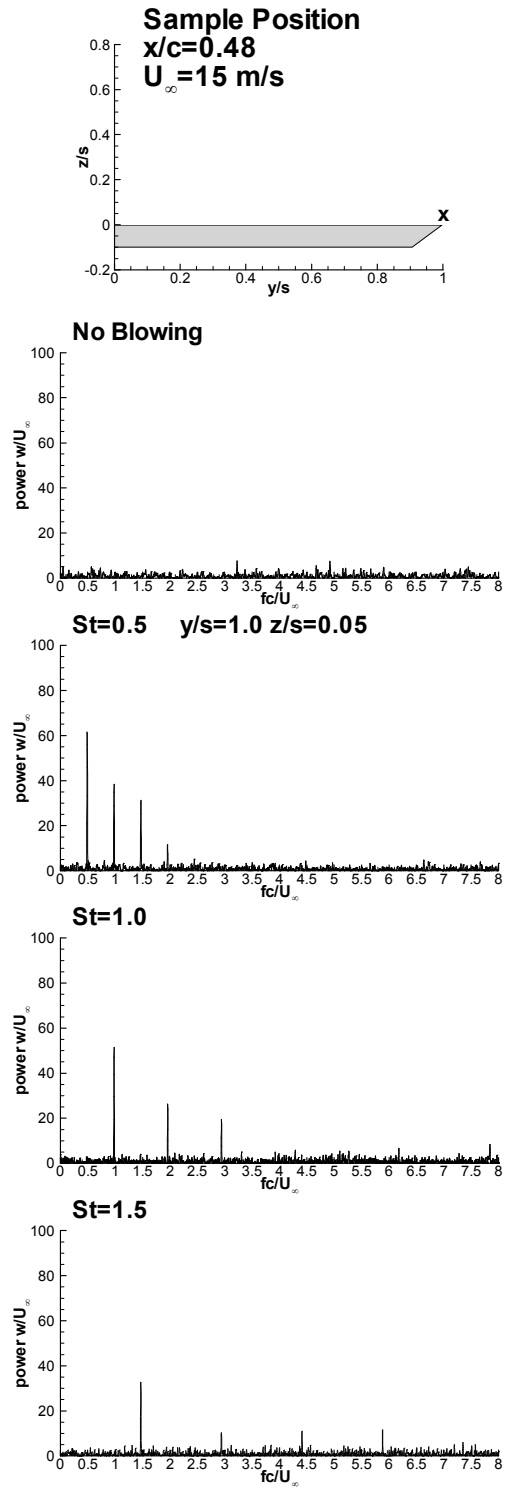

Figure 6-7 Power spectrum for cross-flow velocity components at x/c=0.48, C_μ=0.44%, near to the blowing location. y/s=1.0, z/s=0.05.

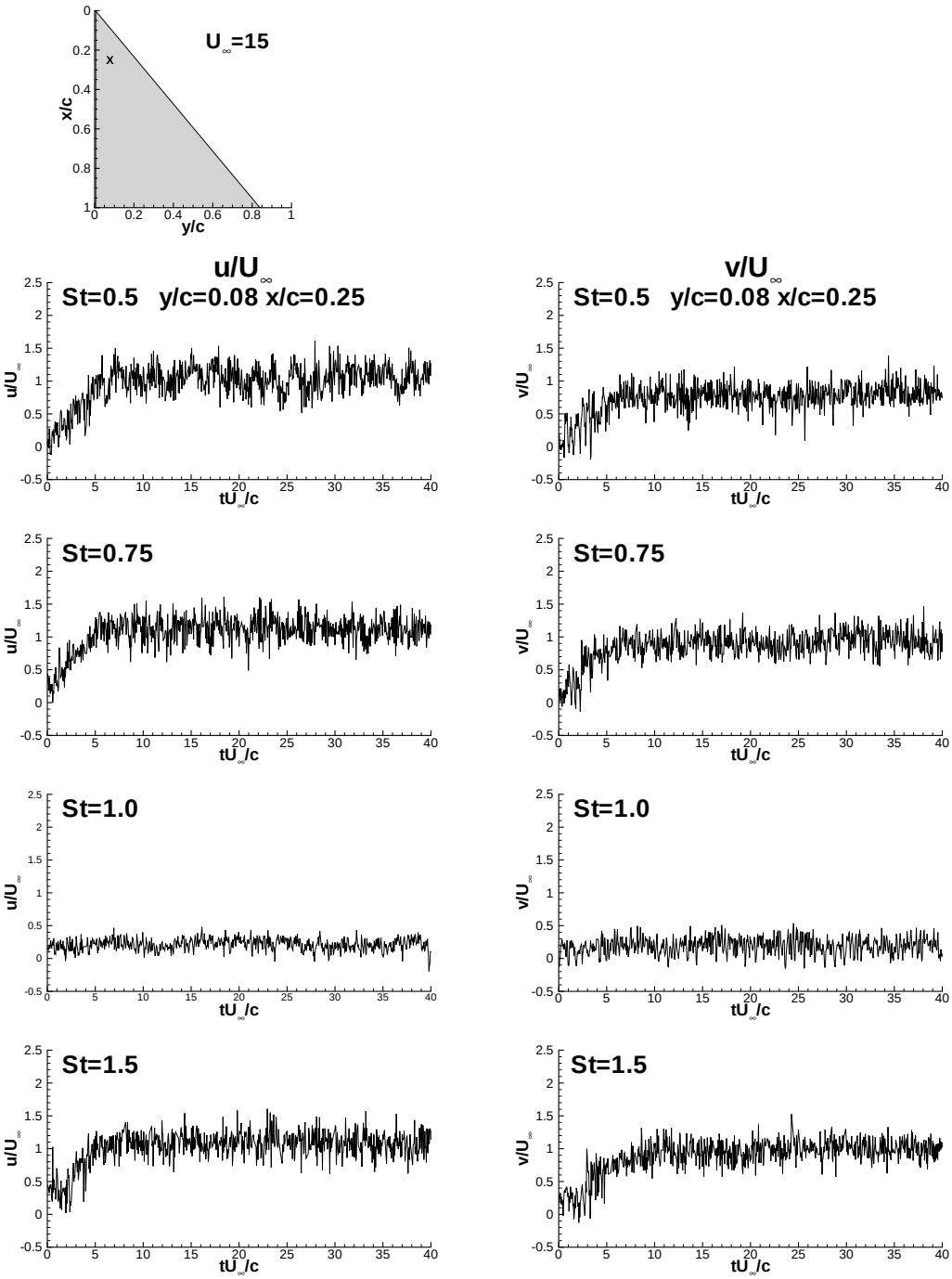

Figure 6-8 Spanwise and chordwise velocity components of near surface flow, C_μ=0.44% y/c=0.08, x/c=0.25.

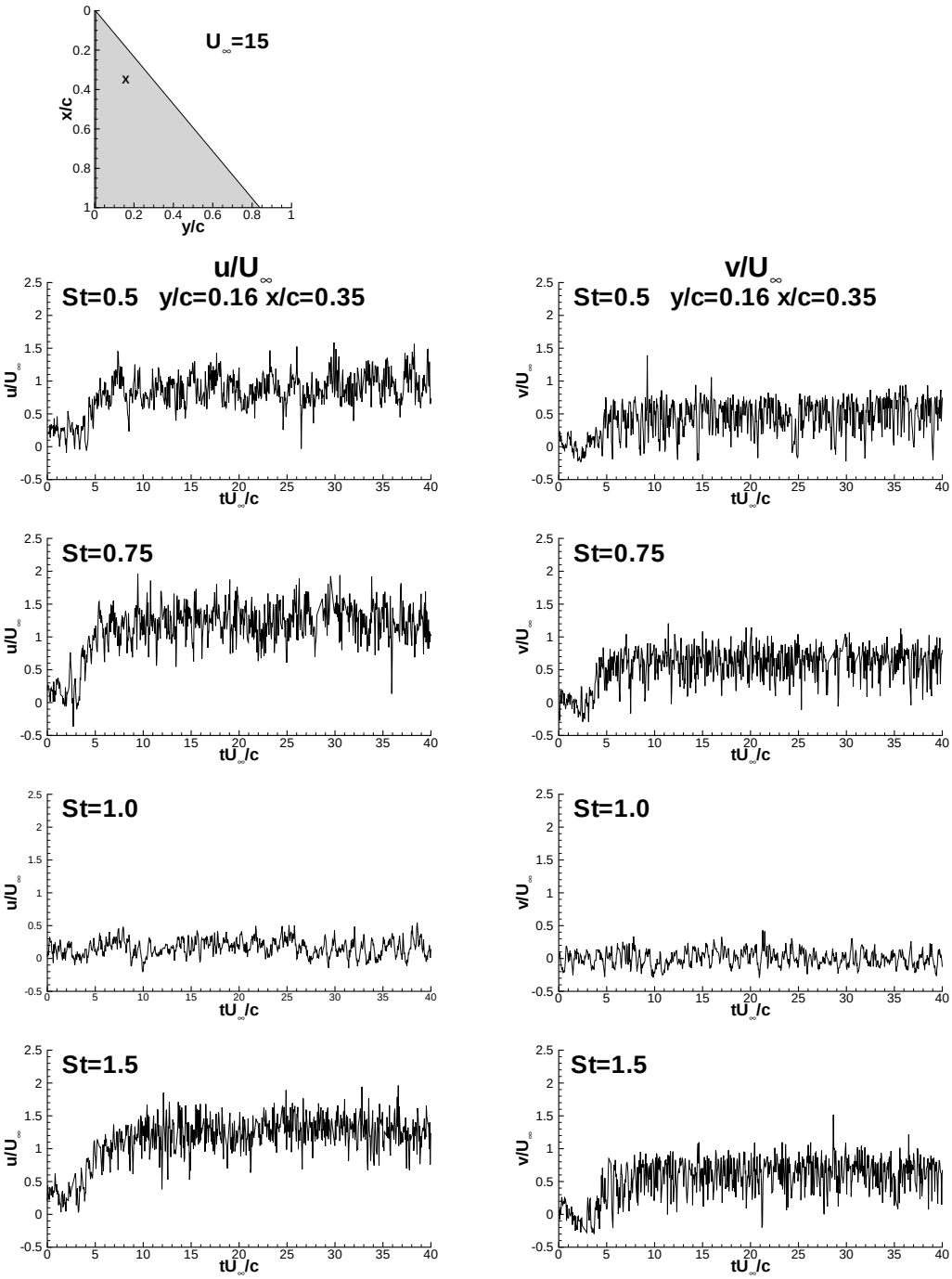

Figure 6-9 Spanwise and chordwise velocity components of near surface flow, C_μ=0.44% y/c=0.16, x/c=0.35.

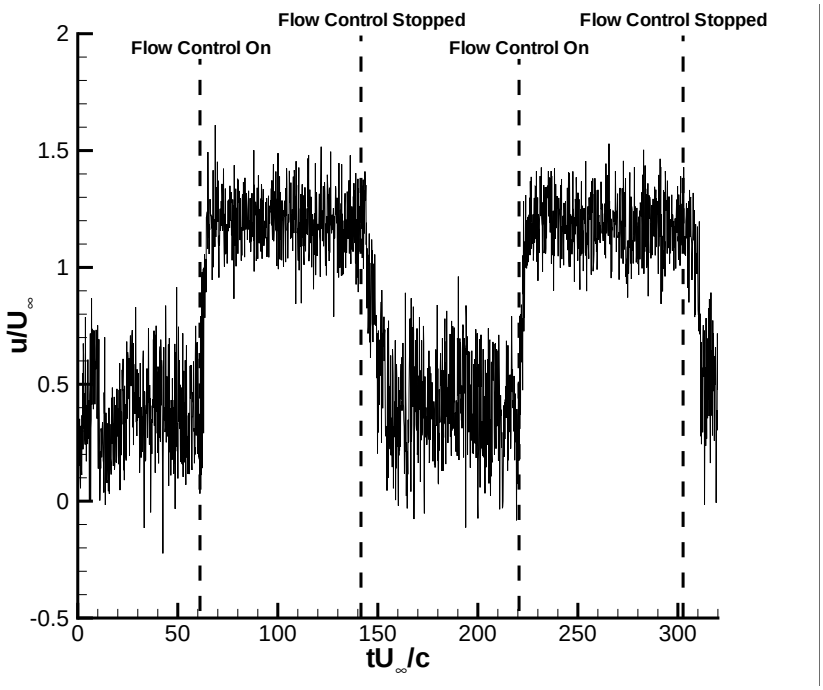

Figure 6-10 Effect of turning off flow control on the chordwise velocity of near surface flow, St=1.5, C_μ=0.44% y/c=0.05, x/c=0.25.

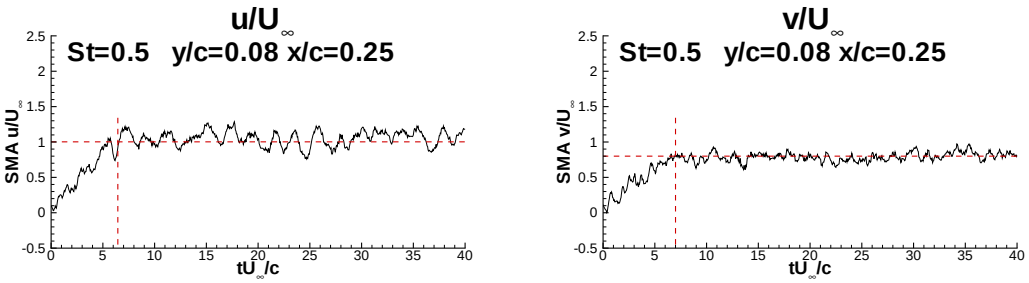

Figure 6-11 Moving average of chordwise and spanwise velocity, used to find time constants.

Table 6-1 Time constants for the range of Strouhal numbers tested.

St	Reattachment Time (tU∞/c)
0.5	6
1.0	N/A
1.5	7
0.75	5

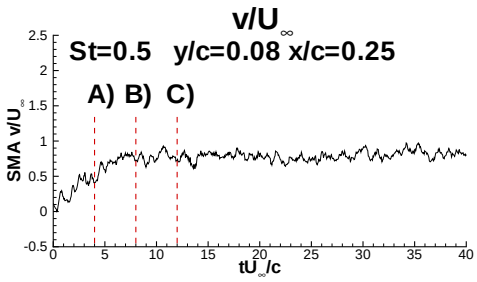

Figure 6-12 Instantaneous PIV vector fields have been compared at the indicated instances, tU_∞/c=0, 4 (A), 8(B), 12(C).

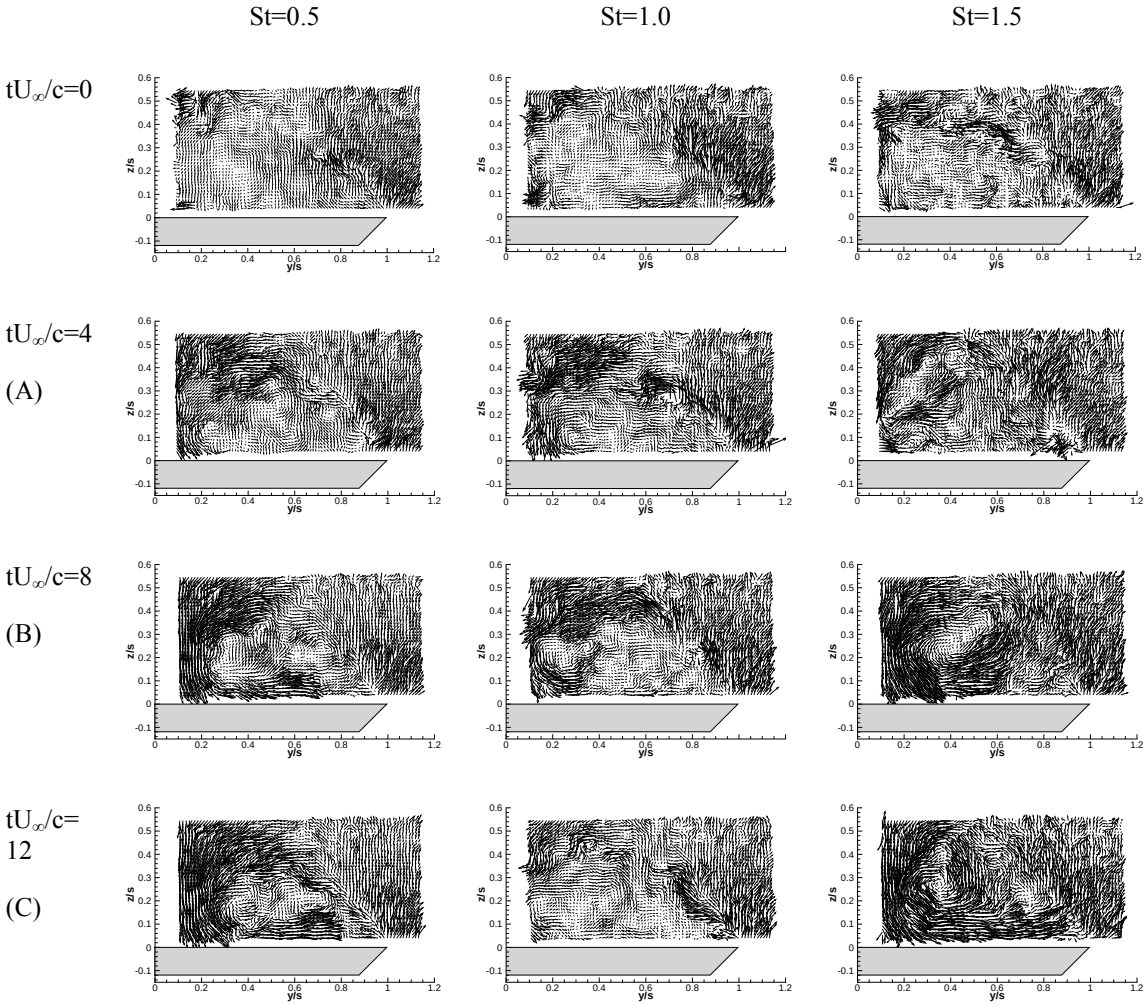

Figure 6-13 Instantaneous cross-flow vector field for the specified tU_∞/c. x/c=0.48 C_μ=0.44%.

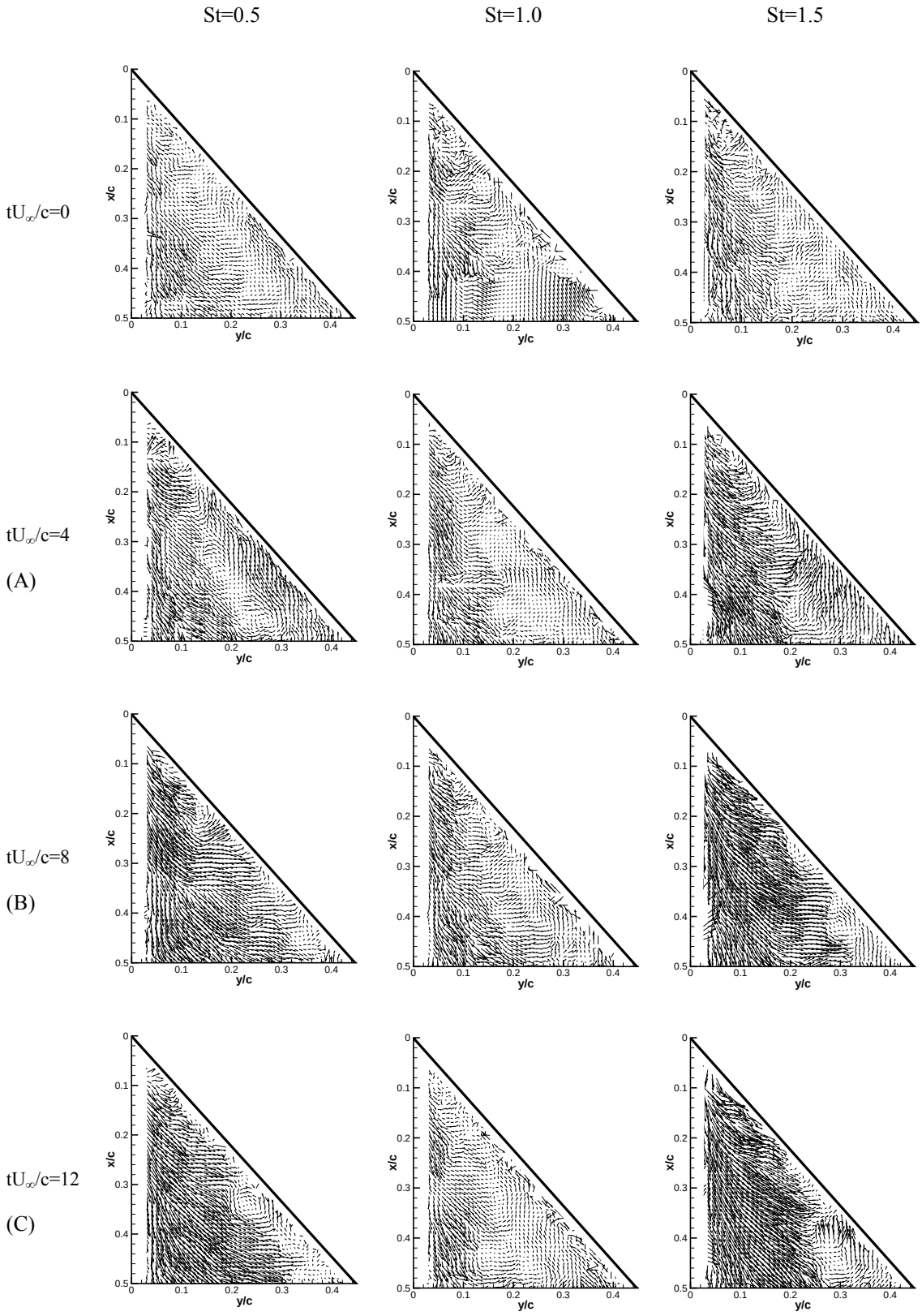

Figure 6-14 Instantaneous near surface flow vector field at specified tU_∞/c. C_μ=0.44%.

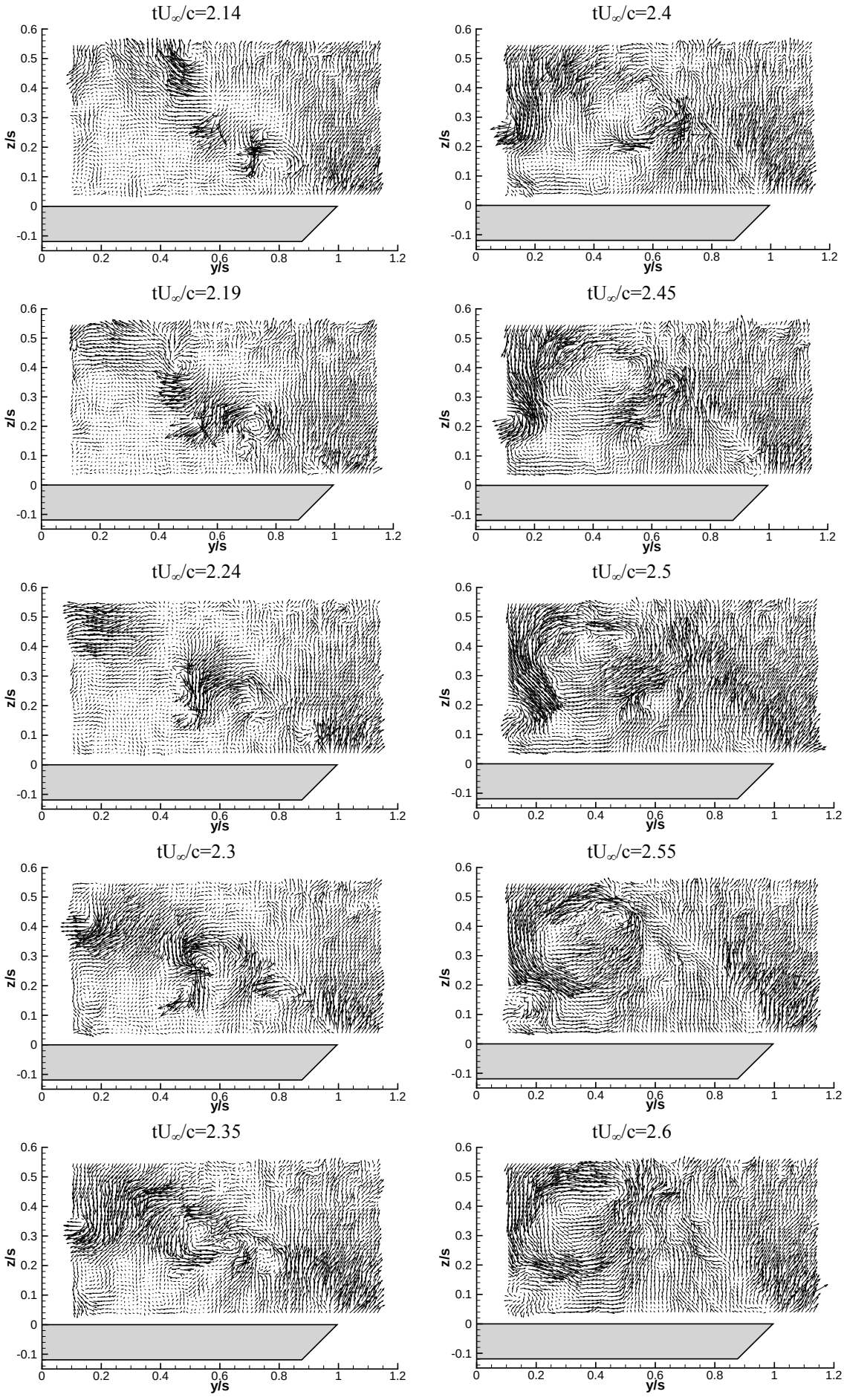

Figure 6-15 Instantaneous cross-flow vector fields showing the initial stage of reattachment. x/c=0.48, St=0.5, C_μ=0.44%.

Chapter 7 Partial blowing

The focus of partial blowing experiments was to develop an understanding of how blowing from different locations along the leading edge affected the reattachment of the shear layer, in particular, what locations were most effective. Experiments were conducted for unsteady blowing from a finite slot length rather than unsteady blowing from the whole length of the leadingedge. This kind of partial (or distributed) blowing may be more realistic for practical applications, as blowing would only need to be incorporated into a localised section of the wing. The effect of blowing from a small section of the wing on reattachment upstream and downstream of the blowing location is also discussed as it appears that blowing from a small section of the wing only can induce reattachment over the surface of the wing.

The setup used for partial blowing, and a summary of the blowing locations tested, is outlined in Figure 3-5. Unsteady blowing from various slot lengths, where the slot location extends from the apex, was investigated and the results are displayed in Figure 7-1, which plots the percentage increase in suction force coefficient against the blowing momentum coefficient for each configuration. All tests were conducted at a Strouhal number of St=1.5. Two general trends can be noted from the plot. The first is that the larger the slot length, the higher the maximum increase in suction force achievable. It was found that blowing from the entire slot length still produces the largest obtainable increase in suction force for large momentum coefficients. This indicates that there is still some benefit to blowing from the final 25% of the leading edge. The second trend applies to slot lengths between 38% and 100% of the leading edge. For blowing at low momentum coefficients it is beneficial to use a slot of a smaller length than the entire leading edge. However, to obtain the maximum suction force coefficient at larger the momentum coefficients, a larger slot is necessary. For practical cases blowing at a low momentum coefficient is desirable, and slots extending from the apex with lengths of between 38% and 50% of the leading edge look promising. Interestingly slot lengths of 10% and 25% of the leading edge showed lower suction force coefficients across the momentum coefficient range in comparison to larger slots. Blowing solely at the apex may be ineffective due to the small semispan and short shear layer near the apex (relative to the size of the perturbation). If perturbations of a similar size to that seen downstream at x/c=0.28 and x/c=0.68 in the phase averaged PIV tests outlined in Chapter 5 were present close to the apex, they may not have the same effect on the reattachment of the shear layer as at stations further downstream. The duty cycle of the unsteady blowing command signal is fixed at 20% of the pulse cycle. From the experiments discussed in Chapter 5 it was noted that as the chordwise station (measurement plane) approaches the apex, the perturbation progresses along the shear layer at a faster rate, due to a shorter local semispan and higher velocities. It is possible that blowing near the apex did not encourage the development of discrete shear layer vortices because the pulse duration is long compared to the time taken for the pulse to travel along the shear layer. A very short, lower velocity pulse may have been more effective very close to the apex.

Unsteady blowing from only a section of the leading edge, as shown in Figure 7-1, looked promising, and this concept was further investigated by systematically varying the location of a slot with a length of 25% of leading edge length. Figure 7-2 shows the percentage increase in the suction force coefficient as a function of momentum coefficient for various slot locations. The inset shows the location of the slot for each case. As a reference, the case of blowing from the entire slot is shown with dashed lines. It is evident that, for some finite span slot locations, partial blowing is more effective than blowing from the entire leading-edge, in particular at low momentum coefficients. This is particularly clear if the slot is located in the forward half of the wing (but not starting from the apex). As the wing was completely stalled for the reference (no blowing) case, the effective location of blowing is not related to the vortex breakdown phenomenon. Of the locations tested, 13%-38%, 25%-50% and 50%-75% (expressed as a percentage of the leading edge length from the apex) showed promising results, and for low momentum coefficients were more effective than blowing along 100% of the slot length. Unsteady blowing from locations 50%-75%, 63%-88% and 75%-100% proved particularly ineffective. By comparing this with the results of Figure 7-1, it appears that blowing from the rear half of the wing is only beneficial when also blowing from the front half of the wing. An interesting point to note is the increase in effectiveness when comparing the 0-25% blowing case to the 13%-38% blowing case. By moving the slot location 13% of the leading edge away from the apex, a significant percentage increase in suction force coefficient was gained, highlighting that blowing close to, but not at the apex is beneficial.

Figure 7-3, Figure 7-4 and Figure 7-5 show the variation of pressure at the three chordwise stations for momentum coefficients of C_μ=0.13%, C_μ=0.25% and C_μ=0.6%. In Figure 7-3, where C_μ=0.13%, only two of the blowing locations, 13%-38% and 25%-50%, show any response to unsteady blowing. Comparing the two, there are slight differences between the pressure distributions, accounting for the difference in the percentage increase in suction force coefficient shown in Figure 7-2. The 25%-50% case shows a slightly broader pressure distribution at all three stations, accounting for the slight increase in suction force coefficient. The peak negative pressures at Station A (x/c=0.28) are slightly higher for the 13%-38% case. The rest of the cases remain in a stalled state. For the particularly promising case of blowing from 25%-50% of the leading edge, the measurement station (x/c=0.28) is just at the beginning of the blowing section (from x/c=0.25 to 0.50). For partial blowing between 25% and 50%, generation of a pressure profile characteristic of "vortex lift" for Cμ=0.13% indicates that partially reattached flow may already be established upstream of the blowing region.

Figure 7-4, where C_μ=0.25%, shows increased response to flow control for the two cases either side of the effective region at C_μ=0.13%. The cases where the slot location is 0-25% and 38%-63% of the leading edge show a response to unsteady blowing, but the pressure distribution appears to fall short of a vortex type pressure distribution, and indicates weak reattachment. All three measurement points are downstream of the blowing location for the 0-25% blowing case, and there may be a higher level of reattachment upstream. The prominence of the suction peak for the 25%-

50% blowing case at x/c=0.28 and x/c=0.48 has increased further over the same configuration at C_μ=0.13%, indicating the formation of a stronger vortical structure, although this is not reflected in the suction force calculation.

Figure 7-5 shows the effect of partial unsteady blowing at C_μ=0.6%. Even at this high momentum coefficient the cases where unsteady blowing is only from the rear half of the wing, starting at a location beyond 50% of the leading edge, show little response to unsteady blowing, and nothing in the pressure distribution indicates the formation of a vortex or reattachment. There is however a significant increase in the negative pressure for the 38%-63% blowing case. This blowing location is well downstream of the x/c=0.28 measurement location, however the blowing has a significant effect on the pressure distribution at x/c=0.28. The pressure distribution at x/c=0.28 is not that of a classical, well defined vortex suction peak. The pressure distribution is rather broader, and indicates some kind of reattachment, but not the high level of vortical flow seen for other cases. For the 25%-50% case, the maximum negative pressure at station A (x/c=0.28) is $-C_P$=2.36, significantly greater than the corresponding maximum negative pressure for the 38%-63% which is $-C_P$=2. The same comparison for station B (x/c=0.48) shows that the maximum negative pressure is lower for the 25%-50% case at $-C_P$=1.48 compared to $-C_P$=1.64 for the 38%-63% case. This indicates that as the blowing location moves further away from the apex, its effect on stations closer to the apex is reduced. The 0-100% unsteady blowing case appears to combine the advantageous pressure distribution for station A (x/c=0.28) from the 25%-50% blowing case, with the advantageous pressure distribution for station B (x/c=0.48) from the 38%-63% blowing case.

A three dimensional view comparing the 25%-50% pressure distribution with that of the 0-100% case, shown in Figure 7-6, highlights the benefits of blowing also at the trailing edge. The x/c=0.28 station shows very little difference between the two cases, but as the measurement station moves towards the trailing edge, the 0-100% case maintains a vortical type pressure distribution with a strong peak. Although the 25%-50% case shows definite suction peaks, their magnitude is significantly lower than for the 0-100% case.

Time averaged cross-flow PIV measurements for the 25%-50% case at x/c=0.68 are shown in Figure 7-7. It is worth noting that this measurement location is well downstream of the blowing location. For the lowest momentum coefficient presented, reattachment occurs, however it is reasonably weak, with velocities near the centreline around half that of the freestream. If the measurement station was closer to the leading edge, a higher level of reattachment would be expected. As the momentum coefficient is increased to C_μ=0.16%, there is a significant increase of the velocity magnitude in the reattachment region, and of the swirl velocities of the vortex. An interesting feature present in the flow field is a change in the direction of the flow in the shear layer between y/s=0.7 and y/s=0.8. It appears as if there is a break in the shear layer at this point. Instead of the velocity immediately below the shear layer being parallel to its direction, the velocity in a region beginning from the surface of the wing and extending upwards through the shear layer is

almost completely vertical. This is a feature that has not been observed for the 0-100% blowing case and is likely to be a result of observing the flow in a measurement plane downstream of the blowing location. This feature will be discussed further with the presentation of the corresponding turbulence intensity plots. The flow is fully reattached with a strong vortical flow pattern at C_μ=0.33% and C_μ=0.62%, further proof that full reattachment can occur outside the blowing location.

The time averaged turbulence intensity corresponding to the plots in Figure 7-7 is presented in Figure 7-8. At C_μ=0.16% a concentration of turbulence is seen at the location of the discontinuity of the shear layer presented for the corresponding case in Figure 7-7. It is possible that this corresponds to the location at which the perturbation, released upstream, intersects with this measurement plane. At higher momentum coefficients, C_μ=0.33% and C_μ=0.62%, outboard of x/c=0.75 the shear layer appears thin with low levels of turbulence. However, immediately inboard of x/c=0.75, there is a high concentration of turbulence. Again, it is possible that this corresponds to the location at which the perturbation, released upstream, intersects with this measurement plane.

Near surface PIV measurements for partial blowing between 25%-50% of the leading edge are presented in Figure 7-9. The velocities for the C_μ=0.16% case are surprisingly low when compared to the cross-flow case. Partial reattachment, indicated by an increase in velocity when compared to the no blowing case, can be seen near the wing's centreline and towards the trailing edge. At C_μ=0.33% high velocity flow dominates the flow field near the centreline, indicating complete reattachment.

Phase averaged cross-flow measurements of the C_μ=0.16% case are shown in Figure 7-10. At t/T=0%, the flow field is similar to that of the mean flow case, with the shear layer appearing to be separated between y/s=0.7 and y/s=0.8. As the percentage of the pulse cycle (t/T) advances from t/T=10% to t/T=30%, this region moves outboard, and a region of high horizontal velocity towards the centreline develops at y/s=0.7. At t/T=50% this region of high velocity rolls up in the shear layer, creating a discrete vortex. The discrete vortex proceeds along the shear layer, until it is directly above the main vortical region at t/T=90%. The discrete vortex appears not to originate from the leading edge, rather originating in the region of high turbulence discussed regarding the C_μ=0.16% case in Figure 7-8. The high level of the fluctuation of velocity in this region which occurs as the discrete vortex forms, or enters the region from upstream, is the likely origin of the high levels or turbulence. The shear layer outboard of the y/s=0.9 does not appear to be altered by the formation of the discrete vortex, which is consistent with the low levels of turbulence in this region.

Phase averaged streamline patterns presented in Figure 7-11 indicate that the formation of the discrete vortex may begin at t/T=30%, as a significant 'kink' can be seen forming in the shear layer, and later developing into a vortex. The streamline patterns also show the discrete vortex interacting with the main vortical region, from t/T=70% to t/T=10%. Corresponding vorticity plots

(Figure 7-12) show an increase in the magnitude of negative vorticity at y/s=0.75 for t/T=30%, which further increases in magnitude, and progresses along the shear layer between t/T=40% and t/T=90%. Continuing through the next pulse cycle, the region of high vorticity becomes indistinguishable from the main vortical region as it enters the reattachment region at around t/T=10%. Figure 7-12 highlights that the discrete vortex does not form at the leading edge at this station. It is likely that it forms at the leading edge upstream of the measurement plane, at the blowing location. It is unclear whether the induced vortex causes a perturbation to develop along the entire shear layer, or if the discrete vortex seen for this case at x/c=0.68 is the induced vortex from upstream, travelling through the measurement plane.

The phase averaged effect of unsteady blowing on PIV measurements in the near surface plane is similar to that of blowing along the entire leading edge. For the partial reattached case at C_μ =0.16%, a thin high velocity region can be seen originating from y/s≈0.4, which slowly moves down the wing. This indicates the reattachment of the high velocity perturbation. It is also interesting to note the presence of a high velocity region between t/T=0% and t/T=20%, adjacent to the leading edge along the region where the blowing occurs. There is no indication of an increase in the velocity magnitude at any point closer to the apex than the blowing location. As the momentum coefficient is increased to C_μ=0.35% (Figure 7-14), the near surface flow field takes a form almost identical to that presented in Figure 5-16, for blowing from 0%-100% of the leading edge at C_μ=0.4%. There is a region of high velocity axial flow near the centreline upstream of x/c=0.4, independent of the position in the pulse cycle which is characteristic of reattachment. It appears that there is reattached flow upstream of the blowing location. There are also the time dependant regions of high velocity that move down the wing's surface. Their location at each instance in the pulse cycle is highly similar to that of the 0-100% blowing case. This indicates that at this higher momentum coefficient, blowing along a portion of the leading edge can cause reattachment of the entire shear layer, both upstream and downstream of the blowing location. In addition to this, it is also likely that a discrete vortex forms at some point over the length of the shear layer.

The corresponding turbulence intensity plot is shown in Figure 7-15. The turbulence intensity plot shows an interesting pattern of high turbulence on the wing's surface. The high turbulence region appears to take the form of a double arc. The first arc starts close to the apex, the second from another downstream location on the wing's centreline. The two arcs appear to move down the wing's surface in a wave like manner with time. When compared to the phase averaged velocity magnitude plot in Figure 7-14, it appears the regions of high turbulence encircle the regions of high velocity, creating the two arcs. This indicates that the centre of each high velocity region has a relatively stable velocity magnitude, with high fluctuations occurring around the edges of the regions. This may indicate that the size of each high velocity region in an instantaneous sense is highly variable. It may also be an indication that there is significant interaction between the high velocity flow regions and the surrounding lower velocity region. For this plot it is also clear that

two pulse cycles are present on the surface of the wing at one time. The PIV measurement at t/T=60% shows two clear undulations or arcs in the high turbulence region.

Partial blowing from limited sections of the leading edge has pointed to configurations that show potential for practical application. Although for all partial blowing cases the maximum increase in suction force was lower than for blowing along the entire leading edge, at low momentum coefficients significant suction force gains can be achieved over the full leading edge blowing case. Even though partial blowing results in a lower maximum suction force, it is still capable of maintaining reattached flow over the wing's surface, both upstream and downstream of the blowing location. Blowing from the front half of the wing, but not directly from the apex proved to be a promising configuration, and blowing from the rear half of the wing was only beneficial if also blowing from the front half of the wing. This type of configuration should be considered if unsteady blowing were applied to a practical configuration.

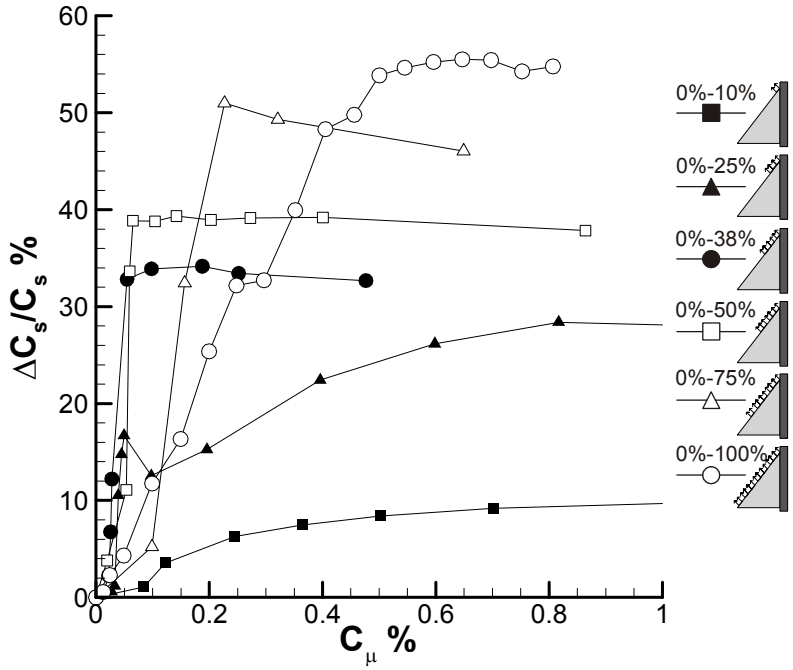

Figure 7-1 Variation of percent increase in suction force coefficient as a function of momentum coefficient for different slot sizes.

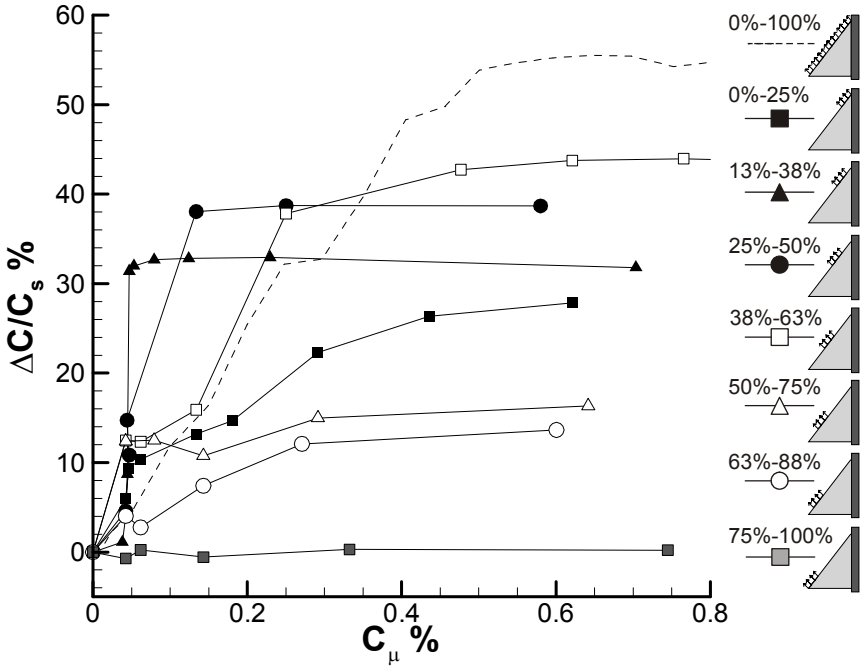

Figure 7-2 Variation of percent increase in suction force coefficient as a function of momentum coefficient for a slot covering 25% of the leading edge at different locations.

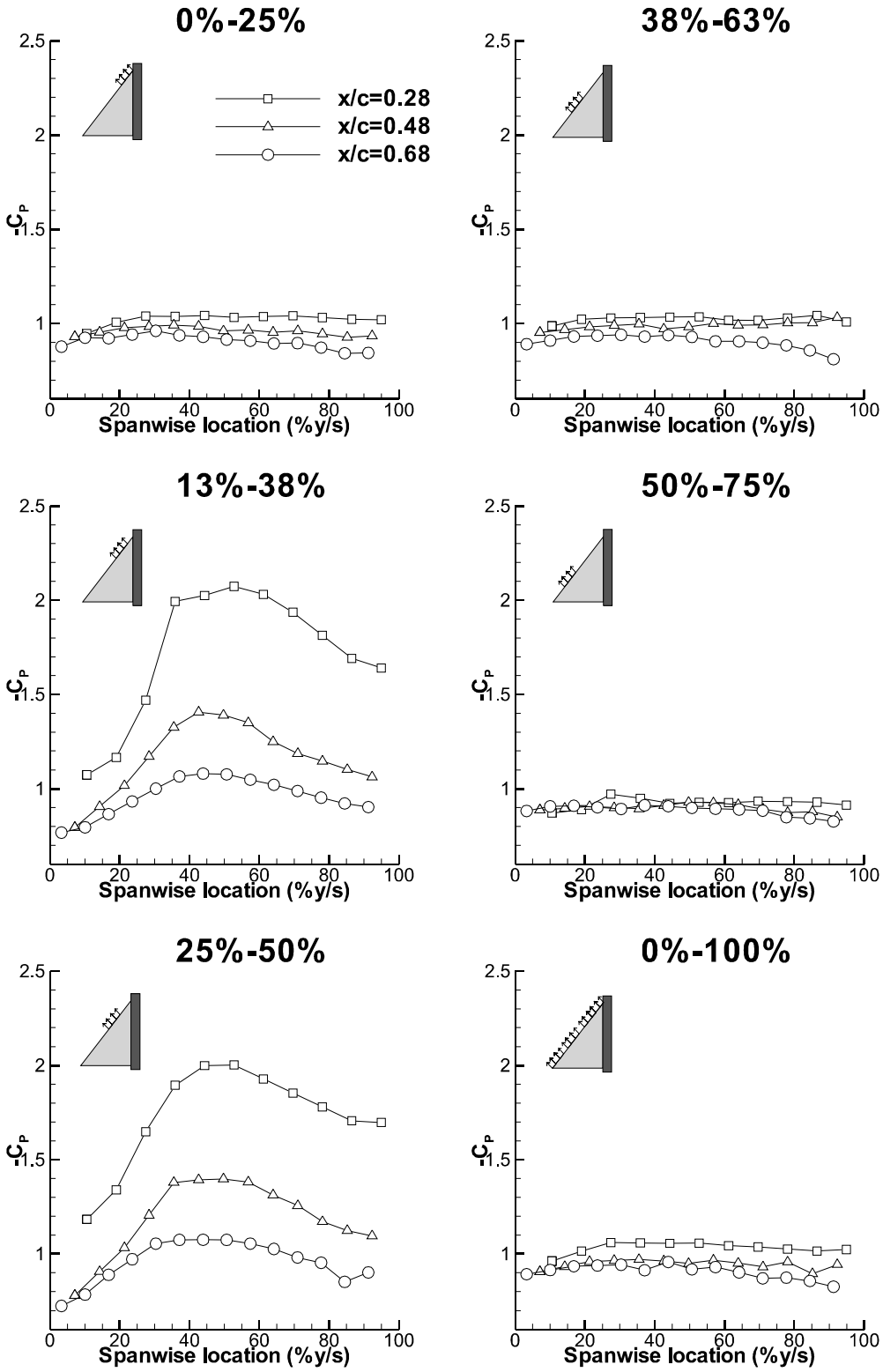

Figure 7-3 Spanwise variation of pressure for x/c=0.28, 0.48 and 0.68 at α=30°, St=1.5 and Cμ=0.13% for different locations of a slot covering 25% of the leading edge.

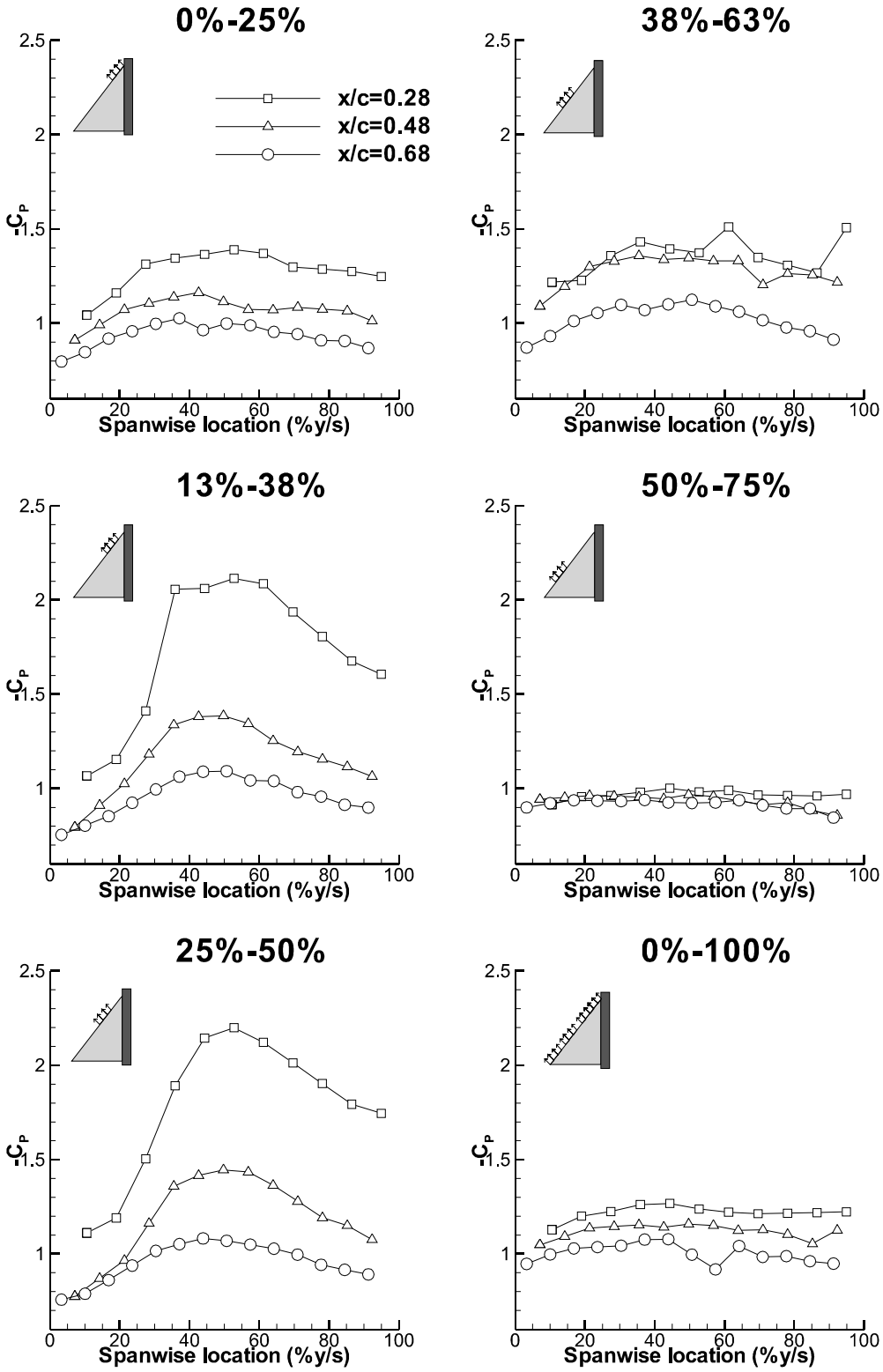

Figure 7-4 Spanwise variation of pressure for x/c=0.28, 0.48 and 0.68 at α=30°, St=1.5 and Cμ=0.25% for different locations of a slot covering 25% of the leading edge.

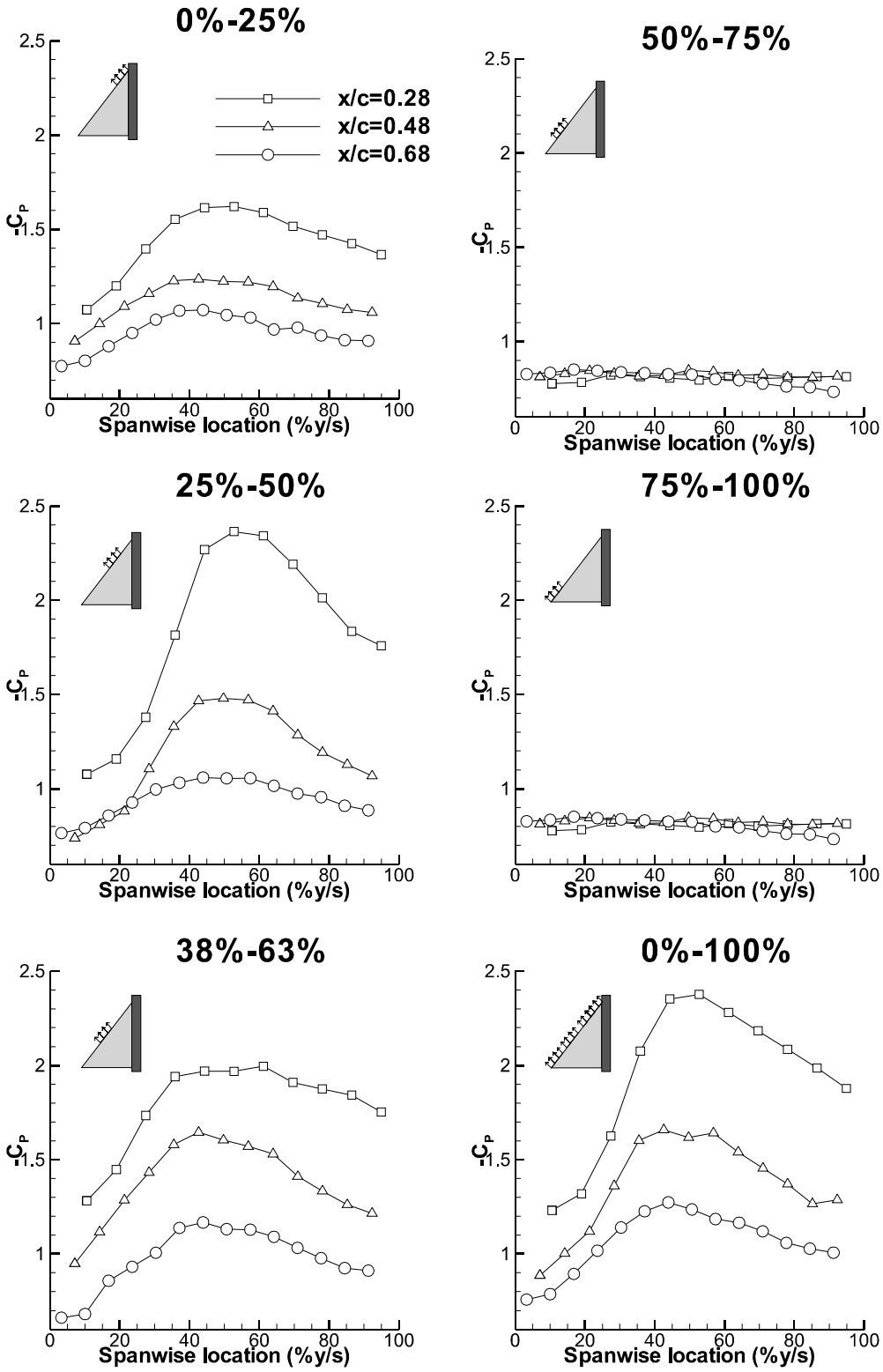

Figure 7-5 Spanwise variation in pressure for x/c=0.28, 0.48 and 0.68 at α=30°, St=1.5 and Cμ=0.6% for different locations of a slot covering 25% of the leading edge.

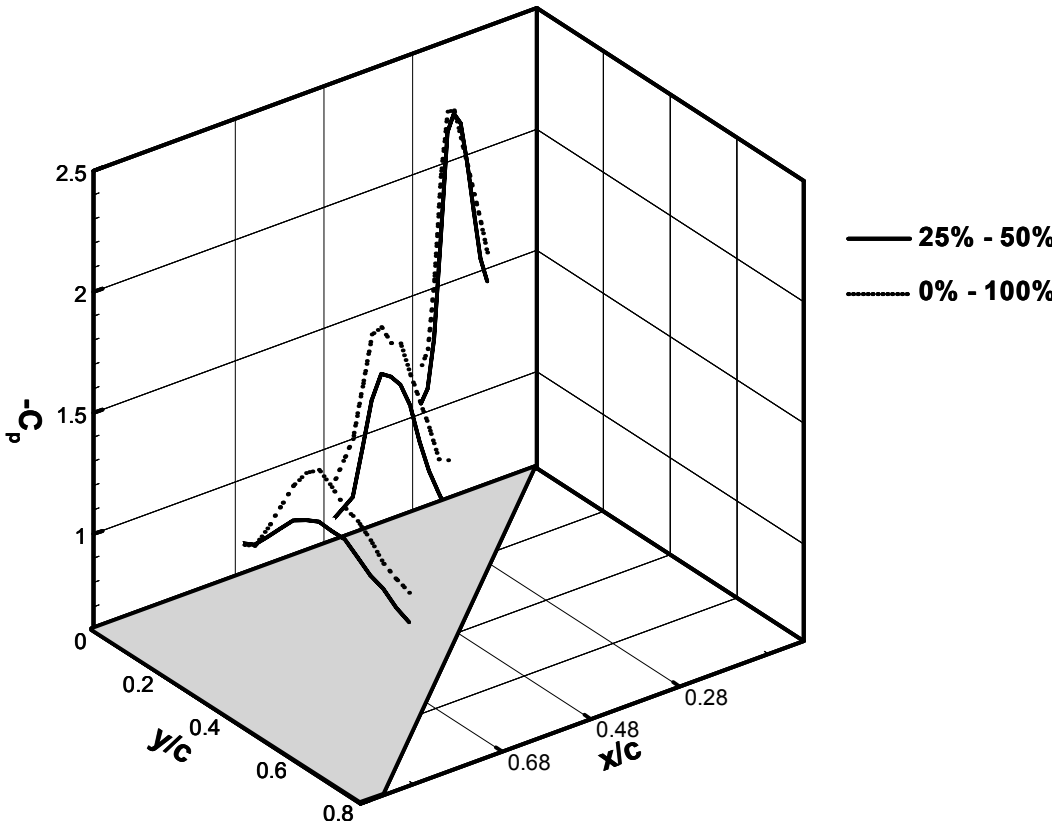

Figure 7-6 A comparison of the three dimensional variation of pressure at α=30°, St=1.5 and Cμ=0.6% for blowing from 0%-100% of the leading edge and 25%-50% of the leading edge.

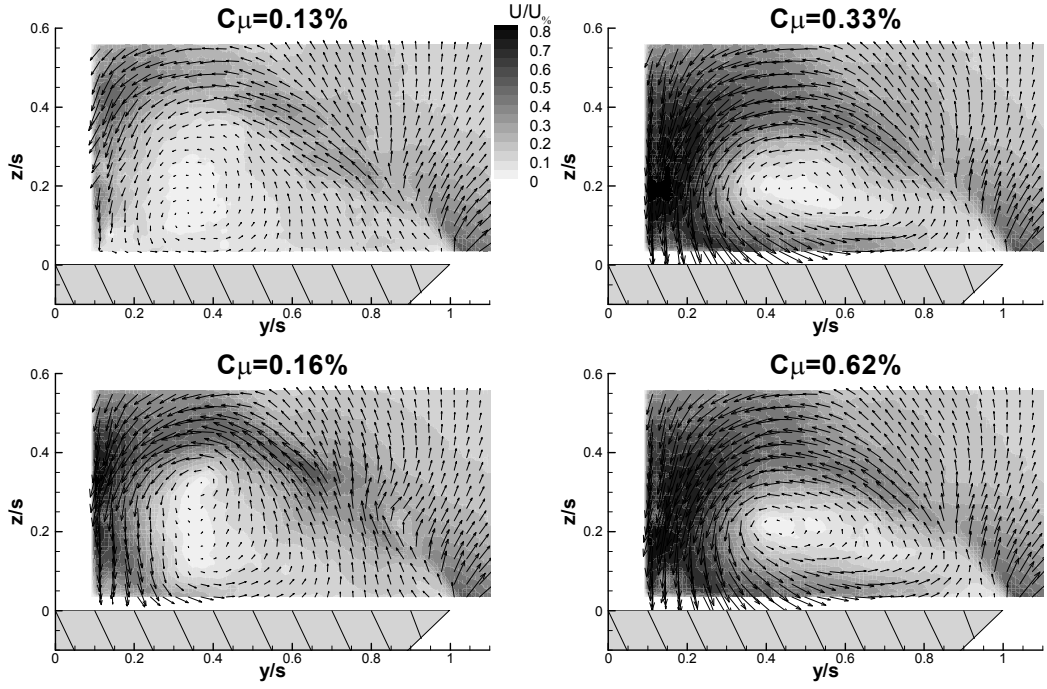

Figure 7-7 Magnitude of time-averaged cross-flow velocity for blowing from a slot between 25%-50% of the leading edge, x/c=0.68, α=30°, St=1.5, 0.13%<C_μ<0.6%

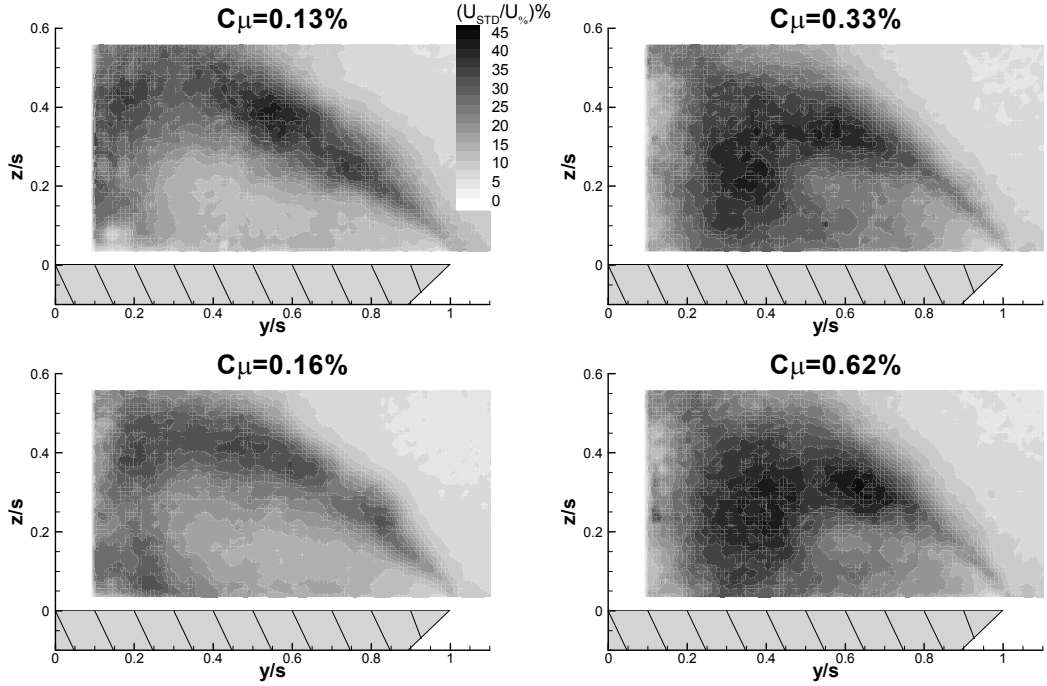

Figure 7-8 Magnitude of time-averaged cross-flow turbulence intensity for blowing from a slot between 25%-50% of the leading edge, x/c=0.68, α=30°, St=1.5, 0.13%<C_μ<0.6%

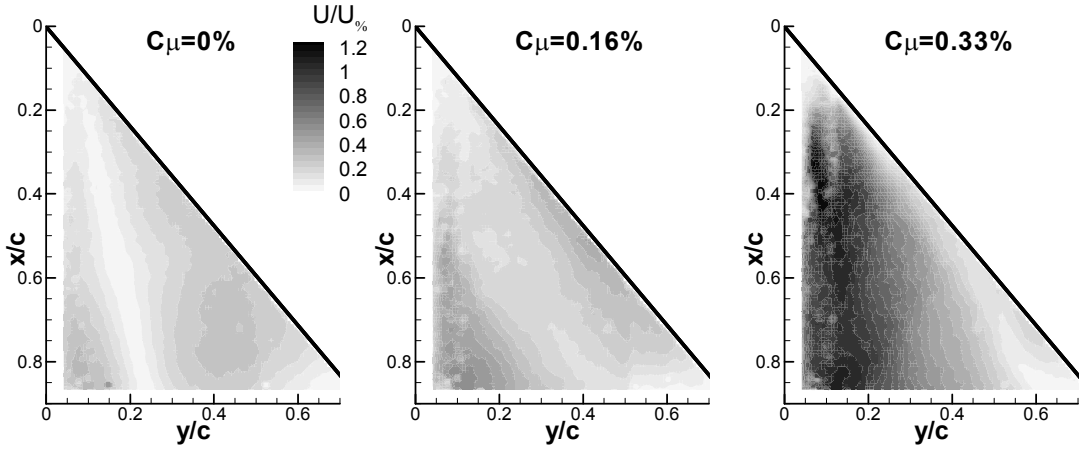

Figure 7-9 Magnitude of time-averaged near surface velocity for blowing from a slot between 25%-50% of the leading edge, α=30°, St=1.5, 0 %<C_μ<0.33%

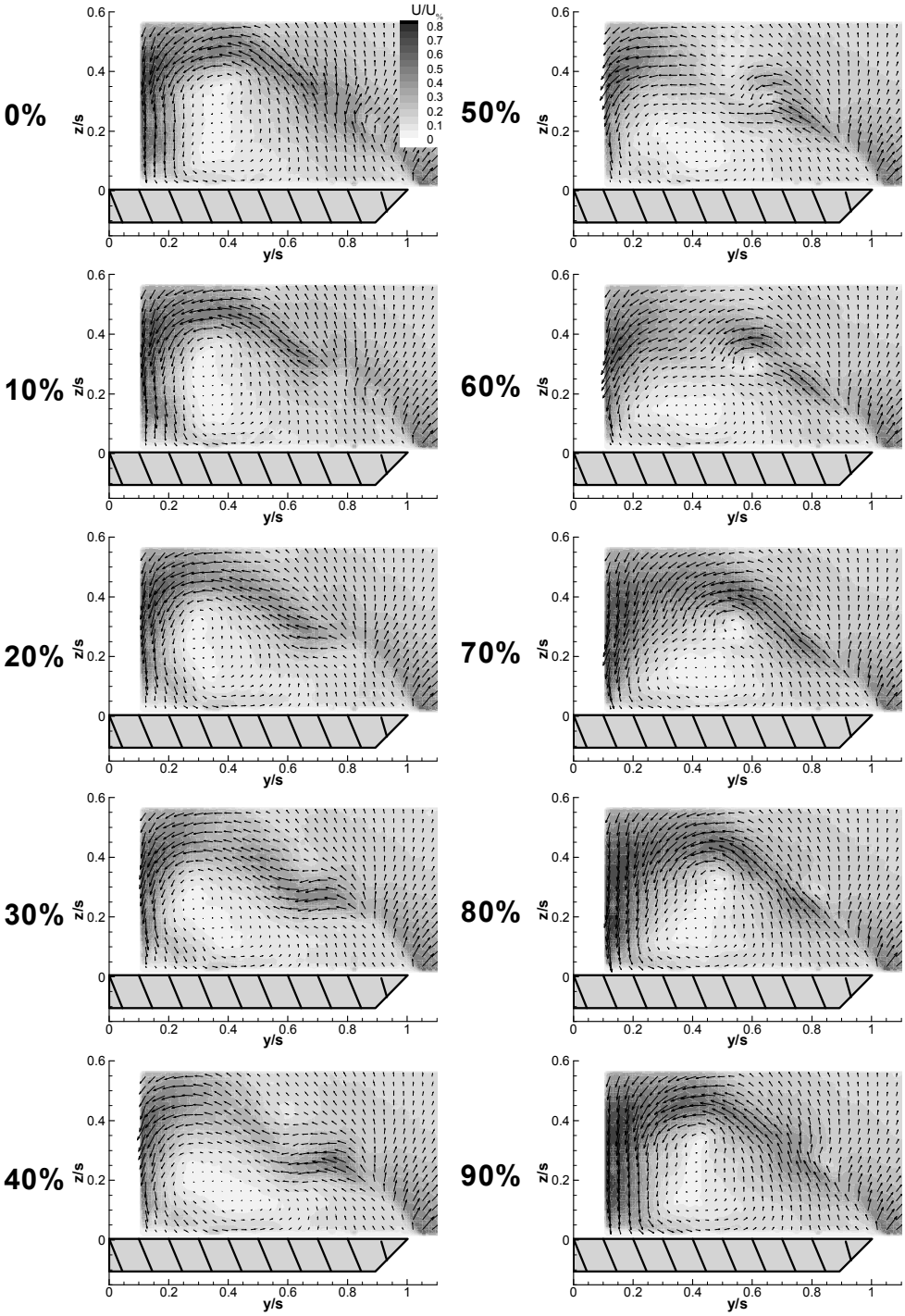

Figure 7-10 Magnitude of phase-averaged cross-flow velocity at x/c=0.68, α=30°, C_μ=0.16%, St=1.5 for blowing from a slot between 25%-50% of the leading edge.

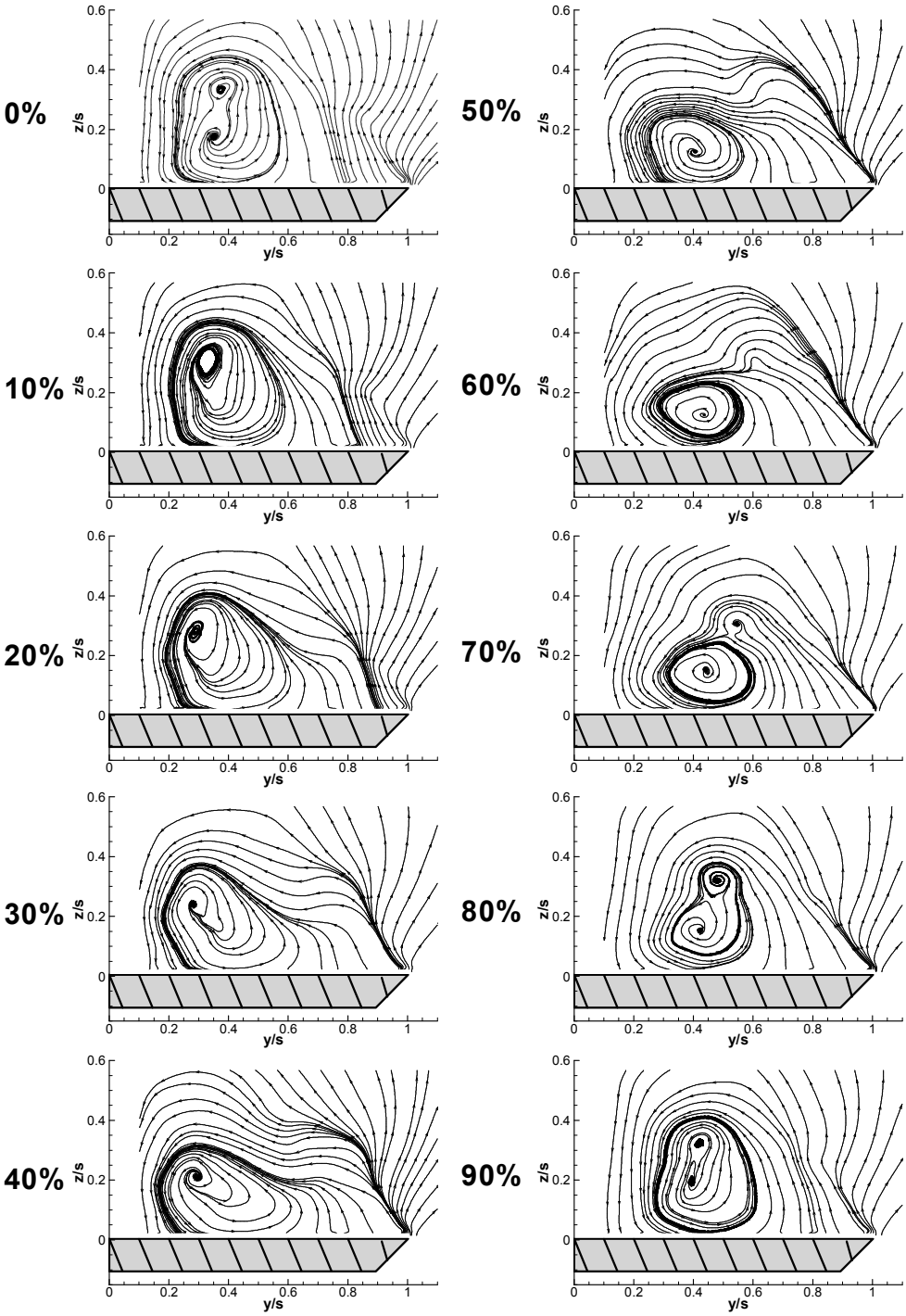

Figure 7-11 Phase-averaged cross-flow streamline patterns at x/c=0.68, α=30°, C_μ=0.16%, St=1.5 for blowing from a slot between 25%-50% of the leading edge.

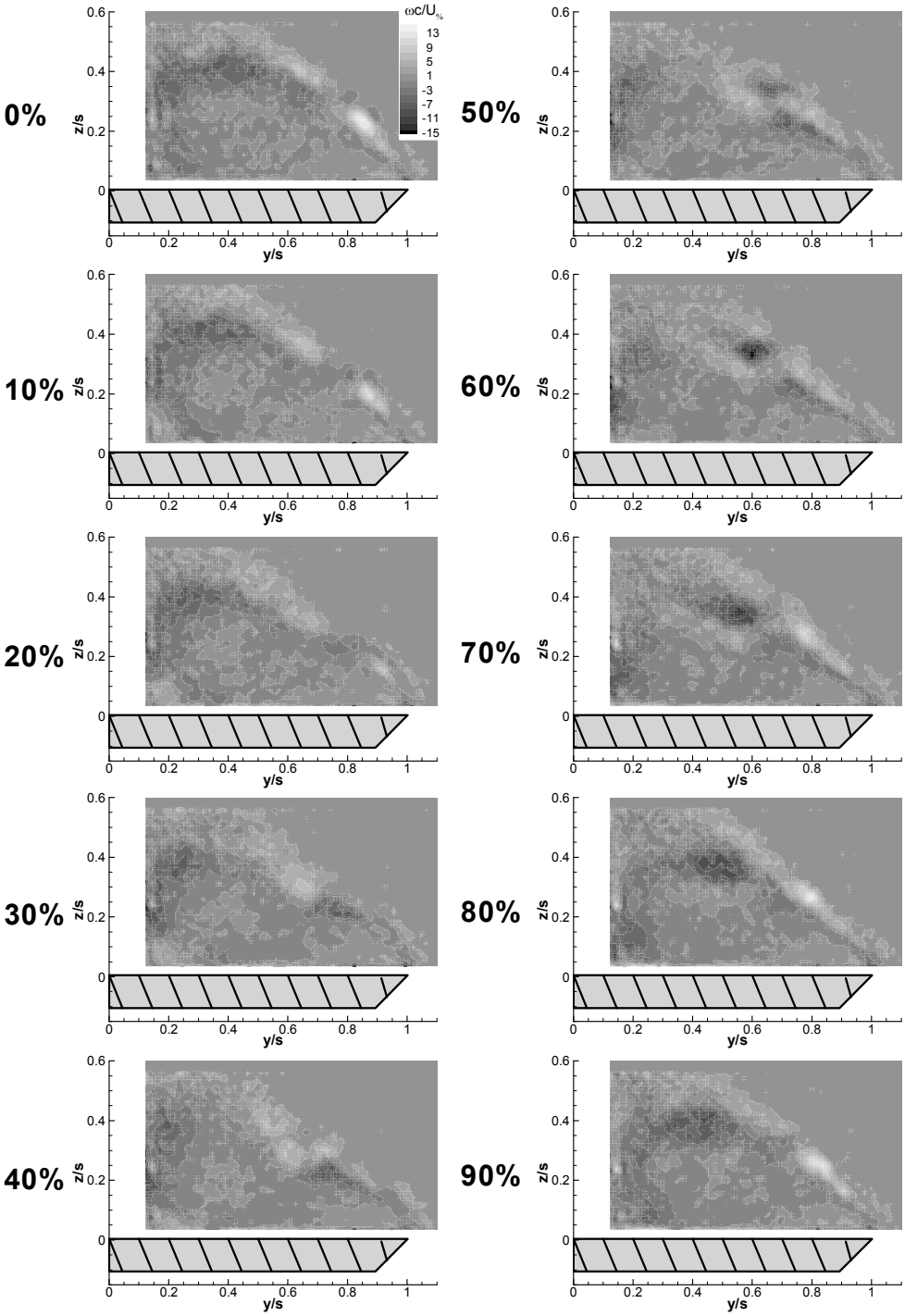

Figure 7-12 Phase-averaged cross-flow vorticity at x/c=0.68, α=30°, C_μ=0.16%, St=1.5 for blowing from a slot between 25%-50% of the leading edge.

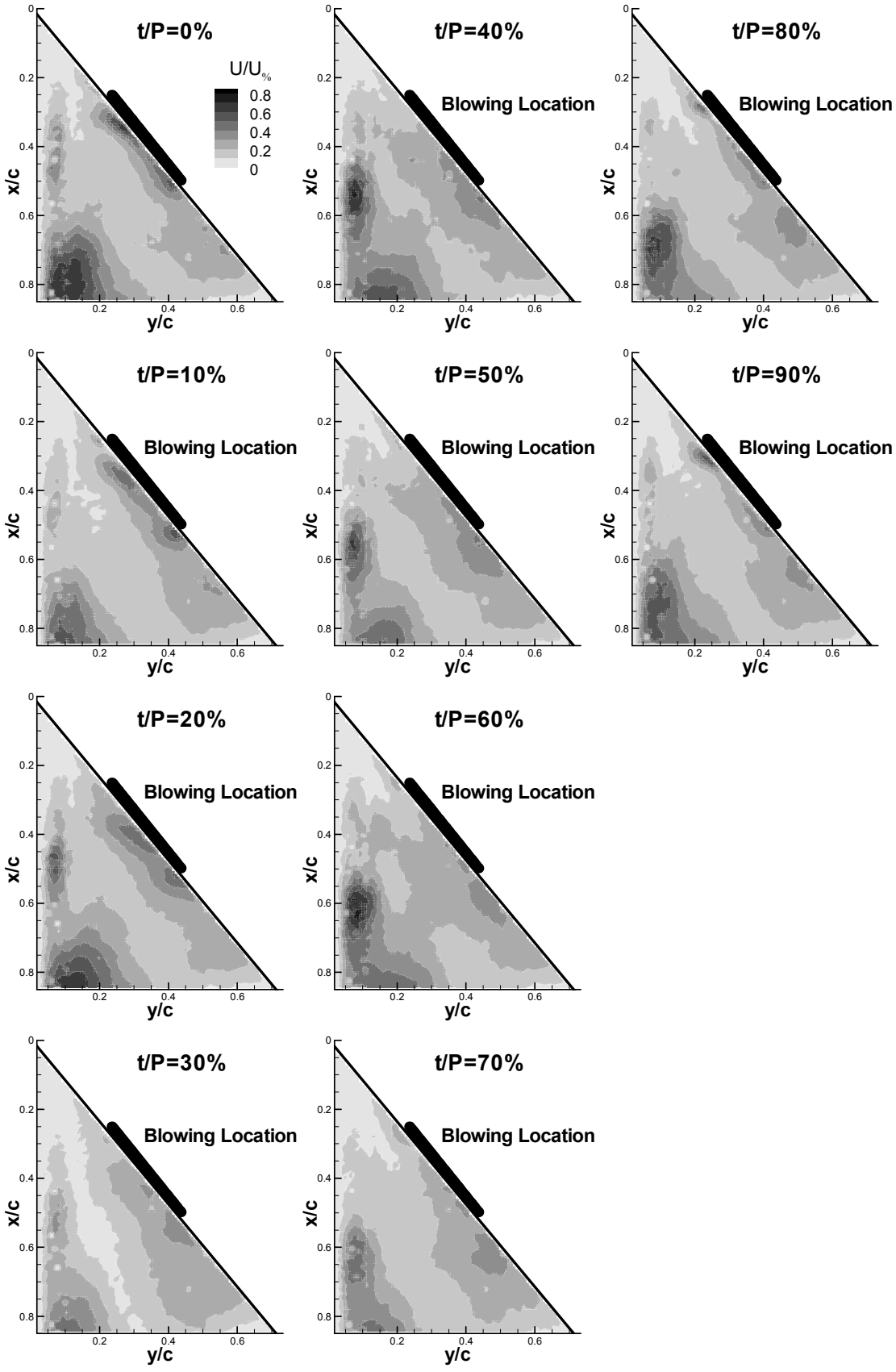

Figure 7-13 Magnitude of phase-averaged near surface velocity at α=30°, C_μ=0.16%, St=1.5 for blowing from a slot between 25%-50% of the leading edge.

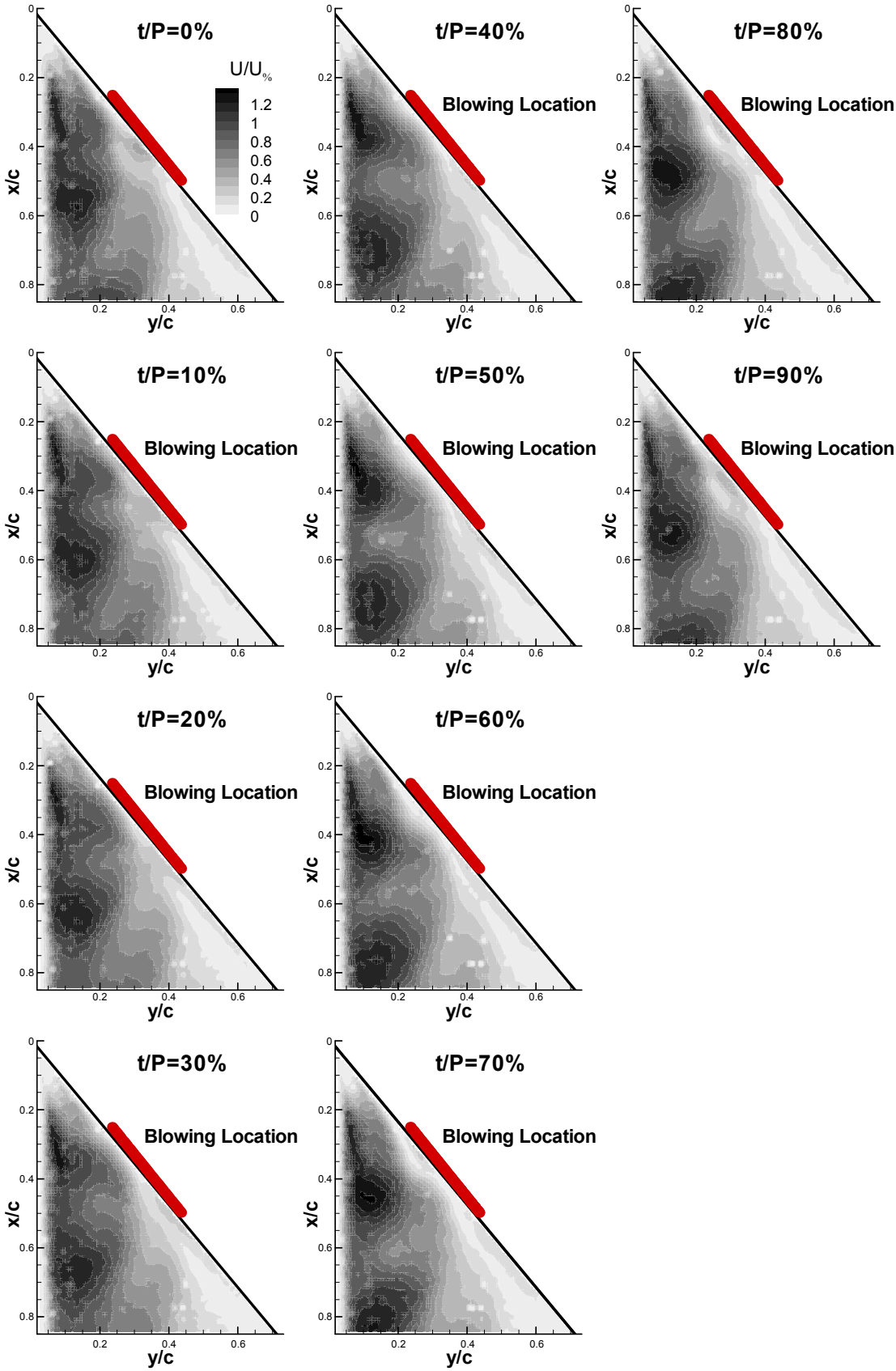

Figure 7-14 Magnitude of phase-averaged near surface velocity at α=30°, C_μ=0.35%, St=1.5 for blowing from a slot between 25%-50% of the leading edge.

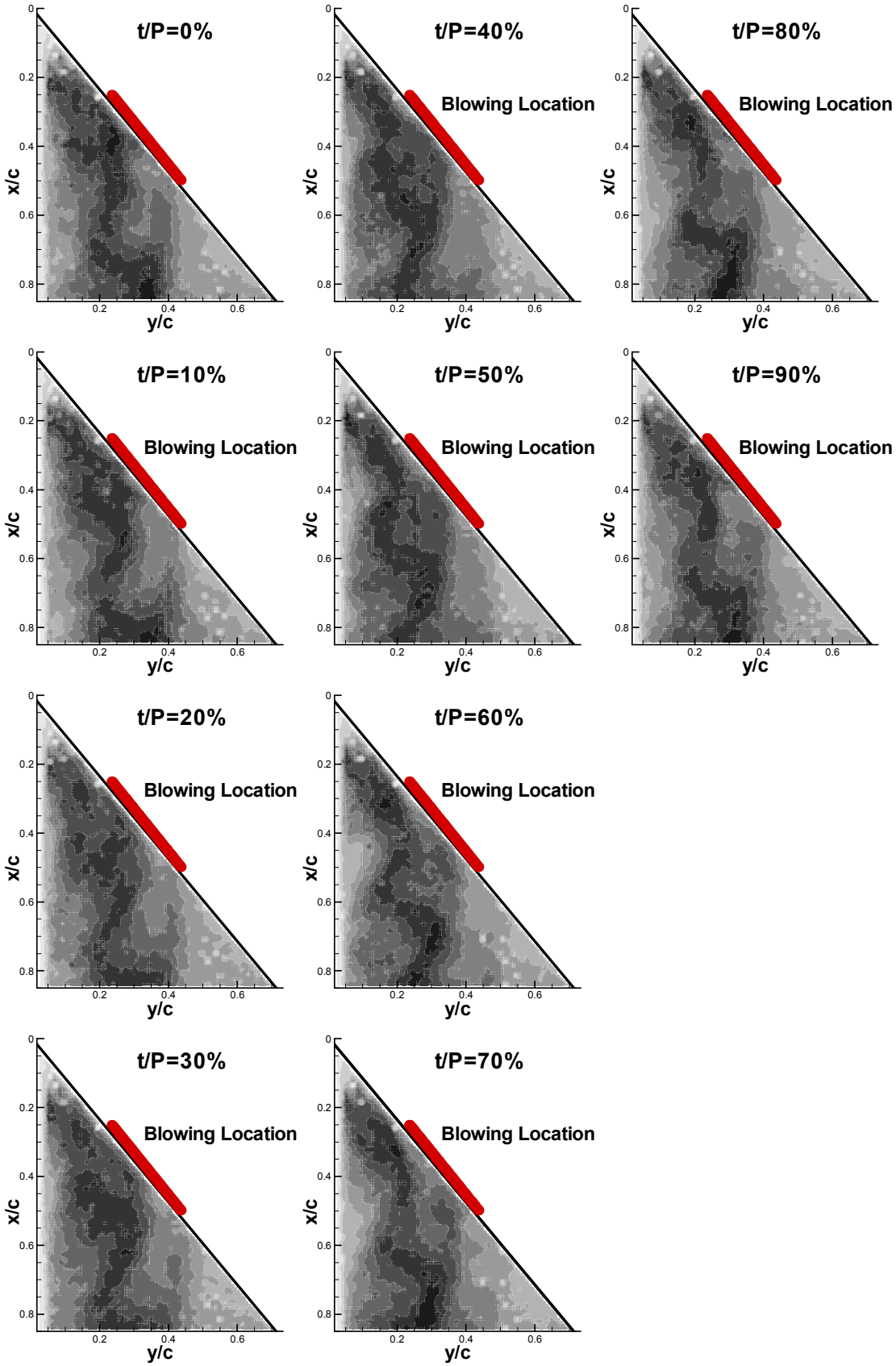

Figure 7-15 Phase-averaged near surface turbulence intensity at α=30°, C_μ=0.35%, St=1.5 for blowing from a slot between 25%-50% of the leading edge.

Chapter 8 Full wing force measurements

Force measurements on a larger full span nonslender delta wing, described in Chapter 3, were conducted in the University of Bath closed circuit wind tunnel. It was important to prove that this method of flow control was effective on full span as well as half span nonslender delta wings. The full wing platform also allowed a more realistic analysis of the potential of unsteady blowing with application to roll control, which has been presented in this chapter. Results from the full wing test are compared to the corresponding half wing case, and the similarities and differences discussed. Results show that unsteady blowing on a full wing platform also shows potential as a method of flow control. Many of the unsteady blowing properties, such as Strouhal number and momentum coefficient, that affect the delay of stall on the half wing model, have a similar effect on the full wing model.

In order to supply air to the leading edge of the wing, highly flexible pipes traversed the force balance. A comparison has been made, presented in Figure 8-1, of the variation in lift coefficient for the no blowing case with and without pipes attached. The effect of the pipes seems to be minor for this case. Additional experiments were conducted where the level of blowing was varied with no free stream velocity and the force measured by the balance was examined. There was a negligible effect on the reading from the force balance when compared to the no blowing case at zero freestream velocity. These results indicated that the addition of the pipes across the balance would not have a significant effect on the forces measured by the force balance.

Initial results obtained using the Dynamco valve setup, described in Chapter 3, are displayed in Figure 8-2. It is worth noting that the angle of attack at which the full wing stalls is much lower than the stall angle that the pressure measurements indicate for the half wing, $\alpha=21°$ for the full wing, compared to $\alpha=23°$-$24°$ for the half wing. The measured stall angle here is consistent with previous experimental results [2], and the difference between the half and full wing stall angle is consistent with the computations of Attar [17]. For a very low momentum coefficient, $C_\mu=0.03\%$, a significant increase in normal force was achieved. The maximum increase in normal force coefficient for this case is 18% at $\alpha=25°$. The increase in maximum normal force coefficient, which is the percentage difference between in the normal force coefficient at stall for each case, is 11%, and stall is delayed by 3°-4°.

An interesting point to note is that at below stall angles of attack, there is a negligible change in normal force coefficient. Pressure measurements outlined in Figure 4-8 with momentum coefficients of $C_\mu=0.05\%$ and above showed a small positive effect on the suction force coefficient for unsteady blowing at pre stall angles of attack. However, measurements at momentum coefficients of $C_\mu=0.01\%$ and $C_\mu=0.02\%$ showed a negligible effect. For this case, at a momentum coefficient of $C_\mu=0.03\%$, it appears the ineffectiveness of unsteady blowing in the pre stall regime is consistent with the half wing results.

The variation in lift and drag coefficient with angle of attack is plotted in Figure 8-3 and Figure 8-4. It is evident that there is a significant increase in lift coefficient with the introduction of unsteady blowing, and a corresponding increase in drag coefficient. Flexible delta wings undergoing self induced vibrations often showed a sudden increase in lift shortly after the stall angle of the corresponding rigid wing case [4]. For the active control case presented, as with the suction force coefficient obtained from pressure measurements, there is no sudden increase in the lift coefficient in the post stall region. Rather, as the no blowing case begins to stall, the lift coefficient for the unsteady blowing case continues to increase with angle of attack, at approximately the same rate as in the pre stall region for the no blowing case. For flexible wings, reattachment occurs as a result of flow induced vibrations of the wing. However, large amplitude flow induced vibrations are only present when the wing is at angles of attack near to stall. When the wing begins to stall, the wing begins to oscillate, reattachment occurs, and there is a sudden increase in lift. Active flow control can be applied before stall occurs, and is not reliant on the wing stalling. The level of reattachment and strength of the vortical region can be increased prior to the onset of stall. As a result the lift curve is smoother through the region where the no blowing case stalls. The increase in maximum lift coefficient, which is the percentage difference between in the lift coefficient at stall for each case, is 8%, witch is less than the optimum case presented by Taylor for a Λ=50° wing of over 20% [4]. As discussed in Chapter 4, it is believed that the level of forcing in the active case presented here is much lower than the level of the forcing associated with flexible wings.

The increase in drag coefficient shown in Figure 8-4 could potentially be useful for rapidly reducing the speed of the aircraft without the loss of lift, for aerodynamic manoeuvres or for landing on short runways. An interesting feature of the plot is that for the no blowing case, after stall the drag coefficient continues to increase, although the rate of increase is reduced. However for the unsteady blowing case, as stall occurs the drag coefficient reduces, and approaches the level of the no blowing case.

Corresponding to the increase in normal force coefficient, there is also a significant increase in magnitude of the negative pitching moment about the apex, shown in Figure 8-5. As with the increase in drag coefficient, this could be useful for the aerodynamic manoeuvres of fighter aircraft and UAVs. It would be beneficial if this increase could also be obtained in the pre stall regime, as indicated by the pressure measurements at higher momentum coefficients.

In an effort to increase the accuracy of the valve system, and the effectiveness of the method, the Dynamco valve was replaced by the Enfield Technologies valve and controller setup discussed in Chapter 3. The slot length was also reduced to 50% of the leading edge, starting at the apex in order to increase the effectiveness of the blowing. Figure 8-6 shows the effect of partial unsteady blowing from 0-50% of the slot length at a range of momentum coefficients. For this case, the tunnel velocity was reduced to alter the momentum coefficient (the valve operating frequency was

also adjusted to achieve a constant Strouhal number). This resulted in a variation of the Reynolds number. As discussed in Chapter 1, it is believed that the change in Reynolds number within this range did not significantly affect the characteristics of the flow. It can be seen from the three momentum coefficients presented, that as the momentum coefficient is increased, the maximum normal force coefficient increases, as does the stall angle. For the highest momentum coefficient, when blowing only over half of the leading edge, unsteady blowing at a C_μ=0.028% delayed stall to α=29°, a delay of 8° over the no blowing case. The percentage increase in normal force coefficient corresponding to Figure 8-6 is shown in Figure 8-7. Unsteady blowing at C_μ=0.028% increases the normal force coefficient by 27% at α=29°. This significant delay in stall and corresponding increase in normal force coefficient highlight that this method of flow control is effective on full delta wings and not just half delta wings.

Figure 8-8 shows that for a fixed angle of attack, in this case α=30°, increasing the momentum coefficient has the effect of increasing the percentage increase in normal force. At some point, increasing the momentum coefficient further results in no further increase in normal force and, as with the pressure measurements, the effect of unsteady blowing becomes saturated. This is seen again for α=27° in Figure 8-9. At all three Strouhal numbers compared in Figure 8-9, the percentage increase in normal force coefficient plateaus. As expected, the Strouhal number of St=1.0 is the least effective of the three Strouhal numbers tested, which is consistent with the results obtained from the pressure measurements. For this angle of attack, it appears that unsteady blowing at St=1.5 generates a higher maximum percentage increase in normal force than unsteady blowing at St=0.75, although both cases result in a significant increase of the normal force coefficient. As indicated by the pressure measurements, this may only be the case for this specific angle of attack, and unsteady blowing at St=0.75 may generate higher normal forces at higher angles of attack. For unsteady blowing at St=1.5 and St=0.75 the momentum coefficient at which the increase in normal force begins to saturate is similar.

The effect of the Strouhal number on the percentage increase in normal force can be seen more clearly in Figure 8-10. For this comparison, momentum coefficients were chosen to be well above the saturation level for the St=1.5 case at α=26°. It is important to note that due to the different chord length of the full wing (c=0.3m) compared to the half wing (c=0.2m), the physical pulsing frequency for a given Strouhal number is different for the full wing case compared to the half wing case. The comparison shows good agreement with results presented for the half wing case in Figure 4-14 and Figure 4-15. For the full delta wing, unsteady blowing at Strouhal numbers around St=1.0 is not as effective at increasing the normal force coefficient as unsteady blowing at Strouhal numbers around St=0.75 and St=1.5. The variation in percentage increase in normal force coefficient is significant, with around an 18% increase achievable at St=1.5, compared to 2% at St=1.0. This shows that the high dependence of the normal force coefficient on the Strouhal number is not a phenomenon restricted to half delta wings and that the effective Strouhal number ranges are similar for both cases. For the full delta wing there are also oscillations in the level of

percentage increase in normal force above St=1.5. The half wing case showed there may be a peak at St=2.0, but this was only eluded to by a singular measurement. The force measurements presented in Figure 8-10 show further peaks in normal force coefficient above St=1.5, in particular at St=1.9. Although there is a definite fluctuation of the percentage increase in normal force above St=1.5, levels do not drop as low as the St=1.1 case.

The potential of using unsteady blowing for roll control has been discussed in Chapter 4 regarding the half wing case. Roll control measurements were made whereby the slot on one side of the leading edge was blocked using a thin layer of tape. The results, presented here for the full wing case for unsteady blowing at St=1.5 and St=1.3, are shown in Figure 8-11. There is some variation in the level of control achievable from blowing from each side of the wing. The right hand side shows a greater level of roll control moment for both Strouhal numbers at the same momentum coefficient. This could be a result of slight geometric discontinuities between the two sides of the wing, or perhaps, more likely, a slight misalignment of the wing to the oncoming flow. In order to correct for this, to make an assessment as to the effectiveness of this method, the roll moment coefficient measured for the two sides has been averaged out, and the results are presented in Figure 8-12. The momentum coefficient used for these results, $C_\mu \approx 0.01\%$, is below the momentum coefficient which indicated that there was potential for pre stall roll control for the half wing ($C_\mu = 0.05\%$). Of the two Strouhal numbers tested for the full wing, the St=1.5 case is more effective than the St=1.3 case at every angle of attack, and the discussion will be based around the St=1.5 case. As discussed in Chapter 1, Nelson [35] estimated that a maximum roll coefficient of $C_l = 0.004$ could be achieved by an aileron at maximum deflection on a $\Lambda = 47°$ UAV model. For angles of attack between $\alpha = 17°$ and $\alpha = 24°$, the roll coefficient produced by the model was greater than $C_l = 0.004$. In addition to this at lower angles of attack, below $\alpha = 17°$, the roll moment coefficient did not drop significantly below $C_l = 0.002$, indicating that at higher momentum coefficients there may be potential to achieve a similar level of roll control to that specified by Nelson, but at angles of attack as low as $\alpha = 11°$. It is difficult to compare the magnitude of the roll moment coefficient from the full wing force measurements to the roll moment coefficient derived from the pressure data of the half wing, due to the approximations made when calculating the roll moment coefficient from the pressure data. When comparing the $C_\mu = 0.01$ case from the pressure measurements presented in Figure 4-18, it is important to look at the difference between the $C_\mu = 0.01\%$ and $C_\mu = 0$ cases to get an appreciation of the level of roll control achievable. The estimated roll coefficient from pressure measurements looks to be approximately 50% less effective than the equivalent roll coefficient from force measurements, however as mentioned above, direct comparisons of magnitude are misleading. Both sets of experiments do display a similar trend, whereby the level of roll control is small at around $\alpha = 15°$, increasing towards the stall angle. That the roll coefficient begins to increase well before stall is different from the behaviour of the normal force coefficient, which at low momentum coefficients tends to increase over the no blowing case only just prior to stall.

Pressure measurements indicated that steady blowing at low momentum coefficients was detrimental and led to a reduction in the suction force coefficient. This is supported by force measurements where blowing at a range of low momentum coefficients reduced the lift coefficient, in particular at angles around stall. Figure 8-13 shows the effect of steady blowing at different angles of attack covering the angle of attack range presented for unsteady blowing. Pre stall ($\alpha<19°$), and well after stall ($\alpha>29°$) steady blowing has little effect on the lift coefficient. This indicates that it is not the momentum of the jet itself that changes the lift coefficient, but rather some interaction between the jet and the shear layer. For angles close to stall there is a reduction in lift coefficient by up to 7% (for $C_\mu=0.031\%$ at $\alpha=21°$). It appears that for the angles of attack around stall, as the momentum coefficient is increased from $C_\mu=0.011\%$ to $C_\mu=0.031\%$, the lift coefficient is reduced. For the momentum coefficient of $C_\mu=0.038\%$, there is an increase in lift coefficient over the $C_\mu=0.031\%$ case, however overall steady blowing at $C_\mu=0.038\%$ remains detrimental. This is similar to the trend shown in for tip 3 for the steady blowing pressure measurements in Figure 4-20, where the suction force coefficient decreases until $C_\mu=0.04\%$, after which it begins to increase. As the decrease in lift is most significant at the stall angle, it appears that steady blowing at low momentum coefficients prevents what would be partial reattached flow from reattaching, and pushes the wing into an early stall.

Further experiments involving unsteady partial blowing from the leading edge of a full span nonslender wing are displayed in Figure 8-14. Here the length of the slot was varied from 25% of the leading edge to 75% of the leading edge (measured from the apex) for an angle of attack of $\alpha=27°$. As expected, the 50% slot length case proved to be more effective at lower momentum coefficients than the 25% slot length case, as well as showing a higher maximum percentage increase in normal force. More surprisingly was the performance of the 75% slot length case. It was expected from pressure measurements that for this case the percentage increase in normal force coefficient would be less than that of the 50% slot length case at low momentum coefficients, and greater at high momentum coefficients. However, the maximum increase in normal force remains below that of the 50% slot length case for all momentum coefficients. In addition, the 75% slot length case appears to plateau at the same rate as the 50% slot length case, and does not appear to increase further at higher momentum coefficients. However, as the momentum coefficients for the full wing case, $C_\mu<0.02\%$, are lower than the momentum coefficients where significant increases in suction force were measured for the half wing case, it is possible that further increases in normal force are achievable at higher momentum coefficients. It is also worth noting that the geometry of the full wing is different to the half wing case and that the angle of attack is also different, $\alpha=27°$ for the full wing partial blowing experiments and $\alpha=30°$ for the half wing partial blowing experiments. Pressure results, studied in more detail than the force measurements presented here, indicated that blowing along a greater portion of the leading edge increased the maximum suction force coefficient achievable.

Force measurements of a slot with a length of 25% of the leading edge length, located at different points on the leading edge, were conducted and are shown in Figure 8-15. Results from the pressure measurements in Chapter 7 indicated that blowing from a slot that begins at the apex is less effective than blowing from a slot that begins at x/c=0.25. In contrast to those results, the force measurements indicated that for a full wing, blowing from the apex (0-25%) was slightly more effective than blowing from 25% to 50% of the leading edge. In addition to this, blowing from 50% to 75% of the leading edge provided a similar level of normal force increase to the 25% to 50% case. As expected, blowing from 75% to 100% of the leading edge proved ineffective. The particular effectiveness of the 0-25% blowing case could be due to a difference in wing geometry between the half and full body wings at the apex. The slot of the half body wing extends to the splitter plate, right to the apex. The slot of the full body wing stops just short of the apex for structural reasons. It may be that this small gap increases the effectiveness of blowing from the region near the apex and reduces any detrimental effects of blowing at the apex. It is also worth considering that although the force measurements appear to plateau, the momentum coefficients are significantly lower than the corresponding pressure measurements shown in Figure 7-2. Pressure measurements at low momentum coefficients, such as the 0-25% case and the 50%-75% case in Figure 7-2, do indicate some low momentum coefficient peaks in this momentum coefficient range, which may be what is presented in Figure 8-15. If the study is to be continued further, force measurements should be conducted for unsteady blowing at higher momentum coefficients.

The force measurements conducted indicate that the potential of unsteady blowing as a means of inducing reattachment and delaying stall is not limited to half wing configurations. For the full wing tested, stall was delayed by up to 8°. Roll control experiments indicated that even for some pre-stall angles, a roll moment could be generated by unsteady blowing from one side of the wing only, indicating that the usefulness of unsteady blowing may not be limited to the delay of stall and increase of lift. One advantage of this method of flow control over flexible wings is that there is no obvious performance change around the normal stall angle of the wing, which means that it may be a more suitable configuration for practical aircraft. The full wing also displayed a very similar response to unsteady blowing at different Strouhal numbers when compared to the half wing, further highlighting Strouhal number as an important parameter. Similarly to the half wing case, steady blowing within the momentum coefficient range tested was not effective for the full wing case.

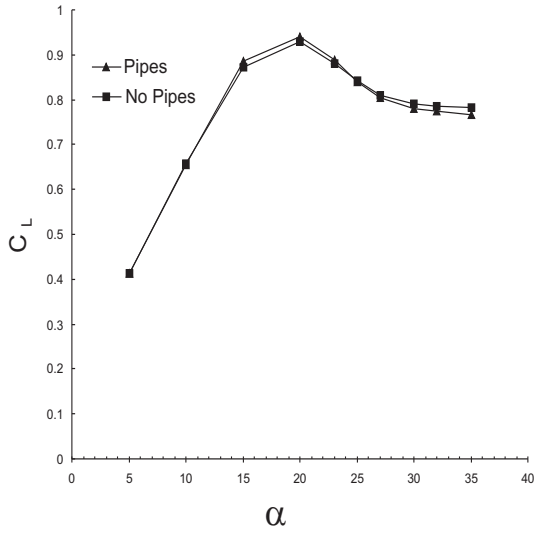

Figure 8-1 Comparison of the lift coefficient for the no blowing case with pipes traversing the force balance, and with no pipes traversing the force balance.

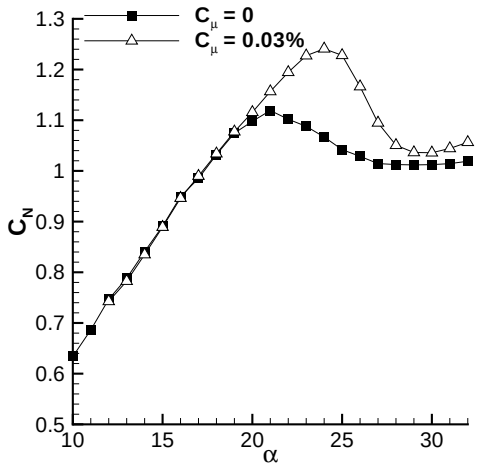

Figure 8-2 Variation in the normal force coefficient with angle of attack for unsteady blowing and no blowing. The Dynamco valve setup was used.

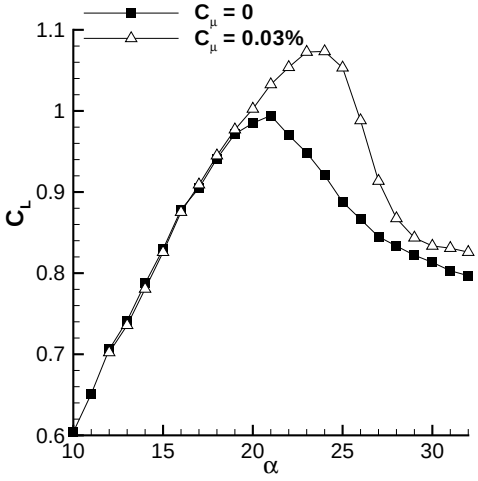

Figure 8-3 Variation in the lift coefficient with angle of attack for unsteady blowing and no blowing. The Dynamco valve setup was used.

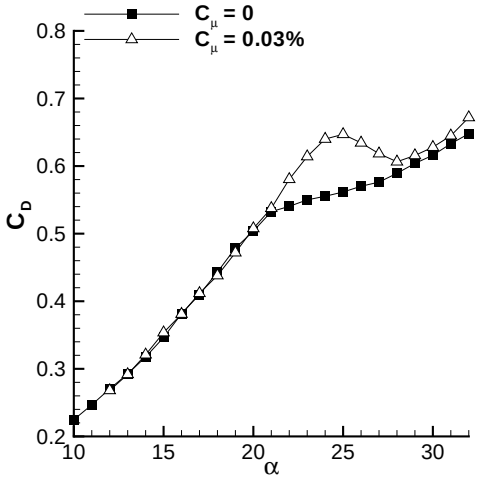

Figure 8-4 Variation in the drag coefficient with angle of attack for unsteady blowing and no blowing. The Dynamco valve setup was used.

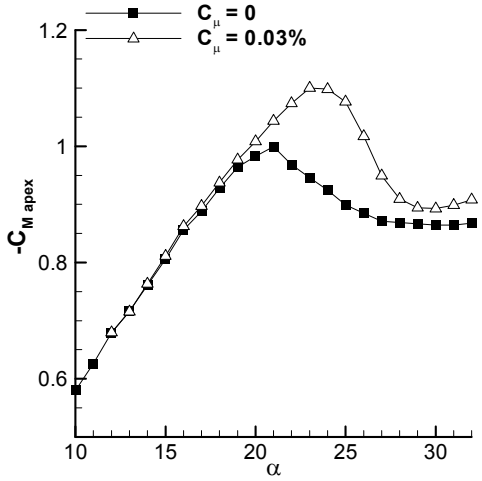

Figure 8-5 Variation in the moment coefficient about the apex with angle of attack for unsteady blowing and no blowing. The Dynamco valve setup was used.

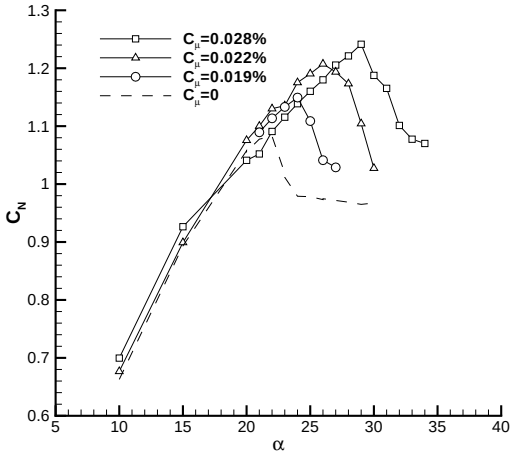

Figure 8-6 Variation in the normal force coefficient with angle of attack for unsteady blowing at a range of momentum coefficients. The Enfield valve setup was used. Blowing from 0-50% of the leading edge. The Reynolds number range was $3.2\times10^5<Re<4.3\times10^5$.

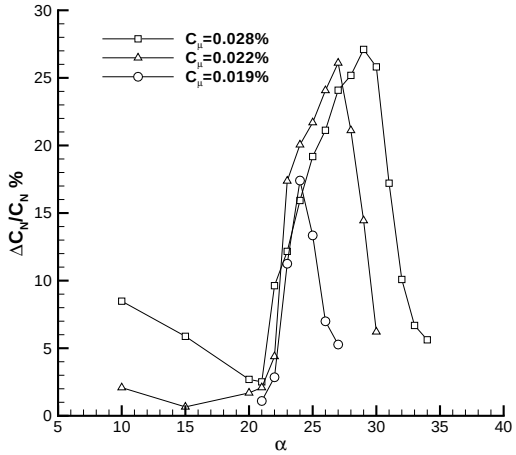

Figure 8-7 Variation in the percent increase in normal force coefficient with angle of attack for unsteady blowing at a range of momentum coefficients. The Enfield valve setup was used. Blowing from 0-50% of the leading edge. The Reynolds number range was $3.2\times10^5<Re<3.2\times10^5$.

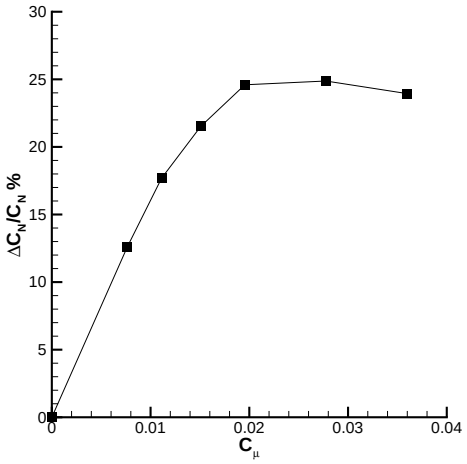

Figure 8-8 Variation in the percent increase in normal force coefficient with momentum coefficient. The Enfield valve setup was used. Blowing from 0-50% of the leading edge. α=30°, St=1.5, Re=3.2×10^5.

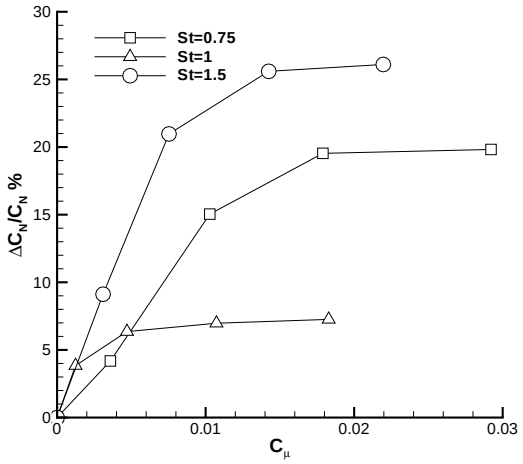

Figure 8-9 Variation in the percent increase in normal force coefficient with momentum coefficient for St=0.75, St=1 and St=1.5. The Enfield valve setup was used. Blowing from 0-50% of the leading edge. α=27°, St=1.5, Re=3.7×10^5.

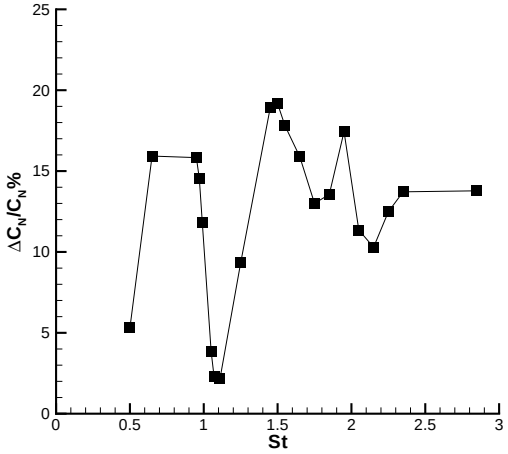

Figure 8-10 The effect of varying the Strouhal number on the percent increase in normal force coefficient. The Enfield valve setup was used. Blowing from 0-50% of the leading edge. 0.5≤St≤2.8. α=26°, Re=3.2×10^5, 0.37%<C_μ<0.47%

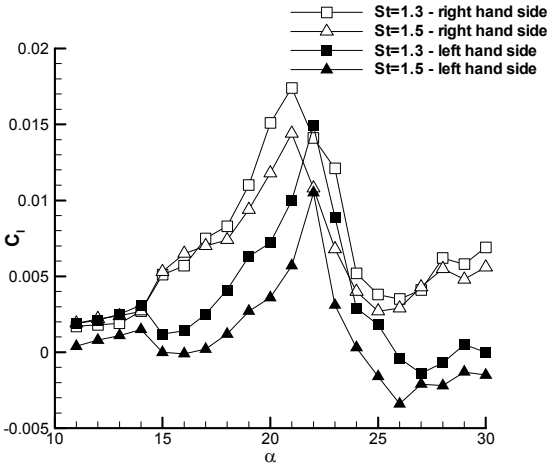

Figure 8-11 Variation in the roll moment coefficient with angle of attack for unsteady blowing from 100% of each side of the wing. Cμ≈0.01%. The Dynamco valve setup was used.

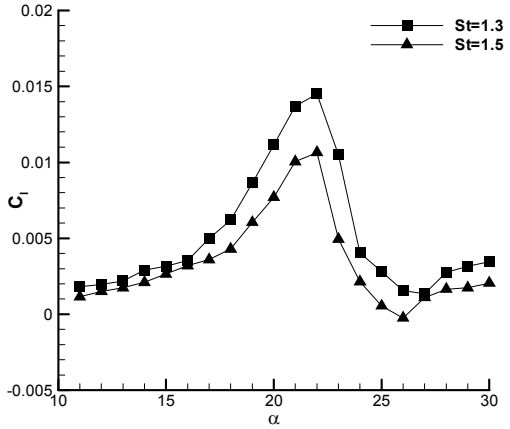

Figure 8-12 Average variation in the roll moment coefficient with angle of attack for unsteady blowing from 100% of one side of the wing. C_μ≈0.01%. The Dynamco valve setup was used.

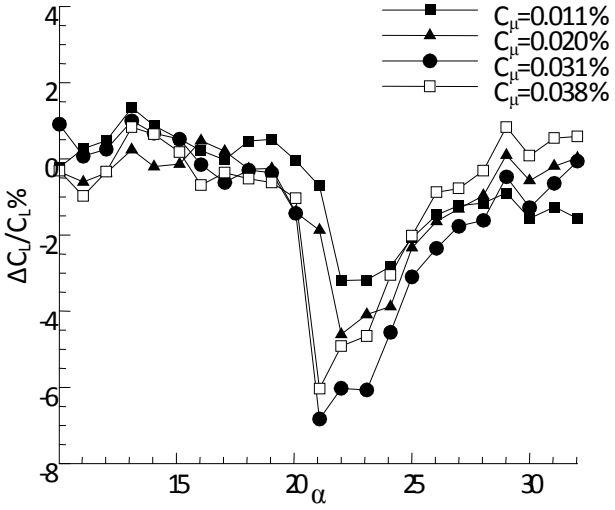

Figure 8-13 Effect of Steady blowing on percent increase in lift coefficient.

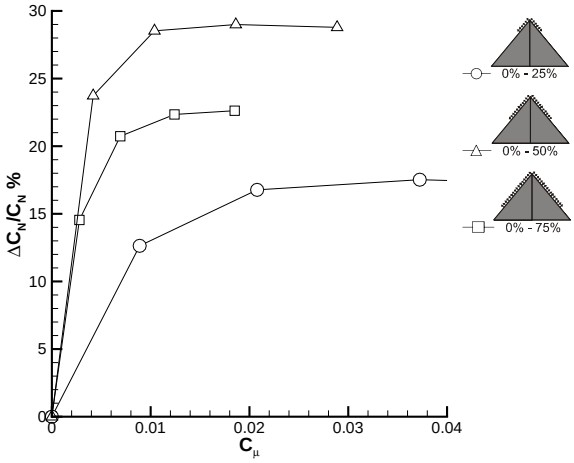

Figure 8-14 The effect of slot length on the percentage increase in normal force coefficient for partial blowing. The Enfield valve setup was used. α=27°, St=1.5, Re=3.2×10^5

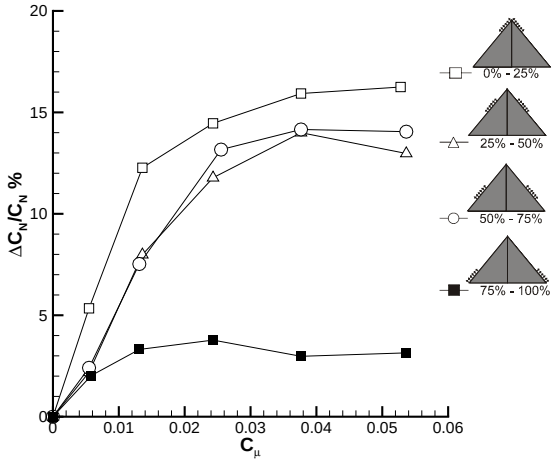

Figure 8-15 The effect of the location of a slot of 25% of the leading edge length on the percentage increase in normal force coefficient for partial blowing. The Enfield valve setup was used. α=27°, St=1.5, Re=4.5×10^5

Chapter 9 Conclusions

Unsteady blowing shows potential as a method of flow control for both full and half span non-slender delta wings with a sweep angle of Λ=50°. Pre-stall flow features, such as a reattached shear layer and strong vortical flow region are maintained well past the natural stall angle of the wing. For the half wing case, unsteady blowing at a sufficient momentum coefficient in the post stall region produces a suction peak which is characteristic of a leading edge vortex. The maximum suction force coefficient can be increased by 17%, and stall delayed by 8° at $C\mu$=0.8%. The suction force coefficient can be increased by 64% at α=32°. Unsteady blowing can have a significant effect on the forces produced over full nonslender delta wings, even at low momentum coefficients. For blowing along the entire leading edge, the normal force was increased by 18% at α=25° and stall delayed by 3°-4° for a momentum coefficient of C_μ=0.03%. By blowing over 50% of the leading edge at C_μ=0.028%, the normal force coefficient was increased by 27% at α=29° and stall was delayed by 8°.

Unsteady blowing causes a more organised and well defined shear layer with a higher concentration of vorticity when compared to the detached shear layer typical of stalled flow. The large region of vorticity associated with the leading vortex is fed by vorticity shed from the leading edge in the form of a discrete perturbation which travels along the shear layer and interacts with the main vortical flow region. The level of circulation in the cross flow plane was increased significantly with unsteady blowing. When pulsing is introduced, the shear layer reattaches to the wing's surface and a vortex flow pattern develops. As the momentum coefficient increases, the centre of the vortex flow pattern moves outboard to a point where the flow becomes fully reattached. After the flow has become fully reattached, the vortical region then ceases to be affected by further increases in momentum coefficient and the affect of unsteady blowing is saturated. PIV measurements through the vortex core indicate that even for cases where the shear layer has reattached to the wing's surface, the vortex undergoes breakdown at or near the apex, upstream of x/c=0.1, forming a turbulent wake with no region of high axial jet like flow beyond this point. This was observed at all momentum coefficients tested.

The main region of vortical flow is highly three dimensional. The perturbation has a cyclic effect on the location of the centre of the vortical region bound by the reattached shear layer, and there is an increasing phase lag in the location of the perturbation in the cross flow plane as the measurement plane is moved down stream. The time taken for the perturbation to travel the length of the shear layer and interact with the main vortical region increases as the measurement plane moves downstream. Near surface experiments show a region of high velocity associated with the attachment of the perturbation to the wing's surface, that moves from near the apex to the trailing edge at a mean chordwise velocity of U/U_∞=0.75.

The time dependant response of the flow to unsteady blowing has been investigated, and it has been found that initially reattachment occurs at the wing's centreline, and moves outboard over

multiple pulsing periods. The time constant for complete reattachment is between $tU_\infty/c=5$ and $tU_\infty/c=7$, depending on the Strouhal number of the unsteady blowing. The time constant for the reattached flow to revert back to stalled flow, once unsteady blowing is stopped, is 2-3 times the time constant for flow reattachment.

Pressure measurements on the wing's suction surface, PIV measurements and force measurements all indicated that the forcing frequency of the unsteady blowing was highly important for effectively controlling the reattachment of the shear layer. Frequencies in the region of to St=0.5 to St=0.75 and St=1.25 to St=1.5 were particularly effective and unsteady blowing at St=1.0 was by comparison ineffective. Cross flow measurements indicate that for the St=0.25, St=0.5, St=1.0 and St=1.25 cases, there appear to be two perturbations shed from the leading edge during every pulse cycle, whereas for St=0.75 and St=1.5, there is only one present. Consistent with these cross flow measurements, the near surface measurements show there are two distinct regions of high velocity per forcing pulse for the St=0.5 case. Spectral analysis of the high frame rate PIV data indicated the presence of an additional instability, confirming the presence of a secondary perturbation.

The most effective blowing geometry was that of tip 3, where the point of blowing was after the flow had separated from the leading edge, but as close as possible to the separation point and perpendicular to the shear layer. Blowing before the separation point had no effect on the pressure distribution over the wing. Steady blowing proved to be ineffective at increasing the suction force coefficient for pressure measurements or the normal force coefficient for force measurements.

For low momentum coefficients, partial blowing from slots in the front half of the wing, but slightly displaced from the apex, can be more effective than blowing across the entire leading edge. However, the larger the slot length, the larger the maximum increase in suction force coefficient. Blowing from the rear half of the leading edge is only beneficial when also blowing from the front half of the leading edge. When blowing from a slot with a length of 25% of the leading edge length, pressure measurements and PIV measurements show that reattachment can occur both upstream and downstream of the blowing location. With partial blowing it is possible to promote reattachment along the length of the wing.

For the purpose of roll control, both pressure measurements and force measurements showed that unsteady blowing has some benefit for pre stall angles of attack. Force measurements showed that for angles of attack between $\alpha=17°$ and $\alpha=24°$ unsteady blowing could achieve a level of roll control similar to that of more conventional flow control techniques of over $C_l=0.004$.

Suggestions for future research

The current work has highlighted important parameters that influence the effectiveness of this method of flow control, such as the momentum coefficient, Strouhal number and the location of partial blowing. Future research into additional combinations of these parameters may provide additional insight into the mechanism initiating reattachment. For example, tests of different

Strouhal numbers for different partial blowing locations may show that the most effective Strouhal number changes with blowing location.

The effect of varying the wing sweep angle has not been studied in the current investigation. Flexible wing experiments highlight this as an important parameter, and an interesting extension of this work would be to conduct research into unsteady blowing at different wing sweep angles.

The PIV experiments conducted in the present work were 2D, either in the cross flow plane, a near surface plane or through the vortex core. It would be interesting to see if stereoscopic PIV data would provide further insight into the flow field. It would also be interesting to conduct further PIV experiments for the full delta wing case, in an effort to better understand the effect of the splitter plate on delaying stall.

The present work has outlined that unsteady blowing at certain Strouhal numbers, such as St=1.0, is not effective at inducing flow reattachment. Another possibility for future research would be to investigate whether the introduction of unsteady blowing at Strouhal numbers with low levels of effectiveness, such as St=1.0, is capable of maintaining already reattached flow. This could be investigated by looking at hysteresis effects as the angle of attack is increased beyond stall with unsteady blowing at St=1.0, or by suddenly switching from a highly effective Strouhal number, such as St=1.5 to a less effective Strouhal number.

The effect of unsteady blowing on pre-stall roll control has only partially been discussed in this investigation, and the majority of work focused on flow control in the post-stall region. Further investigations into the viability of unsteady blowing as a means of pre-stall roll control should be conducted.

In order to further test the practicality of this method of flow control, a pulsing system capable of being used on an aircraft platform will need to be designed. Further work should be conducted into finding practical ways to generate unsteady blowing on an aircraft platform.

References

1 **Gursul, I.** Vortex flows on UAVs: Issues and challenges. *Aeronautical Journal*, 2004, **108**(1090), 597-610.

2 **Taylor, G., Kroker, A. and Gursul, I.** Passive flow control over flexible non-slender delta wings. *43rd Aerospace Sciences Meeting and Exhibit Conference*, pp. 14389-14405 (American Institute of Aeronautics and Astronautics Inc., Reston, VA 20191, United States, Reno, NV, United States, 2005).

3 **Vardaki, E., Gursul, I. and Taylor, G.S.** Physical mechanisms of lift enhancement for flexible delta wings. *43rd Aerospace Sciences Meeting and Exhibit Conference*, pp. 14407-14419 (American Institute of Aeronautics and Astronautics Inc., Reston, VA 20191, United States, Reno, NV, United States, 2005).

4 **Taylor, G., Wang, Z., Vardaki, E. and Gursul, I.** Lift enhancement over flexible nonslender delta wings. *AIAA Journal*, 2007, **45**(12), 2979-2993.

5 **Gad-el-Hak, M.a.B., R. F.** The Discrete Vortices from a Delta Wing. *AIAA Journal*, 1985, **23**(6), 961-964.

6 **Houghton, E.L. and Carpenter, P.W.** *Aerodynamics for Engineering Students*. (Butterworth-Heinemann, Oxford, UK, 2003).

7 **Payne, F.M., Ng, T.T., Nelson, R.C. and Schiff, L.B.** Visualization and Wake Surveys of Vortical Flow Over a Delta-Wing. *AIAA Journal*, 1988, **26**(2), 137-143.

8 **Breitsamter, C.** Unsteady flow phenomena associated with leading-edge vortices. *Progress in Aerospace Sciences*, 2008, **44**(1), 48-65.

9 **Gursul, I., Gordnier, R.** and Visbal, M. Unsteady aerodynamics of nonslender delta wings. *Progress in Aerospace Sciences*, 2005, **41**(7), 515-557.

10 **Taylor, G.S. and Gursul, I.** Buffeting flows over a low-sweep delta wing. *AIAA Journal*, 2004, **42**(9), 1737-1745.

11 **Wang, J and Zhang, W.** Experimental Investigations on Leading-Edge Vortex Structures for Flow over Non-Slender Delta Wings. *Chinese Physics Letters*, 2008, **25**(7), 2250-2253.

12 **Gordnier, R.E. and Visbal, M.R.** Compact differences scheme applied to simulation of low-sweep delta wing flow. *AIAA Journal*, 2005, **43**(8), 1744-1752.

13 **Gursul, I.W., Z. and Vardaki, E.** Review of Flow Control Mechanisms of Leading-Edge Vortices. *3rd AIAA Flow Control Conference* (AIAA, San Francisco, California, 2006).

14 **Yavuz, M.M. and Rockwell, D.** Identification and control of three dimensional separation on low swept delta wing. *AIAA Journal*, 2006, **44**(11), 2805-2811.

15 **Yaniktepe, B. and Rockwell, D.** Flow structure on a delta wing of low sweep angle. *AIAA Journal*, 2004, **42**(3), 513-523.

16 **Earnshaw, P.B. and Lawford, J. A.** Low-Speed Wind-Tunnel Experiments on a Series of Sharp-Edged Delta Wings. *ARC Reports and Memoranda No. 3424*, 1964.

17 **Attar, P., Gordnier, R. and Visbal, M.** Numerical Simulation of the Buffet of a Full Span Delta Wing at High Angle of Attack *47th AIAA/ASME/ASCE/AHS/ASC Structures, Structural Dynamics, and Materials Conference* (American Institute of Aeronautics and Astronautics, Newport, Rhode Island, 2006).

18 **Roos, F.W. and Kegelman, J.T.** Control of Coherent Structures in Reattaching Laminar and Turbulent Shear Layers. *AIAA Journal*, 1986, **24**(12), 1956-1963.

19 **Winant, C.D. and Browand, F.K**. Vortex Pairing - Mechanism of Turbulent Mixing Layer Growth at Moderate Reynolds-Number. *Journal of Fluid Mechanics*, 1974, **63**(APR3), 237-&.

20 **Kostas, J., Soria, J**. and Chong, M.S. Particle image velocimetry measurements of a backward-facing step flow. *Experiments in Fluids*, 2002, **33**(6), 838-853.

21 **Gadelhak, M. and Blackwelder**, R.F. Control of the Discrete Vortices from a Delta Wing. *AIAA Journal*, 1987, **25**(8), 1042-1049.

22 **Gursul, I**. Review of unsteady vortex flows over slender delta wings. *Journal of Aircraft*, 2005, **42**(2), 299-319.

23 **Ol, M.V. and Gharib, M.** Leading-edge vortex structure of nonslender delta wings at low Reynolds number. *AIAA 31st Fluid Dynamics Conference*, 2003, **41**(1), 16-26.

24 **Miau, J.J., Kuo, K.T., Liu, W.H., Hsieh, S.J., Chou, J.H. and Lin, C.K.** Flow Developments Above 50-deg Sweep Delta-Wings with Different Leading-Edge Profiles. *Journal of Aircraft*, 1995, **32**(4), 787-794.
25 **Hasan, M.A.Z. and Khan, A.S.** On the Instability Characteristics of a Reattaching Shear-Layer with Nonlaminar Separation. *International Journal of Heat and Fluid Flow*, 1992, **13**(3), 224-231.
26 **Yoshioka, S., Obi, S. and Masuda, S.** Turbulence statistics of periodically perturbed separated flow over backward-facing step. *International Journal of Heat and Fluid Flow*, 2001, **22**(4), 393-401.
27 **Kim, S., Choi, H. and Yoo, J.Y.** Effect of local forcing on backward-facing step flow with laminar separation. *Journal of Turbulence*, 2007, **8**(6), 1-23.
28 **Yoshioka, S., Obi, S. and Masuda, S.** Organized vortex motion in periodically perturbed turbulent separated flow over a backward-facing step. *International Journal of Heat and Fluid Flow*, 2001, **22**(3), 301-307.
29 **Vardaki, E., Wang, Z. and Gursul, I.** Flow reattachment and vortex re-formation on oscillating low-aspect-ratio wings. *AIAA Journal*, 2008, **46**(6), 1453-1462.
30 **Taylor, G. and Gursul, I.** Lift Enhancement over a Flexible Delta Wing. *2nd AIAA Flow Control Conference* (American Institute of Aeronautics and Astronautics, Inc., Portland, Oregon, USA, 2004).
31 **Gad-el-Hak, M. and Blackwelder, R.F.** Control of the Discrete Vortices from a Delta Wing. *AIAA Journal*, 1987, **25**(8), 1042-1049.
32 **Margalit, S., Greenblatt, D., Seifert, A. and Wygnanski, I.** Delta wing stall and roll control using segmented piezoelectric fluidic actuators. *Journal of Aircraft*, 2005, **42**(3), 698-709.
33 **Rullan, J.M., Vlachos, P.P. and Telionis, D.P.** Flow Control over Trapezoidal-Wing Planforms with Sharp Edges. *44th Aerospace Sciences Meeting and Exibit*Reno, Nevada, 2006).
34 **Rullan, J.M., Vlachos, P.P. and Telionis, D.P.** Aerodynamics and Flow Control over Swept Wings and Wings with Diamond Planform. *45th AIAA Aerospace Sciences Meeting and Exhibit* (American Institute of Aeronautics and Astronautics, Inc., Reno, Nevada, USA, 2007).
35 **Nelson, R., Croke, T., He, C., Othman, H. and Matsuno, T.** Modification of the Flow Structure onver a UAV Wing for Roll Control. *45th AIAA Aerospace Sciences Meeting and Exhibit* (AIAA, Reno, Nevada, 2007).
36 **Greenblatt, D., Kastantin, Y., Nayeri, C.N. and Paschereit, C.O.** Delta Wing Flow Control Using Dielectric Barrier Discharge Actuators. *25th AIAA Applied Aerodynamics Conference* (American Institute of Aeronautics and Astronautics, Inc., Miami, FL, USA, 2007).
37 **John Farnsworth, F.C.**, Marcus Ciuryla, and Michael Amitay and Control of the Stingray UAV at Low Angles of Attack *45th AIAA Aerospace Sciences Meeting and Exhibit* (American Institute of Aeronautics and Astronautics Reno, Nevada, 2007).
38 **Williams, N., Wang, Z. and Gursul, I.** Active Flow Control on a Nonslender Delta Wing. *Journal of Aircraft*, 2008, **45**(6), 2100-2110.
39 **Williams, N., Wang, Z. and Gursul, I.** Active Flow Control on a Nonslender Delta Wing. *AIAA 46th Aerospace Sciences Meeting*Reno NV, 2008).
40 **Margaris, P.** Wing Tip Votex Control by means of Tip Blowing. *Mechanical Engineering* (University of Bath, Bath, 2006).
41 **Moffat, R.J.** Contributions to the Theory of Single-Sample Uncertainty Analysis. *Journal of Fluids Engineering-Transactions of the Asme*, 1982, **104**(2), 250-260.
42 **Moffat, R.J.** Using Uncertainty Analysis in the Planning of an Experiment. *Journal of Fluids Engineering-Transactions of the Asme*, 1985, **107**(2), 173-178.
43 **Bearman, P.W., Harvey, J.K. and Stewart, J.N.** Two and three component velocity measurements in a wind tunnel using PIV. *Aeronautical Journal*, 1999, **103**(1021), 167-173.
44 **Marles, D.** Effect of an axial jet on aircraft wake vortices. *Mechanical Engineering* (University of Bath, 2008).
45 **Lee, G.B., Shih, C., Tai, Y.C., Tsao, T., Liu, C., Huang, A. and Ho, C.M.** Robust vortex control of a delta wing by distributed microelectromechanical-systems actuators. *Journal of Aircraft*, 2000, **37**(4), 697-706.
46 **Yavuz, M.M. and Rockwell, D.** Control of flow structure on delta wing with steady trailing-edge blowing. *AIAA Journal*, 2006, **44**(3), 493-501.
47 **Wang, Z.J., Jiang, P. and Gursul, I.** Effect of thrust-vectoring jets on delta wing aerodynamics. *Journal of Aircraft*, 2007, **44**(6), 1877-1888.

Appendix

Publications from this work:

1 Williams, N., Wang, Z. and Gursul, I. Active Flow Control on a Nonslender Delta Wing. *Journal of Aircraft*, 2008, **45**(6), 2100-2110.
2 Williams, N., Wang, Z. and Gursul, I. Active Flow Control on a Nonslender Delta Wing. *AIAA 46th Aerospace Sciences Meeting*Reno NV, 2008).